Longitudinal Double-Spin Asymmetry of Electrons from Heavy Flavor Decays in Polarized $p+p$ Collisions at $\sqrt{s}=200$ GeV

Katsuro Nakamura

Department of Physics, Kyoto University

January, 2013

Longitudinal Double-Spin Asymmetry of Electrons from Heavy Flavor Decays in Polarized $p + p$ Collisions at $\sqrt{s} = 200$ GeV

A Dissertation Presented

by

Katsuro Nakamura

to

The Graduate School
in Partial Fulfillment of the Requirements
for the Degree of

Doctor of Philosophy

in

Physics

Kyoto University
Jan 2013

abstract

Polarized proton-proton collisions are performed on Relativistic Heavy Ion Collider (RHIC) at Brookhaven National Laboratory for a goal of determination of gluon polarization in a polarized proton. Currently, the gluon polarization $\Delta g(x)$ is well constrained by measurements of double-spin asymmetries for π^0 and jet production at RHIC and polarized deeply-inelastic scattering measurements. Especially, constraints of the gluon polarization in small Bjorken x region is provided by the π^0 double-spin asymmetry measurements. However, achievable Bjorken x region with these measurements is up to the limit of $2\times10^{-2} < x$, because of requirement of minimum transverse momentum for π^0 to satisfy an energy-scale of perturbative chromodynamics (pQCD) technique for theoretical calculations. Due to the lack of measurement, an uncertainty of the polarized gluon distribution in small Bjorken x region, $x < 5\times10^{-2}$, still causes a large uncertainty on the gluon polarization.

We performed the world-first measurement of longitudinal double-spin asymmetry of electrons from decays of hadrons containing heavy flavor (heavy flavor electrons) in longitudinally polarized $p+p$ collisions at $\sqrt{s} = 200$ GeV. The measurement was performed at mid-rapidity ($|\eta| < 0.35$) of the PHENIX detector at RHIC. The heavy flavor quarks are produced by mainly gluon-gluon scattering in the partonic-level interaction. From pQCD calculations of partonic cross section, it is also known that the heavy flavor measurement has large sensitivity for the polarized gluon distribution. Therefore, the double-spin asymmetry is excellent probe to measure $|\Delta g/g(x)|^2$. In addition, because large mass of produced heavy quark supports a minimum energy-scale of the production process, $\sim m_c = 1.4$ GeV (m_c: charm quark mass), the pQCD technique is reliable without transverse momentum requirement in the measurement of the heavy quark electron. Therefore, the measurement enables us to explore the gluon polarization in unexplored Bjorken x region around $x{\sim}2m_c/\sqrt{s} = 1.4 \times 10^{-2}$, and provides essential information for the constraint on ΔG.

The measurement of the heavy flavor electron suffers large electron background, which increases both of statistical and systematic uncertainties on the measured double-spin asymmetry. The dominant background in this measurement is electron pair from Dalitz decay of neutral mesons, especially π^0 and η mesons, and γ conversion in materials. To overcome this challenge, the background was effectively rejected with Hadron Blind Detector (HBD), which was newly installed in PHENIX at 2009. HBD is a position-sensitive gas Čerenkov counter, which not only can identify electron, but also can distinguish between the signal and background electrons by the amount of the produced Čerenkov light around the electron track. Using this feature, a new analysis method with the HBD was developed.

With the HBD, we succeeded to improve the signal purity of the heavy flavor electrons by a factor of about 1.5 compared with a previous result which did not employ HBD. Under the improved purity, the double-spin asymmetry of the heavy flavor electrons with transverse momentum ranging $0.5 < p_T < 3.0$ GeV/c was deduced. The measured asymmetries are consistent with zero within statistical uncertainties. From the measured spin asymmetry, a constraint on the polarized gluon distribution in the proton around $\log_{10} x = -1.6^{+0.5}_{-0.4}$ ($10^{-2} \lesssim x \lesssim 8\times10^{-2}$), $\mu = m^c = 1.4$ GeV was obtained based on a leading order pQCD model as $|\Delta g/g(x,\mu)|^2 < 3.0 \times 10^{-2}$ (1σ).

Contents

Chapter 1

Nucleon Spin Physics

1.1 Outline of Physics Motivation

For many years, human beings have attempted to reveal what material consist of and understand what elemental particles are. For this purpose, inner structure of material has been approached over time, and molecule, atom, nucleus, nucleon, and quark were discovered so far. At the same time, there was a discovery of a new interaction in each step, because they are made up with interactions of different range-scale.

Besides this feature of the discovery, the study of the internal structure plays also an important role to understand the dynamics among the constituent particles. The internal dynamics of a nucleon, which all the materials have, is described as quantum chromodynamics (QCD) among quarks and gluons. The Lagrangian of QCD is already well established as color SU(3) gauge interaction,

$$\begin{aligned} \mathcal{L}_{\mathrm{QCD}} &= \sum\nolimits_q \bar{q}\left(i\not{D} - m_q\right) q - \frac{1}{4} F^a_{\mu\nu} F^{\mu\nu}_a \qquad (1.1) \\ D^\mu &\equiv \partial^\mu + ig\left(\frac{1}{2}\lambda_a A^\mu_a\right) \\ F^{\mu\nu}_a &\equiv \partial^\mu A^\nu_a - \partial^\nu A^\mu_a - g f^{abc} A^\mu_b A^\nu_c, \end{aligned}$$

where q is quark field, m_q is quark mass, A^μ_a $(a = 1 \sim 8)$ is gauge field, λ_a is the Gell-Mann matrix in SU(3), and f^{abc} $(a, b, c = 1 \sim 8)$ is the structure constant of SU(3). However, whereas high energy QCD interaction is well established with the perturbative QCD (pQCD) method, a lot of low energy phenomena, including the QCD dynamics in the nucleon, are still not enough understood.

It is known that nucleon is comprised of three quarks in the naive constituent quark model. However, different from structures of molecule or atom, the dynamic structure of nucleon is not simple due to large strong coupling constant of QCD in the low energy interaction. The quarks in a nucleon create gluons, and the gluons also create quark and anti-quark pairs at every moment. As a result, nucleon can be represented as an aggregation of the three valence quarks and a lot of quarks, anti-quarks, and gluons surrounding them. The microscopic structure of a nucleon is described with a parton model, which represents the quarks, anti-quarks, and gluons (called partons) as distributions of momentum fraction x compared with nucleon momentum (Bjorken x).

The parton distributions have been studied to understand the nucleon structure in the last 40 years. From successes of deep inelastic scattering (DIS) experiments, the parton distributions in an unpolarized nucleon are obtained with accuracy, and then the quark and gluon composition in the nucleon system was revealed. However, they represent only an aspect of spin-independent QCD dynamics in the nucleon, and spin-dependent QCD dynamics is also important especially to build up the nucleon spin 1/2 (in the unit of Planck constant $\hbar$). For further understanding of the nucleon structure including spin-dependent dynamics, it is important to reveal how the partons compose the nucleon spin 1/2.

For the purpose, a lot of polarized DIS experiments were performed. The first breakthrough was achieved by the European Muon Collaboration (EMC) [1, 2] at 1988. They revealed a discrepancy from the Ellis-Jaffe sum rule [3, 4], and suggested that polarization of sea quarks, such as s quark in a nucleon, takes sizable contribution to the nucleon spin. They also suggested that the total polarization of all quark and anti-quark in a proton, $\Delta\Sigma$, is too small to explain the proton spin with the constituent quark model, which expects $\Delta\Sigma = 1$. After these discoveries, experimental efforts [5, 6, 7, 8, 9] focused on a detailed understanding of the spin structure of the proton. The proton spin 1/2 can be decomposed as $\frac{1}{2} = \frac{1}{2}\Delta\Sigma + \Delta G + L_z$ from conservation of angular momentum. The measurements precisely determined $\Delta\Sigma$ to be only about 30% of the proton spin. The remaining proton spin can be attributed to the other components, the gluon spin contribution (ΔG) and/or orbital angular momentum contributions (L_z). Empirically, it is difficult for system in a ground state, like as nucleon, to obtain orbital angular momentum. Therefore, we attempted to understand the gluon polarization ΔG in this work.

The Relativistic Heavy Ion Collider (RHIC) at Brookhaven National Laboratory (BNL), which can accelerate polarized proton beams and collide them at up to the center-of-mass energy of $\sqrt{s} = 510$ GeV, is a unique and powerful facility to study the gluon polarization, because gluon interaction dominantly participates in various production processes in $p + p$ collisions, e.g. π^0, η, jet, heavy quark, and direct γ production. One of the main goals of the RHIC physics program is to determine the gluon polarization through measurements of longitudinal double-spin asymmetries,

$$A_{LL} \equiv \frac{\Delta\sigma}{\sigma}. \tag{1.2}$$

In the equation, σ and $\Delta\sigma$ denote spin-independent and spin-dependent cross sections of a specific process in the polarized $p+p$ collisions. A_{LL} has been measured previously in several channels by the PHENIX and STAR experiments in RHIC, including inclusive π^0 [10, 11, 12, 13], η [14], and jet [15, 16, 17] production.

The total gluon polarization is given by

$$\Delta G(\mu) \equiv \int_0^1 dx \Delta g(x, \mu), \tag{1.3}$$

where x and μ represent Bjorken x and factorization scale respectively. The challenge for the $\Delta G(\mu)$ determination is to precisely map the gluon polarization density $\Delta g(x, \mu)$ over a wide range of x. Using the asymmetries measured of π^0, η, and jet production and the world-data on polarized inclusive and semi-inclusive DIS [5, 6, 7, 8, 9, 18, 19, 20, 21, 22], a global analysis based on pQCD calculations was performed at the next-to-leading order level in the strong coupling constant α_S [23]. The A_{LL} measurements at RHIC as well as the polarized DIS measurements well constrain the gluon polarization $\Delta g(x)$. Especially, constraints of the gluon polarization in small Bjorken x region is provided by the π^0 A_{LL} measurement. However, because of requirement of minimum π^0 transverse momentum $p_T^{\rm min} = 2.0$ GeV/c to satisfy an energy-scale of pQCD calculations, achievable Bjorken x region with the π^0 measurement is up to the limit of about $2{\times}10^{-2}$. Due to the lack of data, large uncertainty of $\Delta g(x, \mu)$ in small Bjorken x region is still remaining, and it causes a substantial uncertainty of the total gluon polarization ΔG.

To overcome above problems, heavy flavor production in p+p collisions, $pp{\rightarrow}Q\bar{Q}{+}X$, is an ideal measurement. The heavy quarks are produced dominantly by the gluon-gluon interaction [24]. And it is known that this process has large sensitivity to $\Delta g(x)$ from spin-dependent cross section calculated with leading order (LO) or next-to-leading order (NLO) pQCD [25, 26, 27]. Therefore, the double-spin asymmetry of the heavy flavor production is excellent probe to measure $(\Delta g/g(x))^2$, because

$$A_{LL}{\sim}\frac{\int dx_1 dx_2\ \Delta\hat{\sigma}_{gg\rightarrow Q\bar{Q}+X}\Delta g(x_1)\Delta g(x_2)}{\int dx_1 dx_2\ \hat{\sigma}_{gg\rightarrow Q\bar{Q}+X}g(x_1)g(x_2)}{\sim}\langle\frac{\Delta\hat{\sigma}_{gg\rightarrow Q\bar{Q}+X}}{\hat{\sigma}_{gg\rightarrow Q\bar{Q}+X}}\rangle\left(\frac{\Delta g(x)}{g(x)}\right)^2, \tag{1.4}$$

where $\hat{\sigma}_{gg\rightarrow Q\bar{Q}+X}$ and $\Delta\hat{\sigma}_{gg\rightarrow Q\bar{Q}+X}$ denote spin-independent and spin-dependent cross sections of the heavy flavor production in the parton interaction, respectively. In addition to the sensitivity for the gluon polarization, this process extends the explored Bjorken x region of $\Delta g(x)$ as follows. In the heavy flavor production, the large mass of the quark (charm: $m_c \sim 1.4$ GeV/c^2 and bottom: $m_b \sim 4.8$ GeV/c^2) requires large center-of-mass energy ($> 2m$) in the partonic interaction and it supports large energy-scale for the reliable pQCD cross section calculations at the whole p_T region. Hence, different from π^0 and jet production, any minimum limits of p_T are not required in the heavy flavor production. For the heavy flavor production in $\sqrt{s} = 200$ GeV $p + p$ collisions, charm quark production $pp{\rightarrow}c\bar{c} + X$ is dominant compared with bottom quark production $pp{\rightarrow}b\bar{b} + X$. The Bjorken x region covered with the charm production is centered at as small as around $2m_c/\sqrt{s} = 1.4 \times 10^{-2}$. Therefore, A_{LL} of this process enable the world-first approach on the gluon polarization in small Bjorken x region $x < 2{\times}10^{-2}$, which is important to reduce the uncertainty on ΔG.

At PHENIX, hadrons containing heavy flavors are identified through their semi-leptonic decays to electrons and positrons, which are called “heavy flavor electrons” (HFe) [28, 29]. Hence, we measured the double-spin asymmetry of the heavy flavor electrons at the PHENIX detector.

The measurement of the heavy flavor electron suffers large electron background. To obtain the double-spin asymmetry of the heavy flavor electron, the double-spin asymmetry of the background process is to be subtracted from the measured double-spin asymmetry of inclusive electron production. Hence, the background enlarges uncertainties of the double-spin asymmetry measurement, and introduces other uncertainties from double-spin asymmetry of the background. The dominant background of the heavy flavor electron is electron pair from Dalitz decay of π^0 and η, and γ conversion in materials. The electron pair has small pair angle because they are produced by real and virtual photon conversions. To remove the background efficiently, Hadron Blind Detector (HBD), which was newly installed in PHENIX at 2009, plays an important role in the present measurement. HBD is a position-sensitive gas Čerenkov counter, which identifies electron using cluster signal created by its Čerenkov light. Whereas heavy flavor electron creates a single cluster on the HBD, electron pair with small opening angle ($\lesssim 0.1$ rad) creates a merging cluster which has about twice amplitude of signal charge. Using the difference of cluster charges between the heavy flavor electron and the electron pair, the HBD can distinguish them from inclusive reconstructed electrons. The HBD also play important role to reduce K decay background. The K decay (K_{e3}: $K \to e\nu\pi$ decay) is other main background of the heavy flavor electron measurement especially at low transverse momentum region $p_T < 1.0$ GeV/c. The double-spin asymmetry of the K_{e3} background is not well known, and therefore it is difficult to be subtracted from the measured asymmetry with accuracy. Since the HBD is installed around the beam vertex and detects only electrons created within radius of $R{\sim}10$ cm, the K_{e3} electrons are significantly rejected by the HBD. The HBD enable us to measure the double-spin asymmetry of the heavy flavor electrons.

In this paper, we describe the first measurement of this asymmetry with the new detector HBD, and a resulting constraint on the gluon polarization with a leading order pQCD calculation. For the sake of simplicity, we use the word “electron” to include both electron and positron throughout this paper, and distinguish by charge where necessary. In the following section, we summarize the physics framework for the spin structure of nucleon and the current status of the gluon polarization in the nucleon, which are also described elsewhere [30, 31, 32, 33, 34, 35, 36, 37].

1.2 Nucleon Spin Structure and Parton Model

1.2.1 Parton Model

Whereas a nucleon in a constituent quark picture is drawn as simple composition of three quarks, namely *uud* for a proton and *udd* for a neutron, the one in a microscopic picture is drawn as a complex of uncountable quarks, anti-quarks and gluons which are distributed in momentum space in addition to the three valence quarks. This microscopic picture is called “parton model”. Figure 1.1(a) and 1.1(b) show the two different pictures of a proton. The u-quark and d-quark appeared in the constituent quark picture are not point-like particles, but they are dressed with quarks, anti-quarks and gluons. Surprisingly, the dressed quarks have almost same physical characteristics (spin, charge, flavor, color, and so on) as the point-like u-quark and d-quark other than their mass and magnetic moment.

The parton model describes nucleon in high energy phenomena, where the nucleon has relativistic velocity. The quark, anti-quark and gluon in the nucleon, which have the same relativistic velocity, are called “partons” and represented as probability distributions of finding the particles of longitudinal momentum fraction x in the parent nucleon. Namely a parton of momentum fraction x in a nucleon of momentum P has momentum xP. The fraction x is called Bjorken x and varies in the range of $0 < x < 1$.

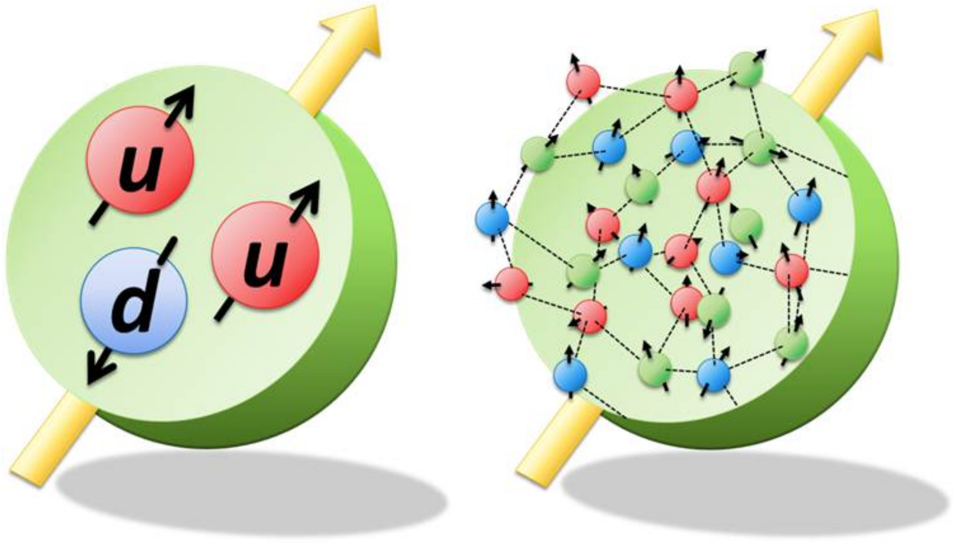

(a) Constituent quark model. (b) Parton model.

Figure 1.1: Comparison of (a) the constituent quark model and (b) the parton model. The large spherical body represents a proton and the small spheres in the proton are the quarks and anti-quarks. In the parton model, dashed lines represent gluons.

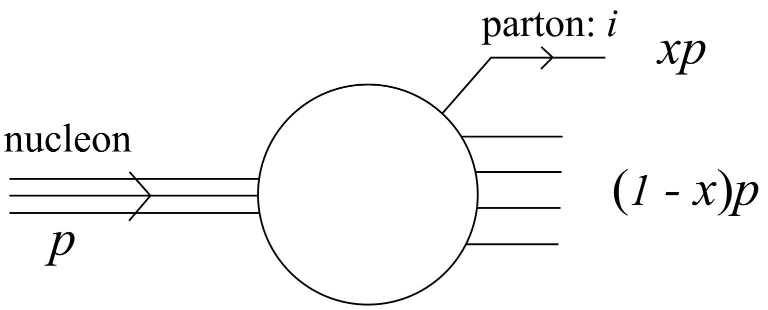

Figure 1.2: A picture of the parton of momentum fraction x in the nucleon of momentum p.

In the parton model, understanding of nucleon structure can be translated into understanding distributions of the quarks, anti-quarks and gluons in the nucleon as functions of Bjorken x. In a primitive parton model, the transverse momentum is ignored. Figure 1.2 displays a picture of a parton of Bjorken x in a nucleon. Considering that quark and anti-quark simultaneously appear (disappear) via a pair creation (annihilation), the net amount of the quarks can be defined as a difference of the amounts of the quarks and anti-quarks. The net quarks are called “valence quarks”, and the other quarks are called “sea quarks”.

The probability distributions of the partons are generally denoted as

$$f_i(x) \equiv \frac{dP_i}{dx}, \tag{1.5}$$

where $i = u, d, s, ..., g$ and P_i is the probability of finding the parton of Bjorken x. The distribution for a specific quark or gluon is also denoted as

$$\begin{array}{ccl} \text{quark, anti-quark} & : & u(x), \bar{u}(x), d(x), \bar{d}(x), s(x), \bar{s}(x), ... \\ \text{gluon} & : & g(x). \end{array} \tag{1.6}$$

These distributions are called parton distribution functions (PDFs).

The momentum conservation requires a sum relation of

$$\sum_i \int_0^1 dx\ x f_i(x) = 1. \tag{1.7}$$

As explained above, difference between the numbers of quarks and anti-quarks should be the number of valence quarks. Then, requirements for charge of +1, baryon number of +1, strangeness of 0 in the proton deduces the following sum rules,

$$\begin{array}{ccccll} \int_0^1 dx\,[u(x)-\bar{u}(x)] & = & \int_0^1 dx\ u_v(x) & = & 2, & \\ \int_0^1 dx\,\left[d(x)-\bar{d}(x)\right] & = & \int_0^1 dx\ d_v(x) & = & 1, & \\ \int_0^1 dx\,[q(x)-\bar{q}(x)] & = & \int_0^1 dx\ q_v(x) & = & 0 & \text{for } q = s, c, b, t, \end{array} \tag{1.8}$$

where $q_v(x)$ represents a PDF for the valence quark.

The PDFs were studied by various deep inelastic scattering (DIS) experiments and their functional shapes were already determined with good accuracy. The experimental determination of the PDFs are described in Sec. 1.3. One of the interesting discoveries from the measurements is that the quarks and anti-quarks carry only about half of momentum of the nucleon. Another half is attributed to gluons. Thus the gluons, which are just radiations from the quarks and anti-quarks, play an important role to describe the proton structure. Before explaining the experimental determination of the PDFs, it is worth to introduce a polarized parton distribution function (polarized PDF), which is a main subject of this work.

1.2.2 Polarized Parton Distribution Function

The next step to understand the proton structure is understanding how the partons form the proton spin $s_z/\hbar = 1/2$. For this purpose, we introduce the polarized PDF. In this polarized parton model, new PDFs which represent spin-dependent parton distributions in a proton polarized along direction of n are defined as

$$\begin{array}{ll} f_i^+(x;n) & \equiv \frac{dP_i^+}{dx}(x;n), \\ f_i^-(x;n) & \equiv \frac{dP_i^-}{dx}(x;n), \end{array} \tag{1.9}$$

where $P_i^{\pm}(x;n)$ represents the probability of finding a parton with Bjorken x and spin $\pm 1/2$ for quarks or ± 1 for gluons along the direction n. By definition, unpolarized PDF can be written as

$$f_i(x) = f_i^+(x;n) + f_i^-(x;n) \tag{1.10}$$

for any n. Especially when n is oriented to the proton momentum direction, longitudinal polarized PDF is defined as net polarization of the parton, namely

$$\Delta f_i(x) \equiv f_i^+(x; p/|p|) - f_i^-(x; p/|p|). \tag{1.11}$$

Here, $f_i^\pm(x; p/|p|)$ is interpreted as PDF of finding helicity ± parton in helicity + proton, respectively.[1]

Because the partons are bound together by means of QCD interaction, the parity conservation of QCD requires

$$f_i^+(x; -p/|p|) = f_i^+(x; p/|p|), \tag{1.13}$$
$$f_i^-(x; -p/|p|) = f_i^-(x; p/|p|). \tag{1.14}$$

The first equation represents that the PDF of helicity − parton in helicity − proton is same as the PDF of helicity + parton in helicity + proton and the second equation is for opposite helicity parton.

1.3 Experiments for PDF Measurement

1.3.1 Deep Inelastic Scattering (DIS) experiment

To investigate the functional shape of the quark PDF, DIS is an ideal method. The DIS is lepton-nucleon inelastic scattering, $l\ N \to l + X$, where time-scale of lepton-parton interaction is enough shorter than one of bounding interaction among partons (impulse approximation). The diagram of the DIS is shown in Fig. 1.3(a). In the parton model, the DIS can be interpreted as interaction between the lepton and a parton in the nucleon at a leading order diagram as shown in Fig. 1.3(b). Since gluon can not interact with the lepton in the leading order, the interacting parton in the diagram is only quark.

We denote four-dimensional momentum of the nucleon as p and four-dimensional momentum of the incident and outgoing lepton as k and k', respectively. Especially in a fixed target experiment with a lepton beam, p can be represented to be $(M, \mathbf{0})$ in the laboratory frame, where M is the nucleon mass. The virtual photon momentum is $q = k - k'$, which can be easily measured in the DIS experiment by detecting the incident and outgoing lepton momenta. q gives energy-scale of the DIS experiment as $Q^2 \equiv -q^2$. The impulse approximation requires large energy-scale such as,

$$Q^2 \gg M^2. \tag{1.15}$$

---

[1] On the other hand, when n is perpendicular to the proton momentum direction, we can also define transverse polarized PDF as

$$\delta f_i(x) \equiv f_i^+(x; r) - f_i^-(x; r), \tag{1.12}$$

where r denotes perpendicular direction to the proton momentum. However, it is beyond the scope of this paper to explain the transversely polarized PDF. For detailed description about the transversity, please see elsewhere [38, 39].

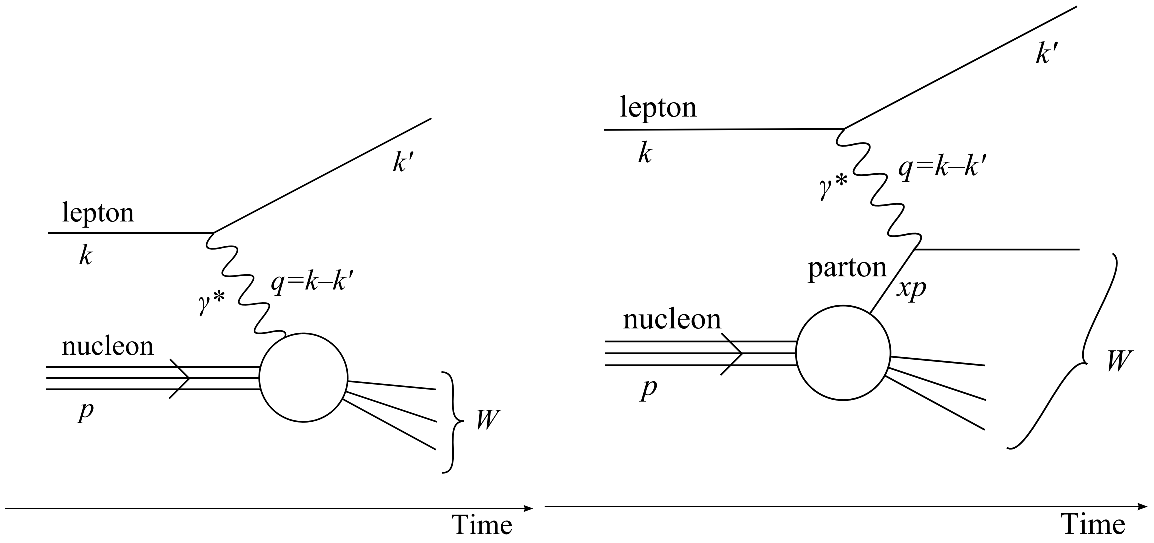

(a) Diagram of DIS.

(b) Diagram of DIS in the parton model.

Figure 1.3: (a) Diagram of DIS in a leading order interaction. (b) Diagram of DIS in the parton model, which is represented as the lepton-parton scattering.

When we consider the virtual photon interacts with a parton of Bjorken x, and therefore the parton has momentum of xp, the mass consistency of the parton before and after the interaction requires

$$(xp)^2 = (xp+q)^2. \tag{1.16}$$

This relation can be translated to be

$$x = \frac{Q^2}{2p\cdot q}, \qquad \text{where} \quad Q^2 \equiv -q^2. \tag{1.17}$$

In a fixed target experiment, $p\cdot q$ is equal to $M\nu$, where ν is energy transfer from the lepton in the laboratory frame, namely $\nu = k_0 - k_0'$. This means Bjorken x of the interacting parton can be obtained by measuring only the kinematics of the lepton.

Figure 1.4 shows kinematics of the DIS experiment in the nucleon rest frame. Using the kinematic variables in Fig. 1.4, unpolarized and polarized cross section of DIS can be represented as

$$\frac{d^2\sigma_{\mathrm{DIS}}}{d\Omega dE'}(E,\theta,E') = \frac{4\alpha^2E'^2}{Q^4}\left(\frac{2\nu}{M}\sin^2\frac{\theta}{2}F_1(x,Q^2)+\cos^2\frac{\theta}{2}F_2(x,Q^2)\right)\frac{1}{\nu}, \tag{1.18}$$

$$\frac{d^2\Delta\sigma_{\mathrm{DIS}}}{d\Omega dE'}(E,\theta,E') = \frac{2\alpha^2}{Q^2}\frac{E'}{E}\left(\frac{E+E'\cos\theta}{M}g_1(x,Q^2)-\frac{Q^2}{M\nu}g_2(x,Q^2)\right)\frac{1}{\nu}\lambda_N\lambda_l, \tag{1.19}$$

where λ_N and λ_l represent the initial helicities (±1) of the nucleon and lepton in the center-of-mass system. F_1, F_2, g_1, and g_2 are called structure functions which describe the nucleon structure.

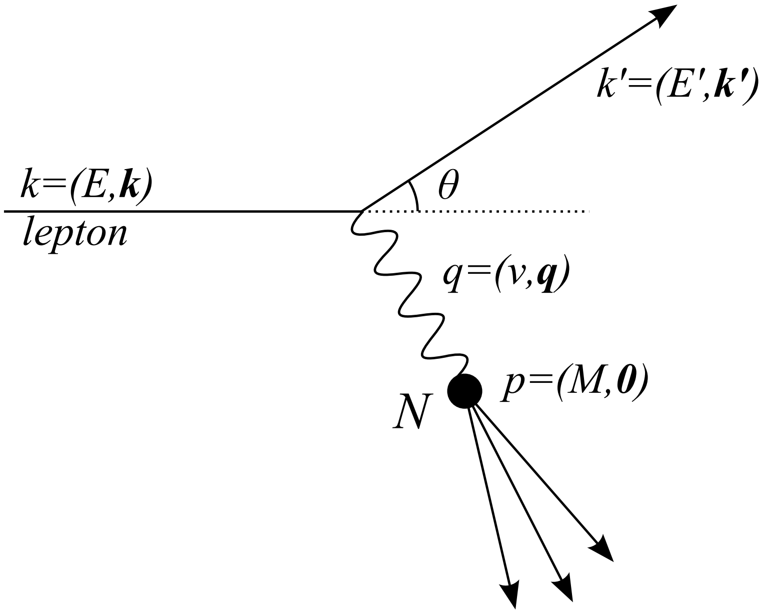

Figure 1.4: Kinematics of the DIS experiment in the nucleon rest frame.

According to Appendix A, the relations between the structure functions and the quark PDFs can be deduced as

$$\begin{aligned} F_1(x,Q^2) &= \frac{1}{2}\sum_q e_q^2 f_q(x), \qquad (1.20)\\ F_2(x,Q^2) &= x\sum_q e_q^2 f_q(x), \qquad (1.21)\\ g_1(x,Q^2) &= \frac{1}{2}\sum_q e_q^2 \Delta f_q(x), \qquad (1.22)\\ g_2(x,Q^2) &= 0. \qquad (1.23)\end{aligned}$$

The measurement of the structure functions with the DIS experiment gives us information of the unpolarized and polarized PDFs.

1.3.2 Semi-Inclusive DIS (SIDIS) experiment

As discussed above, the DIS experiment can access to quark PDF. However, Eqs. 1.20 - 1.23 mean that the measurement can not separate the structure functions into each flavor PDF. To investigate flavor-dependent quark PDF, semi-inclusive DIS (SIDIS) measurement which detects high momentum π or K as well as the scattered lepton in the final state is a useful tool and is performed at the SMC (CERN) [18], HERMES (DESY) [19, 20], and COMPASS (CERN) [21, 22] experiments. A diagram of the SIDIS interaction is shown in Fig. 1.5. The process $D_i^{\pi/K}$ in the figure represents fragmentation of scattered particle i into π or K. In contrast to the inclusive DIS experiment, the detected particles in the SIDIS experiment are high-energy[2] charged π or K in coincidence with the scattered lepton. For large energy fraction $E_{\pi/K}/E_{\gamma^\star}\to 1$ where $E_{\pi/K}$ ($E_{\gamma^\star}$) is energy of the π or K (virtual photon), the most probable occurrence is that the detected π and K contain the struck quark or anti-quark in their valence Fock state. Therefore, they have different sensitivity for the flavor of the struck quark and solve the flavor-separated quark PDF [40].

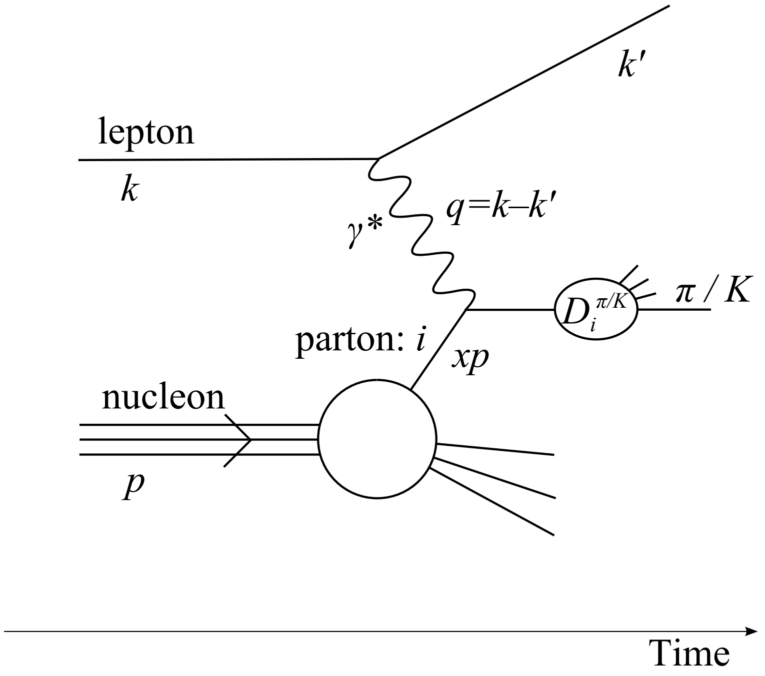

Figure 1.5: Diagram of SIDIS.

In leading order approximation, the structure functions after tagging a hadron h ($=\pi^\pm, K^\pm$) can be represented as

$$F_1^h(x,Q^2) \sim \frac{1}{2}\sum_q e_q^2 f_q(x)\int_{z_{\min}}^1 dz D_q^h(z,Q^2), \tag{1.24}$$

$$F_2^h(x,Q^2) \sim x\sum_q e_q^2 f_q(x)\int_{z_{\min}}^1 dz D_q^h(z,Q^2), \tag{1.25}$$

$$g_1^h(x,Q^2) \sim \frac{1}{2}\sum_q e_q^2 \Delta f_q(x)\int_{z_{\min}}^1 dz D_q^h(z,Q^2), \tag{1.26}$$

$$g_2^h(x,Q^2) \sim 0, \tag{1.27}$$

where $z_{\min} \sim 0.2$. Here $D_q^h(z,Q^2)$ [41] is the fragmentation function for the struck quark or anti-quark q to produce the hadron h carrying energy fraction $z = E_h/E_q$ in the target rest frame. Since $\int_{z_{\min}}^1 dz D_q^h(z,Q^2)$ varies among the initial quark q and the final hadron h, the measurement of the structure functions with tagging several hadrons enable us to solve the flavor-dependent PDFs.

---

[2] typically greater than 20% of the energy of the incident virtual photon

1.3.3 Hadron collision experiment

Since DIS experiments use virtual photon to probe the nucleon, they can not access the gluon contribution in leading order process. Hence, hadron collisions play a role for the complement study of the gluon PDF, which can access gg, gq, and qq interactions at a leading order. In the hadron collisions, the gluon PDF can be studied by measuring cross sections of specific particle productions. Hadron collider experiments are performed at Tevatron ($p\bar{p}$) and LHC (pp), and polarized hadron collider experiment is at RHIC ($\vec{p}\vec{p}$), which is a world-only polarized hadron collider.

The factorization theorem [42, 43, 44] describes relations between the measured cross sections and the parton PDF. It states that large momentum-transfer reactions can be factorized into long and short-distance contributions. The long-distance components contain information of PDF. The short-distance interaction is a hard scattering of partons and can be calculated from perturbation theory. While PDF describes universal properties of the nucleon and is same in different reactions, the short-distance interaction varies depending on the hard scattering.

For an example, we consider the cross section of π production $pp \to \pi + X$, where π has large transverse momentum p_T, ensuring large momentum transfer. The factorization theorem divides the process into three steps as shown in Fig. 1.6, and represents the cross section as

$$\begin{aligned} d\sigma(pp \to \pi + X) &= \Sigma_{a,b,c} \int dx_a \int dx_b \int dz_c \\ &\quad f_a(x_a, \mu) f_b(x_b, \mu) d\hat{\sigma}_{ab\to c}(x_a p_A, x_b p_B, \frac{p_\pi}{z_c}, \mu) D_c^\pi(z_c, \mu), \end{aligned} \tag{1.28}$$

where the sum is over all contributing partonic channels $a+b \to c+X$ with the associated partonic cross section $d\hat{\sigma}_{ab\to c}$. $f_{a,b}$ describe the PDF of partons a and b respectively, which include gluons as well as quarks. The outgoing particle c hadronizes into π with fragmentation function D_c^π. Any factorization of a physical quantity into contributions associated with different length scales will rely on a factorization scale that defines the boundary between what is referred to as short-distance and long-distance. In this case, this scale is represented by μ in Eq. 1.28. Essentially, μ is arbitrary and does not change the resulting cross section. Then, the dependence on μ of the calculated cross section is interpreted as an uncertainty in the theoretical prediction. This dependence on μ decreases in higher-order perturbation theory. The partonic cross section $d\hat{\sigma}_{a+b\to c}$ can be estimated with perturbation theory, and the fragmentation function $D_c^\pi(z)$ has been studied at e^+e^- colliders. Therefore, measuring the cross section, we can study the PDF $f_{a,b}(x)$.

Using the same technique, longitudinally polarized PDF can be investigated by performing longitudinally polarized pp collisions at RHIC. There are four helicity combinations of the colliding two protons. For these combinations, we can define four helicity-dependent cross sections for specific particle production as

$$d\sigma_{++}, \quad d\sigma_{+-}, \quad d\sigma_{-+}, \quad d\sigma_{--}, \tag{1.29}$$

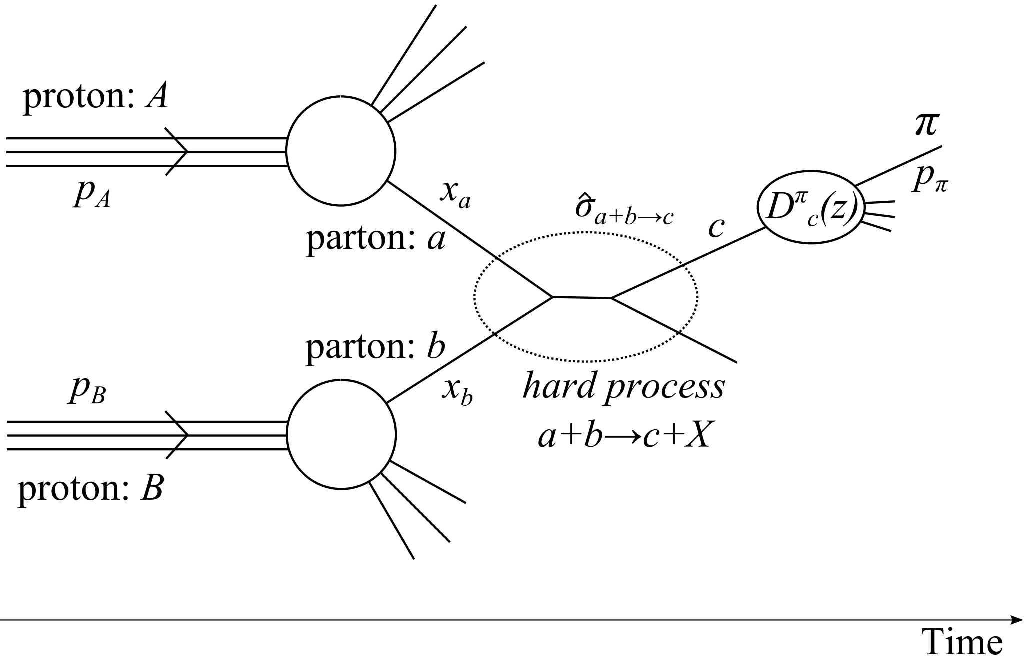

Figure 1.6: Diagram of π production in pp collisions. The process is factorized into three parts: PDF, partonic hard scattering, and fragmentation into hadrons.

where two signs in the subscript represent helicity signs of the colliding two protons in the center-of-mass system. If the interaction in the process involves only QCD and QED, the cross section satisfies the parity conservation:

$$d\sigma_{++} = d\sigma_{--}, \quad d\sigma_{+-} = d\sigma_{-+}. \tag{1.30}$$

The unpolarized cross section in Eq. 1.28 can be represented using the helicity-dependent cross sections as

$$d\sigma = \frac{1}{2}\left(d\sigma_{++} + d\sigma_{+-}\right). \tag{1.31}$$

The polarized cross section is also defined using the helicity-dependent cross sections as

$$d\Delta\sigma \equiv \frac{1}{2}\left(d\sigma_{++} - d\sigma_{+-}\right). \tag{1.32}$$

This polarized cross section can be represented with polarized PDF like as Eq. 1.28. For example, the polarized cross section of the π production can be represented as

$$\begin{aligned} d\Delta\sigma^{\pi} &= \Sigma_{a,b,c}\int dx_a \int dx_b \int dz_c \\ &\quad \Delta f_a(x_a,\mu)\Delta f_b(x_b,\mu) d\Delta\hat{\sigma}_{ab\to c}(x_a p_A, x_b p_B, \frac{p_\pi}{z_c}, \mu) D_c^{\pi}(z_c,\mu). \end{aligned} \tag{1.33}$$

$d\Delta\hat{\sigma}_{ab\to c}$ is partonic polarized cross section which is defined as

$$d\Delta\hat{\sigma}_{ab\to c}\equiv\frac{1}{2}\left(d\hat{\sigma}^{++}_{ab\to c}-d\hat{\sigma}^{+-}_{ab\to c}\right), \tag{1.34}$$

where $d\hat{\sigma}^{+\pm}_{ab\to c}$ represents partonic cross section of $a+b\to c+X$ process when a and b have helicities of + and ±, respectively. The partonic polarized cross section $d\Delta\hat{\sigma}_{ab\to c}$ can be also calculated from perturbation theory as well as $d\hat{\sigma}_{ab\to c}$. $d\hat{\sigma}^{+\pm}_{ab\to c}$ from LO pQCD calculations are listed in Table 1.1 and partonic asymmetries $\hat{a}_{LL}$, which are defined as $\hat{a}_{LL}\equiv d\Delta\hat{\sigma}_{ab\to c}/d\hat{\sigma}_{ab\to c}$, are shown in Fig. 1.7. Using the calculated $d\Delta\hat{\sigma}_{ab\to c}$, the polarized PDF $\Delta f_{a,b}$ can be studied by measuring $d\Delta\sigma$. Experimentally, the polarized cross section is measured as the ratio to the unpolarized cross section, namely

$$A_{LL}\equiv\frac{d\Delta\sigma}{d\sigma}, \tag{1.35}$$

because correlated systematic uncertainties on $d\sigma$ and $d\Delta\sigma$ are canceled out. The asymmetry of the cross section A_{LL} is called "longitudinal double-spin asymmetry" or "double-helicity asymmetry".

Table 1.1: Table of QCD cross sections for definite helicity combinations from LO pQCD calculations [45, 39]. The calculations ignore the quark mass. A common factor $\pi\alpha_S^2/s^2$ is not included in all the cross section.

process	$d\hat{\sigma}^{++}/dt$	$d\hat{\sigma}^{+-}/dt$
$q_\alpha q_\beta\to q_\alpha q_\beta$	$\frac{8}{9}\left[\frac{s^2}{t^2}+\delta_{\alpha\beta}\left(\frac{s^2}{u^2}-\frac{2}{3}\right)\frac{s^2}{tu}\right]$	$\frac{8}{9}\left(\frac{u^2}{t^2}+\delta_{\alpha\beta}\frac{t^2}{u^2}\right)$
$q_\alpha\bar{q}_\beta\to q_\delta\bar{q}_\gamma$	$\frac{8}{9}\left(\delta_{\alpha\delta}\delta\beta\gamma\frac{s^2}{t^2}\right)$	$\frac{8}{9}\left(\delta_{\alpha\delta}\delta_{\beta\gamma}\frac{u^2}{t^2}+\delta_{\alpha\beta}\delta_{\delta\gamma}\frac{t^2+u^2}{s^2}-\frac{2}{3}\delta_{\alpha\gamma}\delta_{\alpha\beta}\delta_{\delta\gamma}\frac{u^2}{st}\right)$
$qg\to qg$	$\left(\frac{2s^2}{t^2}-\frac{8}{9}\frac{s^2}{su}\right)$	$\left(\frac{2u^2}{t^2}-\frac{8}{9}\frac{u^2}{su}\right)$
$gg\to q\bar{q}$	0	$\left(\frac{1}{3}\frac{u^2+t^2}{ut}-\frac{3}{4}\frac{t^2+u^2}{s^2}\right)$
$q\bar{q}\to gg$	0	$\left(\frac{64}{27}\frac{t^2+u^2}{ut}-\frac{16}{3}\frac{t^2+u^2}{s^2}\right)$
$gg\to gg$	$\frac{9}{2}\left(\frac{2s^2}{ut}-\frac{su}{t^2}-\frac{st}{u^2}\right)$	$\frac{9}{2}\left(6-\frac{2s^2}{ut}-\frac{su}{t^2}-\frac{st}{u^2}-\frac{2ut}{s^2}\right)$

Experimental Approach to A_{LL}

From the definition of A_{LL} represented as Eq. 1.35 and relations of Eq. 1.30, 1.31 and 1.32, the helicity-dependent cross section of specific particle production is parameterized using A_{LL} as

$$d\sigma_{\lambda_A\lambda_B}(p_T,y)=d\sigma_0(p_T,y)\left[1+\lambda_A\lambda_B A_{LL}(p_T,y)\right], \tag{1.36}$$

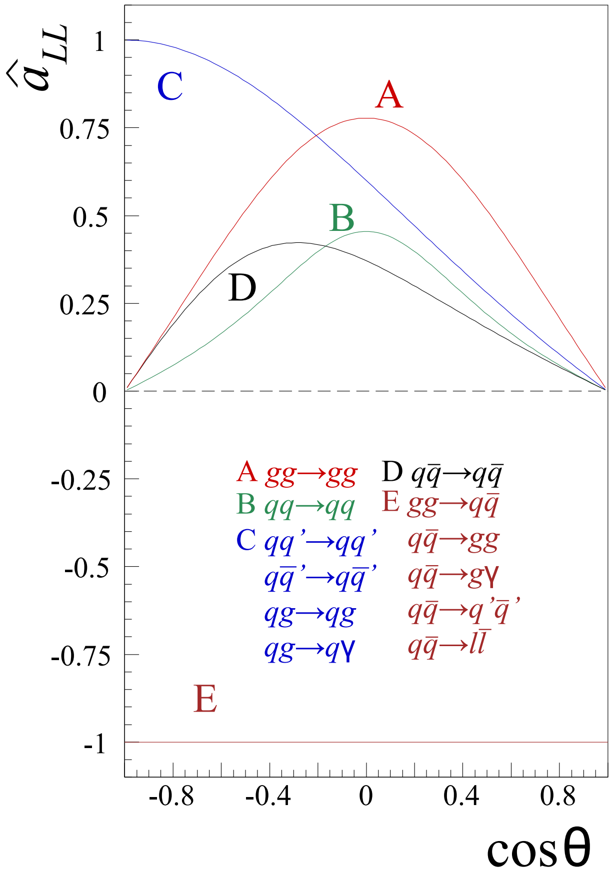

Figure 1.7: The double helicity asymmetry of the partonic cross section ($\hat{a}_{LL}$) as a function of the scattering angle on the partonic center-of-mass system [46]. $\hat{a}_{LL}$ can be derived from helicity-dependent cross sections listed in Table 1.1.

where $d\sigma_0$ is the unpolarized cross section of this process, which can be obtained by averaging spin of the initial protons, and $\lambda_{A,B}$ denotes helicity ($\pm$) of the initial two protons. In the equation, the cross section and spin asymmetry are represented as functions of transverse momentum p_T and rapidity y of the produced particle.

Practically, the protons in the polarized beams are not fully polarized. When we polarize the proton beam to a specific direction, quantized spin state of major protons are in parallel to the direction, but ones of other protons are anti-parallel to the direction. The beam polarization P represents how much protons in the polarized beam are in the parallel spin state to the polarization direction, and is defined as

$$P \equiv \frac{I_+ - I_-}{I_+ + I_-}, \tag{1.37}$$

where I_+ (I_-) is beam intensity for protons in the parallel (anti-parallel) spin state. For the A_{LL} measurement, the polarization direction is set to be longitudinal along the beam axis. By definition, the beam polarization P varies from 0 to 1 since I_+ is greater than I_-, in general.

From Eq. 1.36, the experimentally detected yield of specific particle $N_{h_A h_B}$ can be written as

$$N_{h_A h_B}(p_T, y) = \epsilon_{\text{eff}}(p_T, y) L_{h_A h_B} d\sigma_0(p_T, y) \left(1 + h_A h_B P_A P_B A_{LL}(p_T, y)\right), \tag{1.38}$$

where $h_{A,B}$ denotes the polarization direction of the beam A, B, parallel $(+1)$ or anti-parallel (-1) to the beam momentum, and $L_{h_A h_B}$ is integrated luminosity of *pp* collisions crossing in polarization combination of (h_A, h_B). ϵ_{eff} is detection efficiency of the particle including detector efficiency, acceptance, particle ID efficiency, and trigger efficiency.

Ideally, the efficiency ϵ_{eff} does not depend on the beam polarization $h_{A,B}$. However, the efficiency can be slightly changed in different polarizations due to the following experimental reasons: (1) bunch-by-bunch difference in length of beam bunch and (2) readout electronics specific. These effects are discussed in Sec. 4.3.2. The following description ignores the effects for the sake of simplicity.

The detected yields in the four polarization combination can be also written separately as

$$\begin{aligned}
N_{++}(p_T, y) &= N_0(p_T, y)\left(1 + P_A P_B A_{LL}(p_T, y)\right), \\
N_{--}(p_T, y) &= N_0(p_T, y)\left(1 + P_A P_B A_{LL}(p_T, y)\right)/r_{--}, \\
N_{+-}(p_T, y) &= N_0(p_T, y)\left(1 - P_A P_B A_{LL}(p_T, y)\right)/r_{+-}, \\
N_{-+}(p_T, y) &= N_0(p_T, y)\left(1 - P_A P_B A_{LL}(p_T, y)\right)/r_{-+},
\end{aligned} \tag{1.39}$$

where $N_0 \equiv \epsilon_{\text{eff}} L_{++} d\sigma_0$ represents yield of the particle in unpolarized *pp* collisions under integrated luminosity of L_{++}. $r_{\pm\pm}$ is relative luminosity, which is defined as

$$\begin{aligned}
r_{--} &\equiv L_{++}/L_{--}, \\
r_{+-} &\equiv L_{++}/L_{+-}, \\
r_{-+} &\equiv L_{++}/L_{-+}.
\end{aligned} \tag{1.40}$$

Experimentally, the yields $N_{\pm\pm}$ are observable and the beam polarization $P_{A,B}$ and relative luminosity $r_{\pm\pm}$ can also be measured as accelerator performance. Therefore, the double spin asymmetry A_{LL} can be obtained by fitting the observed yield $N_{\pm\pm}$ according to Eq. 1.39 where A_{LL} and N_0 are set as two fitting parameters. It is worth to mention that, if the efficiency ϵ_{eff} does not depend on the direction of the beam polarization, Eq. 1.39 includes only the detected yields and the beam polarizations, and therefore any detection efficiencies do not affect the A_{LL} measurement.

1.4 DGLAP Equation

The parton model will be improved by introducing the quark and gluon interaction described in QCD. As consequence of the Bjorken scaling violation, the description of the unpolarized PDF $q(x)$ and $g(x)$ also depend on energy-scale of renormalization Q^2. The Q^2 evolution of those distributions is performed by DGLAP equations [47],

$$\begin{aligned}
\frac{dq(x, Q^2)}{d\log Q^2} &= \frac{\alpha_S(Q^2)}{2\pi} \int_0^1 \frac{dy}{y} \left(q(y, Q^2) P_{qq}(\frac{x}{y}) + g(y, Q^2) P_{qg}(\frac{x}{y}) \right), \\
\frac{dg(x, Q^2)}{d\log Q^2} &= \frac{\alpha_S(Q^2)}{2\pi} \int_0^1 \frac{dy}{y} \left(\sum_q q(y, Q^2) \Delta P_{gq}(\frac{x}{y}) + g(y, Q^2) \Delta P_{gg}(\frac{x}{y}) \right),
\end{aligned} \tag{1.41}$$

where $P_{ij}(z)$ are the splitting functions, representing the probability of finding a new parton i carrying a momentum fraction $z(< 1)$ of a parent parton j. The splitting functions are calculated from pQCD calculations as a probability that the real particle i separates into the real particle j with a colinear momentum and a virtual particle.

For the polarized case, the Q^2 evolution equations are drawn in analogous way with respect to the unpolarized case. The Q^2 dependence of the polarized PDF is given

$$\begin{aligned}
\frac{d\Delta q(x,Q^2)}{d\log Q^2} &= \frac{\alpha_S}{2\pi}\int_0^1 \frac{dy}{y}\left(\Delta q(y,Q^2)\Delta P_{qq}(\frac{x}{y}) + \Delta g(y,Q^2)\Delta P_{qg}(\frac{x}{y})\right), \\
\frac{d\Delta g(x,Q^2)}{d\log Q^2} &= \frac{\alpha_S}{2\pi}\int_0^1 \frac{dy}{y}\left(\sum_{q,\bar{q}}\Delta q(y,Q^2)P_{gq}(\frac{x}{y}) + \Delta g(y,Q^2)P_{gg}(\frac{x}{y})\right). \quad (1.42)
\end{aligned}$$

In the equation, the spin-dependent splitting functions $\Delta P_{ij}(z)$ are defined as $\Delta P_{ij}(z) = P^+_{ij}(z) - P^-_{ij}(z)$, where $P^\pm_{ij}(z)$ represents the splitting functions of finding a parton i with helicity ± from a parent parton j with helicity +. It is convenient to separate the polarized quark PDF in a flavor singlet $\Delta q^S(x)$ and non-singlet $\Delta q^{NS}_{3,8}(x)$ defined as

$$\begin{aligned}
\Delta q^S &\equiv \Delta U(x,Q^2) + \Delta D(x,Q^2) + \Delta S(x,Q^2) \\
&= \sum_{q,\bar{q}} \Delta q(x,Q^2), \\
\Delta q^{NS}_3 &\equiv \Delta U(x,Q^2) - \Delta D(x,Q^2), \\
\Delta q^{NS}_8 &\equiv \Delta U(x,Q^2) + \Delta D(x,Q^2) - 2\Delta S(x,Q^2), \quad (1.43)
\end{aligned}$$

where

$$\begin{aligned}
\Delta U(x,Q^2) &\equiv \Delta u(x,Q^2) + \Delta\bar{u}(x,Q^2), \\
\Delta D(x,Q^2) &\equiv \Delta d(x,Q^2) + \Delta\bar{d}(x,Q^2), \\
\Delta S(x,Q^2) &\equiv \Delta s(x,Q^2) + \Delta\bar{s}(x,Q^2).
\end{aligned}$$

Hence, the spin-dependent DGLAP equations, which represent evolution of the polarized PDF, are represented as

$$\begin{aligned}
\frac{d\Delta q^{NS}_{3,8}(x,Q^2)}{d\log Q^2} &= \frac{\alpha_S}{2\pi}\int_0^1 \frac{dy}{y}\Delta q^{NS}_{3,8}(y,Q^2)\Delta P_{qq}(\frac{x}{y}), \\
\frac{d\Delta q^S(x,Q^2)}{d\log Q^2} &= \frac{\alpha_S}{2\pi}\int_0^1 \frac{dy}{y}\left(\Delta q^S(y,Q^2)\Delta P_{qq}(\frac{x}{y}) + 2f\Delta g(y,Q^2)\Delta P_{qg}(\frac{x}{y})\right), \\
\frac{d\Delta g(x,Q^2)}{d\log Q^2} &= \frac{\alpha_S}{2\pi}\int_0^1 \frac{dy}{y}\left(\Delta q^S(y,Q^2)\Delta P_{gq}(\frac{x}{y}) + \Delta g(y,Q^2)\Delta P_{gg}(\frac{x}{y})\right), \quad (1.44)
\end{aligned}$$

where f is the number of quark flavors liberated into the final state ($f = 3$ below the charm production threshold).

1.5 Current Status of Nucleon Spin Structure

1.5.1 Determination of Unpolarized PDF

The unpolarized PDF can be determined from data of DIS and hadron hard-scattering experiments. Recently, the determination of the unpolarized PDF has been performed by several groups, CTEQ [48, 49], MSTW [50], NNPDF [51, 52], HERAPDF [53], ABDM [54], and GJR [55, 56]. These groups provide PDFs with NLO and next-to-next leading order (NNLO) calculations, except CTEQ group which provides an NLO result.

Figure 1.8 shows the resulting unpolarized PDFs at a scale $Q^2 = 4$ GeV^2 from the CTEQ group (CTEQ6). The functional from that CTEQ uses is

$$xf(x, Q_0^2) = A_0 x^{A_1} (1-x)^{A_2} e^{A_3 x} \left(1 + e^{A_4} x\right)^{A_5}, \tag{1.45}$$

where Q_0 is an initial scale of the evolution which is set to $Q_0 = 1.3$ GeV, and $A_{0,\dots,5}$ is an independent parameter. The PDF at all higher Q is determined from NLO DGLAP equations. $f(x, Q)$ represents PDFs of parton flavor combinations $u_v(x) {\equiv} u - \bar{u}$, $d_v(x) {\equiv} d - \bar{d}$, $g(x)$, and $(\bar{u} + \bar{d})(x)$. CTEQ group assumes $s(x) = \bar{s}(x) = 0.2(\bar{u} + \bar{d})$. To distinguish the $\bar{u}$ and $\bar{d}$ distributions, the ratio $\bar{d}/\bar{u}$ is parameterized as

$$\frac{\bar{d}(x, Q_0)}{\bar{u}(x, Q_0)} = A_0 x^{A_1} (1-x)^{A_2} + (1 + A_3 x)(1-x)^{A_4}. \tag{1.46}$$

As Fig. 1.8 shows, valence quarks are dominant in large Bjorken x region, $10^{-1} \lesssim x$. On the other hand, sea quarks and gluons are dominant and increasing in small Bjorken x region, $x \lesssim 10^{-1}$. Especially, large fraction of the partons in this region consists of gluons, which is about ten times larger than other sea quarks.

1.5.2 First Moment of Polarized PDF

Angular momentum conservation

Considering angler momentum conservation as well as momentum conservation shown in Eq. 1.7, spin $s_z/\hbar = 1/2$ of a longitudinally polarized proton is decomposed as

$$\frac{1}{2} = \frac{1}{2} \sum_q \int_0^1 dx \left(\Delta q(x, Q^2) + \Delta\bar{q}(x, Q^2)\right) + \int_0^1 dx \Delta g(x, Q^2) + L_{q,g}, \tag{1.47}$$

where $q(x)$ and $g(x)$ represent quark and gluon PDF respectively and $L_{q,g}$ represents orbital angular momentum of the quark and gluon. This equation is also written as

$$\frac{1}{2} = \frac{1}{2} \Delta\Sigma(Q^2) + \Delta G(Q^2) + L_{q,g}, \tag{1.48}$$

where $\Delta\Sigma(\equiv \int_0^1 dx \Delta q^S)$ and $\Delta G(\equiv \int_0^1 dx \Delta g)$ represent total spin polarizations of the quark and anti-quark, and the gluon, respectively.

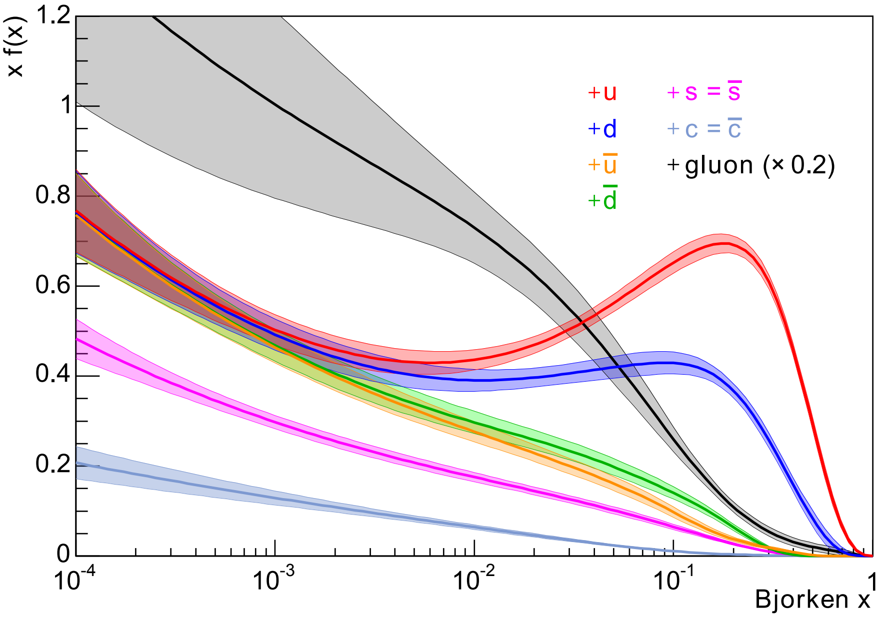

Figure 1.8: Unpolarized PDF at $Q^2 = 4$ GeV^2 as a function of Bjorken x obtained by CTEQ group [48] (CTEQ6). For gluon PDF, $g(x) \times 0.2$ is displayed in this figure for convenience.

Expectation of $\Delta\Sigma$ from the constituent quark model

In the constituent quark model, the simple SU(6) proton wave function

$$|p\uparrow\rangle = \frac{1}{\sqrt{18}}\left(2|u\uparrow u\uparrow d\downarrow\rangle - |u\uparrow u\downarrow d\uparrow\rangle - |u\downarrow u\uparrow d\uparrow\rangle + \text{cyclic}\right) \tag{1.49}$$

yields $\Delta\Sigma = 1$, because the proton spin consists of only the constituent-quark spin. In addition, when we take into account Bag models, the effects of confinement and chiral symmetry violation are to be considered [57]. From the effects, Bag quarks obtain small masses, and therefore relativistic effect can not be ignored [58, 59, 60]. The relativistic effect creates orbital angular momentum even in the lowest partial wave. The orbital angular momentum corrects the $\Delta\Sigma$ expectation into $\Delta\Sigma =\sim 0.65$ [30, 31].

First moment of $g_1(x)$

The first moment of the polarized structure function $g_1(x)$, defined as

$$\Gamma_1 \equiv \int_0^1 dx g_1(x) = \frac{1}{2}\sum_{q,\bar{q}} e_q^2 \int_0^1 dx \Delta q(x), \tag{1.50}$$

has an important information: the quark helicity contribution to the nucleon spin.

Defining ΔU, ΔD, and ΔS as

$$\Delta U \equiv \int_0^1 dx\,(\Delta u(x) + \Delta\bar{u}(x))\,, \tag{1.51}$$

$$\Delta D \equiv \int_0^1 dx\,\left(\Delta d(x) + \Delta\bar{d}(x)\right)\,, \tag{1.52}$$

$$\Delta S \equiv \int_0^1 dx\,(\Delta s(x) + \Delta\bar{s}(x))\,, \tag{1.53}$$

and neglecting the heavy quarks, the first moment for the proton can be written as

$$\Gamma_1^p = \frac{1}{2}\left(\frac{4}{9}\Delta U + \frac{1}{9}\Delta D + \frac{1}{9}\Delta S\right) \tag{1.54}$$

$$= \frac{1}{12}(\Delta U - \Delta D) + \frac{1}{36}(\Delta U + \Delta D - 2\Delta S) + \frac{1}{9}(\Delta U + \Delta D + \Delta S)\,. \tag{1.55}$$

Assuming the isospin symmetry, the first moment for the neutron can be also obtained by $\Delta U \leftrightarrow \Delta D$.

Using Operator Product Expansion (OPE) method, the three terms in Eq. 1.55 are related with the expectation values a_i of the proton matrix element of a flavor SU(3) octet of quark axial-vector currents [3, 4]. a_i is defined as

$$\langle P, S|J^i_{5\mu}|P, S\rangle = M a_i S_\mu, \qquad i = 1...8, \tag{1.56}$$

where M is related to the mass of the quarks. The currents $J^i_{5\mu}$ are given by the λ_i, the Gell-Mann matrices as

$$J^i_{5\mu} = \bar{\psi}\gamma_\mu\gamma_5\frac{\lambda_i}{2}\psi, \qquad \psi = \begin{pmatrix} u \\ d \\ s \end{pmatrix}, \tag{1.57}$$

where ψ represents annihilation operators of flavor SU(3) quarks in free quark field.

The element a_0 is given by the singlet operator

$$\langle P, S|J^0_{5\mu}|P, S\rangle = M a_0 S_\mu, \tag{1.58}$$

$$J^0_{5\mu} = \bar{\psi}\gamma_\mu\gamma_5\psi. \tag{1.59}$$

Finally the correspondence of the expectation values a_i to the terms of Eq. 1.55 is as follows

$$a_3 = \Delta U - \Delta D, \tag{1.60}$$

$$a_8 = \Delta U + \Delta D - 2\Delta S, \tag{1.61}$$

$$a_0 = \Delta U + \Delta D + \Delta S = \Delta\Sigma. \tag{1.62}$$

$$\tag{1.63}$$

The elements a_3 and a_8 are well known from the neutron β decay and the spin 1/2 hyperon decays in the SU(3) baryon octet. These can be expressed in terms of the parameters F and D, obtained from the aforementioned decays [33, 61],

$$a_3 = F + D = |g_A| = 1.2694 \pm 0.0028, \tag{1.64}$$

$$a_8 = 3F - D = 0.585 \pm 0.025, \tag{1.65}$$

where g_A is the axial coupling constant.

The QCD improved parton model leads to some corrections [6] and modifies Eq. 1.55 to

$$\Gamma_1^{p,n} = \frac{1}{12}\left(\left(\pm a_3 + \frac{1}{3}a_8\right) E_{NS}(Q^2) + \frac{4}{3}a_0 E_S(Q^2)\right), \quad (1.66)$$

$$E_{NS}(Q^2) \equiv 1 - \frac{\alpha_S(Q^2)}{\pi} - 3.58\left(\frac{\alpha_S(Q^2)}{\pi}\right)^2 ..., \quad (1.67)$$

$$E_S(Q^2) \equiv 1 - 0.333\frac{\alpha_S(Q^2)}{\pi} - 1.10\left(\frac{\alpha_S(Q^2)}{\pi}\right)^2 ... \quad (1.68)$$

where Γ_1^n represents the first moment of $g_1(x)$ for neutron.

Bjorken Sum Rule

Using Eq. 1.66, we can deduce the Bjorken sum rule,

$$\Gamma_1^p - \Gamma_1^n = \frac{1}{6}a_3 E_{NS}(Q^2). \quad (1.69)$$

The Bjorken sum rule provides the relation between isospin element a_3 (Eq. 1.64) and difference of the proton and neutron first moments. The Bjorken sum rule assumes isospin SU(2) symmetry of quark dynamics in the nucleon.

Ellis-Jaffe Sum Rule

The Ellis-Jaffe sum rule assumes that $\Delta s = \Delta\bar{s} = 0$, and then $a_8 = \Delta\Sigma(= a_0)$. Therefore, using Eq. 1.66, the Ellis-Jaffe sum rule is represented as

$$\Gamma_1^{p,n} = \pm\frac{1}{12}a_3 E_{NS}(Q^2) + \frac{1}{36}a_8\left(E_{NS}(Q^2) + 4E_S(Q^2)\right), \quad (1.70)$$

or

$$\Gamma_1^p + \Gamma_1^n = \frac{1}{18}a_8\left(E_{NS}(Q^2) + 4E_S(Q^2)\right). \quad (1.71)$$

The validity of the Ellis-Jaffe sum rule corresponds to the validity of flavor SU(3) symmetry of quark dynamics in the nucleon and $\Delta S = 0$.

Measurement of the sum rules

To check the validation of the sum rules, various polarized DIS experiments [5, 6, 7, 8, 9] have been performed. These experiments measured $g_1(x, Q^2)$ for proton, deuteron, and neutron. The result for proton as function of Q^2 and Bjorken x is shown in Fig. 1.9, and the results for all particles as function of Bjorken x is shown in Fig. 1.10. The deuteron $g_1(x)$ can be interpreted as a combination of the proton and neutron $g_1(x)$,

$$g_1^d(x) = \frac{1}{2}\left(g_1^p(x) + g_1^n(x)\right)\left(1 - \frac{3}{2}\omega_D\right), \quad (1.72)$$

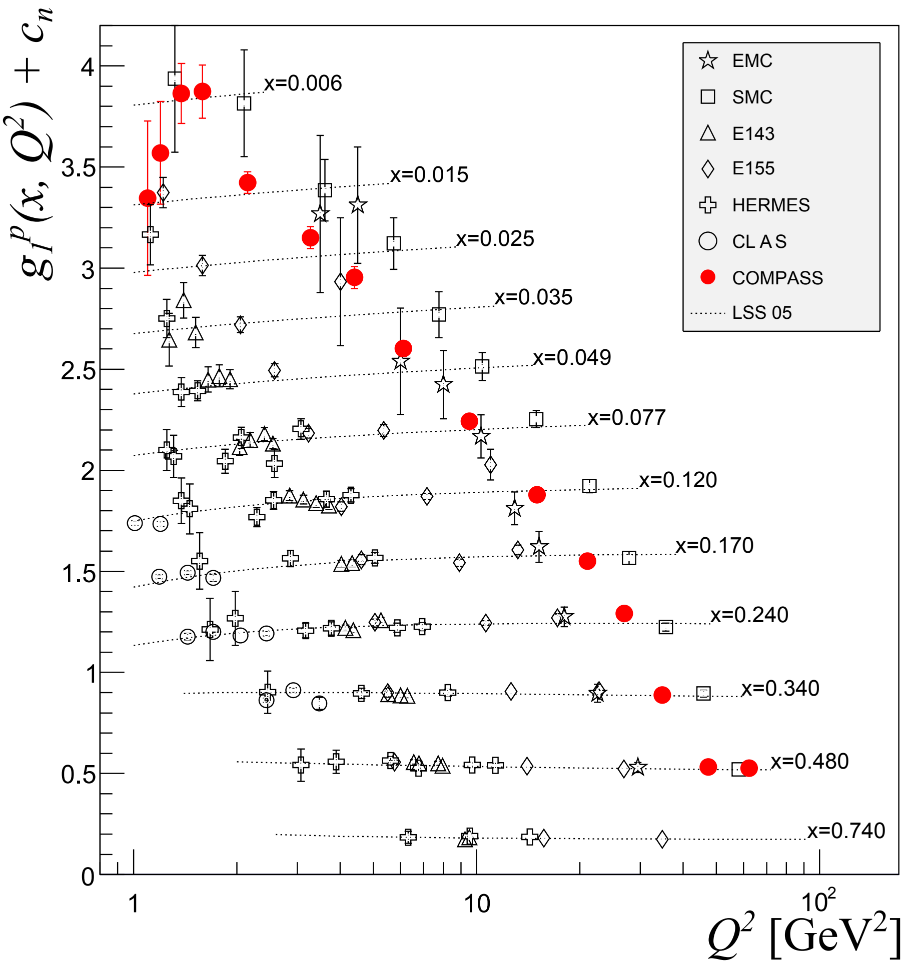

Figure 1.9: World data for $g_1(x, Q^2)$ or the proton with $Q^2 > 1$ GeV^2 and $W \equiv \sqrt{(p+q)^2} > 2.5$ GeV. For clarity a constant $c_n = 0.28 \times (11.6 - n)$ has been added to the $g_1(x)$ values within a particular x bin starting with $n = 0$ for $x = 0.006$. Also shown is the QCD fit curves [62].

where $\omega_D = 0.05 \pm 0.01$ takes into account the D-state admixture to the deuteron wave function.

Using the $g_1(x)$ obtained from the COMPASS experiment, the evolution of the Bjorken sum rule $\int_{x_{\min}}^1 dx g_1^{p-n}(x)$ as a function of $x_{\min}$ as well as the Ellis-Jaffe sum rule $\int_{x_{\min}}^1 dx g_1^{p+n}(x)$ are estimated. The results are shown in Fig. 1.11. Note that the first moment of the $g_1^{p+n}(x)$ saturates at $x \sim 0.05$. Figure 1.11 represents that whereas the Bjorken sum rule is satisfied well, the Ellis-Jaffe sum rule breaks. The violation of the Ellis-Jaffe sum rule corresponds to polarization of the strange quarks in the nucleon or flavor SU(3) violation in the quark dynamics in the nucleon.

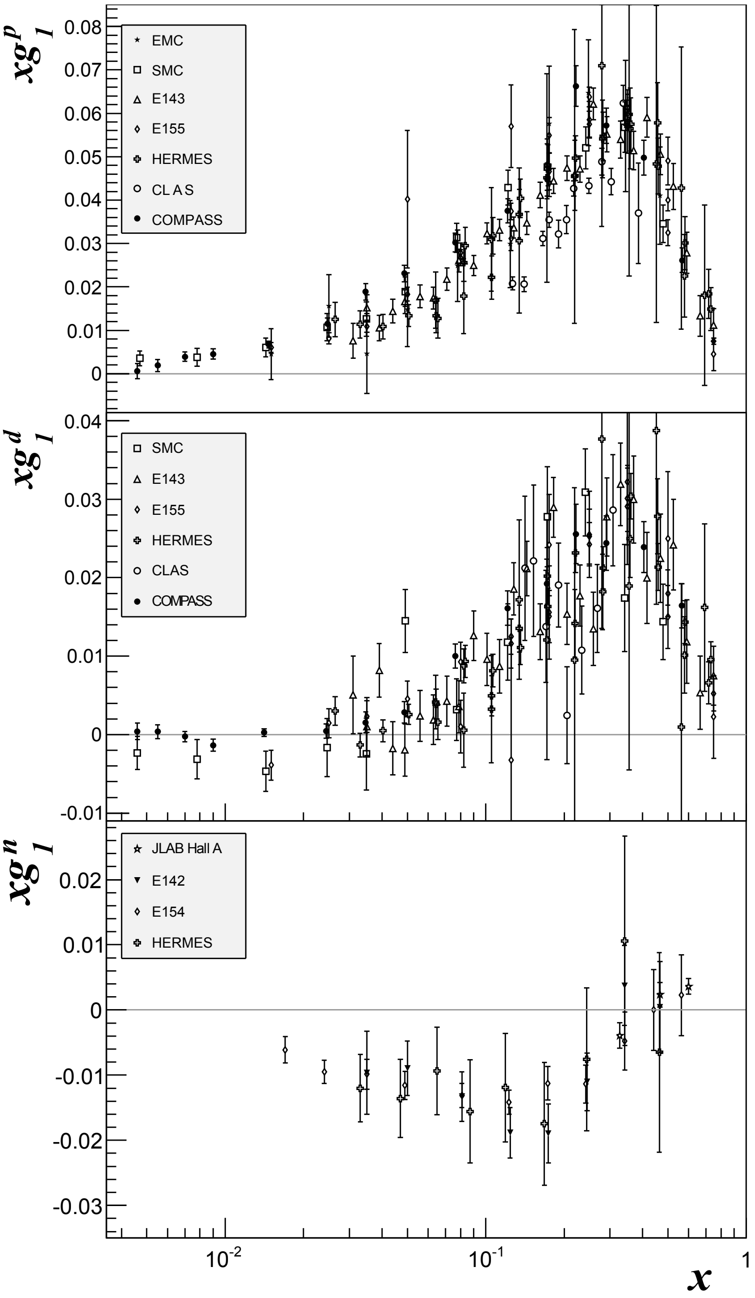

Figure 1.10: World data on $xg_1(x)$ as a function of x for the proton (top), deuteron (middle), and neutron (bottom) at the measurement Q^2. Only data points for $Q^2 > 1$ GeV^2 and $W \equiv \sqrt{(p+q)^2} > 2.5$ GeV are shown.

$\Delta\Sigma$ determination and remaining contribution

Using the measured first moments of proton and deutron and Eq. 1.66, COMPASS obtained

$$\Delta\Sigma(Q^2 \rightarrow \text{inf}) = 0.33 \pm 0.03(\text{stat}) \pm 0.05(\text{syst}). \tag{1.73}$$

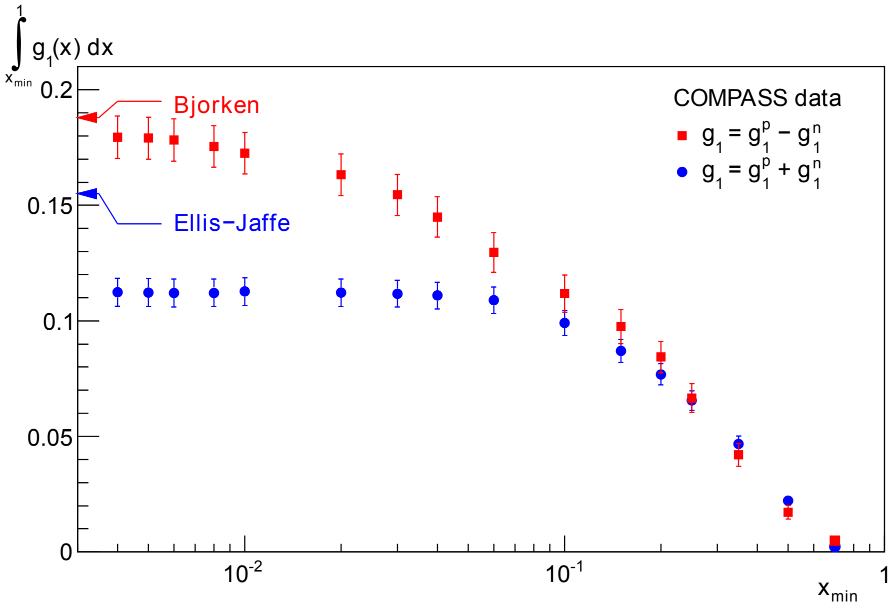

Figure 1.11: Convergence of the first moment integral of g_1 as a function of the lower integration limit $x_{\rm min}$ for the Bjorken integral (isospin non-singlet) and the Ellis-Jaffe integral (iso-singlet) from the COMPASS proton and deuteron data at $Q^2 = 3$ GeV^2. The arrows indicate the theoretical expectations.

This value can not be explained by the expectation values $\Delta\Sigma = 1$ (simple SU(6)) nor $\Delta\Sigma =\sim 0.65$ (SU(6) including the relativistic effect). The remaining proton spin $\sim 70\%$ must be attributed to the gluon polarization ΔG and/or orbital angular momentum L_z. Other than the orbital angular momentum from the relativistic effect explained above, from our empirical knowledge, system in the ground state basically does not have its orbital angular momentum. [3] Therefore, it is natural to expect that the gluon polarization ΔG in Eq. 1.48 contribute the remaining proton spin.[4]

---

[3] Another reason is the technical difficulty for the orbital angular momentum measurement.

[4] The interest to ΔG came also from an axial anomaly correction to $\Delta\Sigma$ [63, 64]. The axial anomaly, which is a fundamental property in quantum field theory, produces an additional term in divergent differential of the axial current as

$$\partial_\mu J_5^\mu = n_f \frac{\alpha_S}{2\pi} \sum_{a=1}^{8} \epsilon_{\mu\nu\rho\sigma} G_a^{\mu\nu} G_a^{\rho\sigma}. \tag{1.74}$$

This anomaly term modifies the relation between singlet element a_0 and quark polarization $\Delta\Sigma$ to be

$$a_0 = \Delta\Sigma - n_f \frac{\alpha_S}{2\pi} \Delta G. \tag{1.75}$$

Therefore, the violation of Ellis-Jaffe sum rule can be attributed to the gluon polarization ΔG. However it requires very large ΔG, $\Delta G > 1$, which is not preferable from recent experimental data.

1.5.3 $\Delta g(x)$ Measurements

The first A_{LL} measurement attempting to look at gluon polarization was made by the FNAL E581/704 Collaboration using a 200 GeV polarized proton beam and a polarized proton target [65]. They measured A_{LL} for inclusive multi-γ and $\pi^0\pi^0$ production consistent with zero within their sensitivities, which suggested $\Delta g/g(x)$ is not so large in the region of $0.05 < x < 0.35$.

DIS experiments can determine $\Delta g(x)$ via Q^2 evolution of $g_1(x, Q^2)$ according to DGLAP equations in Sec. 1.4. Other method to determine $\Delta g(x)$ with DIS is to tag charmed mesons or high p_T hadron pairs in the final state. Both tagging identify $\gamma^* g \rightarrow q\bar{q}$ interaction process in the partonic level as shown in Fig. 1.12. The method of finding high p_T hadron pair leads to large statistics, but these have larger background contributions from QCD Compton processes and fragmentation. The charmed meson method is a clean process, but low statistics. The high-p_T hadron tagging method was employed at the HERMES [66], SMC [67], and COMPASS [68] experiments, and the charmed meson tagging method was employed at the COMPASS experiment [69]. Results of $\Delta g/g(x)$ from these SIDIS measurements are shown in Fig. 1.13. The data are compared to calculations using polarized PDF extracted from a global analysis to polarized world data from the DIS, SIDIS, and RHIC experiments (DSSV [70, 23], which is described in Sec. 1.5.4, and LSS [71]).

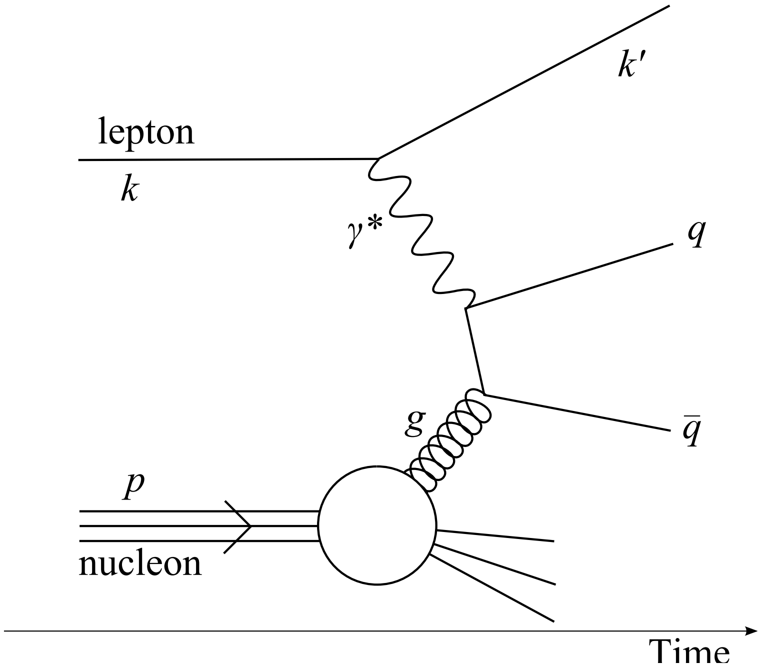

Figure 1.12: Interaction of $\gamma^* g \rightarrow q\bar{q}$ in DIS, which is used for the Δg measurement.

The $\Delta g(x)$ study with pp collisions is being performed in RHIC accelerator described in Sec. 2.1. In RHIC, the Δg is studied in the PHENIX and STAR experiments. The PHENIX experiment performed A_{LL} measurements for π^0 [10, 11, 12, 13], η [14], and jet [17] production and the STAR experiment performed A_{LL} measurements for jet production [72, 15]. The π^0, η, and jet are mainly produced via gg and gq scattering

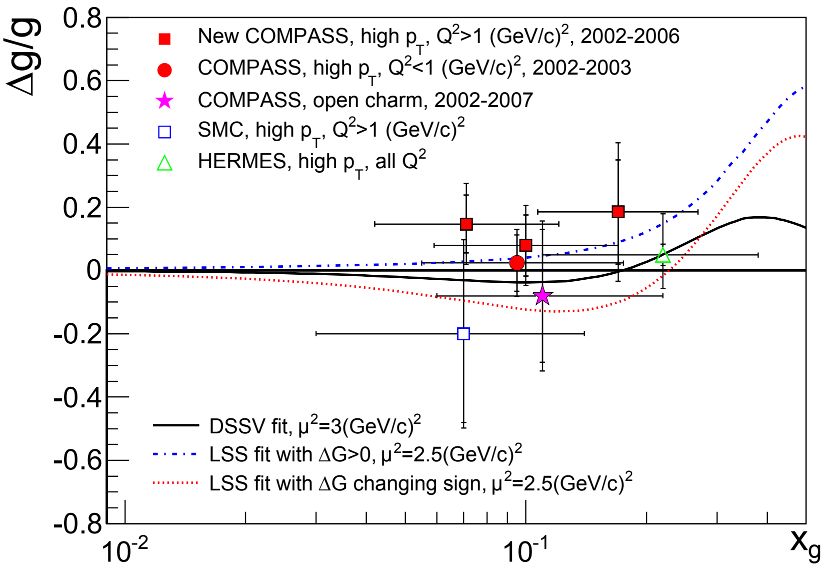

Figure 1.13: Gluon polarization $\Delta g/g(x)$ from leading-order analysis of hadron or hadron-pair production as function of the probed gluon Bjorken x [68]. Also shown are NLO pQCD fit curves (DSSV [70, 23] and LSS [71]).

process in the partonic level. The A_{LL} of the π^0 production in $\sqrt{s} = 200$ GeV pp collisions measured by PHENIX from 2005, 2006, and 2009 (preliminary) is shown in Fig. 1.14 [73]. The data are compared to a calculation using DSSV described in Sec. 1.5.4. Figure 1.15 shows A_{LL} of jet production measured in $\sqrt{s} = 200$ GeV pp collisions by STAR from 2006 and 2009 (preliminary) experiments [15].

1.5.4 Global Analysis for $\Delta g(x)$

As introduced in Sec. 1.5.3, there are a lot of data sets for $\Delta g(x)$ including the DIS, SIDIS, and RHIC experiments, which cover various Bjorken x regions and Q^2 values. To extract $\Delta g(x)$ and other polarized PDFs from these data sets, a global NLO pQCD analysis, DSSV [70, 23], is performed. DSSV optimizes the agreement between the measured spin asymmetries and corresponding theoretical calculations. The assumption of the polarized PDF shapes in DSSV at an initial scale for the evolution of $Q_0^2 = 1$ GeV^2 is

$$x\Delta f_i(x, Q_0^2 = 1\ \mathrm{GeV}^2) = N_i x^{\alpha_i} (1-x)^{\beta_i} \left(1 + \gamma_i\sqrt{x} + \eta_i x\right), \tag{1.76}$$

with free parameters N_i, α_i, β_i, γ_i, and η_i. The PDFs are evolved according to DGLAP evolution formulae in Eq. 1.42. In DSSV, it is assumed $\Delta s(x) = \Delta\bar{s}(x)$, considering the s-quark and $\bar{s}$-quark are produced only via pair creation from gluon and they are symmetric.

π^0 A_{LL} in $\sqrt{s} = 200$ GeV pp collisions from the 2005 and 2006 PHENIX runs and in $\sqrt{s} = 62.4$ GeV pp collisions from the 2006 PHENIX run, and jet A_{LL} in $\sqrt{s} = 200$ GeV

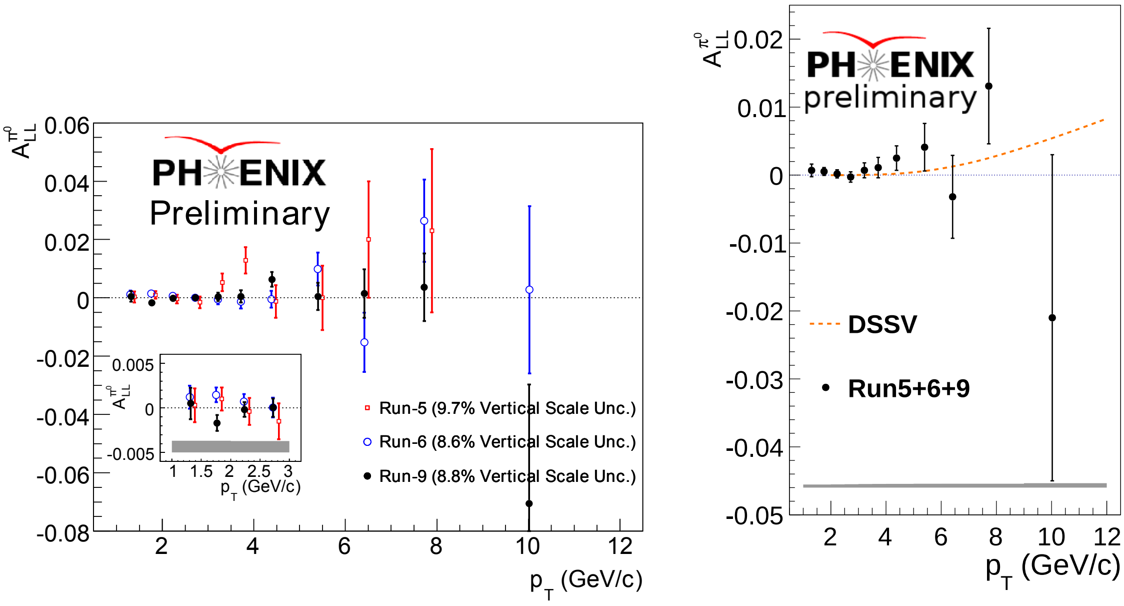

(a) $A_{LL}(p_T)$ in π^0 production from PHENIX experiment.

(b) Combined result.

Figure 1.14: (a) The longitudinal double-spin asymmetry in π^0 production at pseudorapidity ranging $|\eta| < 0.35$ as measured by PHENIX in $\sqrt{s} = 200$ GeV polarized pp collisions as function of π^0 transverse momentum. (b) Combined result compared to the DSSV curve.

pp collisions from the 2005 and 2006 STAR runs are used in the DSSV analysis for the RHIC data. The resulting constraints on the polarized PDFs are shown in Fig. 1.16. Table 1.2 shows resulting $\int_{0.001}^{1} dx\Delta f_i(x)$ and $\int_0^1 dx\Delta f_i(x)$ for each PDF.

Table 1.2: Truncated first moments $\int_{0.001}^{1} dx\Delta f_i(x)$ and $\int_0^1 dx\Delta f_i(x)$ at $Q^2 = 10$ GeV^2. $\int_{0.001}^{1} dx\Delta f_i(x)$ has uncertainty corresponding to $\Delta\chi^2 = 1$ in Fig. 1.16.

	$\int_{0.001}^{1} dx\Delta f_i(x)$	$\int_0^1 dx\Delta f_i(x)$
ΔU	$0.793^{+0.011}_{-0.012}$	0.813
ΔD	$-0.416^{+0.011}_{-0.009}$	-0.458
$\Delta\bar{u}$	$0.028^{+0.021}_{-0.020}$	0.036
$\Delta\bar{d}$	$-0.089^{+0.029}_{-0.029}$	-0.115
$\Delta\bar{s}$	$-0.006^{+0.010}_{-0.012}$	-0.057
$\Delta\Sigma$	$0.366^{+0.015}_{-0.018}$	0.242
ΔG	$0.013^{+0.106}_{-0.120}$	-0.084

Quark polarized PDFs are well determined from DIS and SIDIS data. The data points from SIDIS experiments and the DSSV theoretical curves are shown in Fig. 1.17. While Δu is positive, Δd has negative contribution to the proton spin. Also surprisingly, $\Delta S = 2\Delta\bar{s}$ has about 10% negative contribution. The optimal DSSV fit satisfies the

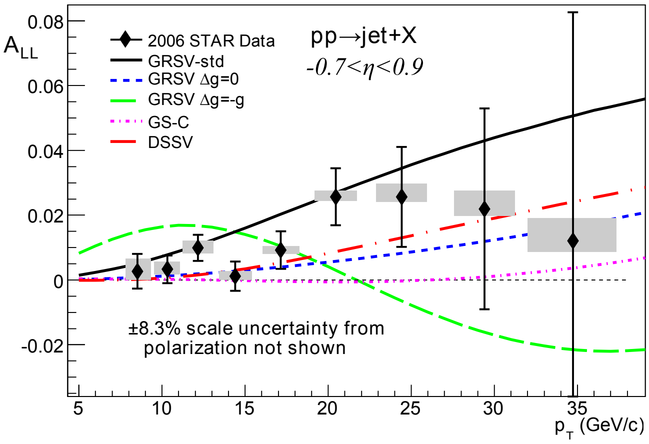

(a) $A_{LL}(p_T)$ in jet production from 2006 STAR experiment.

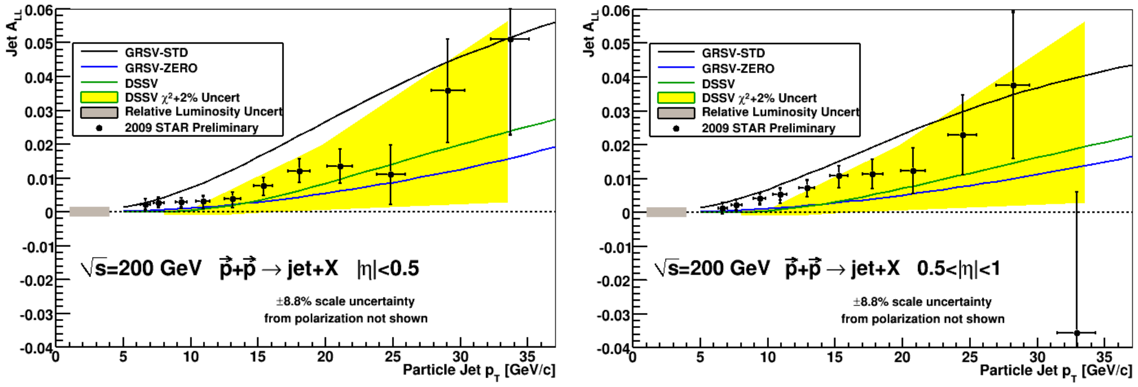

(b) $A_{LL}(p_T)$ in jet production from 2009 STAR experiment at $|\eta| < 0.5$ (preliminary).

(c) $A_{LL}(p_T)$ in jet production from 2009 STAR experiment at $0.5 < |\eta| < 1.0$ (preliminary).

Figure 1.15: The longitudinal double-spin asymmetry in jet production as measured by STAR in $\sqrt{s} = 200$ GeV polarized pp collisions as function of jet transverse momentum. (a) 2006 result at pseudorapidity ranging $-0.7 < \eta < 0.9$ and (b, c) 2009 preliminary results at pseudorapidity ranging $|\eta| < 0.5$ and $0.5 < |\eta| < 1.0$ are shown.

isospin and flavor symmetry relations,

$$\begin{aligned} \Delta U - \Delta D &= (F + D)\left[1 + \epsilon_{SU(2)}\right], & (1.77)\\ \Delta U + \Delta D - 2\Delta S &= (3F - D)\left[1 + \epsilon_{SU(3)}\right], & (1.78)\end{aligned}$$

with discrepancy parameters from exact isospin $SU(2)$ and flavor $SU(3)$ symmetries of $\epsilon_{SU(2)} = 0.0011$ and $\epsilon_{SU(3)} = -0.0035$, where $F + D = 1.269$ and $3F - D = 0.586$ are used.

The RHIC data put a strong constraint on the size of $\Delta g(x)$ for $0.05 < x < 0.2$ as they mainly probe $(\Delta g(x))^2$. $\Delta g(x)$ comes out rather small in $0.05 < x < 0.2$, and prefers to have a node. As can be seen from Table 1.2, the integral of $\Delta g(x)$ in the region of $0.001 < x < 1$ is found to be almost zero and the extrapolation to the region of $0 < x < 1$ is -0.084 at $Q^2 = 10$ GeV^2.

The global analysis of DSSV does not include A_{LL} of π^0 production from the

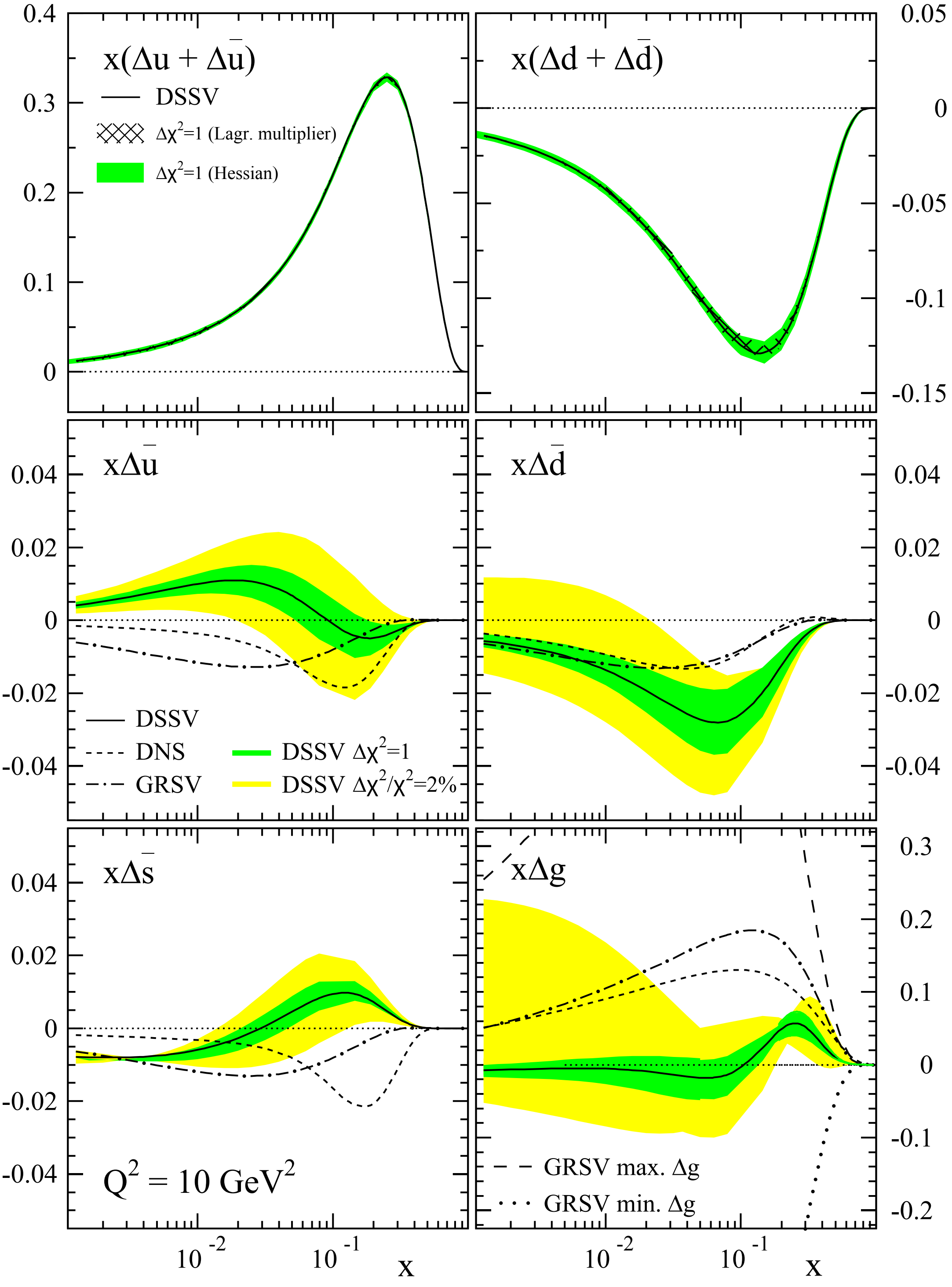

Figure 1.16: DSSV polarized PDF. Sea quark and gluon PDFs are compared to GRSV fits [74]. The shaded bands correspond to alternative fits with (green) $\Delta\chi^2 = 1$ and (yellow) $\Delta\chi^2/\chi^2 = 2\%$.

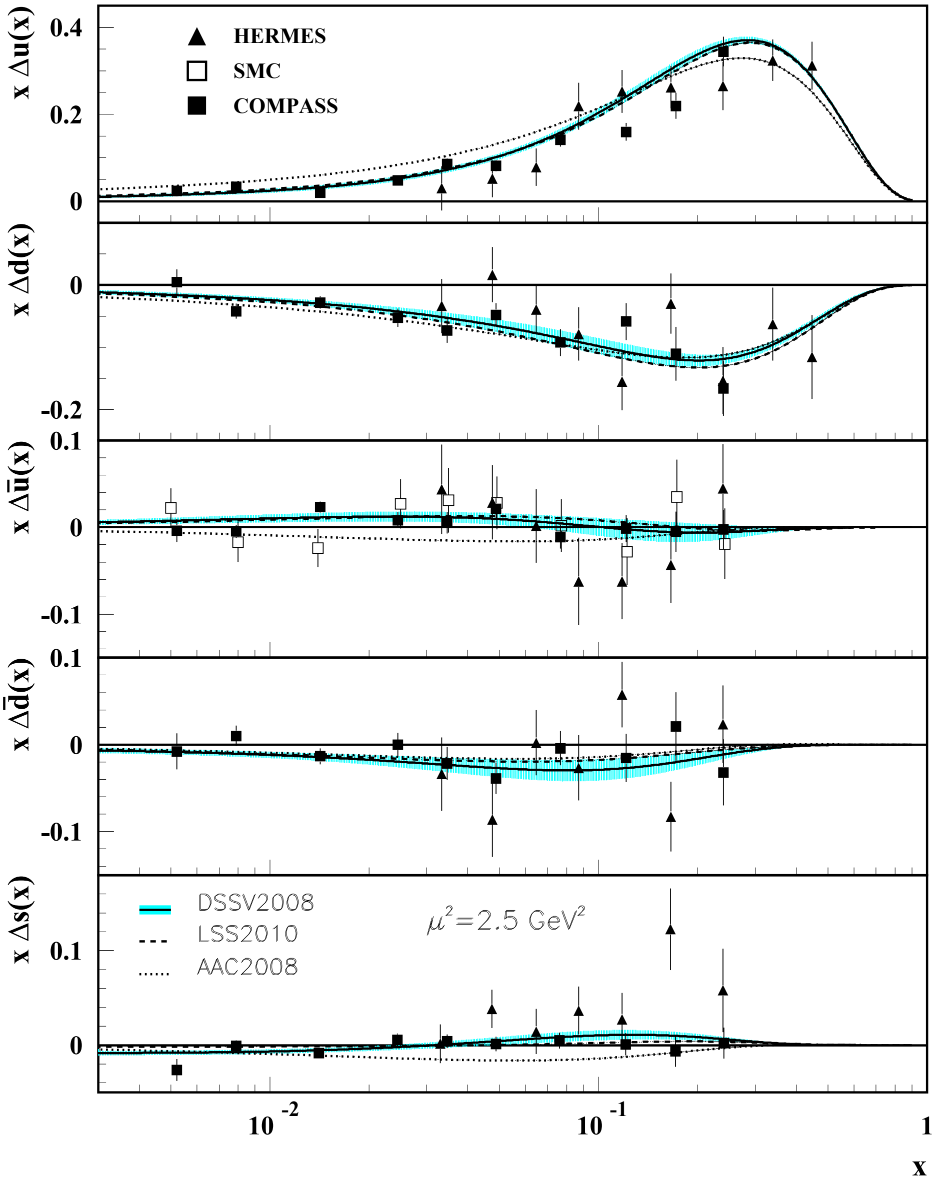

Figure 1.17: Quark polarized PDF at a scale $\mu^2 = 2.5$ GeV^2. The theoretical curves shown in this figure are LSS2010 [71], AAC2008 [75], and DSSV. Points represent data from SMC [18], HERMES [19, 20], and COMPASS [21, 22] SIDIS experiments at $Q^2 = 2.5$ GeV^2. SMC results are extracted under the assumption that $\Delta\bar{u}(x) = \Delta\bar{d}(x)$.

PHENIX 2009 measurement (Fig. 1.14) and A_{LL} of jet production from the STAR 2009 measurement (Fig. 1.15(b) and 1.15(c)), which have larger statistics. These figures also display theoretically calculated curves using DSSV. The theoretical curve in π^0 A_{LL} looks consistent with the combined result of 2005, 2006, and 2009 measurements. However, the theoretical curves in jet A_{LL} has large deviations from the 2009 measurement. The difference of the behaviors between the π^0 and jet A_{LL} results is attributed to difference of sensitive Bjorken x coverage for the two measurements. A new global analysis including these A_{LL} data set and a new COMPASS DIS result [8, 9] is preformed, and called DSSV++. Figure 1.18(a) shows the fitting result of the DSSV++ compared with the π^0 and jet A_{LL} results. Figure 1.18(b) shows the $\Delta g(x)$ result of the DSSV++.

Especially, Fig. 1.18(b) represents unreliability of DSSV and DSSV++ $\Delta g(x)$. While DSSV expects a node structure in $\Delta g(x)$, DSSV++ does not have such node in $0.05 < x < 1$. The node in DSSV $\Delta g(x)$ cancels the positive polarization in $0.1 < x < 1$ and the negative polarization in $x < 0.1$, and expects the integral $\int_{0.001}^{1} dx \Delta g(x)$ to be small, $0.013^{+0.106}_{-0.120}$. On the other hand, DSSV++ shows the positive polarization in almost the whole Bjorken x region, and expects the integral $\int_{0.001}^{1} dx \Delta g(x)$ to be ~ 0.3 as shown in Fig. 1.18(c).

The above unreliability on DSSV and DSSV++ $\Delta g(x)$ comes from the following reasons:

Uncertainty in small Bjorken x region

Large uncertainty of $\Delta g(x)$ in extrapolation to $x \to 0$ is still remaining in the result. There is no data set in the small Bjorken x region of $x \lesssim 0.02$, and the behavior of $\Delta g(x)$ in this region is determined almost by the functional form in the assumption. To constraint ΔG more precisely, the data points in the small Bjorken x region is necessary.

Uncertainty in functional form of $\Delta g(x)$

$A_{LL}(p_T)$ in pp collisions gives an integral with respect to Bjorken x such like

$$\frac{\int dx_1 dx_2 dz \ \Delta f_i(x_1) \Delta f_j(x_2) \Delta\hat{\sigma}(x_1, x_2, p_T/z) D(z)}{\int dx_1 dx_2 dz \ f_i(x_1) f_j(x_2) \hat{\sigma}(x_1, x_2, p_T/z) D(z)}. \tag{1.79}$$

To determine the functional shape of $\Delta g(x)$, we need measurements with other probes, e.g. heavy quark and direct γ production, which has sensitivity on different Bjorken x region and sign of $\Delta g(x)$ from the current measurements.

1.6 Heavy Flavor Production in $p + p$ Collisions

1.6.1 Challenge for $\Delta g(x)$ Determination

As discussed above, there is no $\Delta g(x)$ measurement in small Bjorken x region $x \sim 10^{-2}$, and then $\Delta g(x)$ in such small Bjorken x region resulting from the global analyses is not enough reliable. A_{LL} measurement of π^0 production in $\sqrt{s} = 200$ GeV $p + p$ collisions, which has sensitivity in the smallest Bjorken x region achieved by the current $\Delta g(x)$ measurements, reaches only up to the minimum limit of $x \sim 2 \times 10^{-2}$ ($\log_{10} x \sim -1.7$). This limit is originated by π^0 transverse momentum range of $p_T > 2.0$ GeV/c, where reliability of pQCD calculations is supported.

This lack of the data causes the large uncertainty on $\Delta G(\mu)$. Under the current experimental knowledge, a sizable gluon polarization in small Bjorken x region $x \sim 10^{-2}$

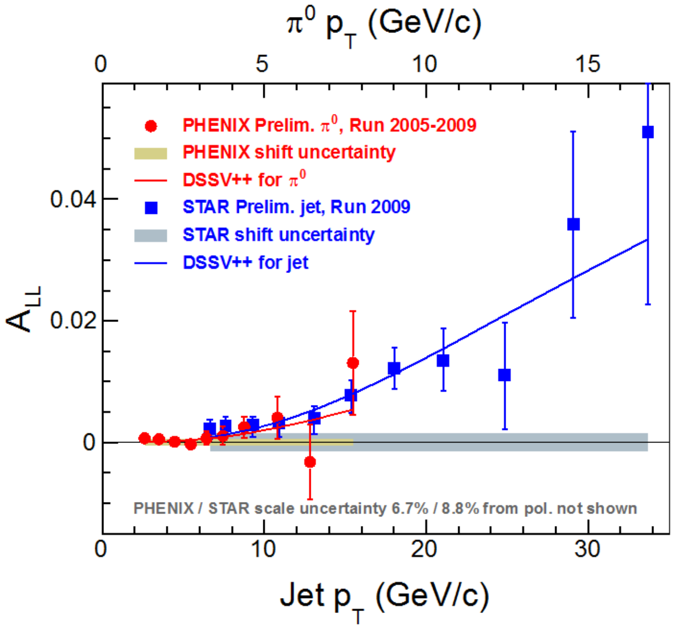

(a) Fitting result of DSSV++ for π^0 and jet A_{LL}.

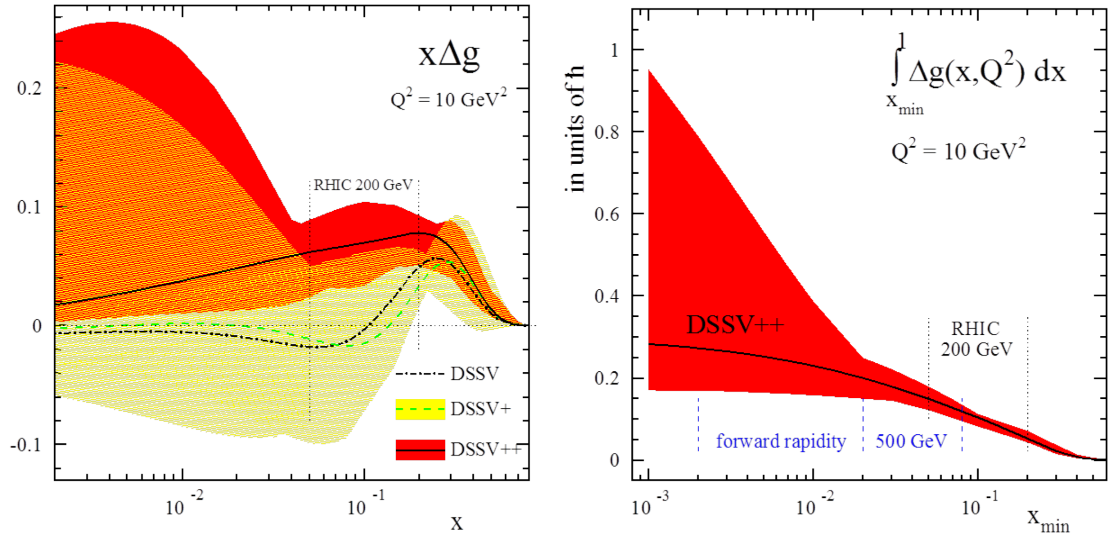

(b) Resulting DSSV++ $\Delta g(x)$.

(c) $\int_{\min}^{1} dx \Delta g(x)$ in DSSV++.

Figure 1.18: (a) Fitting result of DSSV++ for (red circles) π^0 and (blue squares) jet A_{LL} compared with the measured values. (b) Resulting $\Delta g(x)$ from DSSV and DSSV++. This plot also shows the $\Delta g(x)$ from DSSV+ which is a global analysis including only new COMPASS DIS result [8, 9]. The red band represents the uncertainty calculated from $\Delta\chi^2/\chi^2 = 2\%$ in the fitting, which corresponds to almost $\Delta\chi^2 = 8$. (c) The integral computed in the range from $x_{\min}$ to 1. The red band represents uncertainty calculated from $\Delta\chi^2/\chi^2 = 2\%$ in the fitting.

compared to the proton spin 1/2 is not ruled out yet. Hence, a $\Delta g(x)$ measurement in such small Bjorken x region is essential for the further constraint on $\Delta G(\mu)$.

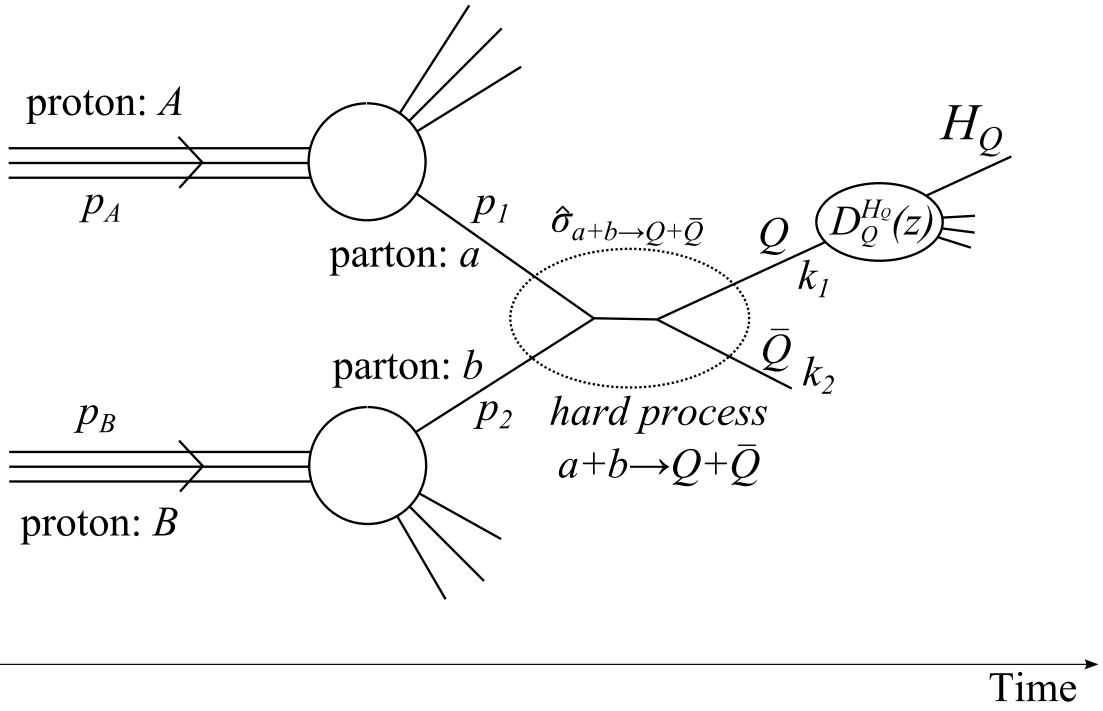

Figure 1.19: A diagram of heavy flavor production in pp collisions. Q ($\bar{Q}$) in the figure represents c ($\bar{c}$) or b ($\bar{b}$) quarks. H_Q represents fragmented hadron from Q. In this measurement, the heavy flavor production is detected by measuring electron from semi-leptonic decay of H_Q (heavy flavor electron).

Heavy flavor quark (charm and bottom quarks) production in the polarized pp collisions is an ideal probe which overcomes above problems and measures gluon polarization as discussed in later, Sec. 1.6.2. The diagram of the heavy flavor production is shown in Fig. 1.19. The PHENIX experiment in RHIC is a suitable facility to measure A_{LL} of this process. Since the PHENIX detector has large spectrometers for electron detection in the mid-rapidity region ($|\eta| < 0.35$), hadrons containing heavy flavors are measured through their semi-leptonic decays to electrons and positrons, which are called “heavy flavor electrons” (HFe) [28, 29]. In this work, A_{LL} of the heavy flavor electron production is measured at the PHENIX experiment to access $\Delta g(x)$.

1.6.2 Production Mechanism for Heavy Flavor Electron

As shown in Eq. 1.28 and 1.33, the spin-independent and spin-dependent cross sections of the heavy quark production from partons i, j interaction in $p+p$ collisions, $\sigma_{ij\to Q\bar{Q}+X}$ and $\Delta\sigma_{ij\to Q\bar{Q}+X}$, can be calculated by using partonic cross sections, $\hat{\sigma}_{ij\to Q\bar{Q}+X}$ and

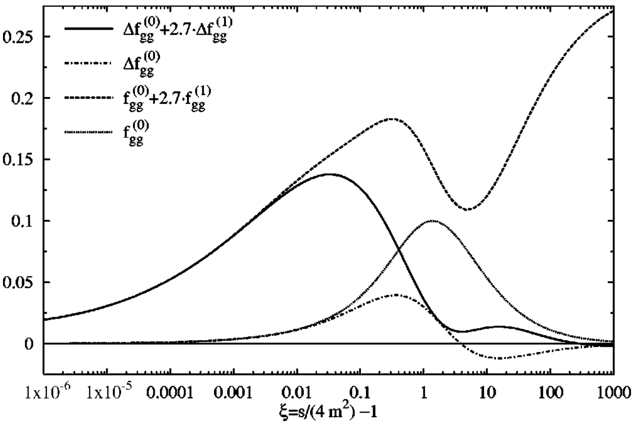

(a) $gg \to Q\bar{Q} + X$

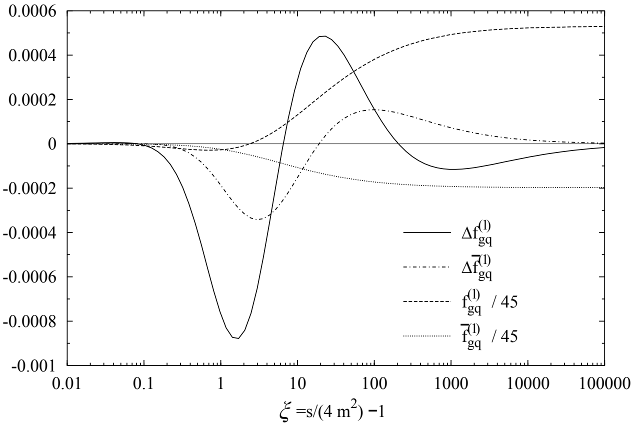

(b) $gq(g\bar{q}) \to Q\bar{Q} + X$

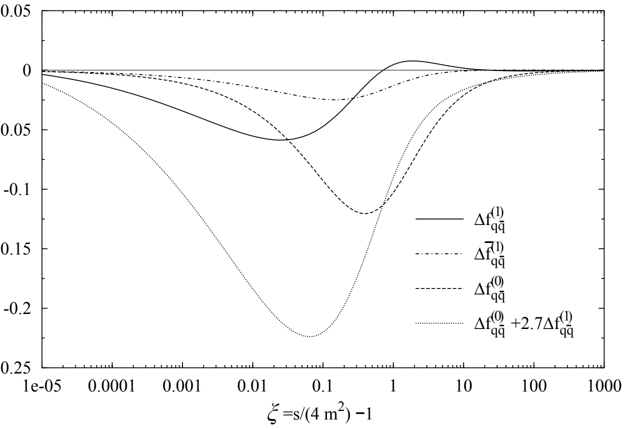

(c) $q\bar{q} \to Q\bar{Q} + X$

Figure 1.20: Partonic cross sections $(m^2/\alpha_S^2)\hat{\sigma}_{ij}$ and $(m^2/\alpha_S^2)\Delta\hat{\sigma}_{ij}$ in LO and NLO ($\overline{\rm MS}$) calculations as a function of $\xi \equiv s/(4m^2) - 1$, where we have set $\mu = 1.4$ GeV for simplicity and $4\pi\alpha_S(\mu = 1.4\ \text{GeV}) = 2.7$ as appropriate for charm production. It is worth to note that there is no LO component in gq interaction, namely $f_{gq}^{(0)} = 0$ and $\Delta f_{gq}^{(0)} = 0$, and helicities in $q\bar{q}$ annihilation are conserved, namely $f_{q\bar{q}}^{(n)} = -\Delta f_{q\bar{q}}^{(n)}$.

$\Delta\hat{\sigma}_{ij\to Q\bar{Q}+X}$, as

$$\begin{aligned} \sigma_{ij\to Q\bar{Q}+X} &= \int dx_i \int dx_j \ \hat{\sigma}_{ij\to Q\bar{Q}+X} f_i(x_i) f_j(x_j) \\ \Delta\sigma_{ij\to Q\bar{Q}+X} &= \int dx_i \int dx_j \ \Delta\hat{\sigma}_{ij\to Q\bar{Q}+X} \Delta f_i(x_i) \Delta f_j(x_j). \end{aligned} \tag{1.80}$$

The partonic cross sections of the heavy flavor quark are well studied with LO and NLO ($\overline{\mathrm{MS}}$) pQCD calculations with respect to order of α_S [25, 26, 27]. The partonic cross sections can be decomposed into LO and NLO components, $f_{ij}^{(0)}$ and $f_{ij}^{(1)}$, as

$$\frac{m^2}{\alpha_S^2(\mu)}\hat{\sigma}_{ij}(s, m^2, \mu) = f_{ij}^{(0)}(\xi) + 4\pi\alpha_S(\mu)\left(f_{ij}^{(1)}(\xi) + \bar{f}_{ij}^{(1)}(\xi)\ln\frac{\mu^2}{m^2}\right), \tag{1.81}$$

$$\frac{m^2}{\alpha_S^2(\mu)}\Delta\hat{\sigma}_{ij}(s, m^2, \mu) = \Delta f_{ij}^{(0)}(\xi) + 4\pi\alpha_S(\mu)\left(\Delta f_{ij}^{(1)}(\xi) + \Delta\bar{f}_{ij}^{(1)}(\xi)\ln\frac{\mu^2}{m^2}\right), \tag{1.82}$$

where s is the available partonic center-of-mass energy squared, and $\beta = (11N_A - 2n_{lf})/3$ (N_A: number of colors, n_{lf}: number of light flavors). Figure 1.20 show the partonic cross sections for gg, qg, $q\bar{q}$ interactions. As these calculations show, partonic cross sections for gg and $q\bar{q}$ scattering are comparable, whereas ones for qg ($\bar{q}g$) are rather small compared to them by a factor of $\sim 10^{-2}$ [26, 27]. Therefore, since the unpolarized gluon PDF is larger than the unpolarized quark PDF in small Bjorken x region around $x \sim 1.4\times10^{-2}$ by a factor of $\sim$ 10, spin-independent cross section of $gg\to Q\bar{Q}+X$ process, $\int\int dx_1 dx_2 \ \hat{\sigma}_{gg} g(x_1) g(x_2)$, is predominant in the heavy flavor production especially for small transverse momentum and contribution from $q\bar{q}\to Q\bar{Q}+X$ process, $\int\int dx_1 dx_2 \ \hat{\sigma}_{q\bar{q}} q(x_1)\bar{q}(x_2)$, is a few percent [24]. In addition, when the polarized gluon PDF in the small Bjorken x region is sizable compared with the polarized quark PDF at Bjorken x of $\sim 1.4\times10^{-2}$ as well as the unpolarized case, the A_{LL} of heavy quark production consist of only the spin-dependent cross section of gg interaction $\Delta\sigma_{gg}$. Therefore, A_{LL} measurement of this process is an ideal probe for the $\Delta g/g(x)$ measurement.

Cross sections of the heavy flavor electron production can be calculated by using the above cross sections of the heavy flavor production. Figure 1.21 shows comparison between the unpolarized and polarized cross sections of the heavy flavor electron production in the $\sqrt{s}$ = 200 GeV pp collisions estimated with the LO and NLO pQCD calculations for the partonic interaction [28, 24]. The hadronization is simulated with fragmentation functions for $c\to D$, $b\to B$, and $b\to c\to D$. The electron pseudorapidity in the calculation is ranging $|\eta| < 0.35$. The top panel corresponds to the unpolarized cross section resulting from CTEQ6 unpolarized PDF and the middle panel corresponds to the polarized cross section resulting from DSSV polarized PDF. The bottom panel shows ratios of the NLO calculation to the LO calculation for the unpolarized and polarized cross sections.

The two left panels in Fig. 1.22 represent the fractions of gg, $q\bar{q}$, and qg contributions in cross sections of the heavy flavor production from the NLO pQCD calculation, shown in Fig. 1.21. The top panel corresponds to unpolarized cross section and the bottom panel corresponds to polarized cross section. The top panel represents that contribution

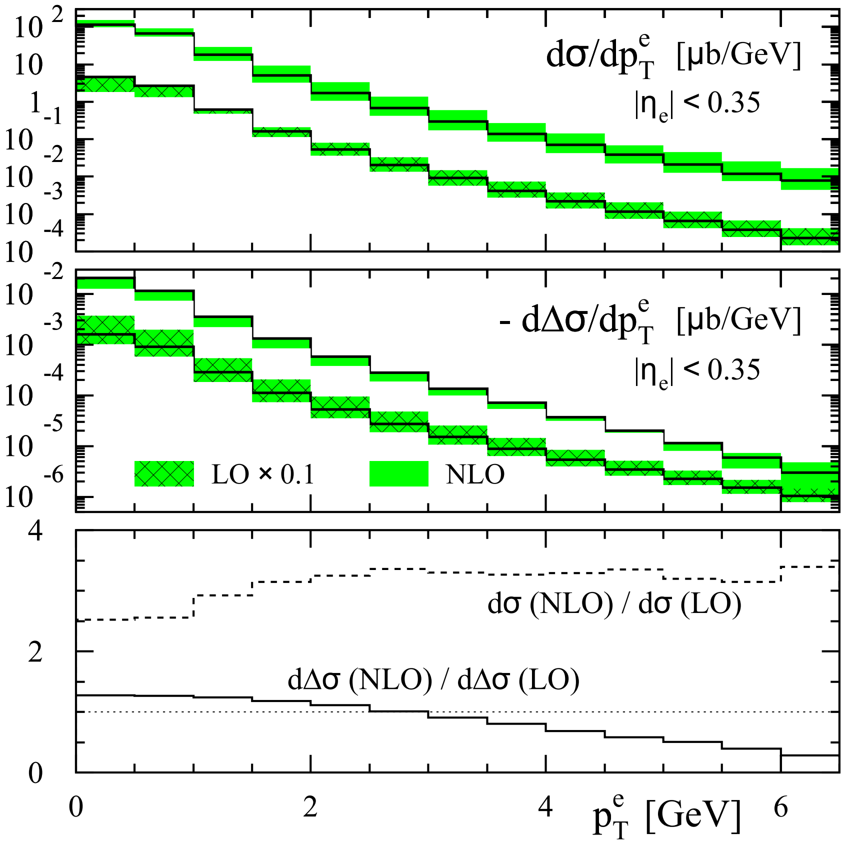

Figure 1.21: Comparison between LO and NLO calculated cross sections of heavy flavor electron production at central rapidity $|\eta| < 0.35$ in $\sqrt{s} = 200$ GeV pp collisions [24]. The top figure shows unpolarized cross sections and the middle figure shows polarized cross sections. Scale is varied simultaneously as $\mu = k\left(m_Q^2 + \left[(p_T^Q)^2 + (p_T^{\bar{Q}})^2\right]/2\right)^{1/2}$ in the range $1/2 < k < 2$ which corresponds to the shaded band. The solid lines correspond to the default scale $k = 1$. The bottom shows the ratio of NLO to LO polarized and unpolarized cross sections.

from $q\bar{q}$ is a few percent and qg is also less than 10% in electron transverse momentum ranging $p_T < 1.5$ GeV/c as mentioned above. The bottom figure for the polarized cross section represents that DSSV expects small gg contribution to the polarized cross section due to its small $\Delta g(x)$ distribution. The polarized cross section in transverse momentum ranging $0.5 < p_T < 1.5$ GeV/c is determined almost by polarized gluon PDF in Bjorken x ranging $10^{-2} \lesssim x \lesssim 8\times10^{-2}$ where there are not enough data sets to constraint $\Delta g(x)$, and especially in $x \lesssim 2\times10^{-2}$ $\Delta g(x)$ had never been explored before this measurement.

The two right panels in Fig. 1.22 represent the fractions of charm and bottom productions in the unpolarized (top-right) and polarized (bottom-right) cross sections. As the unpolarized cross section, the heavy flavor production below $p_T \sim 1.5$ GeV/c

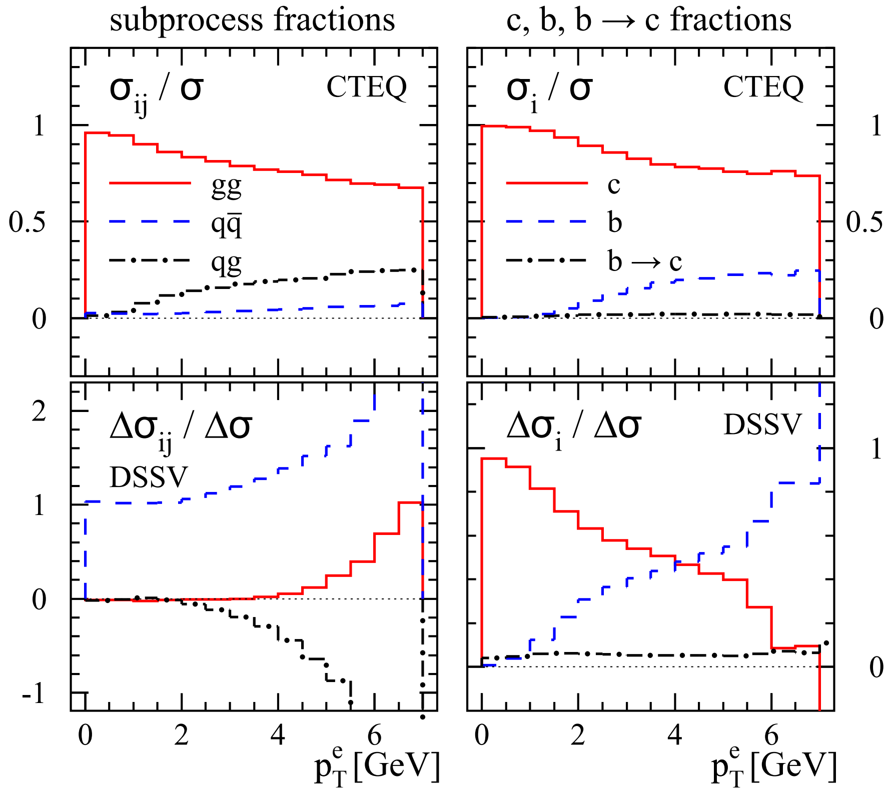

Figure 1.22: Fractional amount of different partonic subprocesses at NLO accuracy (left column) and of charm, bottom, and cascade ($b \to c$) decays (right column) contributing to the p_T spectrum of the heavy flavor electron production [24]. Results are shown for unpolarized (upper row) and polarized (lower row) pp collisions at RHIC using the CTEQ6 and DSSV set of PDF, respectively.

is dominated by charm quark in $\sqrt{s} = 200$ GeV $p + p$ collisions [28, 24]. The bottom panel of Fig. 1.23 shows a distribution of Bjorken x contributing to the heavy flavor electron production of transverse momentum $0.5 < p_T < 1.5$ GeV/c from the charmed hadrons in the $\sqrt{s} = 200$ GeV pp collisions at pseudorapidity ranging $|\eta| < 0.35$. For comparison, the top panel of Fig. 1.23 shows a Bjorken x distribution of π^0 production for several transverse momentum regions at the same pseudorapidity range, where the π^0 A_{LL} measurements at PHENIX have been performed [10]. Both distributions are estimated by using PYTHIA simulation [76, 77]. Whereas the Bjorken x distribution of the π^0 production ranges $2 \times 10^{-2} \lesssim x$, the distribution of the heavy flavor production ranges $10^{-2} \lesssim x \lesssim 8 \times 10^{-2}$, which covers an unexplored small Bjorken x region.

From the unpolarized and polarized cross sections shown in Fig. 1.21, we can obtain $A_{LL}(p_T)$ of the heavy flavor electron production in the $\sqrt{s} = 200$ GeV pp collisions under the assumption of DSSV polarized PDF. DSSV expects A_{LL} of $\sim 2 \times 10^{-4}$ at $p_T < 1.5$ GeV/c. Therefore, the purpose of this measurement is to confirm such small asymmetry and obtain constraints of $\Delta g(x)$ in $10^{-2} \lesssim x \lesssim 8 \times 10^{-2}$, where there are not enough data sets for the constraint so far.

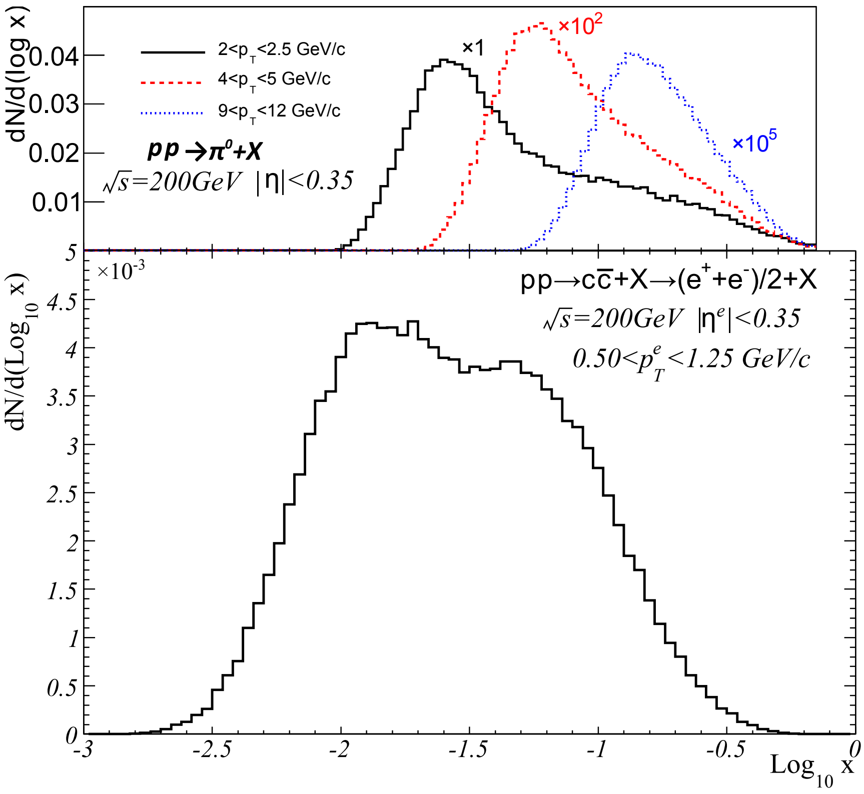

Figure 1.23: Bjorken x distribution contributing to (top) π^0 production [10] and (bottom) heavy flavor electron production in $\sqrt{s} = 200$ GeV pp collisions at pseudorapidity ranging $|\eta| < 0.35$ estimated by using PYTHIA simulation [76, 77]. Both distributions do not include efficiency of the particle detection. Transverse momentum of the heavy flavor electron ranges $0.5 < p_T < 1.5$ GeV/c and transverse momentum of π^0 ranges $2.0 < p_T < 2.5$ GeV/c, $4.0 < p_T < 5.0$ GeV/c, and $9.0 < p_T < 12.0$ GeV/c.

Advantages of heavy flavor electron measurement

We summarize the advantages of the heavy flavor electron measurement here. Due to the large mass of the heavy quarks, the whole p_T region of the heavy quark electron production satisfy large energy scale for pQCD calculations. This feature enables to extend the sensitive Bjorken x region into the current unexplored region, $x < 2\times10^{-2}$. The contributing Bjorken x for the heavy flavor electron measurement in $0.5 < p_T < 1.5$ GeV/c and $|\eta| < 0.35$ is ranging $10^{-2} \lesssim x \lesssim 8\times10^{-2}$. In addition, the heavy flavor electron is dominantly produced by gg interaction and is sensitive to the gluon polarization $\Delta g(x)$. Therefore, the A_{LL} measurement of the heavy flavor electron production efficiently constrains $\Delta g/g(x)$ at small Bjorken x region $10^{-2} \lesssim x \lesssim 8\times10^{-2}$, and provide new information on ΔG.

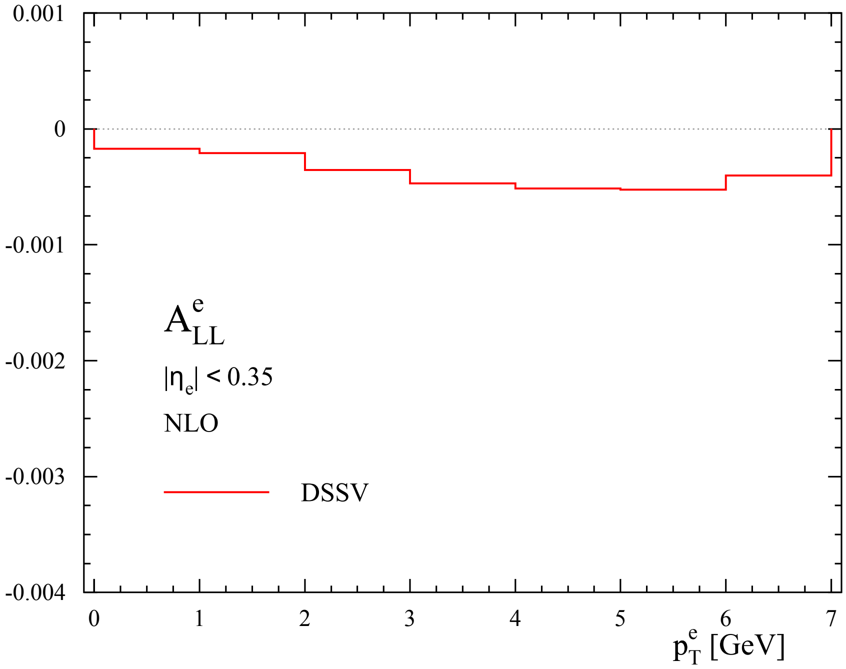

Figure 1.24: Theoretical expected A_{LL} of the heavy flavor electron production in $\sqrt{s} =$ 200 GeV pp collisions at a mid-rapidity region $|\eta| < 0.35$ with DSSV unpolarized PDFs and NLO partonic cross section.

1.6.3 Background for Heavy Flavor Electron Measurement

A challenging point on the heavy flavor electron measurement is large background electrons in the pp collisions. Figure 1.25 shows a comparison of cross section spectra of the heavy flavor electron and background electron. The plotted cross section of the heavy flavor electron is a previously published result which was measured at 2005 experiment [28]. The background electron spectra were estimated by a cocktail method, which is described in Sec. 3.1.6. The cocktail method estimates the spectra with a PHENIX-conventional event generator, which generates the hadrons or photons according to m_T scaling cross sections [78] and simulates their decays with Monte Carlo [29]. To estimate the background electrons from γ conversions and K_{e3} decays, GEANT3 simulation [79] was also used. Especially in a transverse momentum ranging $p_T < 2.0$ GeV/c, the yield of the background electrons is much larger than the heavy flavor electrons.

As Fig. 1.25 shows, the dominant background sources are π^0 and η Dalitz decay ($\pi^0, \eta \rightarrow e^+e^- + \gamma$), γ conversions in material, and K_{e3} decay ($K \rightarrow e\nu\pi$). The first two sources create electron pair via virtual or real photon, and therefore the electron pairs have small pair mass. These electron pairs are called "photonic electrons". The electrons except the photonic electrons are called "non-photonic electrons", which consist of the heavy flavor electrons for the large fraction, electrons from K_{e3} decays, and e^+e^- from light vector meson decays and Drell-Yan process. The K_{e3} electrons significantly contribute only at small transverse momentum $p_T < 0.75$ GeV/c. Ratio of the

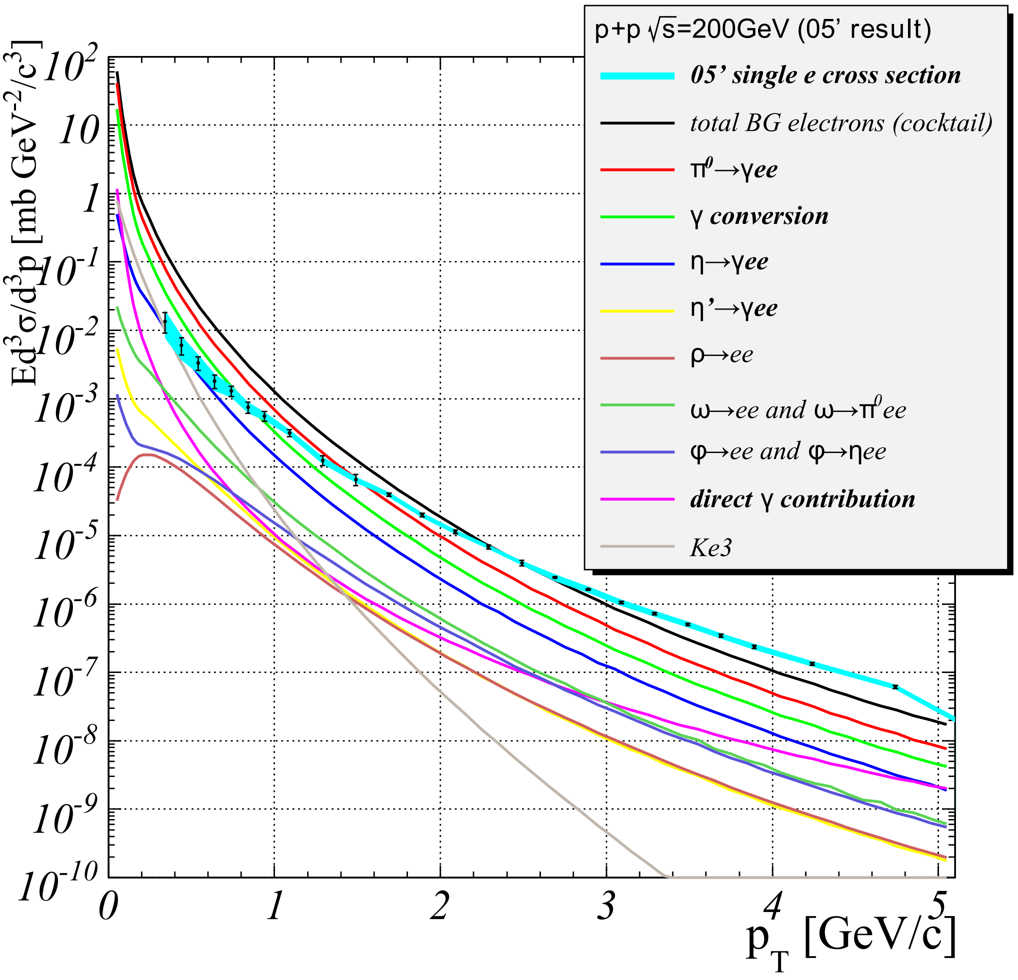

Figure 1.25: Comparison of signal and background cross section spectra. Black points with light-blue systematic uncertainty band represent cross section of heavy flavor electron production, which was measured at the 2005 PHENIX experiment. Several curves represent cross sections of background electron production, which were estimated with an event generator [29]. Estimation of background electrons from γ conversions and K_{e3} decays used also GEANT3 simulation.

non-photonic electrons to the photonic background in PHENIX 2005 run is shown in Fig. 1.26. In small p_T region, $0.4 < p_T < 2.0$ GeV/c, where the statistics is significant in the heavy flavor electron measurement, the ratio is less than 1.

Considering the background electrons (BG), the double spin asymmetry of inclusive electrons (S+BG) can be written as

$$A_{LL}^{\mathrm{S+BG}}(p_T) = D(p_T)A_{LL}^{\mathrm{HFe}}(p_T) + (1 - D(p_T))\, A_{LL}^{\mathrm{BG}}(p_T), \tag{1.83}$$

where A_{LL}^{HFe} represents double spin asymmetry of the heavy flavor electron production, $A_{LL}^{\mathrm{S+BG}}$ and A_{LL}^{BG} represent double spin asymmetry of inclusive electrons and background electrons, and $D(p_T)$ is a dilution factor which represents a fraction of the heavy flavor

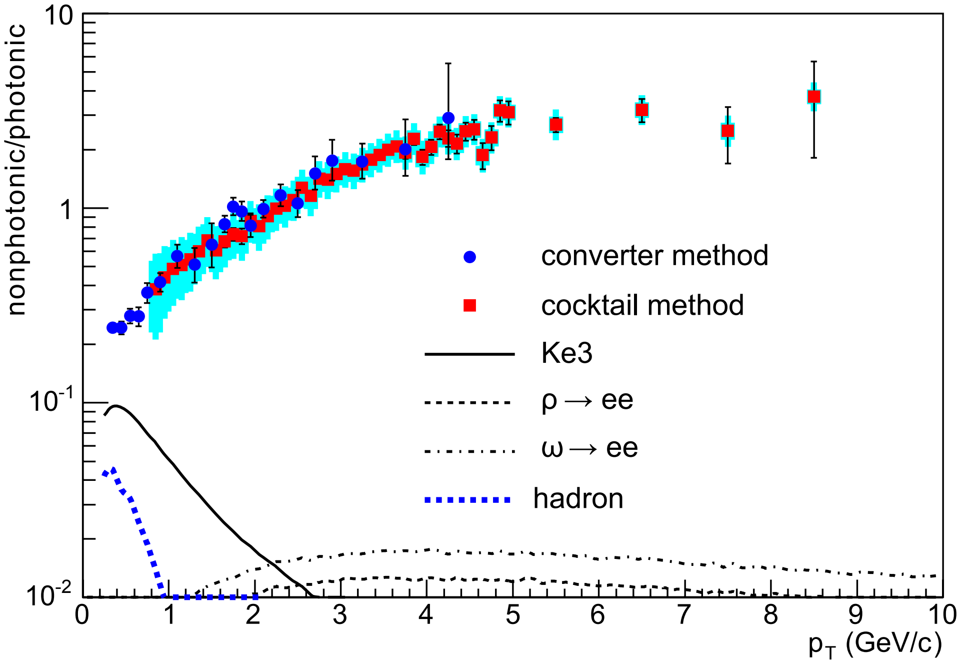

Figure 1.26: Ratio of non-photonic electrons to photonic background in PHENIX 2005 run [28]. The cocktail and converter methods are explained in Sec. 3.1.6. Error bars are statistical errors and the error bands show the cocktail systematic errors. The solid, dashed and dot-dashed curve are the remaining non-photonic backgrounds from K_{e3}, $\rho{\to}e^+e^-$, and $\omega{\to}e^+e^-$, respectively. The blue dot curve is misidentified hadron.

electrons in the inclusive electrons, $N_e^{\mathrm{HFe}}/N_e^{\mathrm{S+BG}}$. Above equation can be transformed into

$$A_{LL}^{\mathrm{HFe}}(p_T) = \frac{1}{D(p_T)}A_{LL}^{\mathrm{S+BG}}(p_T) - \frac{1-D(p_T)}{D(p_T)}A_{LL}^{\mathrm{BG}}(p_T). \tag{1.84}$$

As this equation shows, $D(p_T)$ dilutes the measured $A_{LL}^{\mathrm{S+BG}}(p_T)$ to derive $A_{LL}^{\mathrm{HFe}}(p_T)$. And then, $D(p_T)$ also expands uncertainty on the $A_{LL}^{\mathrm{HFe}}(p_T)$ propagated from uncertainty on the measured $A_{LL}^{\mathrm{S+BG}}(p_T)$. Therefore, the purification of the heavy flavor electrons and the enhanced $D(p_T)$ value is essential to reduce the uncertainty on the resulting $A_{LL}^{\mathrm{HFe}}(p_T)$ value.

In this analysis, we strongly suppressed the background with Hadron Blind Detector (HBD), which was newly installed in PHENIX at 2009. The HBD is a position-sensitive gas Čerenkov counter, and separates the non-photonic electrons and the photonic electrons by using amplitude of produced cluster charge. We developed new analysis method using this HBD feature as explained in Sec. 3.2.

Chapter 2

Experimental Setup

This analysis is based on the data which were taken at Relativistic Heavy Ion Collider (RHIC) with the PHENIX detector at Brookhaven National Laboratory (BNL) in the United States during the 2009 run. In this run, longitudinally polarized $p+p$ collisions at $\sqrt{s} = 200$ GeV were performed for 10 weeks (Apr. 19 $-$ Jun. 29). The integrated luminosity used in this analysis after quality assurance (QA) of data is ~ 6.1 pb^{-1} and the average beam polarizations during this measurement are $\sim 56\%$ for the Blue beam and $\sim 57\%$ for the Yellow beam.

For the heavy flavor electron measurement at PHENIX, a new detector called Hadron Blind Detector (HBD), which started to be operated from this run, is the most important detector to reject the photonic electron background in this analysis. Since it was the first operation of HBD for physics measurement, a new analysis frameworks of HBD was developed and was used in the measurement as described in Sec. 3.2.

In this chapter, RHIC is introduced in Sec. 2.1 and the PHENIX detector system used in this analysis is explained in Sec. 2.2. The detailed description of the HBD is also in Sec. 2.2. The PHENIX DAQ is described in Sec. 2.3.

2.1 Relativistic Heavy Ion Collider (RHIC)

RHIC provides high energy heavy ion collisions and polarized $p+p$ collisions. One of the major goals of the heavy ion experiment is to investigate a new state of matter which is referred to as Quark Gluon Plasma (QGP). RHIC can accelerate ions as heavy as Au up to an energy of 100 GeV per nucleon, which results in heavy ion collisions at $\sqrt{s_{NN}} = 200$ GeV. RHIC can also accelerate and collide polarized proton beams for the first time in the world, which provides us unique opportunities to study the spin property of proton through strong and weak interactions. The maximum energy for the proton beam is 255 GeV which results in collisions at $\sqrt{s} = 510$ GeV with design luminosity of 2×10^{32} cm^{-2}s^{-1}.

Figure 2.1 shows an aerial view of RHIC accelerator complex and Fig. 2.2 represents its schematic. The polarized proton beam is produced at optically-pumped polarized ion source (OPPIS) [80] with the polarization of about 85%. Its intensity reaches 500 µA in a single pulse of 300 - 400 µs, which corresponds to 9 - 12×10^{11} polarized protons.

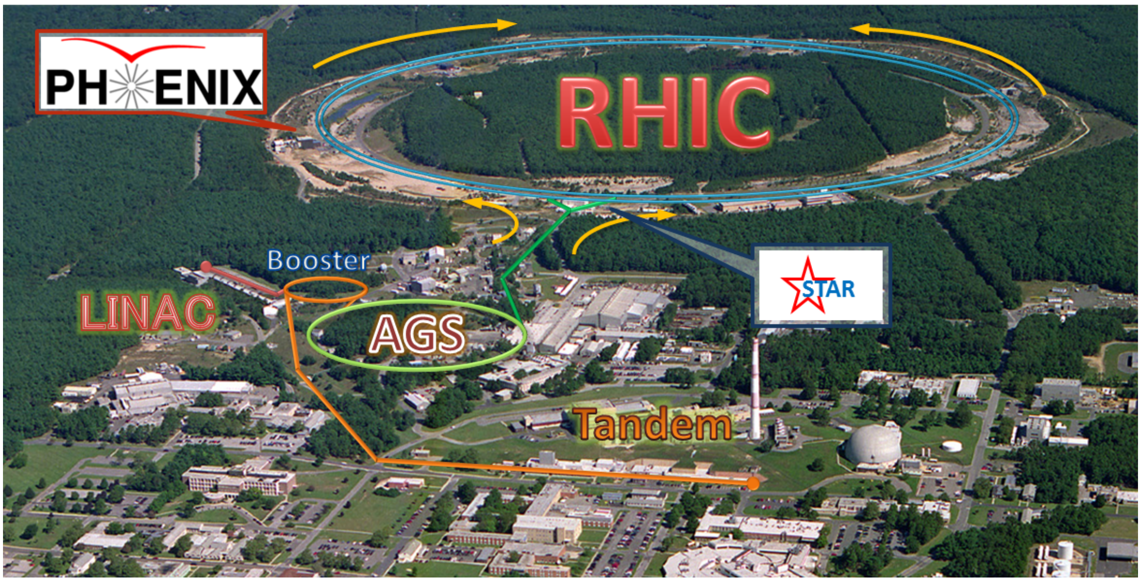

Figure 2.1: Aerial view of RHIC accelerator complex in BNL.

For the first step, the pulse is accelerated by Linear Accelerator (LINAC) to a kinetic energy of 200 MeV. This pulse is again accelerated by Booster up to 1.5 GeV, and also by Alternating Gradient Synchrotron (AGS) up to 24.3 GeV. Then it is injected into two independent rings at RHIC, via AGS-to-RHIC transfer line. Each beam travels in opposite direction and collides each other at interaction points (IPs). Two independent beams are called the Blue (clockwise) and Yellow (anti-clockwise) beams. RHIC has six IPs and they are referred to IP12, IP2 IP4, IP6, IP8, and IP10 as in the case of a clock. The PHENIX detector is placed at IP8 and the STAR detector is placed at IP6 as Fig. 2.1 shows. Also at IP12, there is a polarimeter system which measures the beam polarization. Once RHIC was filled with beams, the beams are kept circulating in the rings to provide collisions at the IPs. When the luminosity becomes too low, beams are dumped and refilled. The sequence from injection to dump of the beam is called a fill. The length of a fill is typically ~ 8 hours.

The polarization of the stored beams in RHIC rings has horizontal direction except around interaction points. Four spin rotators at the both sides of PHENIX IP in Fig. 2.2 changes the polarization direction and enable longitudinally-polarized collisions at PHENIX as shown in Fig. 2.3. The direction of the longitudinal beam polarization at the IP is called beam-helicity.

The beam in RHIC has bunch structure and each ring contains 120 bunches of polarized proton beam, with a time interval of 106 nsec. Each bunch is filled with predetermined beam-helicity pattern and this pattern is changed in different fills in order to confirm no pattern dependence in the spin asymmetry. There are basically four types of the beam-helicity patterns, which are defined as repetitions of the following

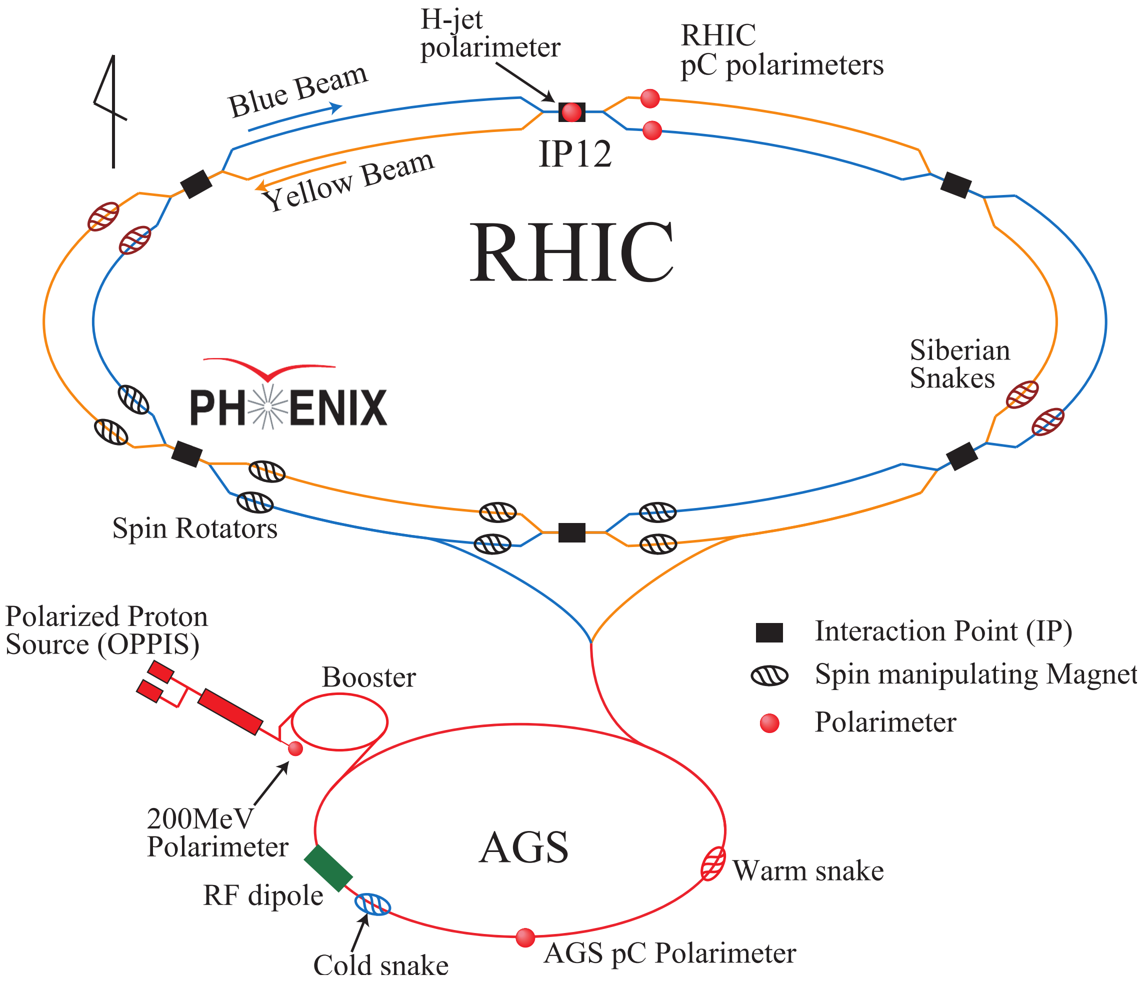

Figure 2.2: Schematic of RHIC accelerator complex.

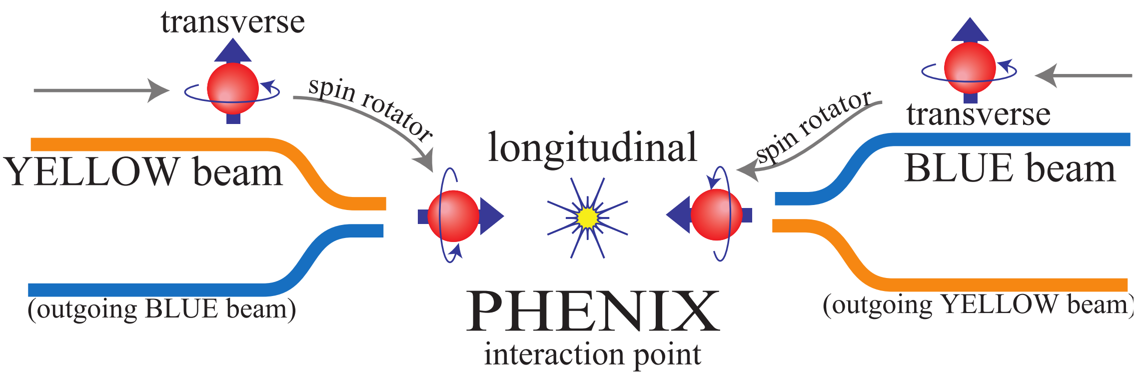

Figure 2.3: Schematic drawing of beam spin rotation near the PHENIX IP with the spin rotators.

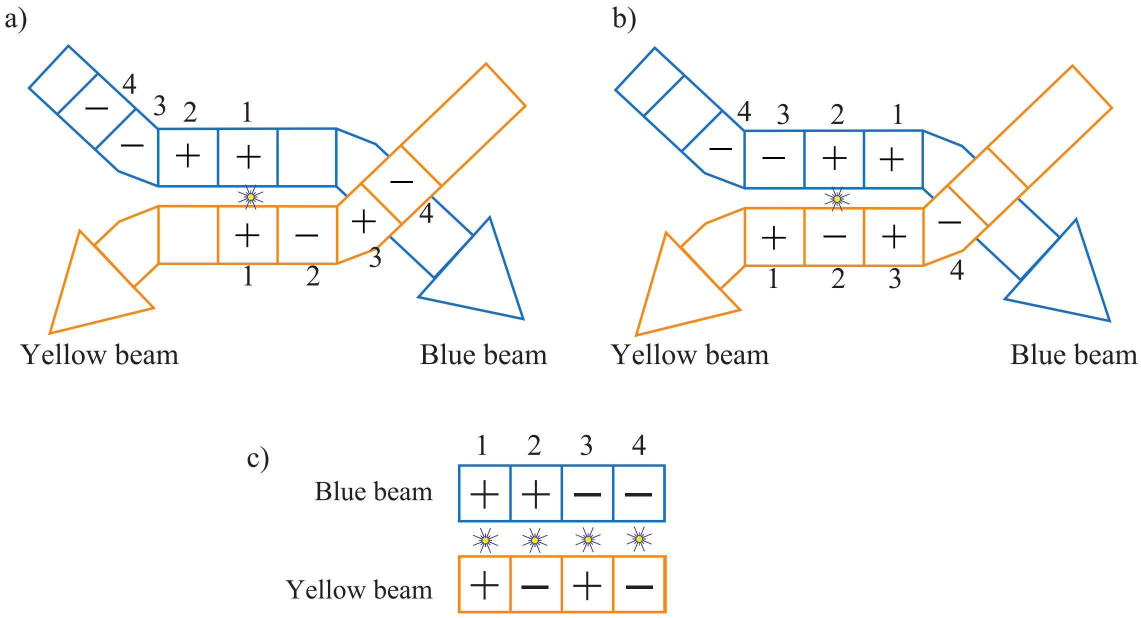

Figure 2.4: An example of the beam-helicity pattern of RHIC polarized proton beams. An arrow represents the direction of a beam. A box corresponds to a bunch and the sign (+ and −) in the box denotes the predetermined beam-helicity state of the bunch. The colors of arrows and boxes represent the Blue and Yellow beams. a) Blue bunch 1 collides at Yellow bunch 1 and provide a helicity combination (+,+) collision. b) One beam clock after, Blue bunch 2 and Yellow bunch 2 collide and provide a (+,−) collision. c) The resulting beam-helicity combinations from the helicity patterns. The helicity pattern provides the all four helicity combinations of collisions.

eight beam-helicity combinations:

$$P1 = \begin{cases} B: + - + - - + -+ \\ Y: + + - - + + -- \end{cases}$$

$$P2 = \begin{cases} B: - + - + + - +- \\ Y: + + - - + + -- \end{cases}$$

$$P3 = \begin{cases} B: + - + - - + -+ \\ Y: - - + + - - ++ \end{cases}$$

$$P4 = \begin{cases} B: - + - + + - +- \\ Y: - - + + - - ++ \end{cases} \quad ,$$

where the combinations appear from left to right. Figure 2.4a and 2.4b shows an example of a helicity pattern for the first four bunches. In this example, the Blue beam has a spin pattern “++−−” while the Yellow beam has a spin pattern “+−+−”. As the result, we obtain helicity combinations of four bunch crossing as (+,+), (+,−), (−,+), and (−,−), where the left and right signs in the parentheses represent the Blue and Yellow beam-helicities respectively, as shown in Fig. 2.4. These four combinations are the all possible helicity combinations. This alternative helicity changing greatly reduced systematic uncertainty which comes from time dependence of the detector responses. In 2009 RHIC run, 109 bunches out of 120 bunches are filled in each ring.

The beam polarizations for the Blue and Yellow beams are measured and monitored by three polarimeters. Two of them are fast carbon ribbon polarimeter (pC polarimeter) [81] and polarized hydrogen gas jet target polarimeter (H-jet polarimeter) [82, 83], installed in the RHIC ring, and another is PHENIX local polarimeter [84], installed at the PHENIX experimental area. These three types of polarimeters measure a sizable transverse single spin asymmetries for elastic scattering or specific particles production. Detailed information of the polarimeters and the polarization measurement are described in Appendix B.

2.2 PHENIX Detector System

PHENIX [85, 86, 87, 88, 89, 90, 91] is one of the largest experimental facilities at RHIC. PHENIX is designed to measure photons, leptons, and hadrons with excellent particle identification capability and to deal with both high-multiplicity heavy-ion collisions and high event-rate $p+p$ collisions.

A conventional Cartesian coordinate is defined in the PHENIX experimental area. The PHENIX collision point is defined as the origin of the coordinate. z-axis is along with the beam pipe, pointing to north, and x and y-axes are pointing to west and vertical top respectively. The polar angle, θ, and the azimuthal angle, ϕ, are also defined translating this Cartesian coordinate into the spherical coordinate. Rapidity and pseudorapidity of particles are also defined as

$$y = \frac{1}{2}\ln\frac{E+p_z}{E-p_z} \tag{2.1}$$

and

$$\eta = \frac{1}{2}\ln\frac{1+\cos\theta}{1-\cos\theta}, \tag{2.2}$$

where E and p_z are energy and z component of momentum respectively.

PHENIX is composed of many sets of detectors. These detectors can be divided into three groups: two central arms, two muon arms, and global detectors. Two east and west central arms cover pseudorapidity range of $|\eta| < 0.35$ and half in azimuthal angle. They are designed to detect photons, electrons, and hadrons. Two north and south muon arms cover $1.2 < \eta < 2.4$ (north) and $-2.2 < \eta < -1.2$ (south) respectively with a full azimuthal coverage. They are designed to detect muons.

Figure 2.5 shows a schematic of the PHENIX detector configuration in 2009. The upper panel is a beam view of a cross section of the configuration at $z = 0$ which shows the two central arms. The proton beams run perpendicular to the paper at the center of the detectors. The lower panel is a side view of a cross section at $x = 0$ which shows global detectors, beam-beam counters (BBCs), zero-degree calorimeters (ZDCs), and shower max detectors (SMDs). The PHENIX coordinate system is also

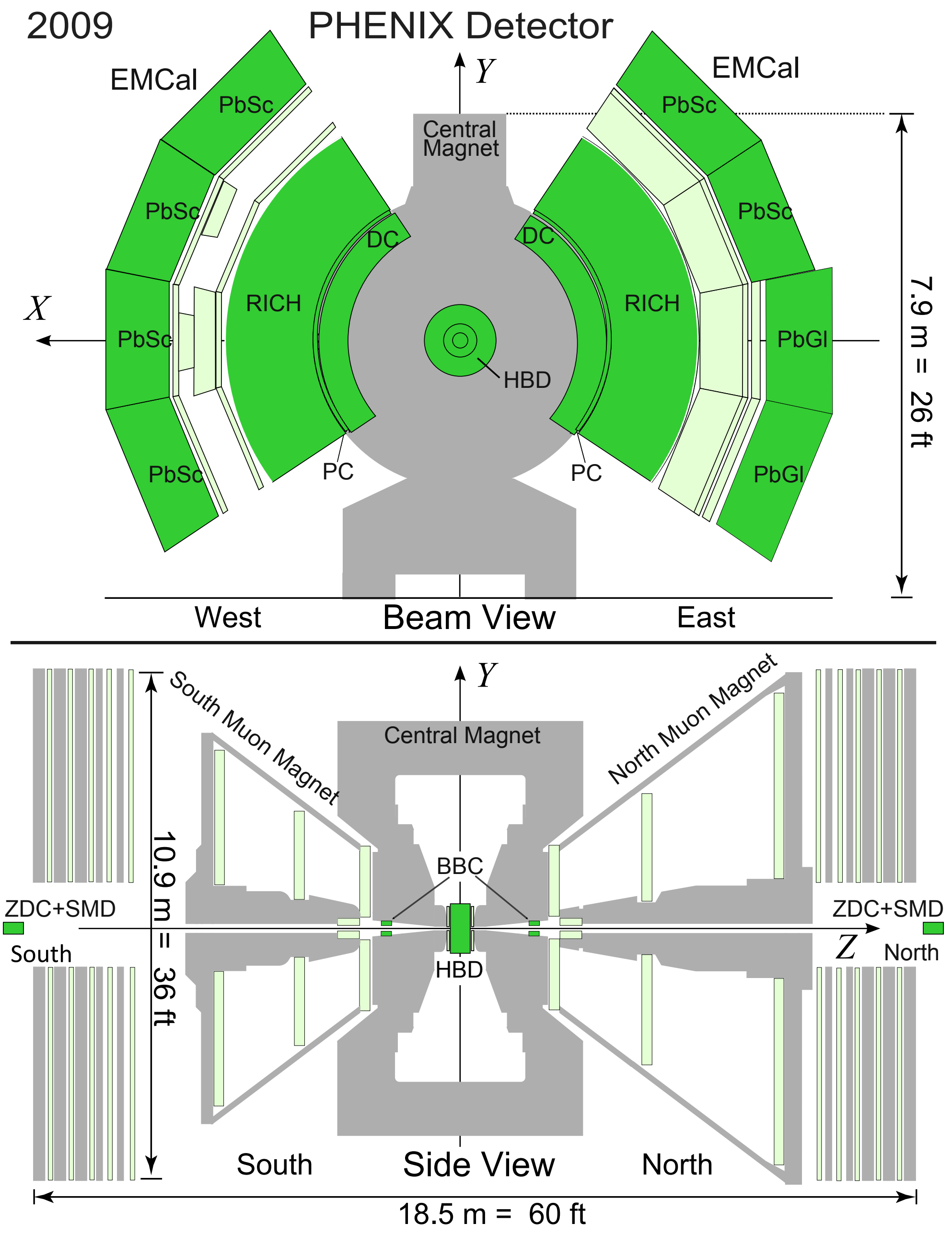

Figure 2.5: (Top) Beam view at $z = 0$ and (Bottom) side view at $x = 0$ of the PHENIX detector configuration in 2009. The positions of the ZDCs and SMDs are not in same scale as other detectors, but they are at 18 m away from the collision point.

shown in Fig. 2.5. The proton beams run along the z-axis and collide at the point of $y = 0$ each other. These central arm spectrometers and global detectors are the main detectors used in this measurement. The BBCs provide the collision point information and the minimum bias (MB) trigger. The count of the MB trigger also provides the luminosity information for the cross section and the spin asymmetry analyses. The electron measurements are made with the two central arm spectrometers that each cover

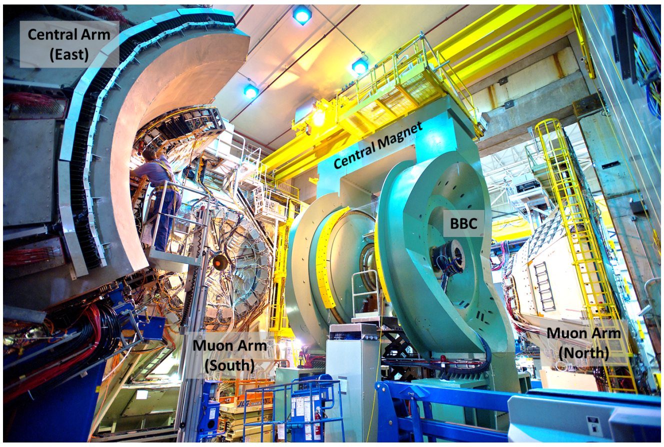

(a) Disassembled PHENIX detector system.

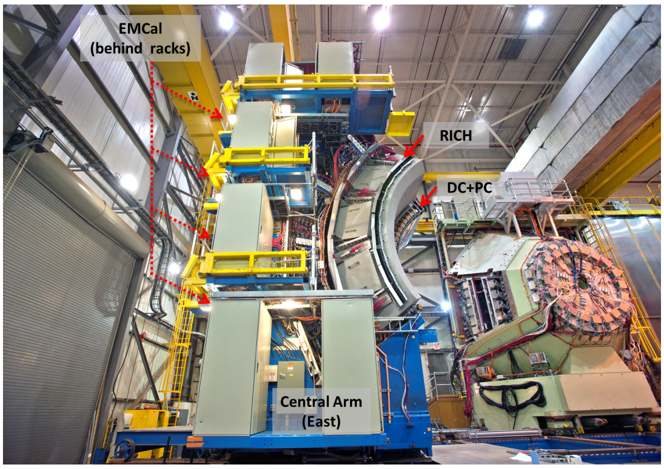

(b) PHENIX central arm (east).

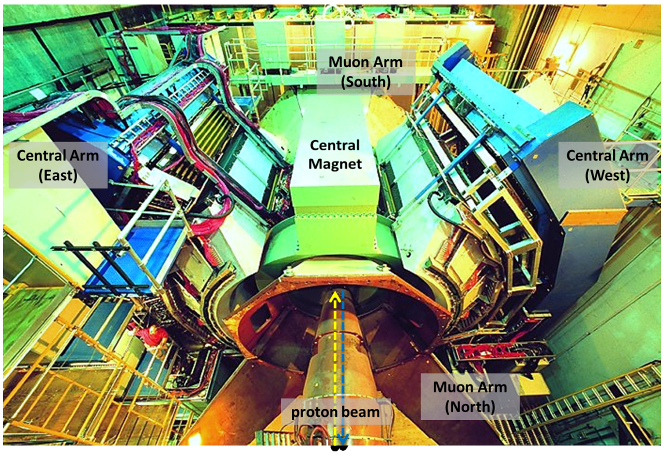

(c) Assembled setup for the experiment.

Figure 2.6: (a) Disassembled PHENIX detector system. In this figure, HBD is removed. (b) PHENIX east central arm. (c) Assembled setup for the experiment.

pseudorapidity $|\eta| < 0.35$ and azimuthal angle $\Delta\phi = \pi/2$. They consist of the central magnet and the drift chamber (DC) and the multi-wire proportional pad chamber (PC) for charged particle tracking, the ring-imaging Čerenkov detector (RICH) for electron identification, the electromagnetic calorimeter (EMCal) for energy measurement, and the hadron blind detector (HBD) [92, 93, 94] for another electron identification and background rejection. The features of the detectors and the magnet are summarized as follows.

2.2.1 Beam-beam counter (BBC)

The BBCs consist of two identical sets of counters positioned at ±1.44 m from the nominal interaction point along the beam direction and pseudorapidity of $3.1 < |\eta| < 3.9$. One placed on $+z$ (north) direction is named BBC-N and another placed on $-z$ (south) direction is named BBC-S.

Figure 2.7(a) displays a picture of a BBC. The outer diameter of the BBC is 30 cm and the inner diameter is 10 cm with a clearance of 1 cm between the BBC and beam pipe. Each BBC consists of 64 hexagonal quartz Čerenkov radiators with a refractive index of ~ 1.5, each of which is attached to a one-inch Hamamatsu R6178 photomultiplier tube. Figure 2.7(b) shows a picture of a pair of a 3 cm quartz radiator and a photo-tube. They are sensitive to charged particles with β greater than 0.7.

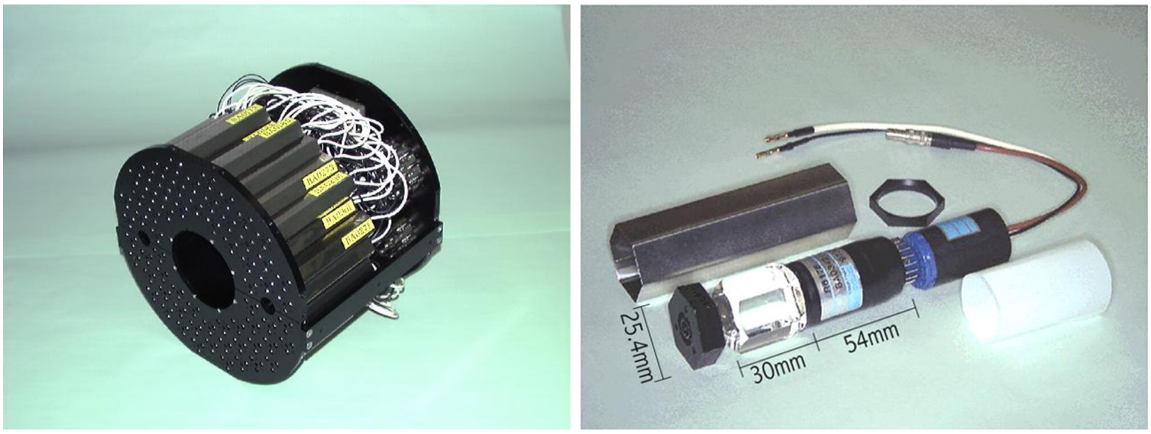

(a) BBC module. (b) A set of the quartz radiator and PMT.

Figure 2.7:

The electronics of the BBC readout consists of discriminators, shaping amplifiers, time-to-voltage converters and flash ADCs (FADC). The timing and pulse height information is digitized online and is stored in Digital Memory Units (DMUs). The BBC hit information is sent to BBC level-1 trigger board to provide BBC trigger as mentioned in Sec. 2.3.1.

They measure the collision vertex along with beam axis by measuring the time difference between the two counters and also provides the MB trigger defined by at least one hit on each side of the vertex. The position resolution for the vertex is ~ 2.0 cm in $p + p$ collision after offline slewing correction.

2.2.2 Zero degree calorimeter (ZDC) and shower max detector (SMD)

The ZDCs and SMDs, which are located at ±18.0 m away from the collision point along the beam direction, detect neutral particles near the beam axis ($\theta < 2.5$ mrad). Figure 2.8 shows the location of the ZDCs and SMDs. They are placed behind the DX magnets and between two beam pipes, thus most of the charged particles are swept away and neutral particles with long life, which are mainly neutrons and photons, hit the ZDCs and SMDs. The neutron identification is explained later. Protons, which are produced with elastic or diffractive scatterings on the collisions, may hit the beam pipes and induce showers. The resulting many charged particles may also hit the ZDCs and SMDs. A scintillation counter are placed in front of each ZDC for charged particle veto. Figure 2.9(a) and 2.9(b) are pictures of the ZDC and SMD.

A ZDC consists of series three modules each of which has 1.7 interaction length or 51 radiation length. Figure 2.10 shows the mechanical design of the module. The module consists of 27 layers of tungsten absorber plates and PMMA (Polymethylmethacrylate) optical fibers. Neutron generates a hadronic shower in the tungsten plates, and charged particles in the shower emit Čerenkov radiation. The radiation is detected through the optical fibers with a photo-tube (Hamamatsu R329-02). The size of a tungsten plate is 10 cm wide, 18.7 cm high and 0.5 cm thick. The tungsten plates and the optical fibers are tilted by 45 degrees to roughly match the direction of the Čerenkov radiation. The energy resolution of the ZDC is obtained to be 21 % for neutrons at an energy of 100 GeV. Neutrons can be separated from photons with the energy deposit in the second module of the ZDC, since the electromagnetic showers from photons cannot penetrate the first module with 51 radiation length and do not reach the second module.

The SMD is scintillator hodoscopes which consist of 7 scintillator strips with a width of 15 mm in the vertical direction to provide x-coordinate, and 8 strips with a width of 20 mm in the horizontal direction to provide y-coordinate. The SMD is placed between the first and second ZDC modules. At the position, the induced shower by neutron reaches maximum. The shower position is determined by weighted average of the SMD hits. The position resolution of the SMD is ~ 1 mm for 100 GeV neutrons.

Coincidence of hits in the ZDCs defines ZDC trigger. The ZDC trigger serves as an independent luminosity measure as well as the BBC trigger. Comparison between BBCs and ZDCs can be used to estimate the uncertainty on luminosity measure.

2.2.3 Central magnet (CM)

The transverse momentum of each charged particle is determined by its bending curvature in the magnetic field provided by the PHENIX central magnet (CM) system [86]. The CM is energized by two pairs of concentric coils and provides an axial magnetic field parallel to the beam direction.

During this measurement, the two coils of the CM were operated in the canceling (“$+-$”) configuration. This configuration is essential for the background rejection of the heavy flavor electron measurement with the HBD as described later. A cross section of the magnetic field produced by the $+-$ configuration is shown in Fig. 2.11, and the

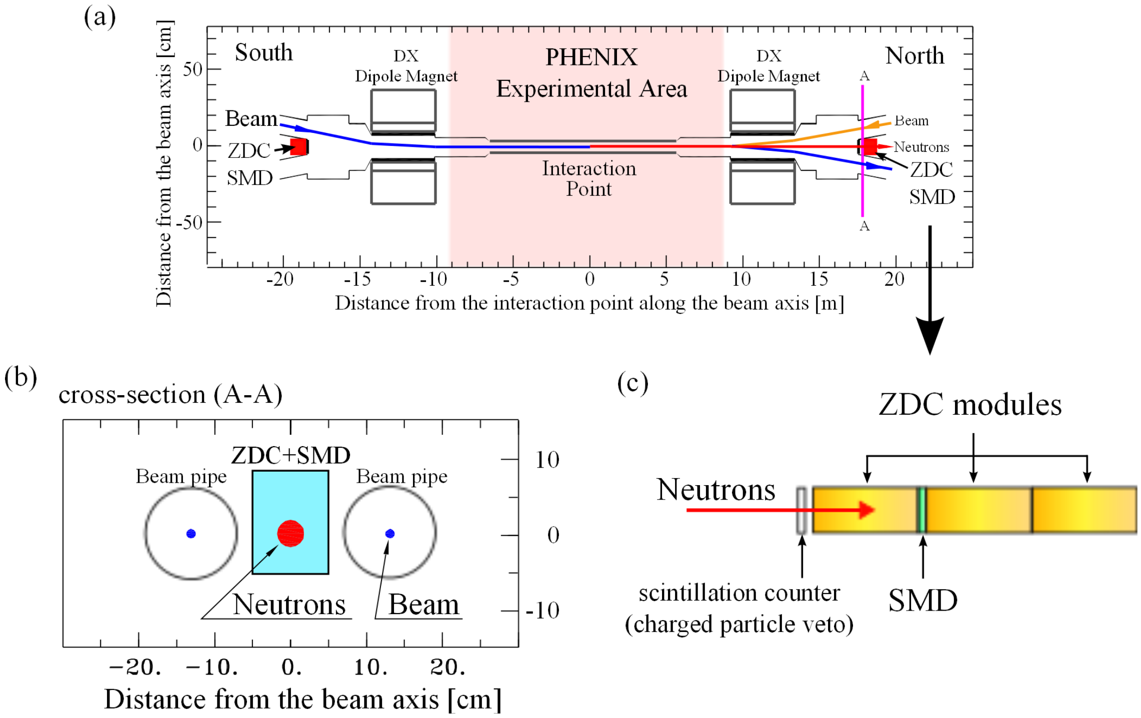

Figure 2.8: (a) Location of the ZDC and SMD from the top view. (b) The view of the cross section in the figure (a). (c) The configuration of the three ZDC modules, SMD, and scintillation veto counter.

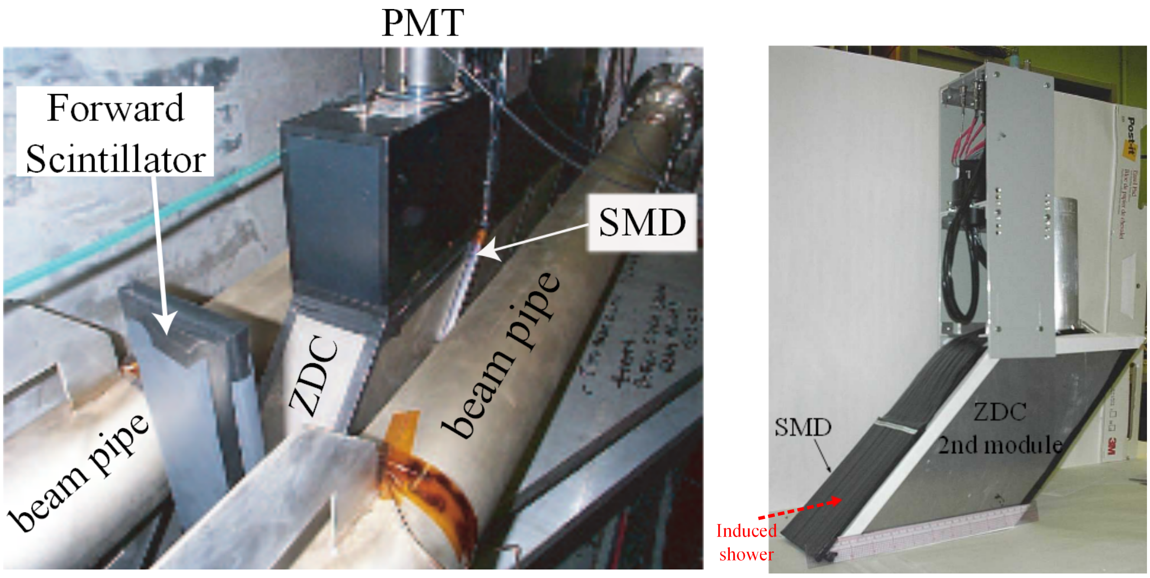

(a) (b)

Figure 2.9: (a) Installed ZDC and SMD. (b) ZDC second module and SMD.

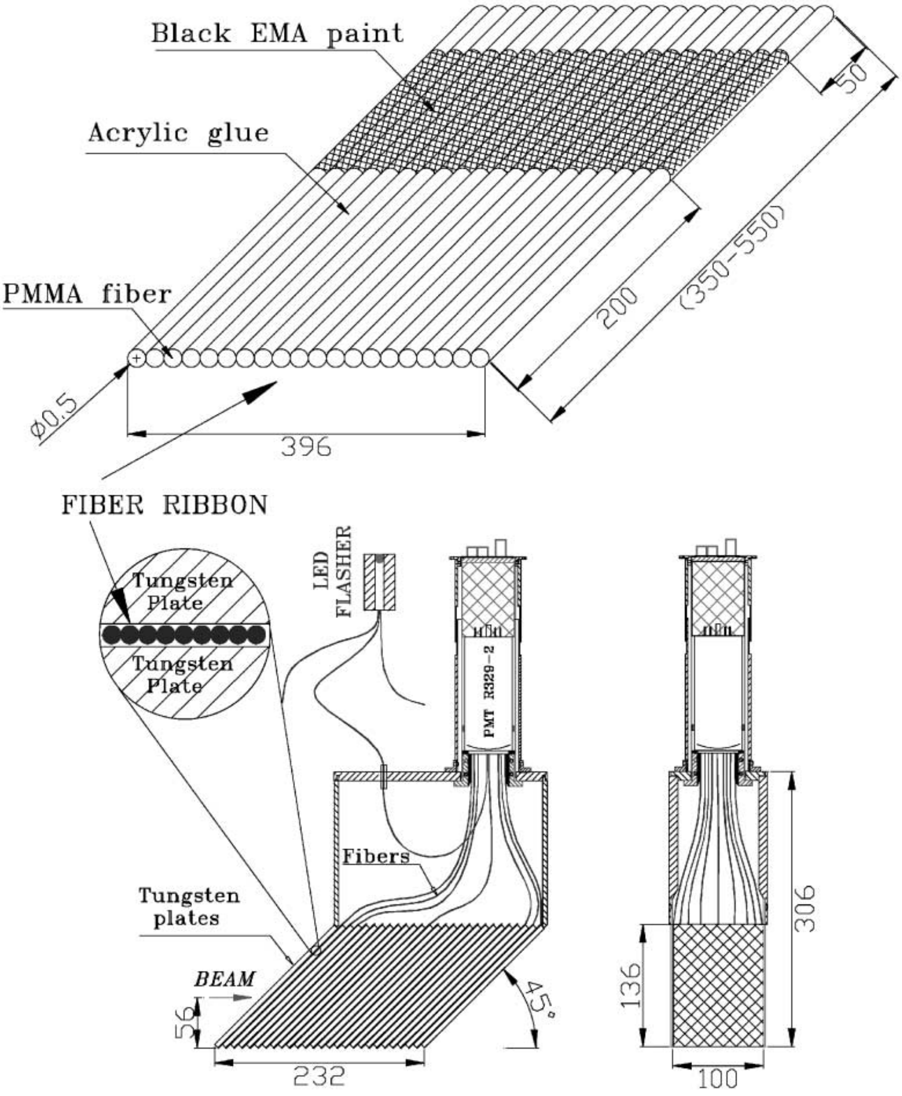

Figure 2.10: Mechanical design of ZDC module.

magnitude of the magnetic field as a function of distance from the collision point is shown in Fig. 2.12. In this configuration, the field is almost canceled out around the beam axis in the radial region $0 < R < 50$ cm, and has a peak value of ~ 0.35 T around $R \sim 100$ cm. The total field integral is $|\int B \times dl| = 0.43$ Tm.[1]

2.2.4 Drift chamber (DC)

The DCs are used to measure the charged particle trajectories in x-y plane and determine the high resolution transverse momentum ($p_T \equiv \sqrt{p_x^2 + p_y^2}$). The DCs are located in the East and West arm at a radial distance of $2.02 < R < 2.46$ m, and each covers 90 degrees in azimuth and $|\eta| < 0.35$ in pseudorapidity (corresponding to 1.8 m in

---

[1] $|\int B \times dl| = 0.78$ Tm for the ++ configuration.

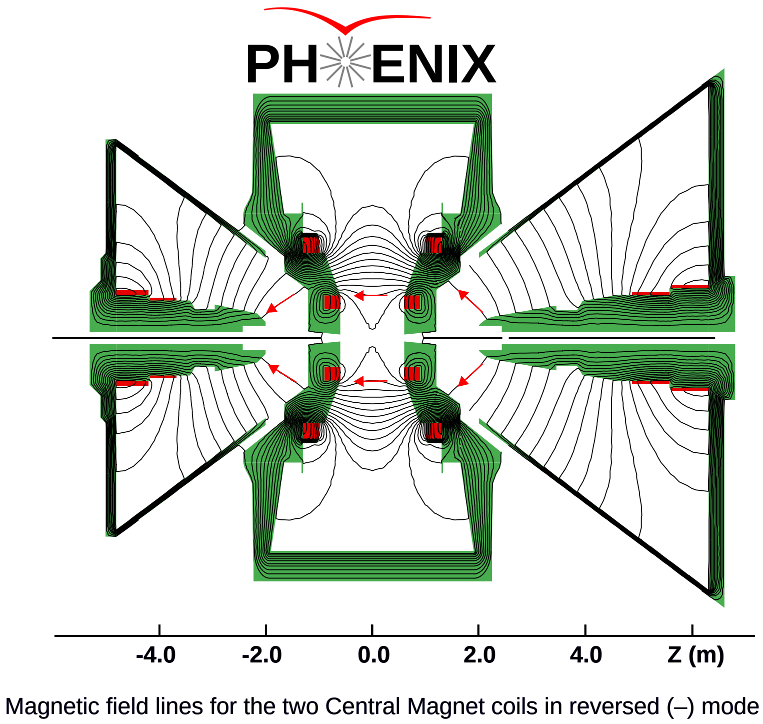

Figure 2.11: Cross section of magnetic field in the $+-$ CM configuration. The magnetic field around the collision point is canceled out and the magnetic field exists only at position with a ~ 1.0 m radius from the collision point.

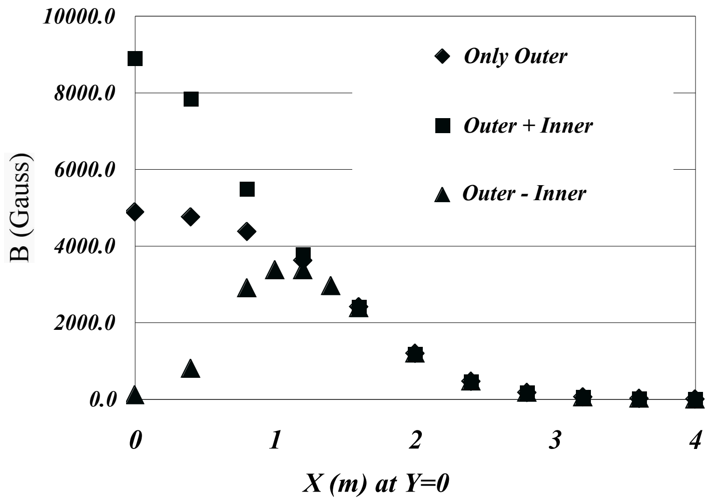

Figure 2.12: Field strength of the CM magnetic fields as a function of distance from the collision point. This plot shows three types of the configuration: using only outer magnet ($+0$), using both outer and inner magnets ($++$), and using outer and reversed inner magnets ($+-$). The $+-$ configuration is employed in this measurement.

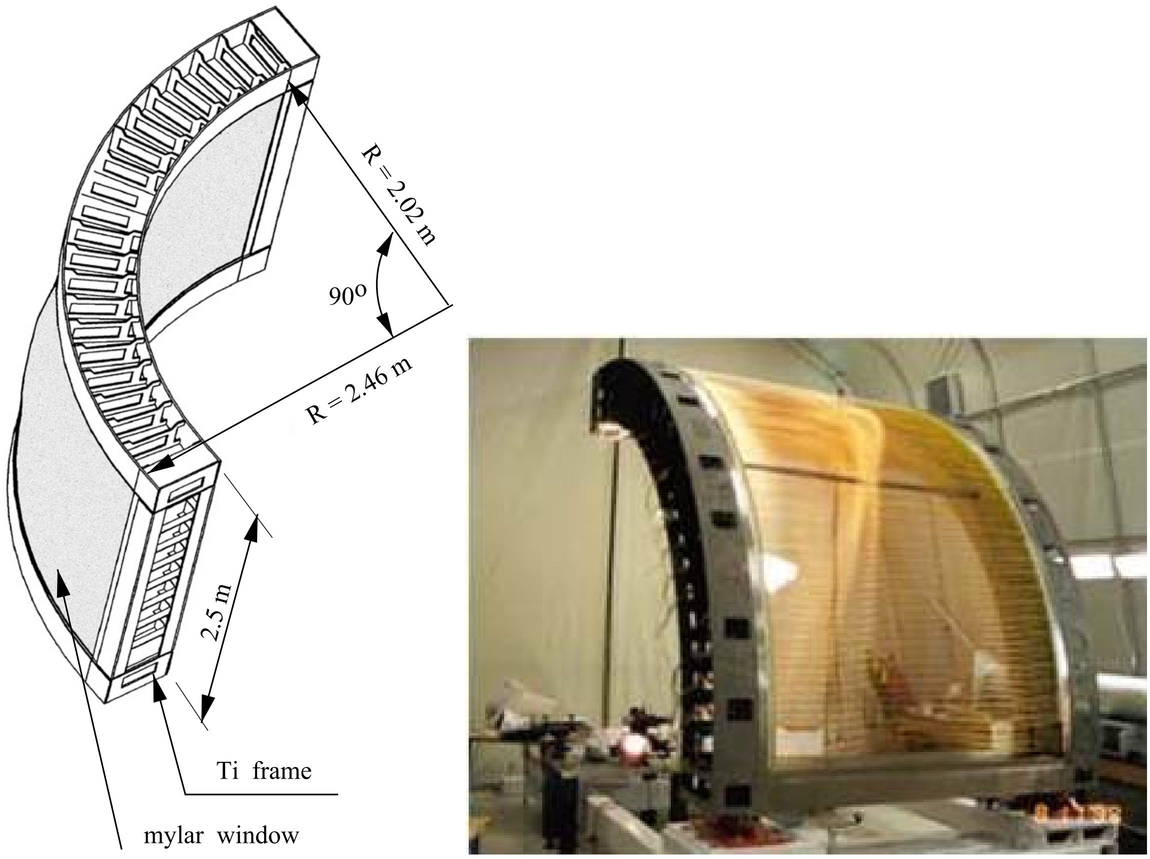

(a) (b)

Figure 2.13: (a) Construction of DC frame. (b) Picture of DC.

z-direction). They use gas mixture of 50% Argon and 50% Ethane.

A schematic drawing of the DC frame and a picture of the DC is shown in Fig. 2.13. Each DC consists of 20 sectors, each of which covers 4.5 degrees in azimuth. In each sector, there are six types of wire modules stacked radially. They are called X1, U1, V1, X2, U2, V2 plane from inner to outer.

The sketch of a sector and the layout of wire position are shown in Fig. 2.14. The X1 and X2 wire cells run in parallel to the beam to perform precise track measurements in x-y plane. These wire cells are followed by two sets of small angle U, V wire planes used in the patter recognition. U1, V1 U2, and V2 wires have stereo angle of about 6 degrees relative to the X wires in order to measure the z-coordinate of the track. Each of X and U, V stereo cells contain 12 and 4 anode (sense) wires, respectively, which form cells with a 2 - 2.5 cm drift space in ϕ direction. With the mixture gas of argon-ethane, the plateau drift velocity is 5.3 cm/µsec for field gradation from 800 V/cm to 1400 V/cm. Therefore, the maximum drift time in a cell is approximately 470 nsec.

The DC signals are read out by ASD (pre-amplifier, shaping amplifier, discriminator) chips and TMC (time memory cell) chips. The ASD chip contains 8 channels for pre-amplifier, and a 6 nsec shaping amplifier, and an externally controlled discriminator.

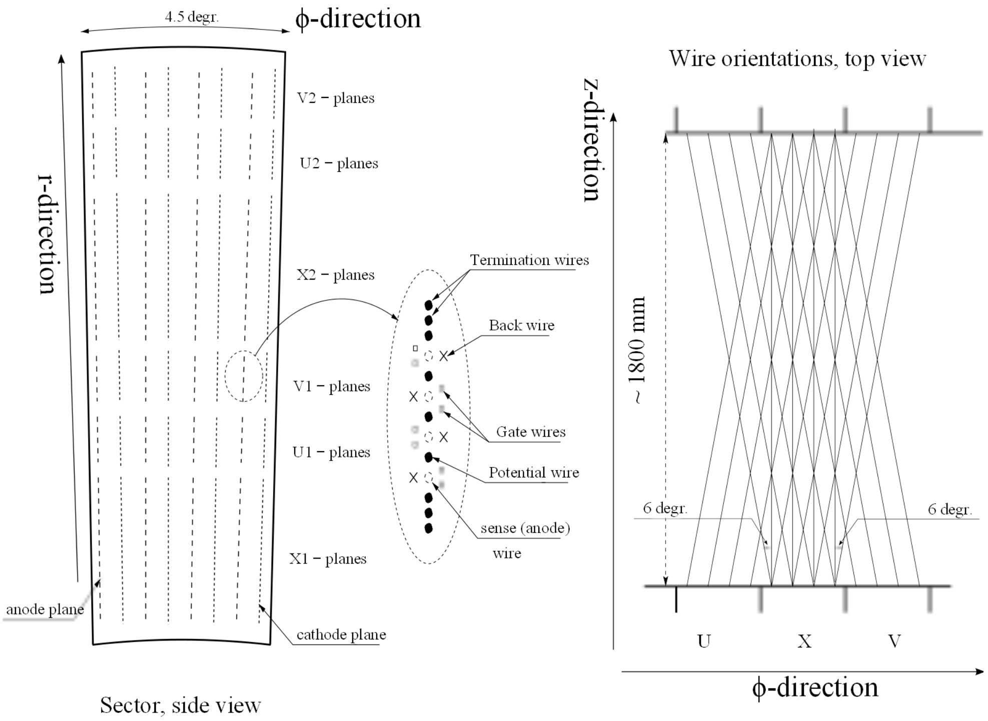

Figure 2.14: (Left) The layout of wire position within one sector and inside the anode plane. (Right) A schematic diagram, top view, of the stereo wire orientation.

The TMC chip can memorize bit information in time bins whose interval is 1/32 of the input clock period. Using four times rate of the RHIC crossing clock as the input clock, the ASDs discriminator output is memorized with a single bin resolution of roughly 0.8 nsec in TMC.

2.2.5 Pad chamber (PC)

The PCs are used to measure the space points which determine momentum in z direction (p_z) with the DC hit information. Figure 2.15 shows the PC mounted on the DC. This position measurement is also important to determine the projection points on RICH, EMCal, and HBD detectors. The PCs are the cathode readout multi-wire proportional chambers located $2.47 < R < 2.52$ m in radial distance from the collision point. Each PC also covers 90 degrees in azimuth and $|\eta| < 0.35$ in pseudorapidity as well as the DC.

Each detector contains a single plane of wires inside a gas volume bounded by two cathode planes as shown in Fig. 2.16. The gas was chosen to be the mixture of 50% Argon and 50% Ethane at atmospheric pressure. One cathode is finely segmented into an array of pixels. A cell structure is made up with three pixels and has a dimension of 8.4×8.4 mm^2 which satisfies the requirement of good position resolution in z direction and a low occupancy even in the high track multiplicities. The position resolution of the PC was measured to be 1.7 mm along the z direction.

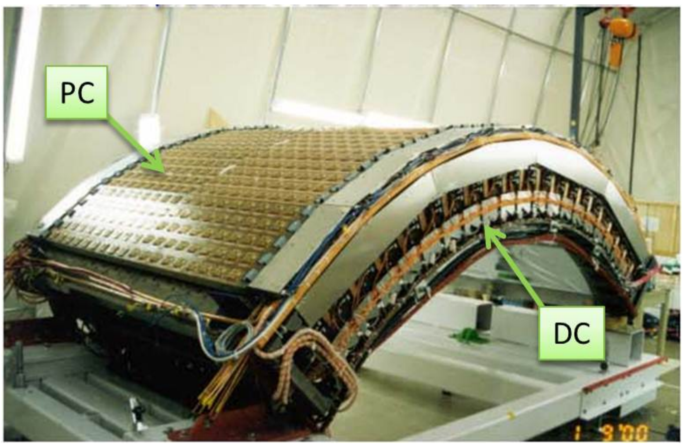

Figure 2.15: PC mounted on DC.

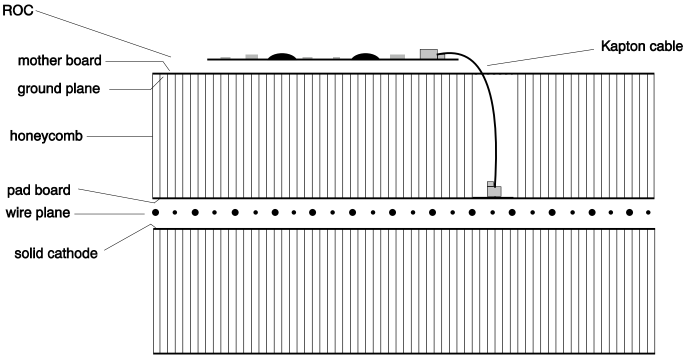

Figure 2.16: Vertical cut through a chamber.

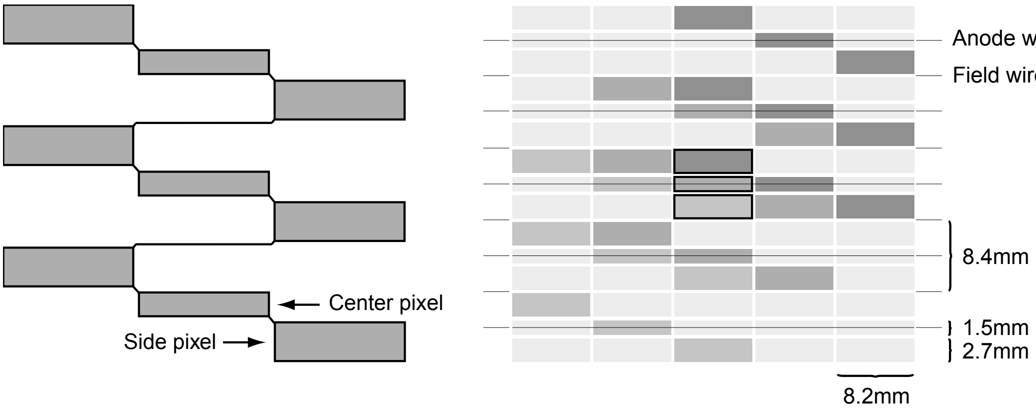

Figure 2.17: (Left) The pixel geometry. (Right) A cell defined by three pixels located the center of the figure.

When a charged particle starts an avalanche on an anode wire, charges are induced on a number of pixels. Figure 2.17 shows the schematic diagram of the PC readout pixels. In order to reduce the amount of electric and other noise, each cell of the PC contains three pixels and an avalanche must be sensed by all three pixels to form a valid hit in the cell. Because of huge electronic channels with this arrangement, the interleaved pixels are gathered together. Nine pixels are connected to a group and to a common readout channel, such that the three pixels in a cell are always connected to different but neighbor channels and each cell is defined by its unique channel triplet. This solution saves a factor of nine in the number of readout channels compared to readout of the all pixels. The PC signals are read out by custom made integrated circuits which contain charge amplifiers and discriminators. Many operational characteristics of the circuits are remotely programmable via serial communication.

2.2.6 Ring-imaging Čerenkov (RICH) Detector

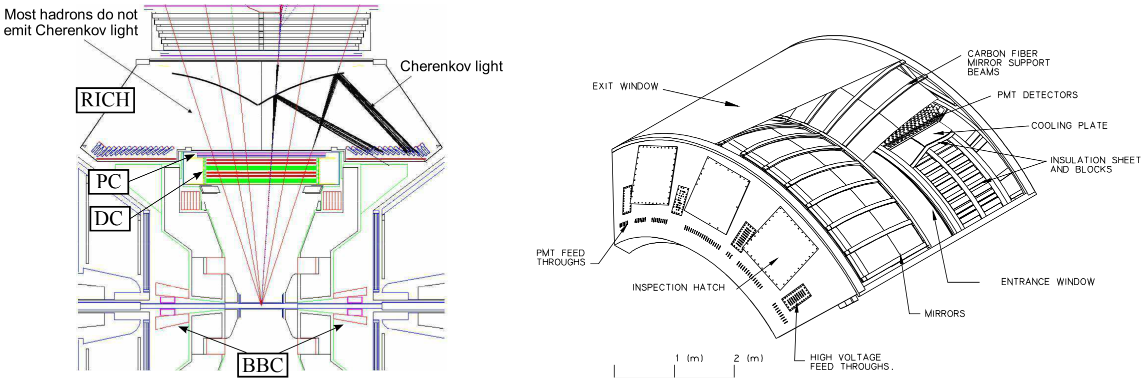

(a) Top view.

(b) Cutaway view.

Figure 2.18: (a) A top view and (b) a cutaway view of the RICH detector.

The RICH is a threshold-type gas Čerenkov counter and the primary detector used to identify electrons in PHENIX and shown in Fig. 2.18(a). The RICH also provides an electron trigger together with the EMCal. It is located in the radial region of 2.5-4.1 m. The RICH covers pseudorapidity $|\eta| < 0.35$ and $2 \times \pi/2$ in azimuth.

Figure 2.18(b) contains a cutaway drawing of the RICH detector. The RICH contains 48 composite mirror panels, forming two intersecting spherical surfaces. The spherical mirrors focus Čerenkov light onto two arrays of 1280 UV PMTs (Hamamatsu H3171S), each located on either side of the RICH entrance window. The PMTs are fitted with $2''$ diameter Winston cones and have magnetic shields that allow them to operate at up to 100 G. The minimum thickness of radiator gas seen by any particle is 87 cm, the maximum is about 150 cm. The RICH is filled with CO_2 gas for the radiator. The radiator gas is maintained at a pressure of $0.5''$ of water above ambient. The RICH has a Čerenkov threshold of $\gamma = 35$, which corresponds to $p > 20$ MeV/c for electrons and $p > 4.9$ GeV/c for charged pions. The average number of hit PMTs per electron track is ~ 5, and the average number of photoelectrons detected is ~ 10. Below the pion threshold the e/π separation is $\sim 10^4$ in $p+p$ collisions.

The preamp output drives both a charge and a timing measurement channel. The timing measurement uses a discriminator followed by a TAC while the charge measurement employs a CMOS charge-integrating amplifier followed by a variable-gain amplifier. Both of the above analog outputs are stored in Analog Memory Units (AMU). The analog data are digitized with ADC boards when the level-1 trigger signal is received.

2.2.7 Electromagnetic calorimeter (EMCal)

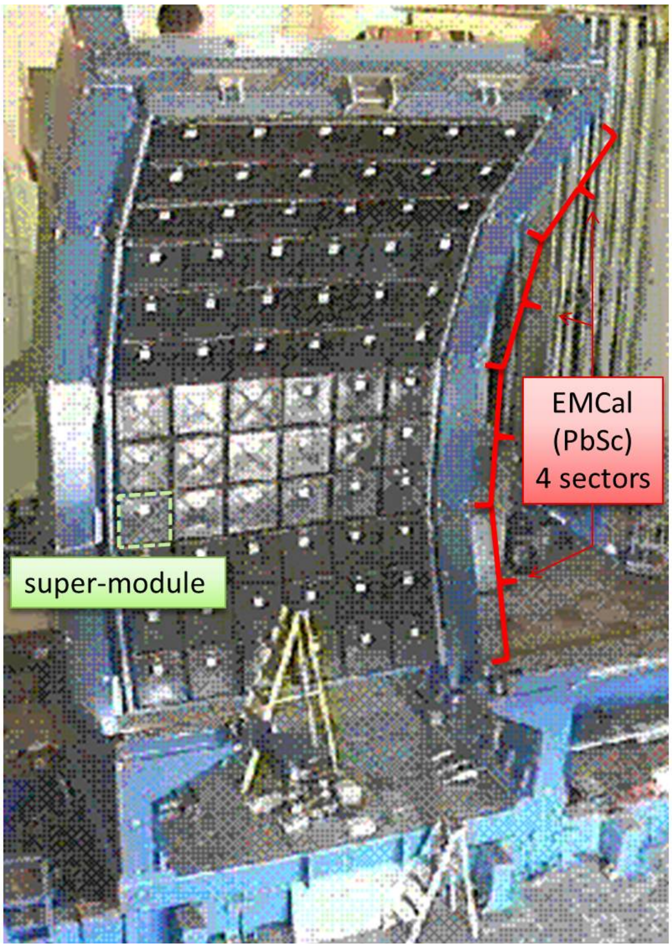

Figure 2.19: Assembled EMCal west arm, which consists of 4 PbSc sectors.

The EMCal [89] plays an important role for the detection of electrons and photons. The EMCal in a half central arm covers central rapidity of $|\eta| < 0.35$ and azimuthal angle of $\Delta\phi = \pi/2$. The EMCal in west arm is shown in Fig. 2.19. EMCal is composed of two types of calorimeters, lead-scintillator (PbSc) and lead-glass (PbGl). The radial distance from collision point is ~5.1 m for PbSc and ~5.4 m for PbGl. A box with a label of PbSc or PbGl in Fig. 2.5 corresponds to a sector. PHENIX has eight sectors of EMCal, six of them are PbSc and other two are PbGl. Both type covers pseudorapidity range of $|\eta| < 0.35$.

A PbSc sector is composed of 3×6 super-modules, and the super-module consists of 6×6 modules, each of which consists of 2×2 towers. The tower is the minimum unit of individual read-out in EMCal. On the other hand, a PbGl sector is composed of 12×16 super-modules, each of which consists of 4×6 towers. The total numbers of towers are 15552 for PbSc and 9216 for PbGl.

The energy, time of flight, and energy sum for electron and photon triggers are derived from EMCal signals. The energy and trigger are used in this analysis. The analog signals from PMTs are processed by ASIC chips on EMCal front-end electronics. An ASIC chip processes four adjacent towers forming 2×2 block, which is the minimum unit for trigger decision. The ASIC divides the signals for TAC process and ADC process. In the TAC process, the divided signal is transformed to a digital signal by a discriminator and sent to the TAC. In the ADC process, the signal is amplified by variable gain amplifier (VGA) with a gain of $\times 4$ - 12 with 5 bit resolution. The signal is summed up with one from other three towers to provide the energy sum of 2×2 towers and sent to trigger boards. As mentioned in Sec. 2.3.1, the analyzed data in this paper is obtained with the 2×2 energy sum trigger with RICH signal. One unit of the trigger decision, namely a group of 2×2 towers, is called a trigger tile.

2.2.8 Hadron blind detector (HBD)

A challenging issue for the heavy flavor electron measurement is to reject the dominant background of electron pairs from γ conversions and Dalitz decays of π^0 and η mesons which are mediated by virtual photons. The HBD aims to considerably reduce the photonic electron pairs utilizing the distinctive feature of the e^+e^- pairs, namely their small opening angles.

The HBD is a position-sensitive Čerenkov detector operated with pure CF_4 gas as the radiator. It covers pseudorapidity $|\eta| < 0.45$ and $2 \times 3\pi/4$ in azimuth. The coverage is larger than the acceptance of the other detectors in the central arm in order to detect photonic electron pairs with only one track reconstructed in the central arm and the other outside of the central arm acceptance. Figure 2.20 shows the top view and exploded view of the HBD. The HBD has a 50 cm long radiator directly coupled in a windowless configuration to a readout element consisting of a triple Gas Electron Multiplier (GEM) stack, with a CsI photo-cathode evaporated on the top surface of the interior GEM and pad readout at the exterior of the stack. The readout element in one half HBD arm is divided into six sectors. The expected number of photoelectrons for an electron track is about 20 and it is consistent with the measured number. Since the HBD is placed close to the collision point, the material thickness should be small to reduce conversions. The total thickness to pass through the HBD is $0.024 \times X_0$ and the thickness before the GEM pads is $0.007 \times X_0$, where X_0 represents the radiation length.

The hadron blindness of the HBD is achieved by operating the detector in the so-called reverse bias (RB) mode as opposed to the standard forward bias (FB) mode (see Fig. 2.21). In the RB mode, the mesh is set at a lower negative voltage with respect to the GEM and consequently the ionization electrons deposited by a charged particle in the drift region towards the mesh as shown in the right panel in Fig. 2.21. Consequently, the signal produced by a charged particle results only from (i) the collection of ionization

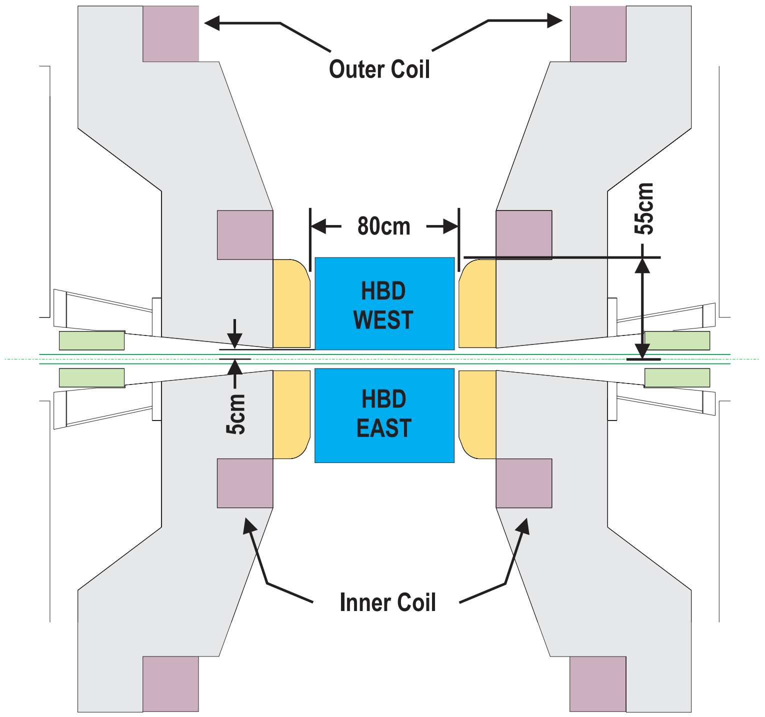

(a) HBD from top view.

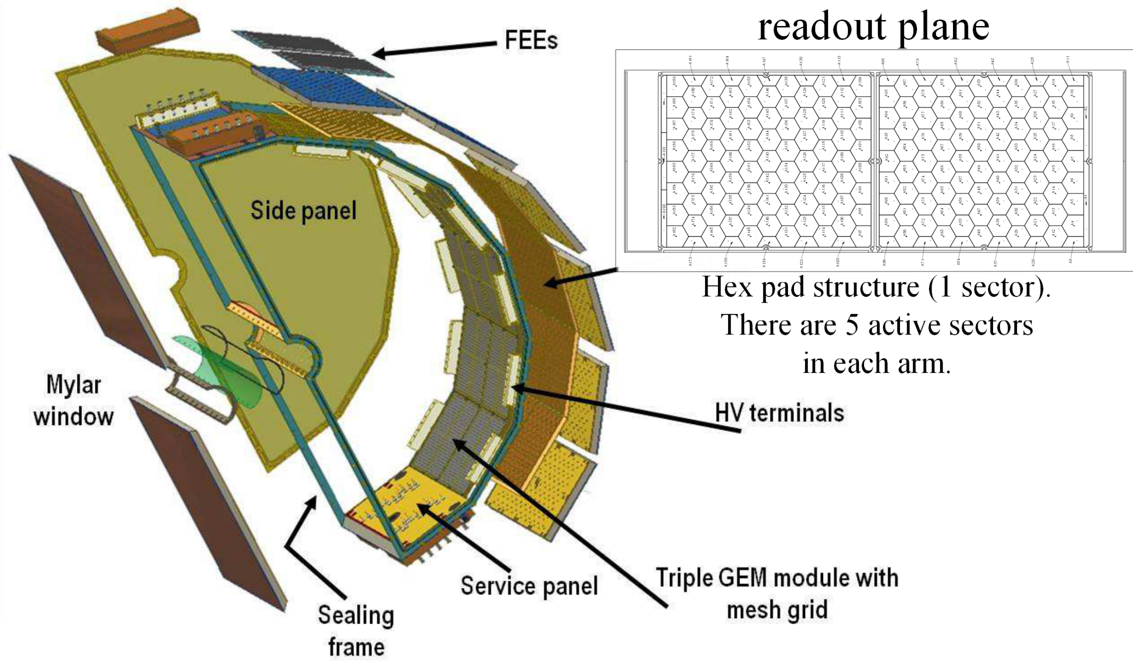

(b) HBD exploded structure.

Figure 2.20: (a) Top view of the HBD showing the location of the HBD in the central magnet. (b) Exploded view of one half HBD arm. CF_4 gas is filled in the volume as the Čerenkov light radiator.

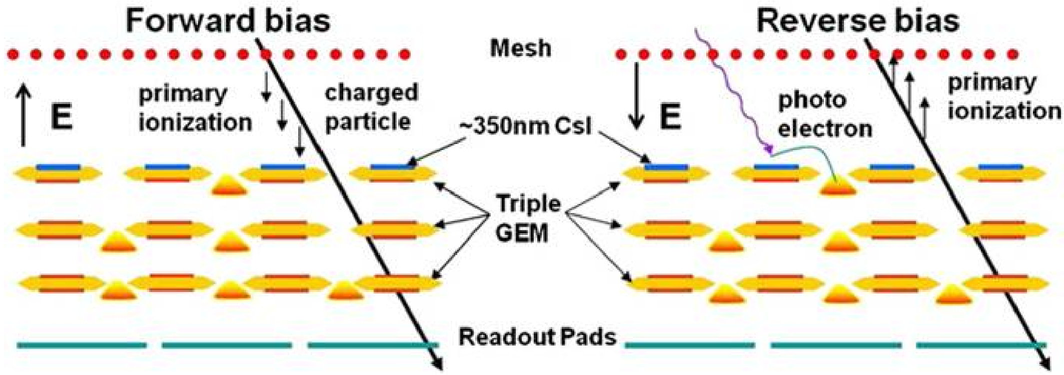

Figure 2.21: Triple GEM stack operated in the forward bias mode (left) and in the hadron-blind reverse bias mode (right). During the experiment, the HBD is operated in the reverse bias mode.

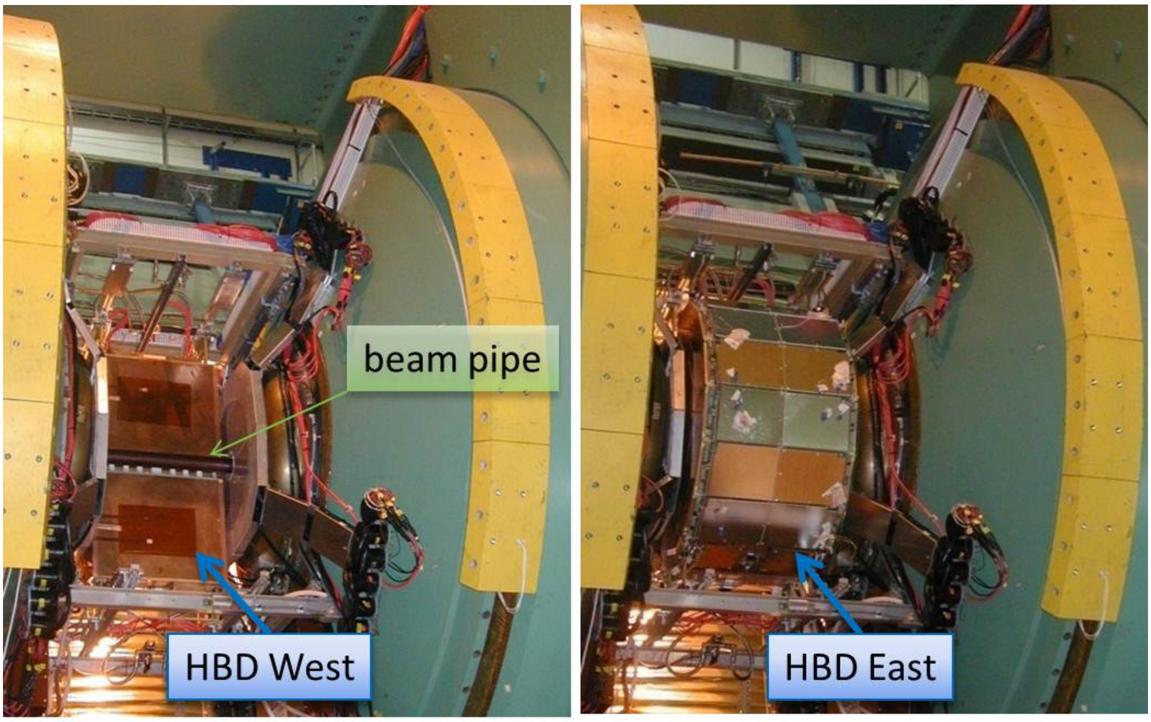

(a) HBD west arm. (East arm is removed.)

(b) HBD east arm.

Figure 2.22: Side views of installed HBD (a) west and (b) east arms.

charge from only a thin layer of ~ 100 µm above the top GEM which is subject to the entire three-stage amplification, and (ii) the collection of ionization charge in the first transfer gap (between the top and the middle GEMs) which is subject to a two-stage amplification only. The ionization electrons produced in the second transfer gap and in the induction gap generate a negligible signal since they experience one and zero stages of amplification, respectively. For a drift region and a transfer gap of 1.5 mm each and a total gas gain of 5×10^3, the mean amplitude of hadron signal drops to $\sim 10\%$ of its value in the FB mode [93].

The readout pad plane consists of hexagonal pads with an area of 6.2 cm^2 (hexagon side length $a = 1.55$ cm) which is comparable to, but smaller than, the blob size which has a maximum area of 9.9 cm^2. Therefore, the probability of a single-pad hit by an electron entering the HBD is very small. On the other hand, a hadron traversing the HBD will produce a signal predominantly localized in a single pad. This provides an additional hadron rejection of the HBD.

The relatively large pad size also results in a low granularity thereby reducing the cost of the detector. In addition, since the signal produced by a heavy flavor electron is distributed between two or three pads, one expects a primary charge of several photo-electrons per pad, allowing the operation of the detector at a relatively moderate gain of a few times 10^3. This is a crucial advantage for stable operation of a UV photon detector.

The HBD is located in a field free region that preserves the original direction of the e^+e^- pair. The two spots images created by the electron pair which has a small opening angle are merged each other. Therefore electron tracks can be identified as originating from electron pairs from π^0 or η Dalitz decays or γ conversion pairs if the corresponding hit in the HBD has an amplitude that is twice to a regular amplitude.

HBD readout electronics

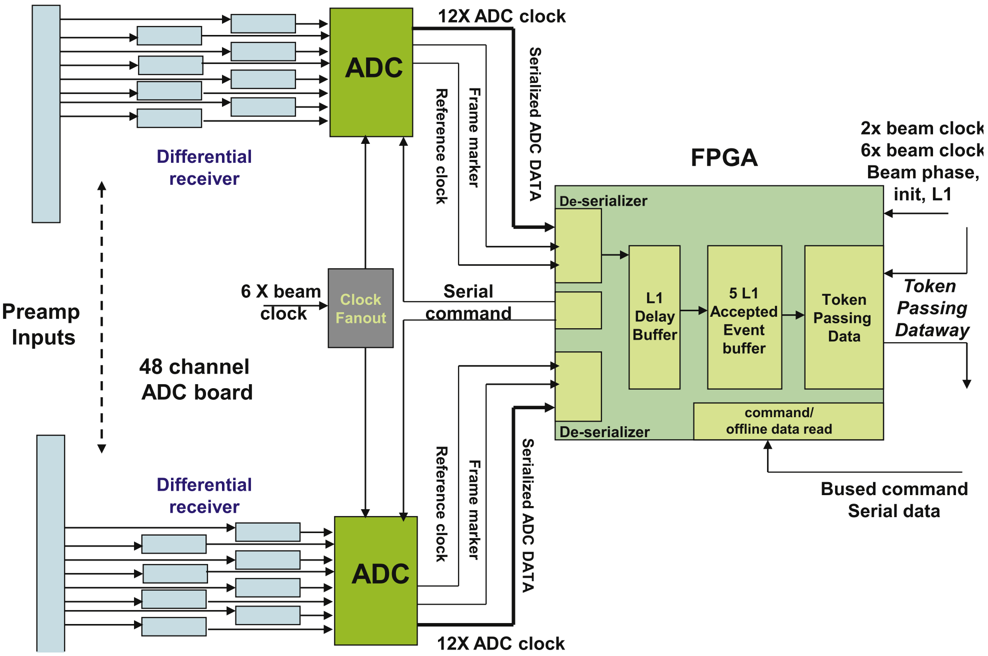

Figure 2.23: Block diagram of HBD front-end module.

The charge signal from each readout pad of the GEMs is amplified by a custom designed hybrid preamplifier (IO1195-1) developed by the Instrumentation Division at

BNL [95]. The gain was set to give an output of ±100 mV for an input signal of 16 fC (10^5 e), which corresponds to an average primary charge of 20 photoelectrons at a gas gain of 5×10^3. It has a peaking time of 70 nsec and a decay time of 1 µsec. When connected to the GEM pad, the noise was measured to be $\sim 10^3$ e, which is equivalent to 0.2 photoelectrons (p.e.) at a gain of 5×10^3. The preamp output is delivered to a shaper located in a HBD front-end electronics.

The overall layout for the HBD front-end electronics is shown in Fig. 2.23, and further details are given elsewhere [96]. The electronics receives the preamp signals using a differential receiver, which provides some additional shaping, and then digitizes them using a 65 MHz 8 channel 12 bit flash ADC. The gain of the shaper was set such that a preamp input charge of 16 fC produces a signal of 160 ADC channels (0.1 fC/ch). The preamp signal was set in the range of ±1.5 V around the ADC common mode voltage, which effectively uses only half of the full dynamic range of the ADC. The output of the ADC is serialized and sent to FPGA (ALTERA Straitx III 60), which encodes the data to accomplish the communication with the PHENIX DAQ system.

HBD gain control during experiment

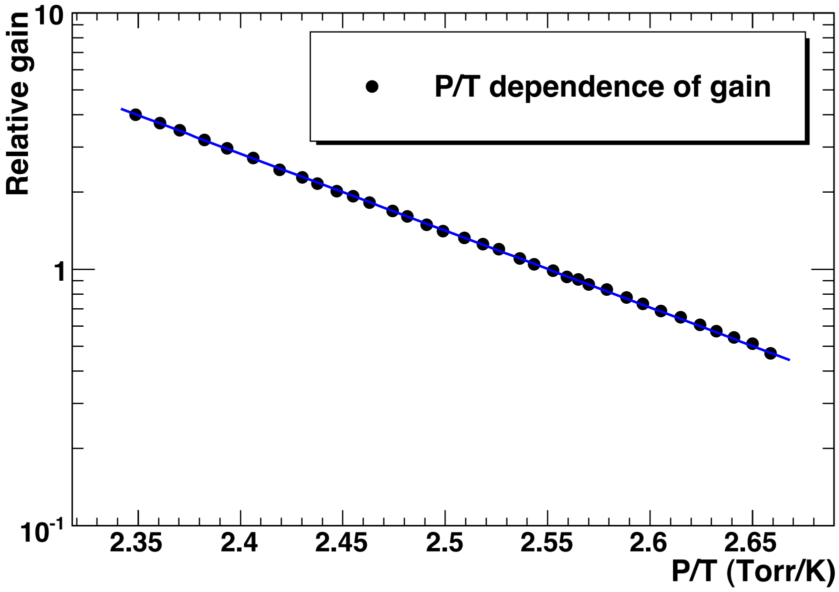

Figure 2.24: P/T dependence of relative gas gain of HBD GEM filled with CF_4. The gain is normalized to 1 at $P/T = 2.55$ Torr/K. The line represents a fit of the data points with an exponential function.

The gas gain of the GEM pads filled with CF_4 is sensitive to gas density. The gas density can be determined by the ratio of the pressure, P, and the temperature, T, of the HBD volume, namely P/T. Figure 2.24 shows the P/T dependence of the gas gain [92]. A P/T change by 1% induces a $\sim$ 20% change in the gas gain.

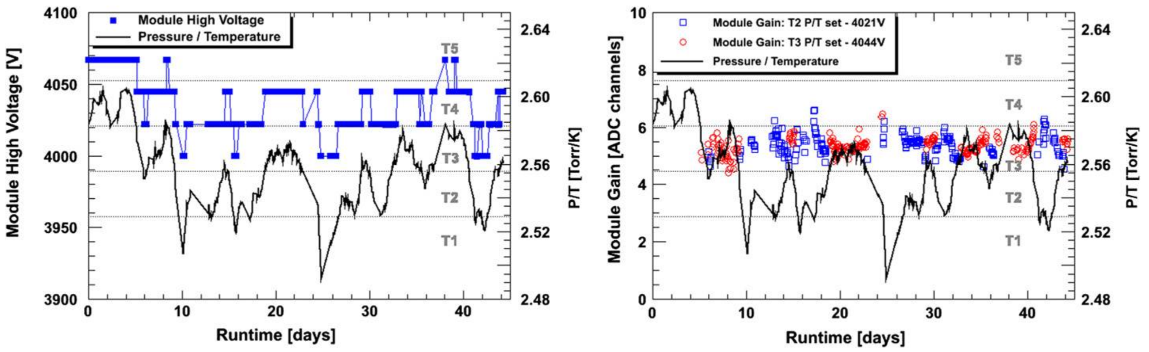

Figure 2.25: (Left) P/T variation during 2010 experiments. This plot also shows the adjustment of HV corresponding to the P/T variation. (Right) Gas gain variation during same period in one HBD sector as a result of the HV adjustment. The vertical axis represents calibration constants for the HBD gain which will be mentioned in Sec. 3.1.5. Blue and red points correspond to 4021 V and 4044 V HV configurations, respectively. Due to the HV control, the variation of the gas gain is inhibited and kept constant within $\sim 10\%$.

To avoid these large excursions of the gain, the operating HV was discretely adjusted during this experiment to compensate the gain variations by monitoring P/T in HBD. The left plot in Fig. 2.25 shows the P/T variation during 2010 experiment. About 2% variation was observed during this experiment. This plot also shows the adjustment of HV corresponding to the P/T variation. The right plot in Fig. 2.25 shows the gas gain variation during same period as a result of the HV adjustment. Blue and red points in the figure correspond to 4021 V and 4044 V HV periods, respectively. The HV adjustment reduced the variation of the gas gain and kept it constant within $\sim 10\%$ deviations.

2.3 PHENIX Data Acquisition

2.3.1 Triggers

The RHIC beam bunches in the blue beam and the yellow beam cross each other in 9.4 MHz frequency (106 nsec period) at the PHENIX interaction region and the total data volume from PHENIX detectors to be recorded for an event in this $p+p$ 200 GeV run was about 40 kB. Due to the high frequency of collisions and the data volume, the acquisition of the event data from the all collisions is not realistic. Therefore, we need a Level-1 trigger for the data selection in online level.

To issue the Level-1 trigger, several trigger signals from PHENIX detectors specified to measure different physics channels are combined. For examples, triggers from BBC are for minimum-bias data sampling, triggers from ZDC are for forward neutron analysis, and triggers from a combination of EMCal and RHIC are for mid-rapidity electron and photon analysis. These triggers are named as local Level-1 (LL1) triggers.

In this section, two main LL1 triggers used in this analysis, a minimum-bias trigger (MB trigger) and a EMCal/RICH trigger for electron (ERT-E trigger), are explained.

MB trigger

The least-biased trigger for detecting inclusive $p + p$ inelastic collisions is the MB trigger which consists of a coincidence between signals from BBC-N and BBC-S. In this $p + p$ $\sqrt{s} = 200$ GeV run, the MB trigger required one or more hit tubes for both of BBC-N and BBC-S (each counter consists of 64 tubes).

The timing information of BBC-N and BBC-S can be utilized to determine the position of the collision vertex in online level with a resolution of ~ 5 cm. However the timing cut was not applied because the rejection power of the MB trigger was enough for the electron analysis.

The MB trigger was utilized in the electron analysis in order to require the signals on BBC-N and BBC-S modules and determine the vertex position (Sec. 3.1.1) and also for the estimation of the trigger efficiency of the ERT-E trigger (Sec. 4.2.3).

ERT-E trigger

ERT-E trigger selects collisions with electron tracks in the mid-rapidity region. This trigger is provided by signals from EMCal and RICH which are sensitive for electron tracks [97]. Basic idea of the trigger is to find a EMCal energy deposit over a threshold and also require a RICH hit signal in an acceptance associated with the position of the EMCal hit.

Each EMCal readout electronics for the ERT-E trigger processes the signals from 144 (12×12) EMCal towers. The readout electronics has 6 daughter cards which hold 6 ASIC chips (36 ASIC chips in total) and each ASIC chip processes the signals from a block of 2×2 EMCal towers. The ASIC sums up the energy deposit in the 2×2 towers. When the total energy is over a threshold, the ASIC issues a trigger bit (ERT-2×2 signal) to a ERT-LL1 electronics. The threshold during this $p + p$ 200 GeV run corresponds to ~ 0.8 GeV. All 2×2 towers in the both arms are numbered serially as Fig. 2.26(a) shows.

RICH has 5120 PMTs (2 (arms) × 2 (north and south) × 80 (ϕ-direction) × 16 (z-direction)). The RICH readout electronics for the ERT-E trigger forms PMT tiles including $5(\phi)\times4(z)$ PMTs. Those tiles are not overlapping, and therefore there are $2 \times 16 \times 4 = 128$ tiles in one arm. Each PMT tile sums up all analog signals from the 5×4 PMTs and digitizes the analog sum. When the electronics find a hit in the digitized signals, a trigger bit (ERT-RICH signal) is issued to the ERT-LL1 electronics. All PMT tiles are also numbered serially as Fig. 2.26(b) shows.

The trigger bits from EMCal and RICH are sent to the ERT-LL1 electronics which decides the LL1 triggers for electron and photon analyses. For the ERT-E trigger decision, the ERT-LL1 electronics requires coincidence of the trigger bits of ERT-2×2 and ERT-RICH. The ERT-LL1 electronics also requires the acceptance matching between the hit positions of ERT-2×2 and ERT-RICH. The matching check is done with a look-up table created by Monte Carlo simulations. The look-up table is shown in Fig. 2.27 where the horizontal axis and the horizontal axis correspond to the number of EMCal

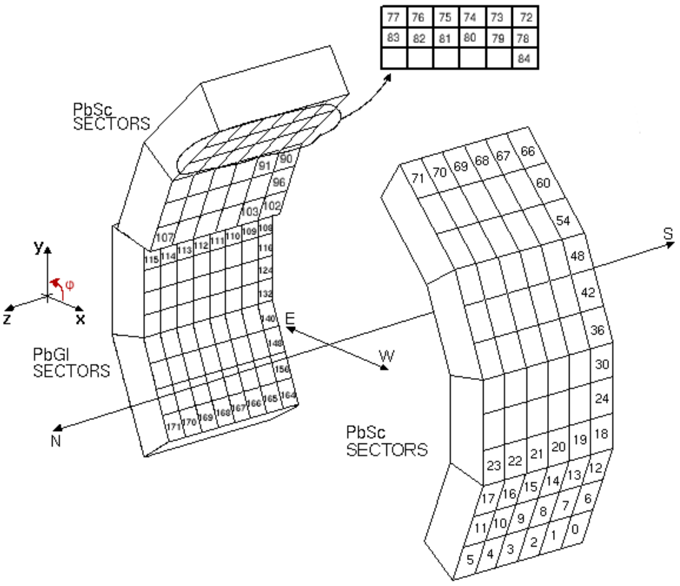

77	76	75	74	73	72
83	82	81	80	79	78
					84

(a) EMCal 2 × 2 towers.

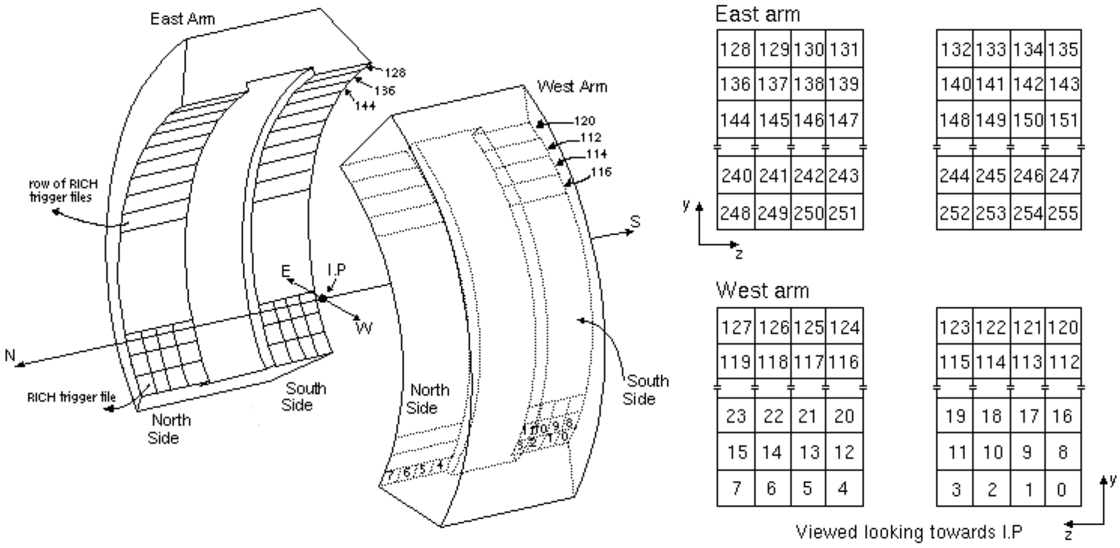

East arm

128	129	130	131
136	137	138	139
144	145	146	147
240	241	242	243
248	249	250	251

132	133	134	135
140	141	142	143
148	149	150	151
244	245	246	247
252	253	254	255

West arm

127	126	125	124
119	118	117	116
23	22	21	20
15	14	13	12
7	6	5	4

123	122	121	120
115	114	113	112
19	18	17	16
11	10	9	8
3	2	1	0

(b) RICH PMT tiles.

Figure 2.26: Numbering definitions of (a)EMCal 2 × 2 towers and (b)RICH PMT tiles.

2 × 2 towers and RICH PMT tiles defined in Fig. 2.26(a) and Fig. 2.26(b) respectively. As an example, the 13th EMCal towers need to be compared with 16th, 17th, 18th, 19th, 20th, 24th, 25th, 26th, 32nd, 33rd and 34th RICH channels. If any one of the EMCal channels has a corresponding RICH hit, the ERT-E trigger is issued.

The ERT-E trigger was utilized for the data selection of the electron analysis.

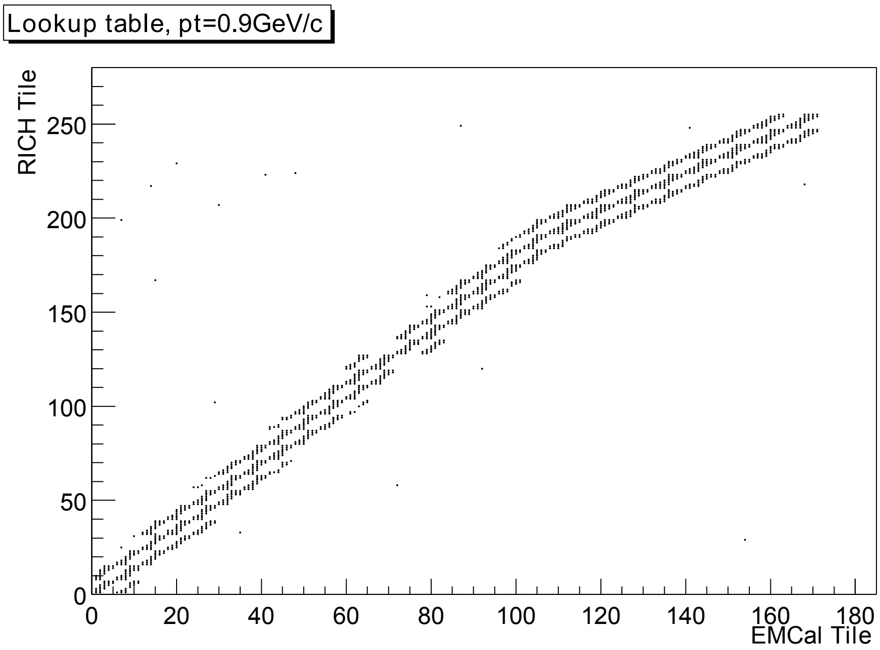

Figure 2.27: Look-up table of EMCal 2 × 2 tower and RICH PMT tiles matching obtained by Monte Carlo simulation. The horizontal axis represents the number of the EMCal 2 × 2 tower and the vertical axis represents the number of the RICH PMT tiles. Because PbSc corresponds to the EMCal tiles from 0th to 107th and PbGl corresponds to the EMCal tiles from 108th to 171st (see Fig. 2.26(a)), slope of the matching table changes between the two regions. This look-up table is utilized for the ERT-E trigger decision.

2.3.2 Data acquisition system

The signals from the PHENIX detectors were taken with the PHENIX data acquisition system (DAQ) [98]. Figure 2.28 shows a block diagram of the PHENIX DAQ.

As mentioned in Sec. 2.3.1, signals from some of PHENIX detectors are utilized for the local Level-1 (LL1) trigger decisions. The LL1 triggers are transmitted to a global Level-1 (GL1) module which scales down the LL1 triggers and decides the Level-1 trigger issuance considering combinations of the scaled down LL1 triggers and also busy signals from DAQ. When the GL1 module accepts the LL1 trigger for an event, a Level-1 trigger signal is issued to granule timing modules (GTM) and then distributed to front-end modules (FEM) on the PHENIX detectors in the PHENIX interaction region.

FEM is a readout electronics implemented for each detector. FEM processes the raw signals from the detector with amplification and shaping and converts them into digital data. Since the RHIC beams have the bunch structures and collide in a 9.4 MHz period, FEM receives a 9.4 MHz RHIC beam-clock (BCLK) synchronized with the collisions for the data processing. BCLK is provided by the accelerator and distributed to FEM by GTM as well as the Level-1 trigger signal. The digitized data are buffered for up to

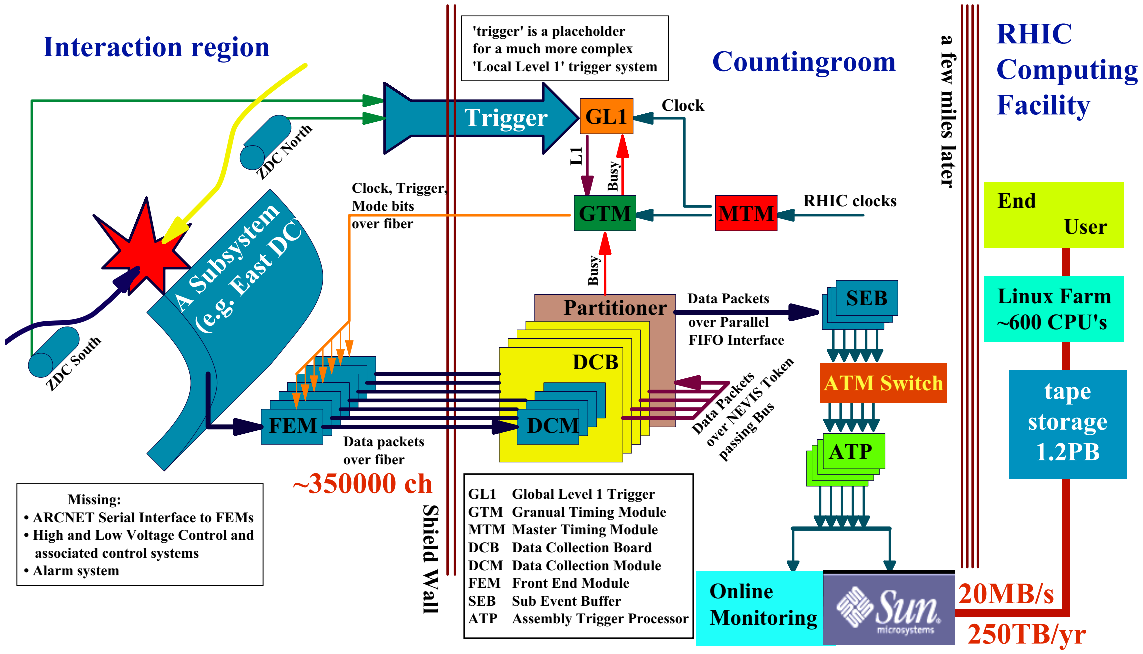

Figure 2.28: Block diagram of the PHENIX DAQ. PHENIX detectors are called as subsystems in this figure. See the text for details.

40 BCLK periods (about 4 μsec) to allow FEM to wait the Level-1 trigger reception. When FEM receives the Level-1 trigger, FEM transmits the data to a data collection module (DCM) with a tag of a event number which is a universal counter for all FEM system.

Each detector system also has its own DCMs as well as FEMs. DCM performs zero suppression for the received data to compress the data volume and also error checking. This procedure produces compressed data packets.

Compressed data packets from all detector system are sent to PHENIX event builders (EvB) in parallel for event assembly. EvB consists of sub-event buffers (SEB), an asynchronous transfer mode (ATM) switch and assembly/trigger processors (ATP). SEB is a buffer to allow for the event assembly on ATP. To assemble data on ATP, data packets from a large number of SEBs must converge on one ATP. This convergence causes excesses of data volumes sent to ATP over an acceptable size. The ATM switch solves the problem with ATM technology based on quality-of-service features. As the result, the detector-by-detector data packets are assembled to the event-by-event data packets on ATM.

The assembled data are transmitted to Linux machines to be recorded on hard drives and tape storages (HPSS). The data are also transmitted to online monitoring system to control data qualities in online level. End users can use the recorded data on the storages for offline analysis.

During this run, the trigger rate of $\sim$ 5 kHz and the DAQ band width of $\sim$ 200 MB/s were achieved with this PHENIX DAQ.

Chapter 3

Electron Analysis

3.1 Conventional Techniques for Electron Analysis

For electron selection in the PHENIX central arms, some conventional techniques using the detector signals from other than the HBD are already established and form the basis for the electron analysis. Also in the electron measurement using the HBD, we utilized these techniques as well as the HBD response information. We explain these conventional methods in the following sections.

In Sec. 3.1.1-3.1.5, we introduce the basic electron selection with the PHENIX detectors. Electrons sampled by these techniques largely include photonic and non-photonic background. In the previous measurement, two methods, "cocktail method" and "converter method", were used to estimate the background fraction [29]. Though our new measurement with the HBD basically does not use these methods other than a part of the "cocktail method" results of dielectron decays of light vector mesons as described in Sec. 3.2.6, we briefly explain these estimation methods in Sec. 3.1.6 to make clear the difference of the analysis techniques between the new and previous measurements. The detailed description about these methods can also be found elsewhere [29].

3.1.1 Vertex position determination

In the PHENIX experiment, the collision vertex position is obtained by using the timing difference between the hits in BBC-N and BBC-S. The vertex position, $z_{\rm vtx}$, and the collision timing, T_0, are represented as

$$z_{\rm vtx} = \frac{c\,(T_S - T_N)}{2} \tag{3.1}$$

$$T_0 = \frac{T_S + T_N}{2} - \frac{L}{c}, \tag{3.2}$$

where T_N and T_S represent the measured hit timing in BBC-N and BBC-S and L represents the half of the distance between the BBC-N and BBC-S and is equal to 1440 mm, and c is the speed of light. The obtained vertex position $z_{\rm vtx}$ is utilized for vertex cut and the track reconstruction with DC and PC information. The collision timing T_0 is also used for the measurement of the drift time in DC.

3.1.2 Track reconstruction by DC and PC

Charged track reconstruction and momentum reconstruction

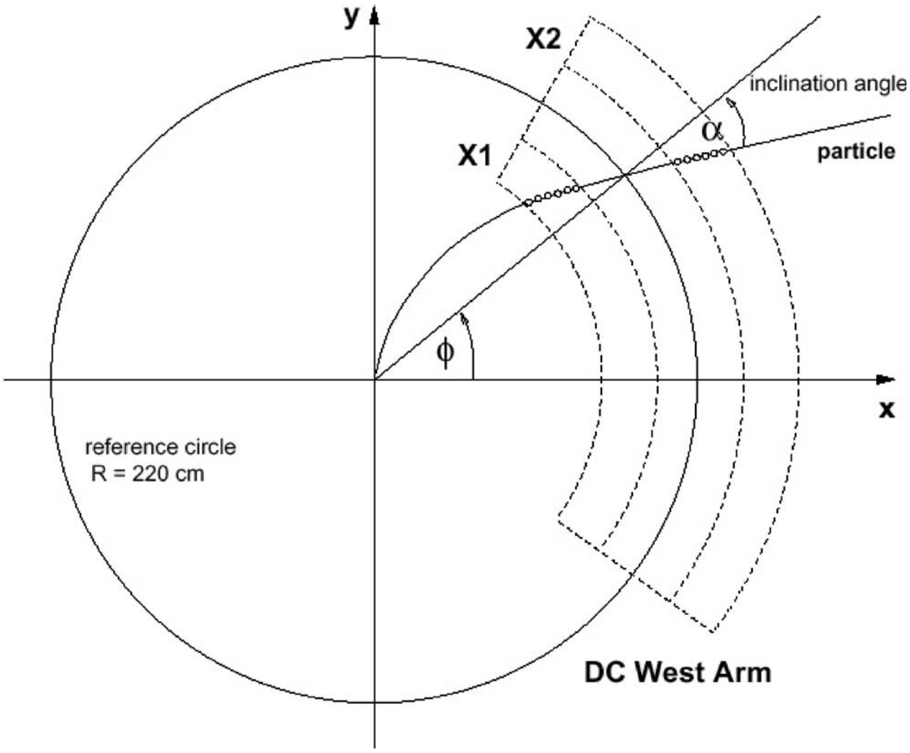

Figure 3.1: A particle trajectory and the parameters used in the DC track reconstruction in the beam view of PHENIX central arm.

Track reconstruction for charged particles is preformed with hit information of the DC and PC, and vertex position z_{vtx} [99, 100]. At the first step, reconstruction of the projected track on the X-Y plane for the DC hits is performed employing a combinatorial Hough transform technique [101, 102]. In this technique, the drift chamber hits in $X1$ and $X2$ planes are mapped pair-wise into ϕ-α space, where ϕ is the polar angle at the intersection of the track with a reference radius near the mid-point of the DC ($R = 220$ cm) and α is the inclination of the track at that point. Figure 3.1 provides a schematic illustration of these variables. Since the orientation of the magnetic field in CM is parallel to the Z axis, the inverse of α is corresponding to the transverse momentum of the particles.

After the reconstruction of the projected track in the X-Y plane, track reconstruction in the Z direction for the DC hits is first attempted by integrating information from reconstructed PC clusters, which contain z information. If there is a unique PC association, the three-dimensional track on the DC and PC is reconstructed by the z-coordinate of the PC cluster and vertex position z_{vtx}. If there is no PC cluster association, or if there are multiple PC association solutions, the reconstruction in the Z direction is performed by the DC stereo wires with a Hough transform again. If the

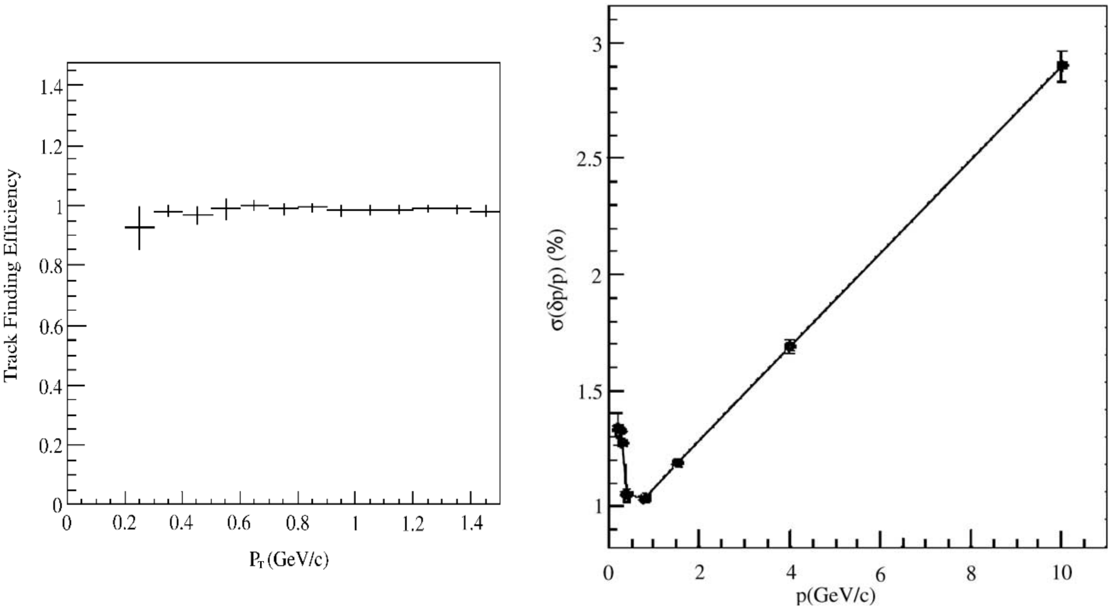

(a) Track reconstruction efficiency.

(b) Momentum reconstruction resolution.

Figure 3.2: (a) The reconstruction efficiency in simulated central Au + Au collisions as a function of the transverse momentum of the track. (b) Momentum resolution in muon events as a function of momentum of the muons. [99, 100]

stereo wires find a unique associated track and determine the z-coordinate at the reference radius in the DC, the three-dimensional track on the DC is reconstructed by the determined z-coordinate on the DC and vertex position z_{vtx}. The track reconstruction also determines the polar angle of the track momentum at the reference radius in the DC, θ.

Due to non-uniformity of the focusing magnetic field along the flight path of the charged particle traversing the CM, a field-integral grid which is a look-up table of the path-integrated field for the particle trajectory from the collision point to a radius position r was employed for track and momentum reconstruction. The grid is defined on discrete inputs of z_{vtx}, the magnitude of the momentum of the track at the collision vertex p, and its polar angle θ_0. To interpolate the integrated field to any input values, a fast Runge-Kutta method [103] is employed.

For each reconstructed track, the interpolated field integral and the trajectory determined by the field integral are calculated iteratively adjusting the input values, p and θ_0, and also the azimuthal angle of the track momentum at the collision vertex, ϕ_0, so that the trajectory represents the all DC and PC hits associated to the reconstructed track. For the first iteration, the initial θ_0 is set to be measured θ and the initial p is set to be an expected value from measured α. Using the iterative procedure, the p, θ_0, and ϕ_0, namely the three-dimensional momentum vector, are reconstructed.

Figure 3.2(a) shows the reconstruction efficiency of above method in simulated central Au + Au collisions as a function of the transverse momentum of the track, and Fig. 3.2(b) shows the momentum resolution in this reconstruction for simulated muon events with event vertices ranging $|z_{\rm vtx}| < 40$ cm, which will not decay as a function of momentum of the muons [99, 100]. Multiple scattering dominates the resolution at low momentum, while detector resolution determines the resolution at higher momentum.

The reconstructed track is extrapolated or interpolated to RICH, EMCal and HBD to obtain the projected positions on the detectors. The projected position is used to search associated hit on the detector around the track.

DC alignment correction

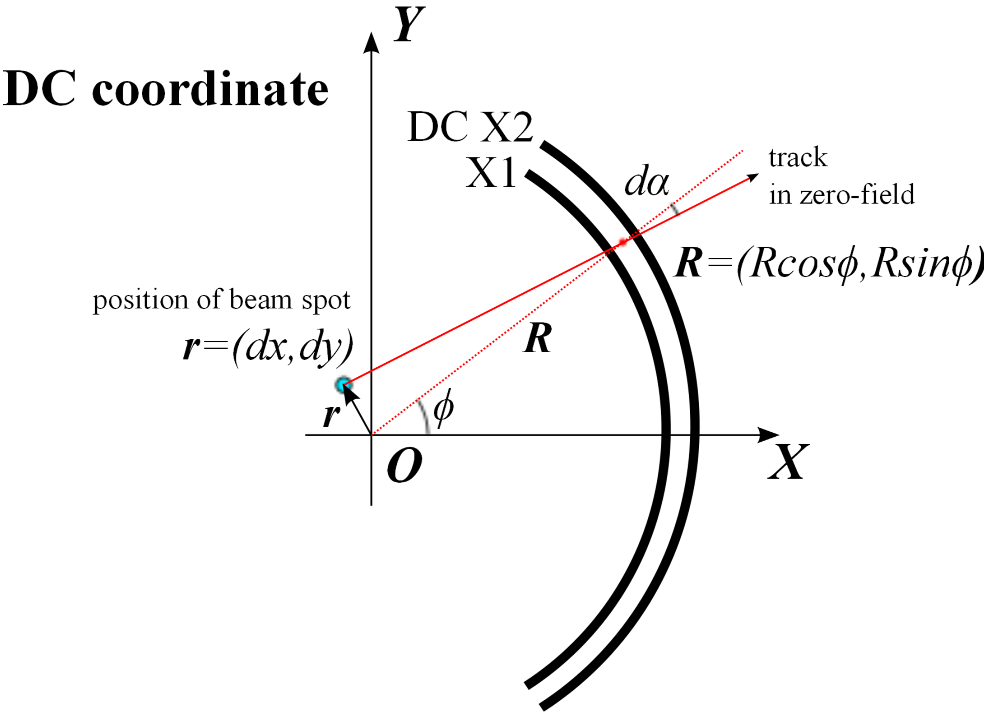

Figure 3.3: Parameters of DC hit information and beam spot position in the DC alignment analysis.

To measure the momentum precisely, alignment of the wires in the DC was corrected by using charged tracks in zero magnetic filed obtained during this run. If there is no magnetic filed, the tracks do not bend and α should be zero. Any deviation from zero indicates that the cards do not set at correct positions which we suppose. The wrong alignment can be corrected by this measured deviation in α.

The first step in the alignment procedure is to find the beam offset which is assumed to be at the original point of the DC coordinate in momentum reconstruction as explained above. The actual position of the beam may be different from the center of the arms. Also, since the carriage gets moved out occasionally, this also relatively adds to a beam offset effect. Figure 3.3 shows a cartoon of the geometry. The beam offset in the x and y directions, dx and dy respectively, are related to $d\alpha$ and ϕ, where

$d\alpha$ represents the measured α in the zero-field events. Thus plotting α vs. ϕ gives us a way to extract dx and dy. The relation between these variables are

$$\tan(\phi + d\alpha) = \frac{R\sin\phi - dy}{R\cos\phi - dx}, \tag{3.3}$$

or

$$\sin d\alpha = \frac{-dy\cos\phi + dx\sin\phi}{R} \tag{3.4}$$

assuming $dx, dy \ll R$, where R is the middle radius of X1 and X2 in DC which is equal to 220 cm. This function is fitted to the plot of α vs. ϕ to extract dx and dy.

The second step of the alignment is a correction for the rotation and tilt of anode cards, which the anode wires of the DC are attached to. Though the anode cards are physically held in place with pins, they can shift slightly. The rotation of the card induces non-zero α in zero-field events. Using the measured α's at the X1 layer and the X2 layer, the rotation of the card can be corrected. The card tilt also causes z dependent deviation of ϕ. This deviation is relatively corrected looking at $\Delta\phi = \phi_2 - \phi_1$ vs. z, where ϕ_1 (ϕ_2) is the ϕ measured at the X1 (X2) layer. In these zero-field events, ϕ_1 and ϕ_2 should be identical in whole z coordinate.

3.1.3 Electron ID by RICH

The number of hit RICH PMTs in an annular region with an inner radius of 3.4 cm and an outer radius of 8.4 cm around the track projection on the RICH is counted and was required to be more than 1 hit PMTs in this measurement. With the requirement, the RICH detector can provide a pion rejection factor better than 10^4 with an electron efficiency close to 100% in 200 GeV $p + p$ collisions.

3.1.4 Electron ID by EMCal

EMCal cluster

The electromagnetic shower of an incident particle at EMCal spreads among several towers. To extract the energy deposit, it is necessary to cluster the group of hit towers which associate to the shower. The detailed description for the clustering method and energy reconstruction of EMCal hits are already described elsewhere [104, 105]. The total energy in the cluster towers is calculated as the energy deposit and corrected for the incident angle dependence which is determined from beam tests [106]. The position of the cluster is determined by the weighted average of tower energies, and also corrected with the incident angle of the particle.

EMCal calibration

The detailed EMCal calibration procedure is also described elsewhere [107, 108, 105]. The time dependence of the tower-by-tower energy gain is corrected using the laser system for both PbSc ad PbGl, which is described in Sec. 2.2.7. The remaining long-term time dependence and gain non-uniformity among the towers is also calibrated using π^0 peak measurement by 2γ pair reconstruction in offline analysis. This calibration procedure is divided into three steps: long-term time dependence correction for the global towers, tower-by-tower dependence correction, and energy non-linearity correction.

The long-term time dependence of the EMCal gain is performed with run-by-run π^0 peak reconstruction. The invariant mass spectra of reconstructed 2γ pairs are fitted to the combination of Gaussian (signal) and polynomial (background). The correct peak position must be larger than the real π^0 mass of 135.0 MeV/c^2 [61], due to finite energy resolution and steep p_T shape of π^0 cross section [108]. Displacement of the peak position from the correct position is calibrated tuning the global EMCal gain.

The tower-by-tower gain correction is also performed with same technique as above. For each tower, 2γ pairs which create a cluster hit on that tower are sampled and invariant mass spectrum for the pairs are created. Using the π^0 peak position, the tower gain is calibrated. Since the peak position is also affected by the other tower gains, this step is iterated several times for the whole towers.

After above calibrations, an energy non-linearity still remains due to the energy threshold for the EMCal towers ($\sim$ 10 MeV). For the energy non-linearity correction, a fast Monte Carlo simulation (FastMC), which is a simple numerical simulator of the detector response, is used to determine the non-linearity as a function of the detected cluster energy. For the simulation, $\pi^0 \rightarrow 2\gamma$ events are generated using the measured π^0 cross section. The FastMC simulates the energy and position fluctuation and the shower profile to reproduce the energy deposit on the EMCal towers and compares it with the real incident energy.

Electron identification by EMCal

For electrons, the energy deposit on EMCal, E, and the magnitude of the reconstructed momentum on DC and PC, p, must be identical due to their small mass. Therefore the ratio, E/p, was required to be close to 1. Practically, the peak position of electron E/p distribution is located at ~ 0.98 for electrons of $p_T > 1.0$ GeV/c. It is because the depth of the shower from an electron is one radiation length ($\sim$ 2 cm) shallower than that from a γ which is used in EMCal energy calibration, and thus the light from the electron is slightly more attenuated in the fibers than the light from the γ [104]. Since the energy resolution of the EMCal depends on the momentum of the electron track, the cut boundaries were changed in different momentum range. The shower profile of the EMCal cluster was also required to be as the electromagnetic shower.

The association with the DC/PC reconstructed track is required for the EMCal cluster. The displacement between the projected position of the track and the EMCal cluster position is decomposed in ϕ and z directions and required within 4.0 σ deviation for the both directions, where σ represents RMS of Gaussian fitted to the displacement distributions for these components.

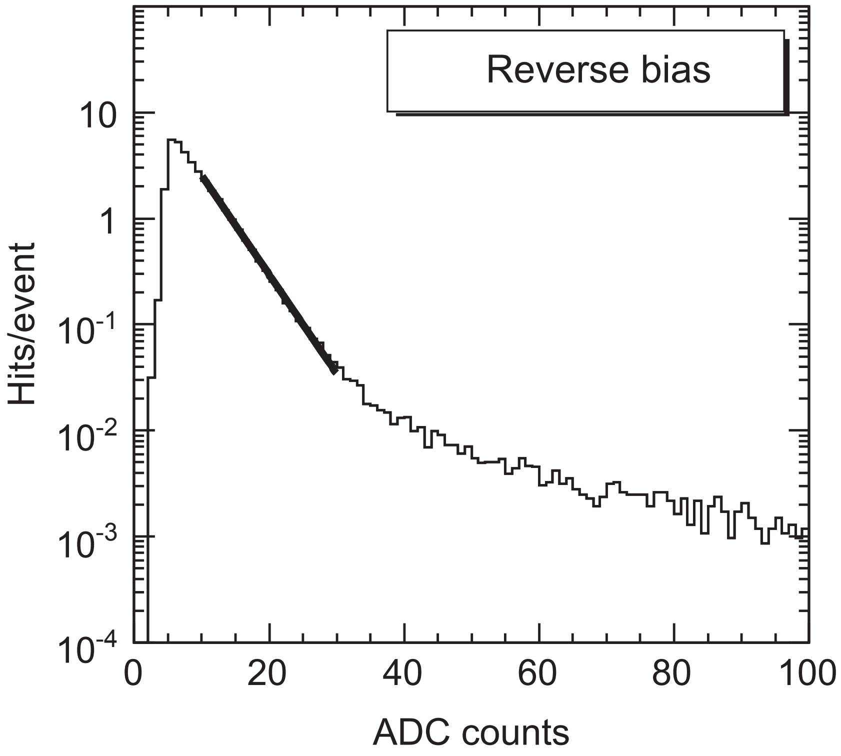

Figure 3.4: Pulse-height distribution in a HBD pad.

3.1.5 Electron ID by HBD

HBD gain calibration

The gain of each detector module is conveniently and precisely determined by exploiting the scintillation light produced by charged particles traversing the CF_4 radiator and translated into the unit of number of detected photoelectrons (p.e.). The scintillation signal is easily identified in the low amplitude part of the pulse-height distribution as illustrated in Fig. 3.4. A steep exponential distribution at very low amplitudes attributed to scintillation photons can be seen in the figure. A longer tail at higher amplitudes corresponds to ionization of the gas in the drift gap.

The mean value of the exponential distribution corresponds to the inverse slope of the distribution. Therefore the gain G of the detector is obtained from

$$G = \frac{S^{-1}}{\langle m \rangle} \tag{3.5}$$

where S is the slope of the scintillation exponential shape at low amplitudes and $\langle m \rangle$ is the average number of scintillation photons in a fired pad. In $p+p$ collisions at $\sqrt{s} = 200$ GeV, $\langle m \rangle$ is enough close to 1 such that the gain is readily given by the inverse slope of the exponential distribution, $G = 1/S$.[1] A line in Fig. 3.4 represents

---

[1] In Au+Au collisions, however, the inverse slope increases with the number of charged particles traversing the detector since $\langle m \rangle$ increases with the number of the scintillation light.

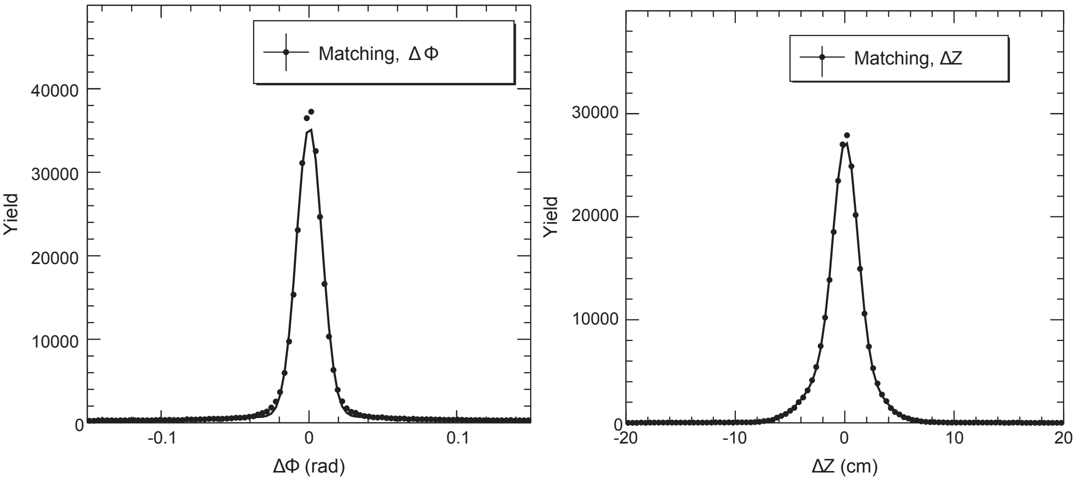

(a) ϕ-direction. (b) z-direction.

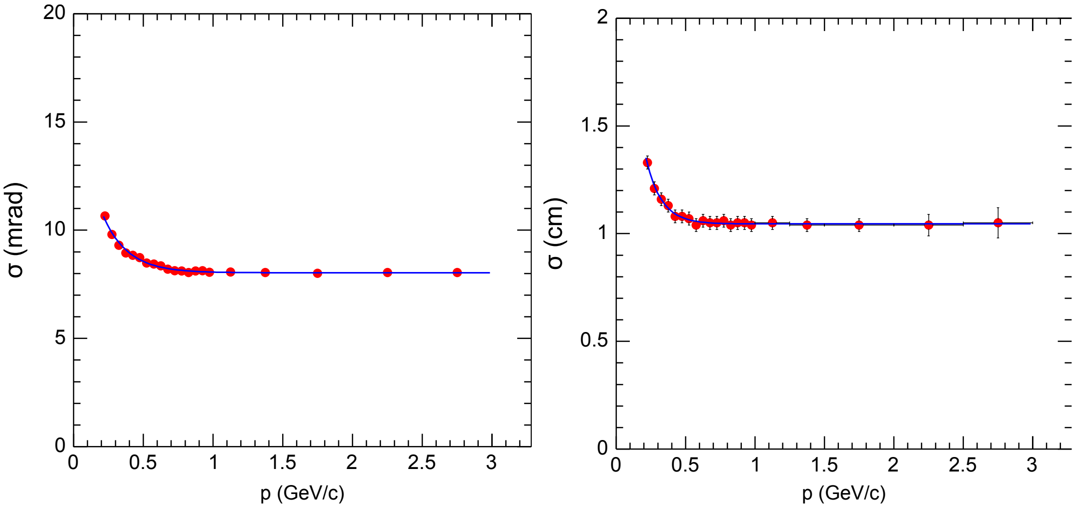

(c) σ in ϕ-direction. (d) σ in z-direction.

Figure 3.5: (a, b) Matching of electron tracks in ϕ (a) and z (b) directions. The solid lines represents the fits to a Gaussian function. (c, d) Matching resolution of electron tracks σ_ϕ (c) and σ_z (d) as a function of momentum.

the determined slope by fitting. The typical calibration constant is $\sim$ 10 ADC/p.e..

HBD cluster

The HBD was not implemented in the previous PHENIX measurements and was first used in this electron measurement. The electron identification using the HBD is discussed in this section.

In the 200 GeV $p+p$ collisions, multiplicity in the HBD is small enough so that clustering method for the HBD signals works for this analysis. Figure 3.6 is an event display showing hit pads at a typical multiplicity. In the figure, a projection position of a reconstructed electron track is also shown with a yellow-filled circle. The associated

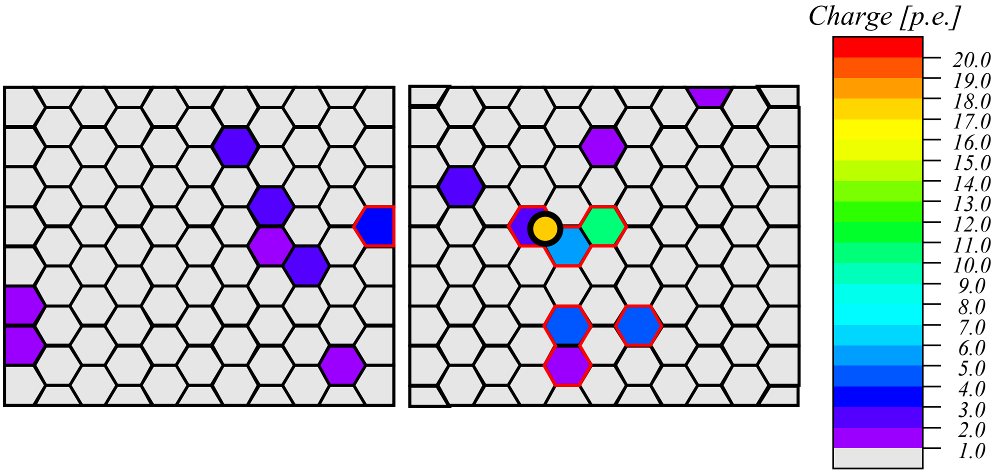

Figure 3.6: Event display of one HBD sector. Yellow filled circle represents the projection position of reconstructed electron track. Groups of pads surrounded with red lines are reconstructed HBD clusters. There is an associated cluster at the projection position of the reconstructed track.

cluster can be found around this track.

The clustering is proceeded by the following procedure. The hit pads are separated into two categories by their charge. One of the two is "seed pad" that has a signal charge more than 3.0 p.e. and the another one is "non-seed pads" that has a signal charge from 1.0 p.e. to 3.0 p.e.. For the first step, seed pads neighboring each other are clusterized and create a "seed cluster". For each seed cluster, all non-seed pads neighboring this seed cluster are searched and added to the seed cluster to obtain the final cluster for the analysis. This clustering is performed across the HBD sectors. The position of the cluster is defined as the center of pad charge and the cluster charge is defined as the sum of the all pad charges. Association of the cluster with the DC/PC reconstructed track is required. The matching between the HBD cluster position and reconstructed track is shown in Fig. 3.5. The position of the cluster is required within 3.5 σ deviation in the both ϕ and z directions as well as the EMCal cluster. The clusters created by this algorithm is also enclosed with red lines in Fig. 3.6.

3.1.6 Heavy flavor electron estimation in previous measurements

Electrons sampled by these techniques consist of heavy flavor electrons, photonic background from Dalitz decays of light neutral mesons and γ conversions, and non-photonic background from K_{e3} decays, dielectron decays of light vector mesons, and Drell-Yan process. The yield of the background is to be known to estimate the yield of the heavy flavor electrons. In the previous measurement, the background yield was estimated with the "cocktail method" and "converter method" as follows (see also detailed descriptions elsewhere [28, 29]).

Cocktail method

A cocktail of electron spectra from background sources is calculated using a Monte Carlo event generator of hadron decays and then subtracted from the inclusive electron spectra. This technique requires the precise cross section spectra of these hadrons.

π^0 cross section spectrum have been well determined from charged and neutral π measurements and π^0 is the largest component in the background. Cross section spectra of light mesons, η, ρ, ω, η', and ϕ mesons, can be reproduced by m_T scaling from the π^0 cross section with an accuracy within $\sim 20\%$ [78]. The normalization of the spectra relative to the π^0 spectrum was obtained by the ratios of the mesons to the pions at high p_T region ($p_T > 5.0$ GeV/c).

Since K meson has large decay lengths, electrons from K_{e3} decays have different acceptance and different detection efficiency from other electrons which come from the collision point. Therefore, the estimation of the contribution from the K_{e3} decays needs a full GEANT simulation taking into account the exact electron selections. The method of the K_{e3} electron estimation is also used in the present analysis as described in Sec. 3.2.6.

Heavy flavor electrons from heavy quarkonia decays (J/ψ and Υ), which are also signal electrons in this analysis, have been also estimated using the cocktail method. J/ψ cross section measured at PHENIX was utilized for the $J/\psi \rightarrow e^+ + e^-$ contribution, and Υ cross section calculated by NLO pQCD was utilized for the $\Upsilon \rightarrow e^+ + e^-$ contribution. As the result, the J/ψ contribution to the total heavy flavor electrons was found to be less than 2% in $p_T < 1.25$ GeV/c and increased to $\sim 20\%$ up to $p_T = 5.0$ GeV/c, whereas the Υ contribution was less than 1% in $p_T < 4.0$ GeV/c and increased to $\sim 3\%$ up to $p_T = 5.0$ GeV/c.

The Drell-Yan background have also been estimated by using LO pQCD calculated cross section. This contribution was less than 0.5% in $p_T < 5.0$ GeV/c and negligibly small in this analysis.

Converter method

With the converter method, the yields of photonic and non-photonic electrons are obtained by measuring the difference between inclusive electron yields with and without a photon converter of precisely known thickness: a brass sheet of 1.680% radiation length. These yields can be expressed as the following relations:

$$N_e^{\text{Conv-out}} = N_e^{\text{ph}} + N_e^{\text{non-ph}}, \tag{3.6}$$

$$N_e^{\text{Conv-in}} = R_{\text{ph}} N_e^{\text{ph}} + (1-k) N_e^{\text{non-ph}}. \tag{3.7}$$

Here $N_e^{\text{Conv-out}}$ ($N_e^{\text{Conv-in}}$) is the measured electron yield without (with) the converter. N_e^{ph} ($N_e^{\text{non-ph}}$) is the photonic (non-photonic) electron yield. k represents a small loss of $N_e^{\text{non-ph}}$ owing to the converter, which was evaluated to be $\sim 2.1\%$. R_{ph} represents how much the photonic electron yield is increased by the converter, which is calculated to be ~ 2.41 using material information around the collision point within accuracy of

±2.0%. This value was also confirmed with a GEANT simulation including geometrical effects.

The yields from non-photonic background can not be estimated only with the converter method. Though these contributions are smaller than the photonic electrons, they can not be negligible especially in the low p_T region. The results of the cocktail method for K_{e3} decays and light vector mesons were used for the estimation.

3.2 Heavy Flavor Electron Analysis with HBD

3.2.1 Overview

With the improved purity from the HBD, the double helicity asymmetry of the heavy flavor electrons was obtained. In this section, we discuss how the heavy flavor electron analysis and the purification of the heavy flavor electron sample using the HBD were performed.

3.2.2 Data selection

Data used in this analysis were recorded by PHENIX from the end of April to the beginning of July 2009. The data set was selected by the ERT-E trigger in a coincidence with the MB trigger for the single electron analysis and by the MB trigger for the detector calibration, where the ERT-E and MB triggers are described in Sec. 2.3.1.

The tracking efficiency of the PHENIX central detectors, especially due to HBD, is sensitive to the track vertex position. Hence a collision vertex cut of $|z_{\mathrm{vtx}}| < 20$ cm was applied for the data selection.

After a vertex cut of $|z_{\mathrm{vtx}}| < 20$ cm and data quality cuts, an equivalent of 1.4×10^{11} MB events, corresponding to 6.1 pb^{-1}, sampled by the ERT-E trigger were analyzed.

3.2.3 Electron selection

The electron selection cuts for this analysis are named eID-Cut and listed in Table 3.1. As described in Sec. 3.1.1, hit signals of RICH, EMCal, and HBD around the projected positions of the reconstructed charged track and E/p ratio selection were required in the eID-Cut.

In addition to these conventional electron selection, we also applied another selection for HBD cluster signal for further background rejection as follows. For the new selection based on HBD, we introduced a new variable, q_{clus}, as

hbdcharge: q_{clus}

Total charge of the associated HBD cluster calibrated in units of the number of photoelectrons (p.e.). The applied thresholds are different for one sector due to its lower efficiency compared with other sectors in this measurement.

Charged particles traversing the CF_4 volume in the HBD produce also scintillation light, which has no directivity and creates hits with only small charge on random locations in

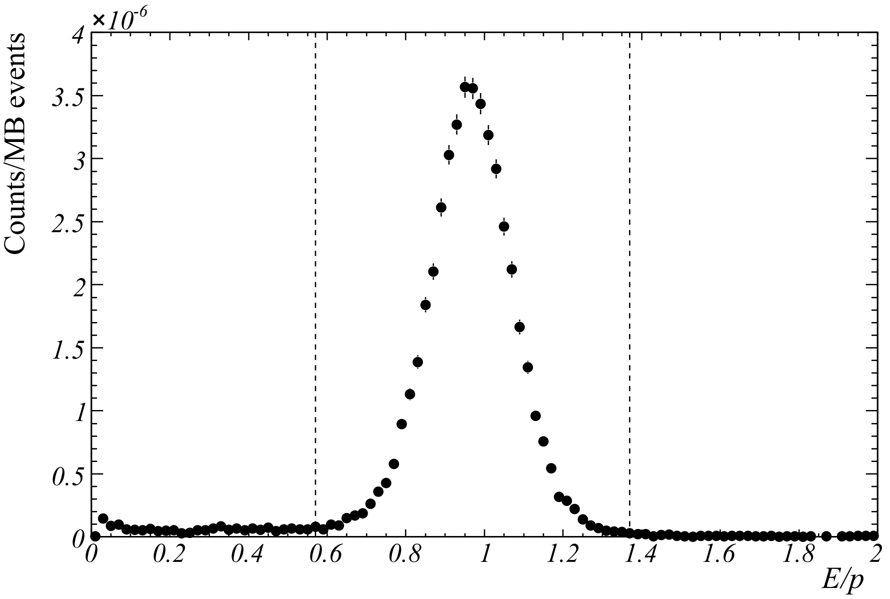

Figure 3.7: E/p distributions for 0.5 GeV/c $< p_T <$ 1.0 GeV/c reconstructed charged tracks with the eID-Cut except the E/p cut. The boundaries of the E/p cut for the momentum region are shown by dashed lines in the plot.

the GEM pads. To remove the background hits from the scintillation light, a minimum charge and a minimum cluster size were required for the HBD hit clusters. During this measurement, the efficiency for the Čerenkov light in one HBD sector was low compared with other sectors. Hence we applied a different charge cut to that HBD sector for the electron selection.

The E/p distribution for the selected tracks with these eID-Cut without the E/p cut is shown in Fig. 3.7. The clear peak around $E/p = 1$ corresponds to electrons and the continuous distribution around the peak consists of mainly electrons from K_{e3} decays and mis-identified hadrons. The reason that the peak position is slightly smaller than 1.0 is due to the difference of EMCal shower depth between electron and photon as explained in Sec. 3.1.4. As the figure shows, the fraction of these background tracks in the reconstructed electrons after applying eID-Cut was small. The fractions of the K_{e3} decays and the mis-identified hadrons are described in Sec. 4.1.1 and Sec. 4.1.2.

As mentioned in Sec. 2.2.8, we can remove the photonic electrons and purify the heavy flavor electrons on the basis of the associated HBD cluster charge. The selection cut is represented as npe-Cut (non-photonic electron cut) and also shown in Table 3.1.

3.2.4 Detector stability

The stability of the DC, EMCal and HBD were checked with run dependence of multiplicities in the detectors. For the stability check, we used multiplicity calculated from MB trigger dataset, which has no trigger bias.

Table 3.1: Electron ID cuts and non-photonic electron cuts used in the electron analysis.

eID-Cut (electron ID cut)
4.0σ matching between track and EMCal cluster
# of hit tubes in RICH around track ≥ 2
3.5σ matching between track and HBD cluster
shower profile cut on EMCal
$0.57 < E/p < 1.37$ (0.5 GeV/c $< p_T <$ 1.0 GeV/c)
$0.60 < E/p < 1.32$ (1.0 GeV/c $< p_T <$ 1.5 GeV/c)
$0.64 < E/p < 1.28$ (1.5 GeV/c $< p_T <$ 5.0 GeV/c)
# of hit pads in HBD cluster ≥ 2
$q_{\mathrm{clus}} > 8.0$ p.e.
($q_{\mathrm{clus}} > 4.0$ p.e. for one low-gain HBD sector)

npe-Cut (non-photonic electron cut)
$8.0 < q_{\mathrm{clus}} < 28.0$ p.e.
($4.0 < q_{\mathrm{clus}} < 17.0$ p.e. for one low-gain HBD sector)

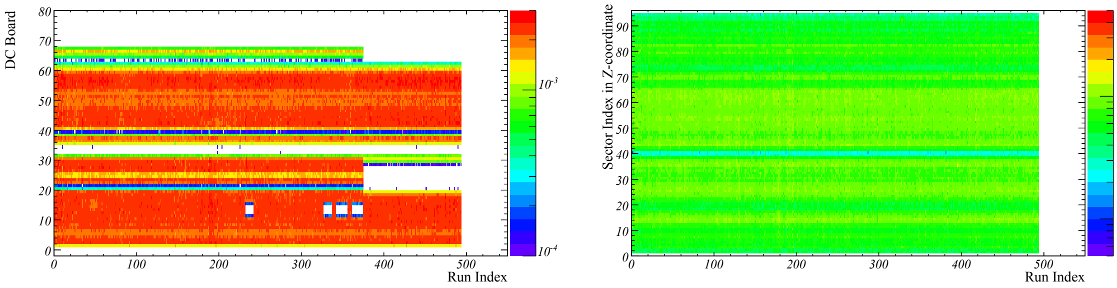

(a) DC (East-South) (b) EMCal (Sect0)

Figure 3.8: (a) Run number dependence of DC track multiplicity as function of a variable corresponding to ϕ_0 in half of one DC arm. (b) Run number dependence of EMCal hit multiplicity as function of tower number projected in z-direction in a EMCal sector.

Figures 3.8(a) and (b) display run dependence of multiplicity of reconstructed tracks in a typical DC region and multiplicity of EMCal clusters in a typical EMCal region, respectively. The horizontal axis in Fig. 3.8(a) is run number and the vertical axis corresponds to track azimuth at vertex position ϕ_0, which is described in Sec. 3.1.2. The color gradation represents the multiplicity of the reconstructed tracks in a MB trigger event. Because we separated the all runs into four different groups and required different fiducial-acceptance for these groups, ϕ_0 distribution is changing during the experiment and ϕ_0 distribution in same fiducial-acceptance cut is stable. Each group

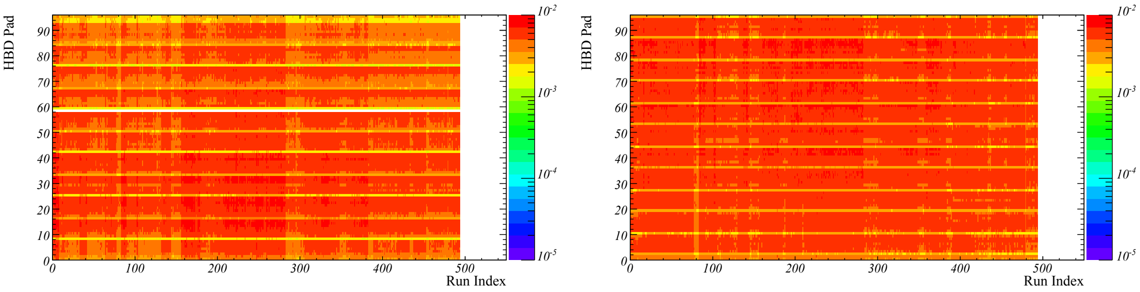

(a) Sect9 South

(b) Sect9 North

Figure 3.9: HBD pad-by-pad multiplicity as a function of run number in a typical HBD sector.

with same fiducial-acceptance is called "run group". For the calculation of the heavy-flavor-electron cross section, the yields of heavy flavor electrons in the four run groups are separately estimated, because each run group has a different acceptance coverage. The horizontal axis in Fig. 3.8(b) is run number and the vertical axis is EMCal sector number projected in z-direction. The color gradation represents the multiplicity of the reconstructed clusters in a MB trigger event. We confirmed the fluctuations of these multiplicities are consistent within statistical fluctuations.

Figure 3.9 shows the hit multiplicity in a typical HBD sector. Hit pads with HBD cluster charge of $q > 1.0$ p.e. were selected for this study. The fluctuation of the HBD multiplicity is large compared with the DC and EMCal due to the difficulty of the HBD operation with a stable gain control.

Run dependence of the resulting electron yield after eID-Cut and npe-Cut per an MB trigger event is shown in Fig. 3.10. Figure 3.10(a) is the result after applying the cuts related with HBD (HBD signal association, q_{clus} selection, and HBD cluster size cut) and figure 3.10(b) is the one before applying them. The different run groups are distinguished by four colors, red, blue, green, and yellow. We confirmed that the yields per a MB trigger in each run group are consistent with each other during this experiment.

3.2.5 Non-photonic electron analysis with HBD

We categorize the HBD clusters into three types according to the sources of the clusters. A cluster created by a single spot of Čerenkov light from a non-photonic electron as shown in Fig. 3.11(a) is defined as a *single cluster*. On the other hand, a cluster created by merging spots of Čerenkov light from a track pair of photonic electrons as shown in Fig. 3.11(b) is defined as a *merging cluster*. However a portion of the photonic electrons which has a large enough opening angle such that the two cluster are not merging (typically $\gtrsim 0.1$ rad) creates two separated single clusters as shown in Fig. 3.11(c). Therefore the single cluster is created by both of the non-photonic electron and the photonic electron with a large opening angle.

We also define a third type of HBD cluster created by scintillation light, which we call a *scintillation cluster*. Scintillation hits which accidentally have large hit charges

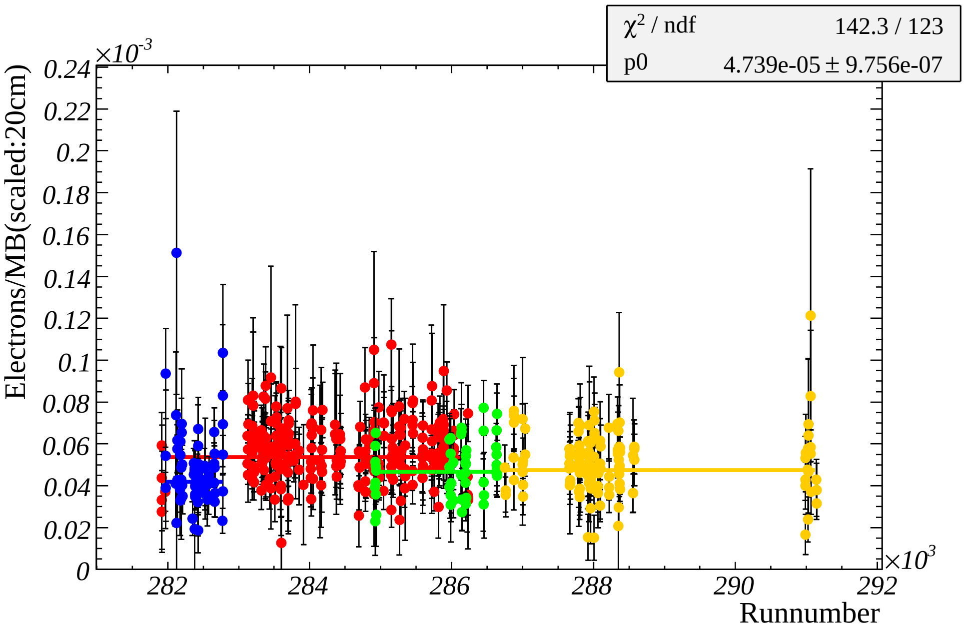

(a) with HBD cut

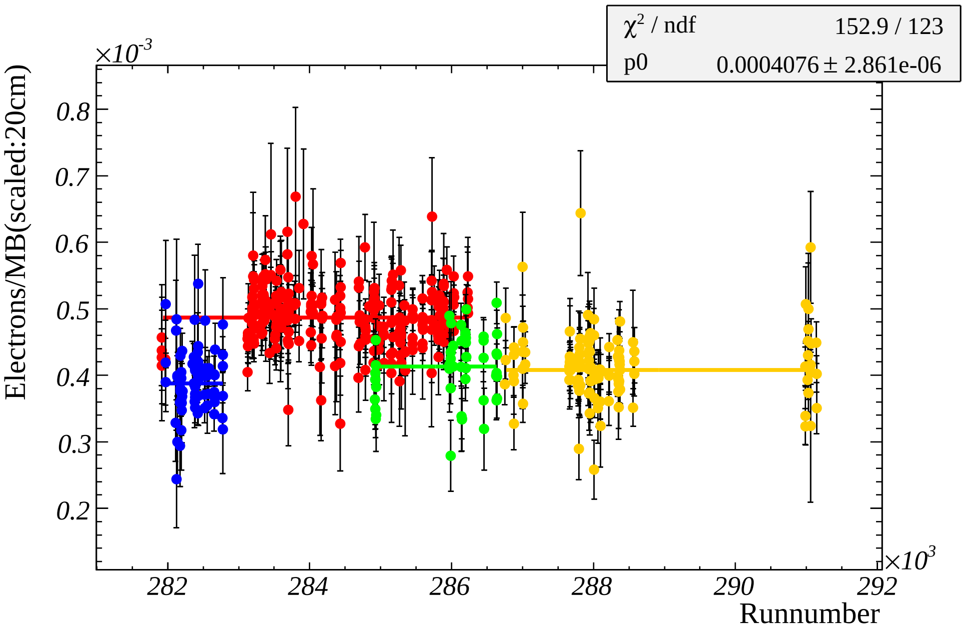

(b) without HBD cut

Figure 3.10: (a) Reconstructed electron yield per an MB trigger event after applying eID-Cut and npe-Cut, and $p_T > 0.5$ GeV/c per an MB trigger event. (b) Reconstructed electron yield per an MB trigger event without HBD related cuts. Red, blue, green and yellow points represent to different run groups.

and have neighboring hit pads can comprise clusters. Photonic electrons from γ conversions after the HBD GEM pads do not create Čerenkov light in the HBD gas volume. Hence they basically do not have associated clusters in the HBD and they are rejected

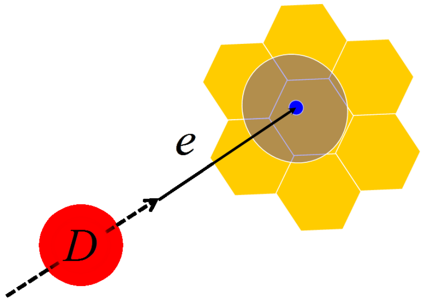

(a) Non-photonic electrons.

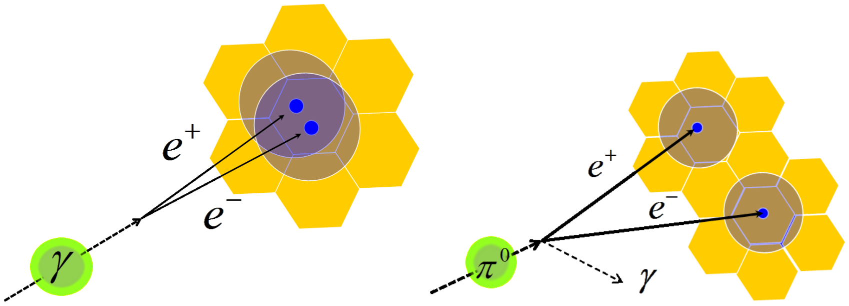

(b) Photonic electrons (merging cluster).

(c) Photonic electrons (separated clusters).

Figure 3.11: Responses of the HBD for (a) non-photonic electrons and (b, c) photonic electrons. (b) Most of the photonic electron pair create merging clusters. (c) However a portion of photonic electrons, which have a large opening angle, creates separated clusters.

by the HBD hit requirement in the eID-Cut. However, a portion of these are accidentally associated with scintillation clusters, satisfy the eID-Cut, and survive in the reconstructed electron samples.

We estimated yields of these clusters from the distribution shape of the HBD cluster charge. We also estimated the fraction of the small component of *single clusters* generated by photonic electrons which have the large opening angles as described. Then we determined the non-photonic electron yield. Subtracting additional background electrons from K_{e3} decays and e^+e^- decays of light vector mesons, we obtained the yield of the heavy flavor electron yield. In the following section, details of the above procedures are described.

HBD cluster charge distributions

All clusters associated with the reconstructed electrons can be classified into the above three types. The yield of the electrons associated with the single clusters must be evaluated in order to estimate the yield of the heavy flavor electrons. The shapes of the $q_{\rm clus}$ distributions for the three cluster types are quite different since merging clusters have basically double the charge of single clusters and the charge of scintillation clusters is considerably smaller than the charge of the single cluster. Using the difference in the

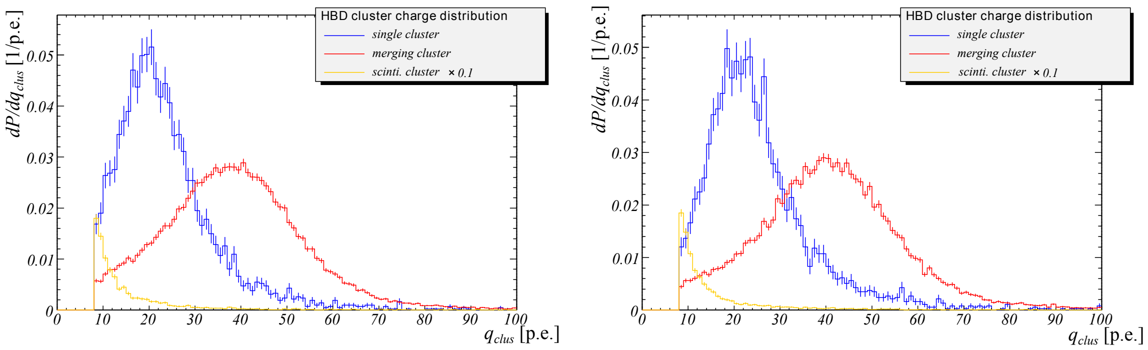

(a) Sect9 South

(b) Sect9 North

Figure 3.12: HBD cluster charge (q_{clus}) probability distribution. The distributions are normalized as integral = 1 for single cluster (blue) and merging cluster (red) and integral = 0.1 for scintillation cluster (yellow).

shapes, we estimate yields of these clusters as follows.

The q_{clus} distributions of single and merging clusters were estimated by using low-mass unlike-sign electron pairs reconstructed with only the eID-Cut, which consist of almost photonic electron pairs. We defined the unlike-sign electron pairs whose two electrons were associated with two different HBD clusters as separated electron pairs and the pairs whose two electrons were associated to the same HBD cluster as merging electron pairs. The q_{clus} distribution of the single clusters were estimated by the q_{clus} distribution of the separated electron pairs and the q_{clus} distribution of the merging clusters were estimated by the q_{clus} distribution of the merging electron pairs. These distributions were normalized to each other with respect to their integrals.

The above estimations of q_{clus} distributions for the single and merging clusters are not identical to ideal definitions of these clusters. The ideal definition of the single cluster is a cluster which consists of Čerenkov light only from one electron or positron track, and one of the merging cluster is a cluster which consists of Čerenkov light from both of electron and positron tracks. Therefore, the q_{clus} distributions of the above estimation and the ideal definition are slightly different. The difference is attributed to a bias from the reconstruction of the electron pairs, which requires a minimum momentum for the tracks. This effect was estimated by using a GEANT3 simulation and found to modify the q_{clus} distributions $\sim\pm 5\%$. The modification was applied to the distributions.

The normalized distributions are denoted as $f_{\mathrm{c}}^{\mathrm{s}}(q_{\mathrm{clus}})$ for the single clusters and $f_{\mathrm{c}}^{\mathrm{m}}(q_{\mathrm{clus}})$ for the merging clusters. The q_{clus} distribution for the scintillation clusters was also estimated by the distribution of the hadron tracks reconstructed by the DC/PC tracking and the RICH veto. The distribution was also normalized and is denoted as $f_{\mathrm{c}}^{\mathrm{sci}}(q_{\mathrm{clus}})$. These estimated distributions in a typical sector are plotted in Fig. 3.12. The peak q_{clus} of the merged clusters (red) is about twice as large as one of the single clusters (blue). The distribution of the scintillation clusters (yellow) has small q_{clus} values compared with the distribution of the single clusters. The distribution functions introduced above are summarized in Table 3.2 for the reference.

Yield estimation of single clusters

The $q_{\rm clus}$ distribution for the reconstructed electrons by applying eID-Cut is fitted with a superposition of the three normalized distribution

$$\begin{array}{rl} n_{\rm s} \times f_{\rm c}^{\rm s}(q_{\rm clus}) & + \\ n_{\rm m} \times f_{\rm c}^{\rm m}(q_{\rm clus}) & + \\ n_{\rm sci} \times f_{\rm c}^{\rm sci}(q_{\rm clus}), & \end{array} \tag{3.8}$$

where $n_{\rm s}$, $n_{\rm m}$ and $n_{\rm sci}$ are the fitting parameters and represent the numbers of the reconstructed electrons associating to single clusters, merging clusters and scintillation clusters after applying eID-Cut respectively. The variables are also summarized in Table 3.2. The fraction of non-photonic electrons and photonic electrons are different in different p_T region of the reconstructed electron sample. Therefore the fitting was performed for each p_T region and $n_{\rm s}(p_T)$, $n_{\rm m}(p_T)$ and $n_{\rm sci}(p_T)$ for each p_T region were determined. In fitting the different p_T regions, p_T independent normalized distributions, $f_{\rm c}^{\rm s}(q_{\rm clus})$, $f_{\rm c}^{\rm m}(q_{\rm clus})$ and $f_{\rm c}^{\rm sci}(q_{\rm clus})$, were employed because the velocity of electrons in p_T region of interest is close enough to the speed of light in vacuum such that the yield of Čerenkov light from the electron is nearly p_T independent. We also compared the shapes of the distributions in different p_T regions to confirm that the effect from the track curvature is small enough to be ignored even if at $p_T \sim 0.5$ GeV/c. On the other hand, $f_{\rm c}^{\rm s}(q_{\rm clus})$, $f_{\rm c}^{\rm m}(q_{\rm clus})$ and $f_{\rm c}^{\rm sci}(q_{\rm clus})$ for different HBD sectors vary about 10% between HBD sectors with nominal gain, and fitting is performed for each sector individually to account for this variation. The single low-gain sector exhibits a larger variation and is fitted separately.

The $q_{\rm clus}$ distribution for the reconstructed electrons with transverse momentum p_T ranging from 0.75 GeV/c to 1.00 GeV/c and the fitting result are shown in Fig. 3.13 for one HBD sector. The charge distribution of the reconstructed electrons can be reproduced by the superposition of the 3 components excellently.

The total numbers of the reconstructed electrons after applying both of eID-Cut and npe-Cut for the three cluster types, which are represented as $\tilde{n}_{\rm s}$, $\tilde{n}_{\rm m}$ and $\tilde{n}_{\rm sci}$, are calculated by applying the npe-Cut efficiencies of $\int_{q_{\rm min}}^{q_{\rm max}} dq f_{\rm c}^{\rm s}(q)$, $\int_{q_{\rm min}}^{q_{\rm max}} dq f_{\rm c}^{\rm m}(q)$ and $\int_{q_{\rm min}}^{q_{\rm max}} dq f_{\rm c}^{\rm sci}(q)$ to the fitting results, $n_{\rm s}$, $n_{\rm m}$ and $n_{\rm sci}$, respectively. In the integrals, $q_{\rm min}$ and $q_{\rm max}$ represent the HBD charge boundaries in the npe-Cut of 8 p.e. and 28 p.e. (4 p.e. and 17 p.e. for the low-gain sector). The variables, $\tilde{n}$, are also summarized in Table 3.2 for the reference. Figure 3.14 shows the yield spectra from the calculation as functions of p_T.

Yield estimation of separated photonic electrons

The estimated $\tilde{n}_{\rm s}$ is the sum of the numbers of non-photonic electrons and photonic electrons which create the separated clusters on HBD. In the following description, we denote the photonic electrons which create merging clusters as *merging photonic electrons* (MPE) and those which create separated single clusters as *separated photonic electrons* (SPE). In this section, the number of SPE is estimated to obtain the yield of the non-photonic electrons.

Table 3.2: Summary of variables used in **hbdcharge** analysis.

variable	description
$f_{\mathrm{c}}^{\mathrm{s}}$	Distribution for the single clusters normalized with respect to the integral.
$f_{\mathrm{c}}^{\mathrm{m}}$	Distribution for the merging clusters normalized with respect to the integral.
$f_{\mathrm{c}}^{\mathrm{sci}}$	Distribution for the scintillation clusters normalized with respect to the integral.
n_{s}	Number of single clusters after applying eID-Cut.
n_{m}	Number of merging clusters after applying eID-Cut.
n_{sci}	Number of scintillation clusters after applying eID-Cut.
$\tilde{n}_{\mathrm{s}}$	Number of single clusters after applying eID-Cut and npe-Cut.
$\tilde{n}_{\mathrm{m}}$	Number of merging clusters after applying eID-Cut and npe-Cut.
$\tilde{n}_{\mathrm{sci}}$	Number of scintillation clusters after applying eID-Cut and npe-Cut.

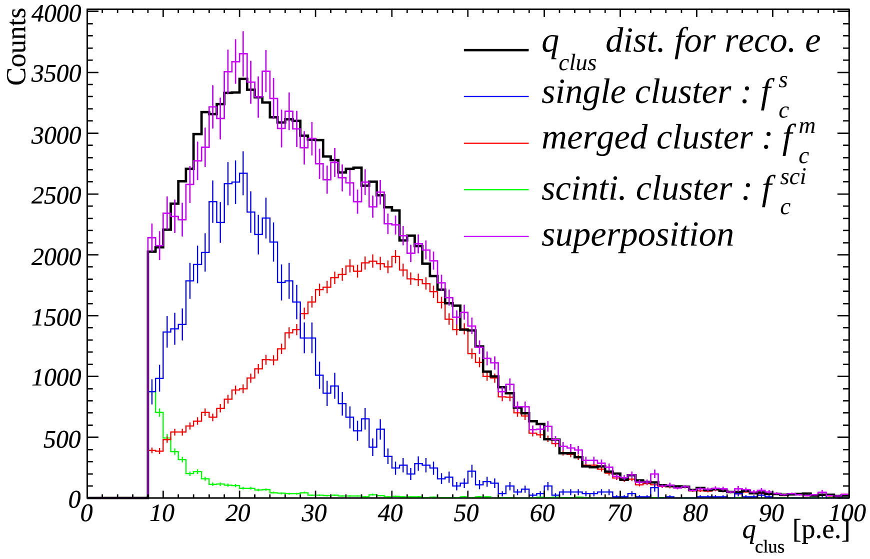

Figure 3.13: Charge distribution of HBD clusters associated with reconstructed electrons with a transverse momentum ranging from 0.75 GeV/c to 1.00 GeV/c (black), and the charge distribution for each component, i.e., single clusters ($n_{\mathrm{s}} f_{\mathrm{c}}^{\mathrm{s}}$, blue), merging clusters ($n_{\mathrm{m}} f_{\mathrm{c}}^{\mathrm{m}}$, red), and scintillation clusters ($n_{\mathrm{sci}} f_{\mathrm{c}}^{\mathrm{sci}}$, green). The superposition of these components is also shown (purple).

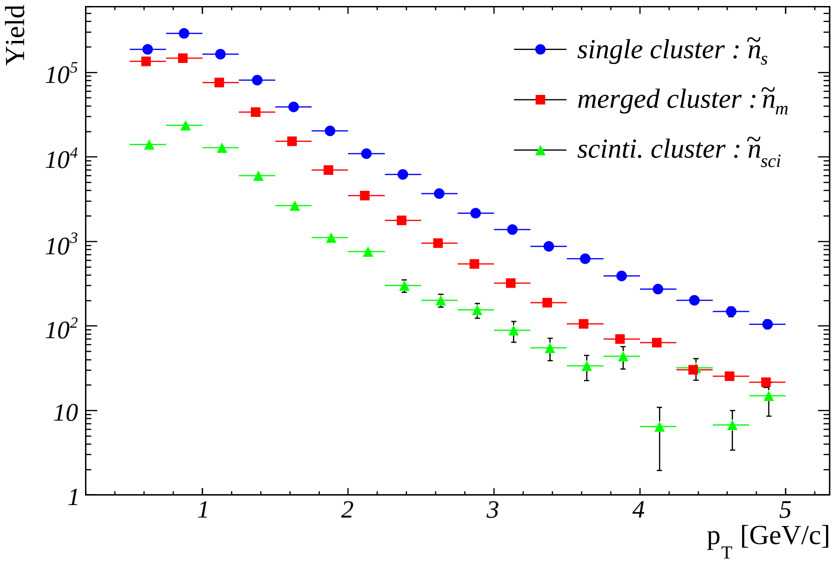

Figure 3.14: Yield spectra of HBD clusters after applying eID-Cut and npe-Cut estimated from the HBD cluster charge fitting. The plot shows the spectrum for the single clusters ($\tilde{n}_{\mathrm{s}}$, blue), the spectrum for the merging clusters ($\tilde{n}_{\mathrm{m}}$, red) and the spectrum for the scintillation clusters ($\tilde{n}_{\mathrm{sci}}$, green). The error bars represent fitting errors.

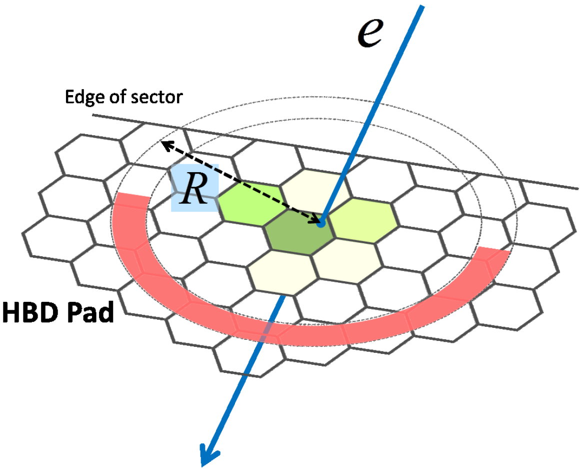

Figure 3.15: A half of an annular region around the reconstructed electron track on the HBD for the definition of **hbdringcharge**. The inner and outer radii of the annular region are 7.0 cm and 8.0 cm respectively. The direction of the half region is determined as the opposite side to the edge of the HBD sector to avoid inefficiency around the edge.

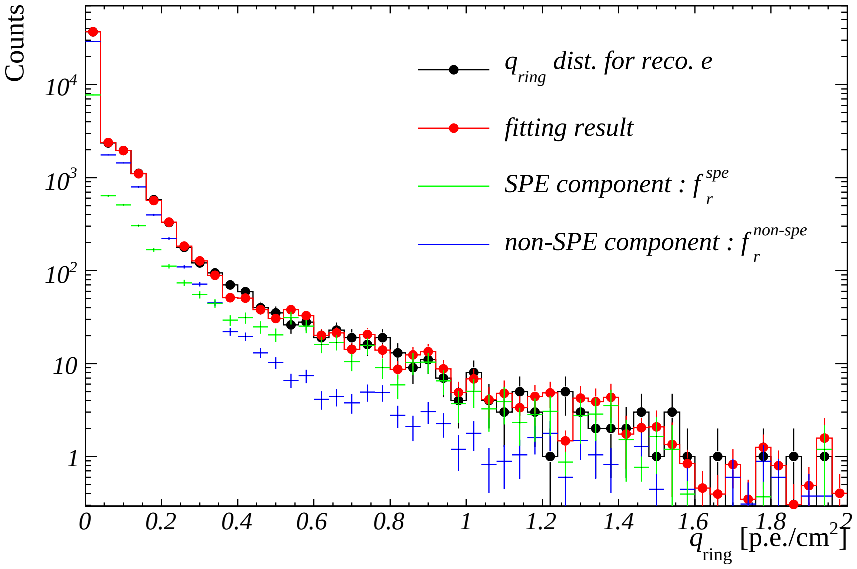

Figure 3.16: HBD charge distribution in the annular region for the reconstructed electrons with a transverse momentum ranging from 0.75 GeV/c to 1.00 GeV/c (black), and the fitting result of the charge distribution for electrons with correlated charges ($n_{\mathrm{spe}} f_{\mathrm{r}}^{\mathrm{spe}}$, green) and without correlated charges ($n_{\mathrm{non\text{-}spe}} f_{\mathrm{r}}^{\mathrm{non\text{-}spe}}$, blue), and the superposition of the fitting results (red).

In the case where an electron track was reconstructed and it was SPE, the partner electron track of the pair will have created an additional HBD signal around the recon-

Table 3.3: Summary of variables used in **hbdringcharge** analysis.

variable	description
$f_{\mathrm{r}}^{\mathrm{spe}}$	Distribution for SPE normalized with respect to the integral.
$f_{\mathrm{r}}^{\text{non-spe}}$	Distribution for non-photonic electrons and MPE normalized with respect to the integral.
n_{spe}	Number of SPE after applying the eID-Cut and npe-Cut.
$n_{\text{non-spe}}$	Number of electrons other than SPE after applying the eID-Cut and npe-Cut.

structed track, as Fig. 3.11(c) shows. This property is utilized to estimate the number of SPE. For this estimation, we defined a new value, q_{ring}, as

hbdringcharge: q_{ring}

The total charge in the HBD pads centered on a half of an annular region with an inner radius of 7.0 cm and an outer radius of 8.0 cm around the track projection of HBD as shown in Fig. 3.15. Avoiding inefficiency around the edge of the HBD sector, we employed a half of the annular region and the direction of the half region is determined as the opposite side to the edge as the Fig. 3.15 shows. The q_{ring} value is normalized by the area of the half of the annular region in the definition.

The choice of 7.0 cm to 8.0 cm comes from three facts: (1) the distribution of distance between separated clusters of SPE has a maximum around 7.0 cm, (2) few HBD clusters have radii larger than 7.0 cm, and (3) larger area includes more scintillation background and makes the ratio of the signal to the background worse.

Whereas the q_{ring} distributions for the non-photonic electrons and MPE consist of signals only from scintillation light, the one for SPE consists of the correlated signals around the tracks as well as signals from scintillation light. In the following description, we denote the q_{ring} distribution for SPE as $f_{\mathrm{r}}^{\mathrm{spe}}(q_{\mathrm{ring}})$ and one for the non-photonic electrons and MPE as $f_{\mathrm{r}}^{\text{non-spe}}(q_{\mathrm{ring}})$ as summarized in Table 3.3.

$f_{\mathrm{r}}^{\text{non-spe}}(q_{\mathrm{ring}})$ can be estimated by hadron tracks and electron tracks with large q_{clus} values which consist almost entirely of MPE. Because hadrons as well as MPE do not create any correlated signals around their tracks, the q_{ring} distributions of the tracks are created by only the scintillation light.

$f_{\mathrm{r}}^{\mathrm{spe}}(q_{\mathrm{ring}})$ was estimated by using simulations. The dominant photonic electrons come from the Dalitz decays of π^0 and η and γ from their decays which convert in materials. We simulated the detector responses for the Dalitz decay and the γ conversion events of the neutral mesons by a GEANT3 simulation [79] configured for the PHENIX detector system. With the simulation, the q_{ring} distributions for the Dalitz decays and the photon conversions from π^0 and η were determined. The q_{ring} distribution for the correlated signals was obtained as the summation of these distribution with known branching ratios and a production ratio between π^0 and η which is determined by Tsallis distributions, which are the m_T scaling spectra for hadron productions [78]. In the simulation, the contribution from the scintillation light was not included. Considering the contribution, $f_{\text{r}}^{\text{non-spe}}(q_{\text{ring}})$, which is identical to the q_{ring} distribution from only the scintillation light, was convoluted to the result to obtain $f_{\text{r}}^{\text{spe}}(q_{\text{ring}})$. Both distributions, $f_{\text{r}}^{\text{spe}}(q_{\text{ring}})$ and $f_{\text{r}}^{\text{non-spe}}(q_{\text{ring}})$, were normalized with respect to the integrals.

The q_{ring} distribution for the reconstructed electrons by applying eID-Cut and npe-Cut was fitted with the superposition of the q_{ring} distributions, $f_{\text{r}}^{\text{spe}}(q_{\text{ring}})$ and $f_{\text{r}}^{\text{non-spe}}(q_{\text{ring}})$, as

$$n_{\text{spe}} \times f_{\text{r}}^{\text{spe}}(q_{\text{ring}}) + n_{\text{non-spe}} \times f_{\text{r}}^{\text{non-spe}}(q_{\text{ring}}), \tag{3.9}$$

where n_{spe} and $n_{\text{non-spe}}$ are fitting parameters and represent the numbers of SPE and other electrons in the q_{ring} distribution respectively as summarized in Table 3.3. As well as the fitting for the q_{clus} distribution, the fitting for the q_{ring} distribution was also performed for each electron p_T region and each HBD sector. Figure 3.16 shows a fitting result in one HBD sector in the electron p_T region from 0.75 GeV/c to 1.00 GeV/c.

3.2.6 Non-photonic background estimation

Yield estimation of heavy flavor electrons

Using the above fitting results of $\tilde{n}_{\text{s}}$ and n_{spe}, the yield of non-photonic electrons, N^{npe} was estimated as

$$N^{\text{npe}}(p_T) \;\; = \;\; \tilde{n}_{\text{s}}(p_T) - n_{\text{spe}}(p_T). \tag{3.10}$$

The remaining background for the heavy flavor electrons in the non-photonic electron sample comes from K_{e3} decays and e^+e^- decays of light vector mesons. Electrons from the Drell-Yan process are also background. However, the Drell-Yan contribution is known to be less than 0.5% of total heavy flavor electrons in p_T range of $0.0 < p_T < 5.0$ GeV/c and can be ignored. Therefore, we can determine the yield of the heavy flavor electrons from N^{npe} by subtracting the components of the K_{e3} electrons and the electrons from light vector mesons, which are described in the following sections, as

$$N^{\text{HF}\ e}(p_T) = N^{\text{npe}}(p_T) - N^{Ke3}(p_T) - N^{\text{LVM}}(p_T), \tag{3.11}$$

where $N^{Ke3}(p_T)$ and $N^{\text{LVM}}(p_T)$ represent the electrons from the K_{e3} decays and the light vector meson decays, respectively. With this method, the heavy flavor electron yield, $N^{\text{HF}\ e}(p_T)$, was obtained.

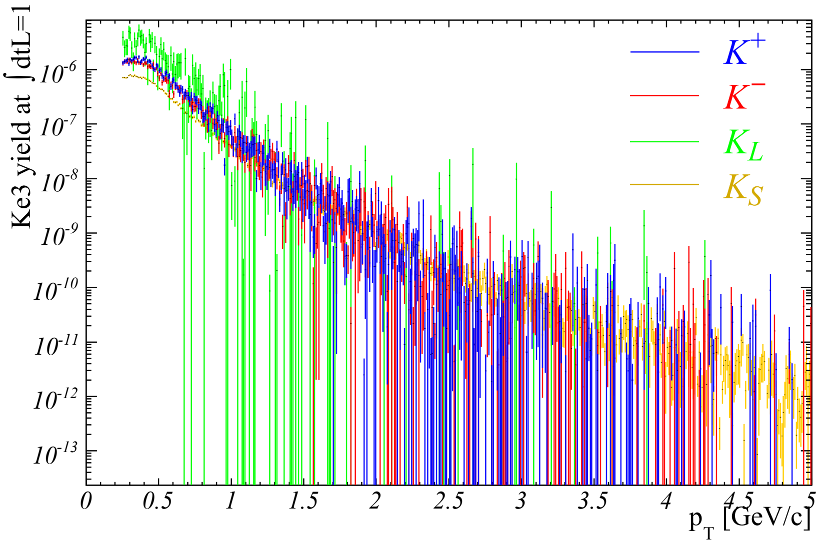

Figure 3.17: Yield of electrons from K_{e3} decays of K^+ (blue), K^- (red), K_L (green) and K_S (yellow) normalized as integrated luminosity, $\int dtL$, is equal to 1 mb after applying eID-Cut and npe-Cut.

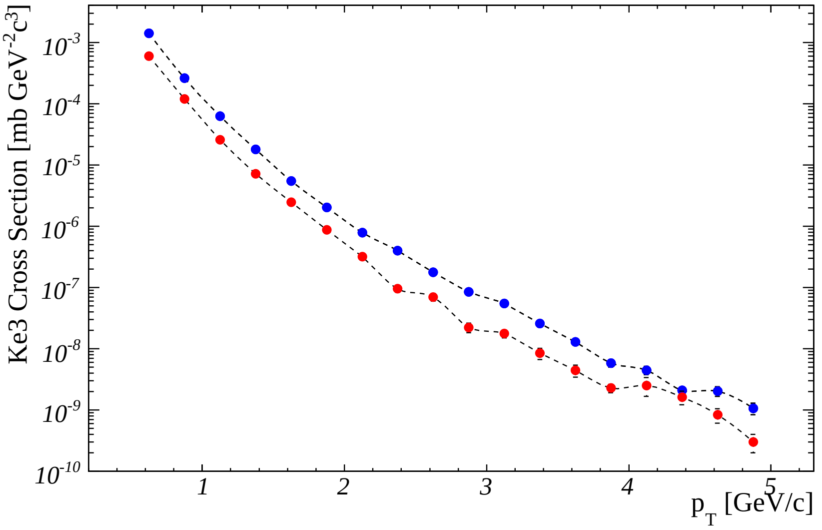

Figure 3.18: Estimated cross section of K_{e3} in Run9 configuration. The red spectrum represents after applying eID-Cut and npe-Cut and the blue spectrum represents after applying same cuts without all HBD cuts.

Non-photonic background electrons from K_{e3} decays

Electrons from K_{e3} decays are main non-photonic background for the heavy flavor electrons especially at low p_T region. Then, the yield of the K_{e3} electrons is to be subtracted from the total non-photonic electron yield. In addition, because the K_{e3}

electrons have unknown background spin asymmetry of the K production, it introduces systematic uncertainty in the spin asymmetry. Hence, it is essential to suppress the K_{e3} electrons as much as possible for this spin asymmetry measurement.

Though the previous analysis already estimated the effective cross section of the K_{e3} electron production, this cross section can not be used in this analysis because the new electron selections based on HBD signals, q_{clus} cut and cluster size cut, significantly affect the cross section. The HBD selections require only K_{e3} decays occurring inside the HBD gas volume. Therefore, the K_{e3} electron cross section under the new selections needs to be estimated.

We generated 8M + 8M $K^{\pm}$, 2M K_L, and 2M K_S events with an event generator. For the K cross section in the generator, we employed a m_T scaled cross section which has been measured in PHENIX [78] and assumed that cross section spectra of all K productions are identical. We set parameters in the m_T scaled cross section as $d\sigma/dy = 4.23$ mb and $T = 125.4$ MeV and $n = 9.81$, where the parameter notations are consistent with the previous measurement [78]. Decays of K mesons were simulated by GEANT3.

Same electron selections as the single electron analysis, namely eID-Cut and npe-Cut, are employed. The estimated yields of these reconstructed K_{e3} are shown in Fig. 3.17 as functions of p_T^e. The yield spectra are normalized as $\int dtL = 1$ mb. The blue spectrum corresponds to K^+, the red to K^-, the green to K_L and the yellow to K_S.

The small statistics of K_L decays come from long flight length of K_L, $c\tau \sim 15$ m. The statistical uncertainties on K_L decays are too large to subtract K_{e3} contribution from the non-photonic electron yield. Hence, K_{e3} yields of K_L decays was estimated from K_{e3} yield of $K^{\pm}$ decays. The requirement of the E-p matching on eID-Cut constrains the flight length of the K_{e3} decay to $l < 60$ cm, and the requirement of the association with HBD signal constrains the flight length to $l < 20$ cm. The radius of the HBD volume (55 cm) is enough small compared with the decay lengths of $K^{\pm}$ and K_L, $c\tau$ =3.7m and $c\tau$ =15m, to assume the flight length distribution of these K_{e3} decays in the HBD volume are flat. Ignoring the curvature of the tracks of $K^{\pm}$ due to their charges, the yield of the K_{e3} electrons from K_L can be estimated with the yields from $K^{\pm}$. The relation between these yields can be written as,

$$N_L^{Ke3} = \frac{N_+^{Ke3} + N_-^{Ke3}}{2} \frac{\text{BR}_L/c\tau_L}{\text{BR}_{\pm}/c\tau_{\pm}}, \tag{3.12}$$

where $N_{\pm,L}^{Ke3}$ represent the yield of the K_{e3} decays from $K^{\pm}$ and K_L and $\text{BR}_{\pm}$ represents the branching ratio of $K^{\pm} \to e^{\pm}\nu\pi^0$ and BR_L represents the branching ratio of $K^L \to e^{\pm}\nu\pi^{\mp}$ and $c\tau_{\pm,L}$ represent the decay lengths of $K^{\pm}$ and K_L.

From the obtained yield of K_{e3} electrons, the K_{e3} electron cross section is determined from the yield and the acceptance and reconstruction efficiency for the single electrons in $|\eta| < 0.5$, $A\epsilon_{\text{rec}}$, which were estimated using a GEANT3 simulation. The detailed $A\epsilon_{\text{rec}}$ estimation is described in a later section for cross section estimation (Sec. 4.2). The spectrum of $A\epsilon_{\text{rec}}(p_T, \Delta\eta = 1)$ is shown in Fig. 4.6. Using $A\epsilon_{\text{rec}}$, the K_{e3} cross section can be represented as,

$$E\frac{d^3\sigma}{dp^3}|_{Ke3} = \frac{1}{2\pi p_T} \frac{1}{A\epsilon_{\text{rec}}(\Delta\eta = 1)} \frac{N^{Ke3}}{\Delta p_T}, \tag{3.13}$$

where $N^{Ke3} \equiv N_{+}^{Ke3} + N_{-}^{Ke3} + N_{L}^{Ke3} + N_{S}^{Ke3}$ represents total yield of the K_{e3} electrons in the simulation and Δp_T represents the bin width of p_T. The obtained K_{e3} cross section is shown in Fig. 3.18. The red spectrum is the cross section after applying eID-Cut and npe-Cut and the blue spectrum is the cross section after applying the same cuts without all HBD related cuts (HBD cluster association cuts, q_{clus} cuts, and HBD cluster size cut). Comparing the read and blue spectra, we found that the HBD reduced the K_{e3} electrons by a factor of ~0.4. It is a sizable contribution to measure the spin asymmetry of the heavy flavor electrons. For this single electron analysis, the red spectrum was subtracted from the obtained non-photonic electron cross section spectrum.

Background electrons from light vector mesons

The large opening electron pairs from decays of light vector mesons $V \to e^+e^-$ (where V denotes a vector meson) are another non-photonic background of the heavy flavor electrons. The fraction of this background in the heavy flavor electrons is small, less than 2%, over whole p_T region in this measurement. The light vector mesons have another e^+e^- decay mode of $V \to e^+e^- + S$ (where S denotes a pseudoscalar meson), but the electron pair is photonic electron and has small opening angle as same as Dalitz decay $\pi^0, \eta \to e^+e^- + \gamma$ and is dropped in the above HBD analysis.

The cross sections of the background electrons from the light vector mesons have been already estimated in the previously published result [28]. The cross sections were used to estimate the background.

Possible hadron background

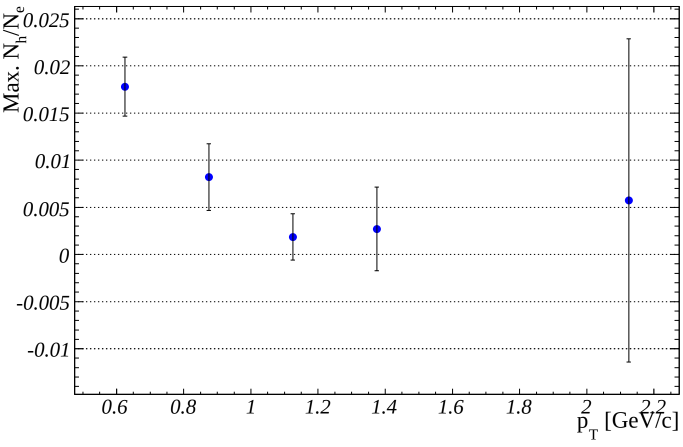

Figure 3.19: Upper limit of hadron fraction in the inclusive electron events after applying eID-Cut and npe-Cut as a function of p_T. I added sum of the center value and the RMS to the systematic uncertainty of the heavy flavor electron yield.

The RICH, EMCal, and HBD selections effectively reject hadrons. However, small fraction of hadrons can be included in the electron tracks. For the hadron estimation, we prepared two datasets, electron enhanced data (e-TrkSet) and hadron enhanced data (h-TrkSet). The e-TrkSet consists of reconstructed tracks on the DC/PC with an associated EMCal cluster which has electromagnetic shower profile, and the h-TrkSet consists of reconstructed tracks with an associated EMCal cluster which does not have such profile. We applied electron selections (eID-Cut and npe-Cut without shower profile selection: e-Cut) and hadron selections (h-Cut), which consists of track quality selection and RICH veto. Then, four datasets were created by (e-TrkSet, h-TrkSet)×(e-Cut, h-Cut). The e-TrkSet after applying e-Cut (e-TrkSet&&e-Cut) is identical to the dataset after applying eID-Cut and npe-Cut. Since hadrons are dominant compared with electron tracks in charged tracks produced in *pp* collisions, the three datasets other than e-TrkSet&&e-Cut include a lot of hadron tracks.

To estimate the number of hadrons in e-TrkSet&&e-Cut, we used following relation,

$$\begin{aligned}\#\text{ of hadrons in }(\mathbf{e\text{-}Cut}\&\&\mathbf{e\text{-}TrkSet}) =& \\ \#\text{ of hadrons in }(\mathbf{h\text{-}Cut}\&\&\mathbf{e\text{-}TrkSet}) \times& \\ \left(\frac{\#\text{ of hadrons in }(\mathbf{e\text{-}Cut}\&\&\mathbf{h\text{-}TrkSet})}{\#\text{ of hadrons in }(\mathbf{h\text{-}Cut}\&\&\mathbf{h\text{-}TrkSet})}\right).&\end{aligned} \tag{3.14}$$

The reconstructed tracks in h-TrkSet&&h-Cut consists almost of hadron tracks. Therefore, we can determine upper limit of the number of hadrons in e-TrkSet&&e-Cut as

$$\begin{aligned}\#\text{ of hadrons in }(\mathbf{e\text{-}Cut}\&\&\mathbf{e\text{-}TrkSet}) <& \\ \#\text{ of tracks in }(\mathbf{h\text{-}Cut}\&\&\mathbf{e\text{-}TrkSet}) \times& \\ \left(\frac{\#\text{ of tracks in }(\mathbf{e\text{-}Cut}\&\&\mathbf{h\text{-}TrkSet})}{\#\text{ of tracks in }(\mathbf{h\text{-}Cut}\&\&\mathbf{h\text{-}TrkSet})}\right).&\end{aligned} \tag{3.15}$$

The resulting upper limit of hadrons as a function of p_T is shown in Fig. 3.19. We added sum of the center value and the RMS to the systematic uncertainty of the heavy flavor electron yield for $p_T < 1.25$ GeV/c, and added same value as $1.00 < p_T < 1.25$ GeV/c region for $1.25 < p_T$ GeV/c.

Chapter 4

Results

4.1 Heavy Flavor Electron Yield

4.1.1 Systematic uncertainty on raw yield

The systematic uncertainties for the heavy flavor electron yield come from the fits for q_{clus} distribution and q_{ring} distribution, the estimations of K_{e3} background, and the mis-identified hadron background.

The most significant source in these contributions is the fitting uncertainty for the q_{ring} distribution. We changed the inner and outer radii of the annular region into 6.0 cm and 7.0 cm, and also into 8.0 cm and 9.0 cm, respectively, from the default radii of 7.0 cm and 8.0 cm. The uncertainty of the fitting was estimated from variations of obtained n_{spe} after these changes. The estimated uncertainties depend on the momentum and decrease from about 16% of the heavy flavor electron yield at the low momentum region, $0.50 < p_T < 1.00$ GeV/c, to about 2% above 1.75 GeV/c.

The fitting uncertainty for the q_{clus} distribution comes from the estimation of the bias in the charge distribution shape due to the electron pair reconstruction. The systematic uncertainty from this effect is estimated to be less than 2% by simulations.

In the low momentum region, $0.50 < p_T < 1.00$ GeV/c, uncertainties from the K_{e3} contribution and the hadron mis-reconstructions are also not negligible. The uncertainty from the K_{e3} contribution comes almost from the uncertainty on the cross section of K meson production used in the K_{e3} estimation. The systematic error from the uncertainty is about 4% of the total heavy flavor electron yield in the low momentum region and decreases to less than 1% over 0.75 GeV/c. We also estimated the upper limits of the hadron contamination due to mis-reconstructions employing a hadron-enhanced dataset. As a result, we determined the upper limits as 4% of the total heavy flavor electron yield in the low momentum region which decreases to less than 1% over 1.5 GeV/c. The upper limits are assigned as the systematic uncertainties from hadron mis-reconstructions. Table 4.1 and Fig. 4.1 summarizes the systematic uncertainties on the heavy flavor electron yield.

Table 4.1: Relative systematic uncertainties given in percent on the heavy flavor electron yield.

source	uncertainty	p_T range (GeV/c)
hbdringcharge fitting	16%	($0.50 < p_T < 0.75$)
	6% $\sim$ 4%	($0.75 < p_T < 1.75$)
	2%	($1.75 < p_T$)
hbdcharge fitting	2%	($0.50 < p_T < 0.75$)
	$< 1\%$	($0.75 < p_T$)
K_{e3}	4%	($0.50 < p_T < 0.75$)
	$< 1\%$	($0.75 < p_T$)
hadron mis-ID	4%	($0.50 < p_T < 0.75$)
	$< 1\%$	($0.75 < p_T$)

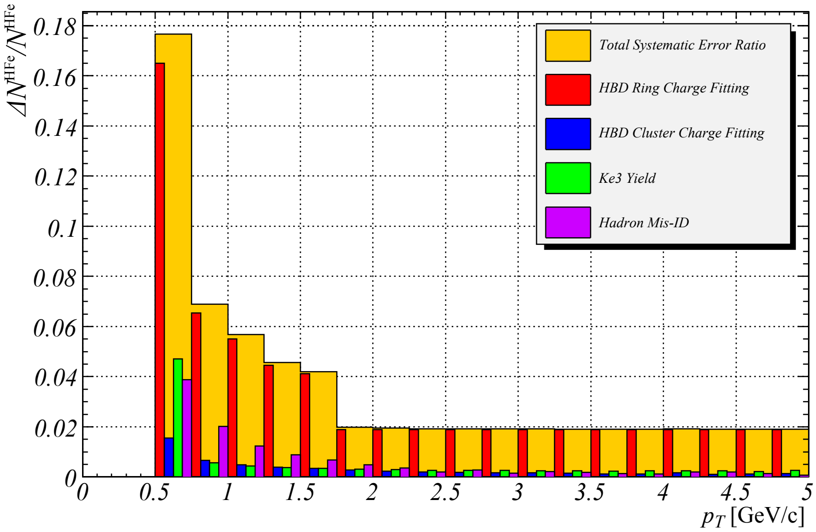

Figure 4.1: Systematic uncertainties of the single electron yield for all sources. These uncertainties are normalized by the single electron yield. The histograms represent total uncertainty (yellow), uncertainty from the HBD ring charge fitting (red), from the HBD cluster charge fitting (blue), from K_{e3} estimation (green) and from hadron contamination estimation (purple).

4.1.2 Raw yield and signal purity of heavy flavor electron

From Eq. 3.10 and Eq. 3.11 and the discussion in the Sec. 4.1.1, the heavy flavor electron yield spectrum with the systematic uncertainties is obtained. The spectrum is shown in Fig. 4.2. We also show the yield of inclusive reconstructed electrons after applying the eID-Cut and npe-Cut and the estimated K_{e3} contribution. The electrons from e^+e^- decays of the light vector mesons are not shown in Fig. 4.2, but they are less than 5%

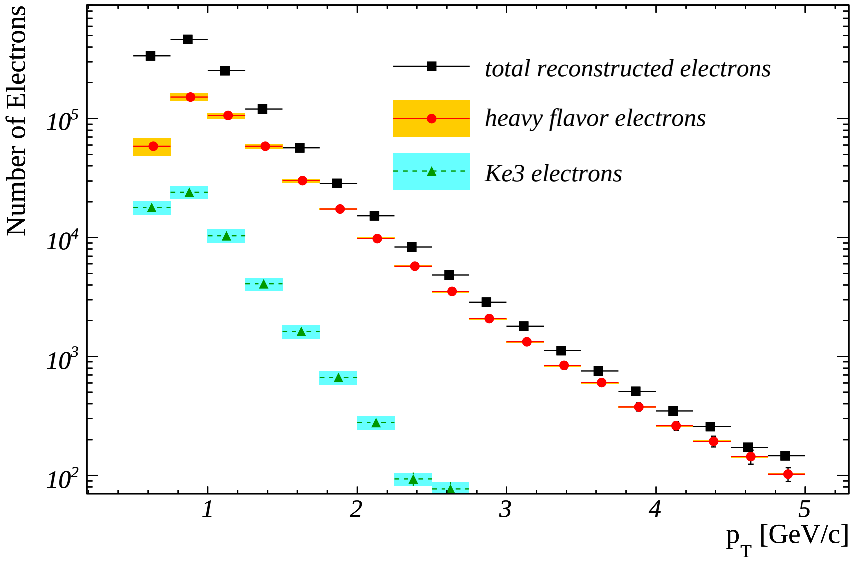

Figure 4.2: Heavy flavor electron yield spectrum. The black square points represent the total number of the reconstructed electrons after applying the eID-Cut and npe-Cut. The red circle points represent the estimated yield of the heavy flavor electrons. The yellow bands represent the systematic uncertainties for the heavy flavor electron yield. The green triangle points with dashed lines represent the estimated K_{e3} contribution with systematic uncertainties shown by light-blue bands.

compared with the heavy flavor electron yield in this p_T range.

The ratio of the non-photonic electron yield to the photonic electron yield in this measurement,

$$R(p_T) \equiv \frac{N^{\mathrm{npe}}(p_T)}{N_e^{\mathrm{reco}}(p_T) - N^{\mathrm{npe}}(p_T)} \tag{4.1}$$

where N_e^{reco} denotes the total number of reconstructed electrons after applying the eID-Cut and npe-Cut, is shown as the top plot in Fig. 4.3. In Eq. 4.1, we assumed the fraction of mis-identified hadrons in the reconstructed electrons after the cuts is negligible as shown in Fig. 3.7, and so the number of photonic electrons can be represented as $N_e^{\mathrm{reco}}(p_T) - N^{\mathrm{npe}}(p_T)$. The measured ratio in the previous measurement [28] is also shown in Fig. 4.3. The previous measurement employed another methods for the background estimation, namely a cocktail method and a converter method. In the cocktail method, a cocktail of electron spectra from various background sources was calculated using a Monte Carlo event generator of hadron decays. On the other hand, in the converter method, an additional photon converter around the beam pipe was introduced for part of the experiment to estimate the photonic electron background. The ratio is improved by a factor of about 2 or more in $p_T > 1.0$ GeV/c compared with the previously measured result due to the rejection of photonic electrons with the HBD.

The signal purity is defined as the ratio of the yield of the heavy flavor electrons to the reconstructed electrons after applying the eID-Cut and npe-Cut,

$$D(p_T) \equiv \frac{N^{\mathrm{HF\ e}}(p_T)}{N_e^{\mathrm{reco}}(p_T)}. \tag{4.2}$$

The result is shown as the bottom plot in Fig. 4.3. We also show the result of the signal purity in the previous measurement. Comparing with the previously measured result, the signal purity is improved by a factor of about 1.5 around p_T of 0.75 GeV/c to 2.00 GeV/c.

4.2 Cross Section of Heavy Flavor Electron

The invariant cross section is calculated as,

$$E\frac{d^3\sigma}{dp^3} = \frac{1}{2\pi p_T}\frac{1}{L}\frac{1}{A\epsilon_{\mathrm{rec}}\epsilon_{\mathrm{trig}}}\frac{N(\Delta p_T, \Delta y)}{\Delta p_T \Delta y}, \tag{4.3}$$

where L denotes the integrated luminosity, A the acceptance, ϵ_{rec} the reconstruction efficiency, ϵ_{trig} the trigger efficiency, and N the estimated number of heavy flavor electrons.

4.2.1 Integrated luminosity

The luminosity, L, was calculated from the number of obtained MB triggers divided by the cross section of MB trigger acceptance. For the latter cross section, a value of 23.0 mb with a systematic uncertainty of 9.6% was estimated from van-der-Merr scan results [109] corrected by the relative changes in the BBC performance.

4.2.2 Detector acceptance and reconstruction efficiency

The combination of the acceptance and reconstruction efficiency, $A\epsilon_{\mathrm{rec}}(p_T)$, was estimated with a GEANT3 simulation, which simulates the full detector responses. In the acceptance calculation, it is important to check that the acceptance of each detector in the real data and the simulation agrees. Therefore, hit distributions of the reconstructed electrons in each detector with the MB dataset and those of the simulation dataset were compared. The acceptance and reconstruction efficiency can be determined to be $A\epsilon_{\mathrm{rec}} = N^{\mathrm{rec}}(p_T^{\mathrm{rec}})/N^{\mathrm{gen}}(p_T^{\mathrm{gen}})$, where N^{rec} (N^{gen}) is the number of reconstructed (generated) electrons and p_T^{rec} (p_T^{gen}) is reconstructed (generated) p_T of the electrons. The results are shown in Fig. 4.4 and Fig. 4.5. In Fig. 4.4, the black histogram represents the data distribution and the red histogram represents the simulation distribution. Figure 4.5 shows the difference of the data and simulation (data − sim) divided by total hit counts in the simulation data (the integral of simulation histogram). The total fractions of all positive difference (blue number) and all negative difference (red number) are also shown separately. From these fractions, we assigned

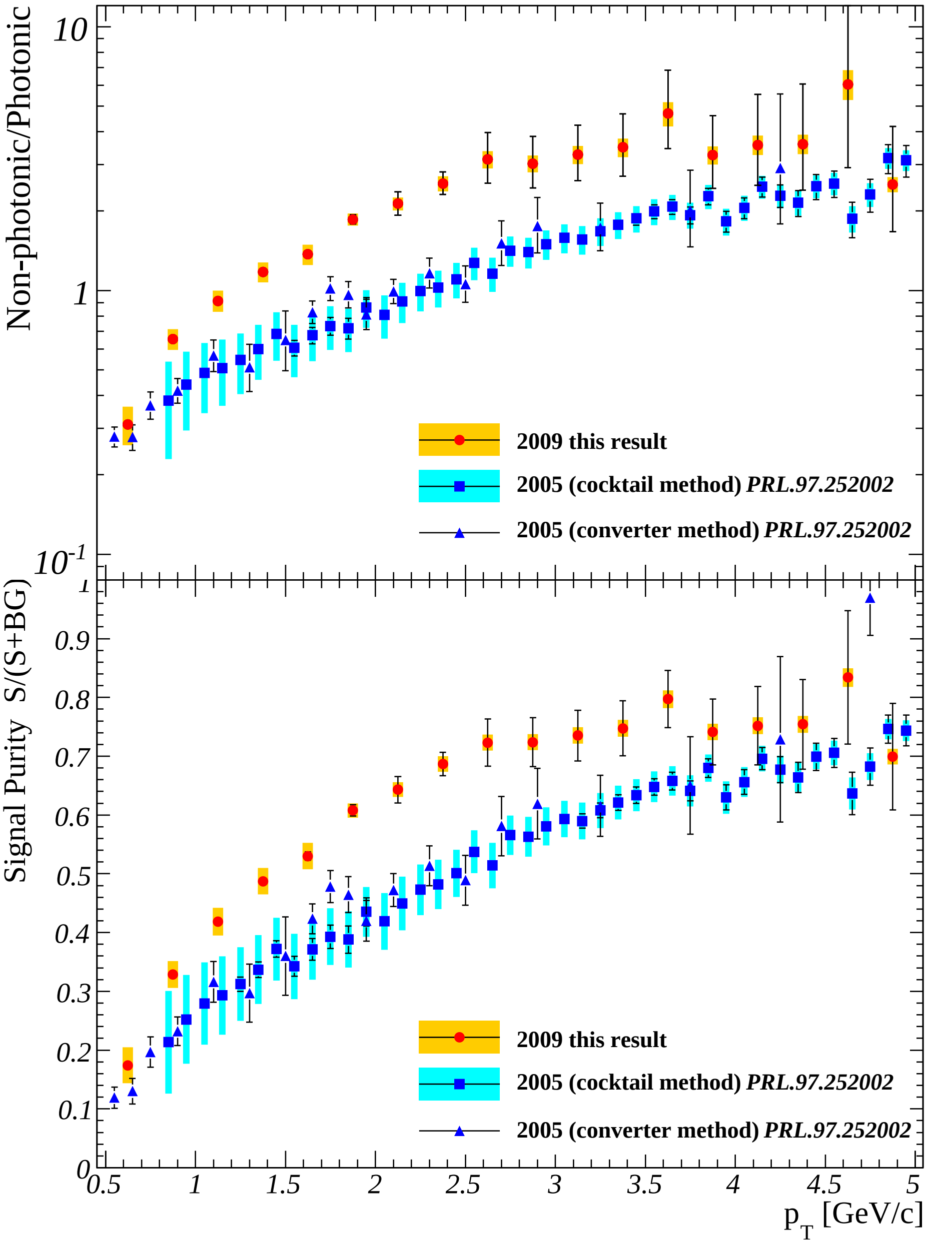

Figure 4.3: (top) Ratio between the yields of the non-photonic electrons and the photonic electrons in the reconstructed tracks. The red circles and the blue squares represent this analysis result and the previous result respectively. The error bars and bands represent the statistic and the systematic errors. (bottom) Signal purity which is a ratio of the yield of the heavy flavor electrons to the total reconstructed electrons.

a systematic uncertainty from the acceptance estimation is assigned to be 8% as a conservative value.

From the GEANT3 simulation, it was found that $A\epsilon_{\mathrm{rec}}(p_T)$ has very small p_T dependence at $p_T > 0.5$ GeV/c and the value is 4.7%. The estimated $A\epsilon_{\mathrm{rec}}(p_T)$ is shown

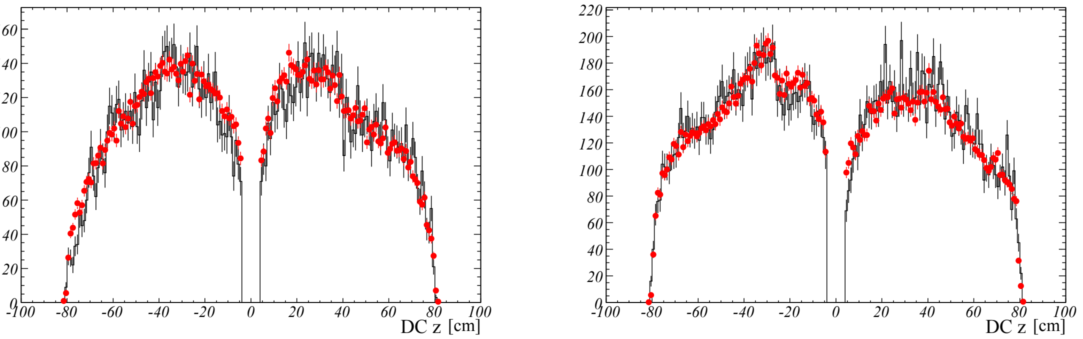

(a) z distribution of hits in east DC (b) z distribution of hits in west DC

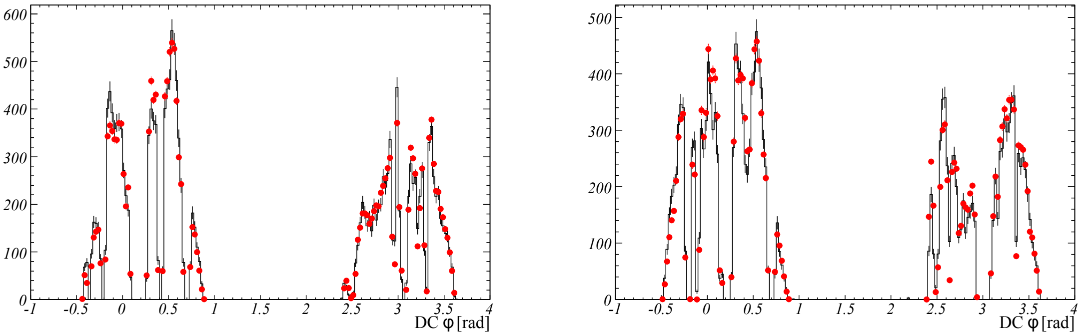

(c) ϕ distribution of hits in north-side DC (d) ϕ distribution of hits in south-side DC

Figure 4.4: (a - d) Comparison of DC hit distributions in data and GEANT3 simulation. Figures (a) and (b) correspond to z distributions of hits in East and West DC, respectively, and figures (c) and (d) correspond to ϕ distributions of hits in North-side and South-side DC, respectively.

in Fig. 4.6.

The applied electron cuts other than the cuts related to the HBD are identical to the previous measurement. Therefore, we employed same criteria to assign the systematic uncertainties from the efficiency of the electron identification as the previous measurement. The assigned uncertainties on the DC, RICH and EMCal cut are the following:

RICH eID cut
2%

prob cut
0.5%

e/p cut
2%.

We also estimated systematic uncertainty from HBD cuts. There are two HBD cuts for the electron identification, namely q_{clus} cut and cluster size cut. We compared the

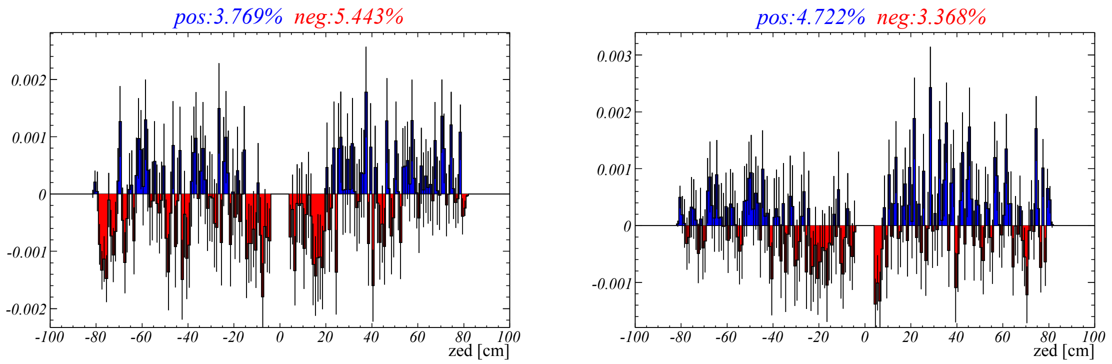

(a) z distribution of hits in east DC (b) z distribution of hits in west DC

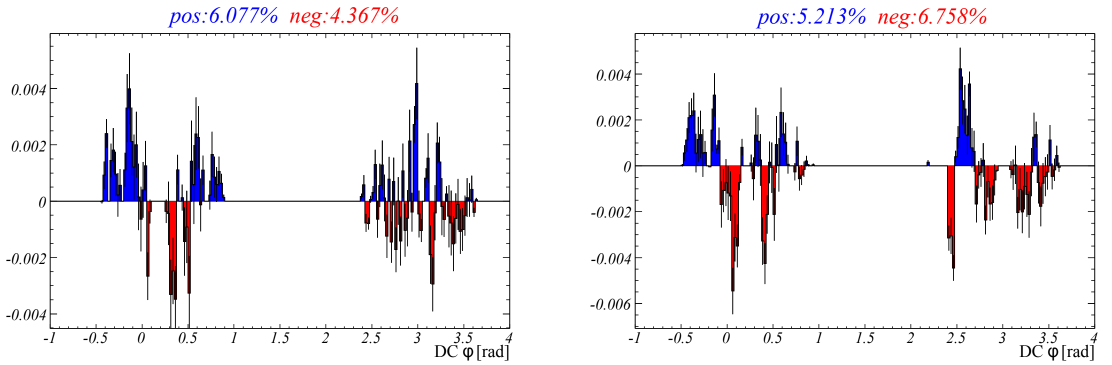

(c) ϕ distribution of hits in north-side DC (d) ϕ distribution of hits in south-side DC

Figure 4.5: (a - d) Difference of the data and simulation (data − sim) divided by total hit counts in the simulation data. Figures (a - d) correspond to Fig. 4.4(a - d), respectively. The positive (negative) region is filled with blue (red). The two numbers at the top of the plots represent fractions of the integrated positive and negative area with respect to the integrated area of the original histograms in Fig. 4.4.

$q_{\rm clus}$ distribution and the cluster size distribution for non-photonic electrons between data and simulation. Figure 4.7 shows the comparison of the data (black line) and the simulation (red circles). The distributions of the data are estimated by using single cluster hits in photonic electron pair events on the HBD.

In the cluster size distributions, this method can introduce a bias on the distributions, which enhances events with larger cluster size, because the single cluster can include additional hit pads created by Čerenkov light or scintillation light from the counterpart electron of the electron pair, which are accidentally not clusterized into the another HBD cluster associated with the counterpart track. Therefore, we compared also cluster size distributions estimated from electron pairs associated to $J/\psi \rightarrow e^+ + e^-$ decays. For this estimation, the electron pairs with pair mass $2.8 < M_{e^+e^-} < 3.3$ GeV/c^2 were selected from data. The electron pairs from J/ψ have large opening angle, and then the HBD hits of a track do not affect to the ones of the another track. Hence, the cluster size distribution from the J/ψ decays has no bias and suitable for the comparison.

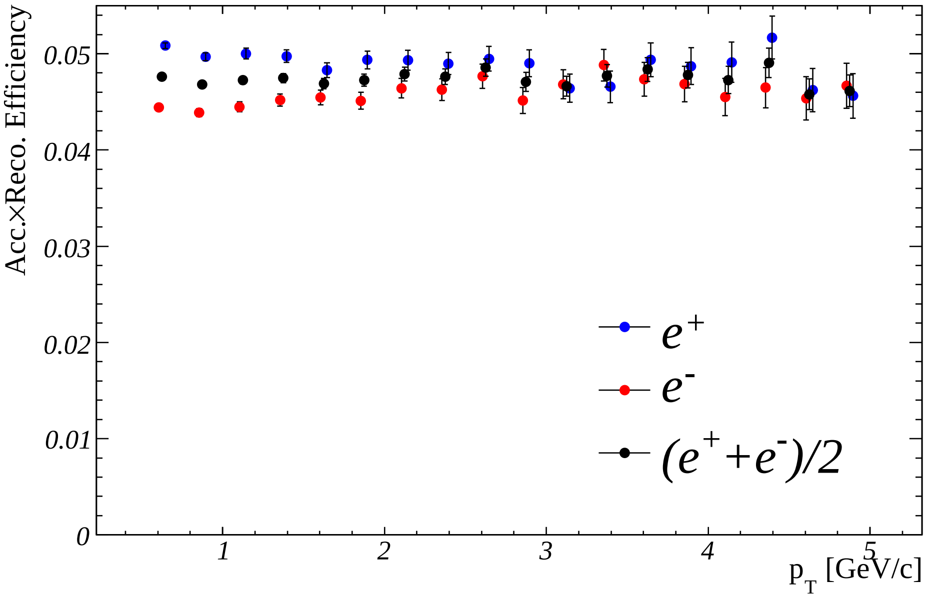

Figure 4.6: $A\epsilon_{\text{reco}}$ spectra as functions of electron p_T after applying eID-cut and npe-Cut. The blue and red points are positron and electron, respectively. The black points are the averaged $A\epsilon_{\text{reco}}$ for positrons and electrons.

The distributions of data and simulation are enough consistent each other so that we can conservatively assign the systematic uncertainty from efficiency of the HBD hit selection to be half value of percentage of rejected electron tracks by these selections. Figure 4.8 shows HBD cluster charge distribution of the simulation data without the charge cuts, and Fig. 4.9 shows HBD cluster size distribution of the simulation data without the cluster size cut. The fractions of rejected events by the cuts are also shown in the plots. From the differences of comparisons and the fractions of the cuts, we assigned systematic uncertainties as:

HBD cluster charge cut

3%

HBD cluster size cut

3.5%.

As the result, the acceptance and reconstruction efficiency including systematic uncertainties is obtained as $A\epsilon_{\text{rec}}(p_T) = 4.7\% \times (1 \pm 8 \times 10^{-2}(\text{acc.}) \pm 6 \times 10^{-2}(\text{reco.}))$.

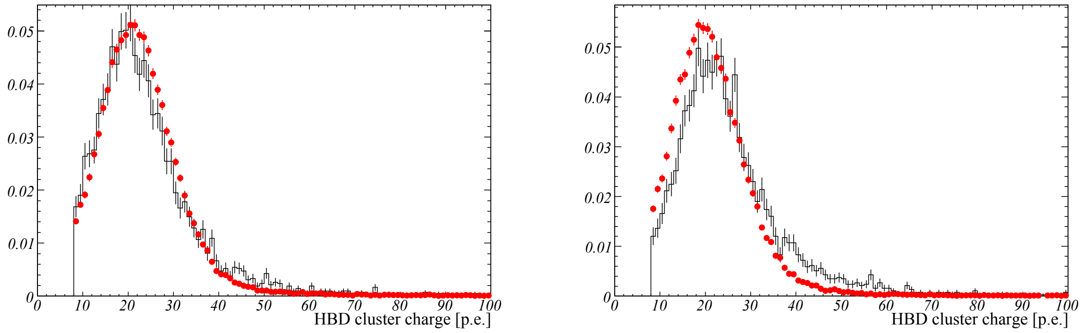

(a) $q_{\rm clus}$ distribution (Sect9 South) (b) $q_{\rm clus}$ distribution (Sect9 North)

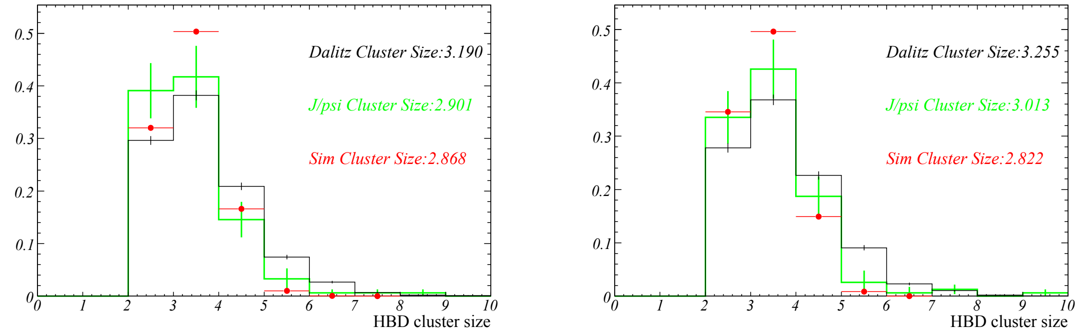

(c) HBD cluster size distribution (Sect9 South) (d) HBD cluster size distribution (Sect9 North)

Figure 4.7: Comparisons between (black lines) data and (red circles) GEANT3 simulation for (a, b) $q_{\rm clus}$ distribution and (c, d) HBD cluster size distribution for non-photonic electrons at a typical sector, respectively. The $q_{\rm clus}$ distribution and the cluster size distribution from the data are estimated by using single cluster hits in photonic electron pair events on the HBD. The green lines in the plots (c, d) represent the cluster size distribution estimated by electron pairs from J/ψ ($2.9 < M_{e^+e^-} < 3.3$ GeV/c^2) in data.

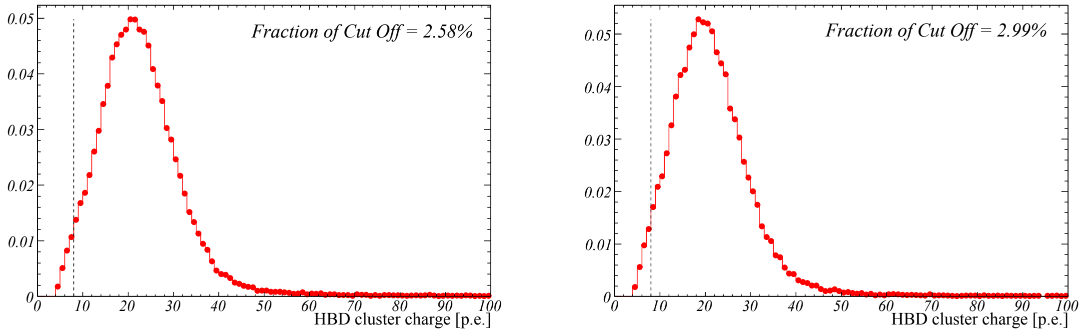

(a) Sect9 South (b) Sect9 North

Figure 4.8: q_{clus} distributions from GEANT3 simulation without q_{clus} cuts at a typical HBD sector. The numbers shown at corners of the plots are the fractions of cut-off electrons by the q_{clus} cut of $q_{\text{clus}} > 8.0$ p.e..

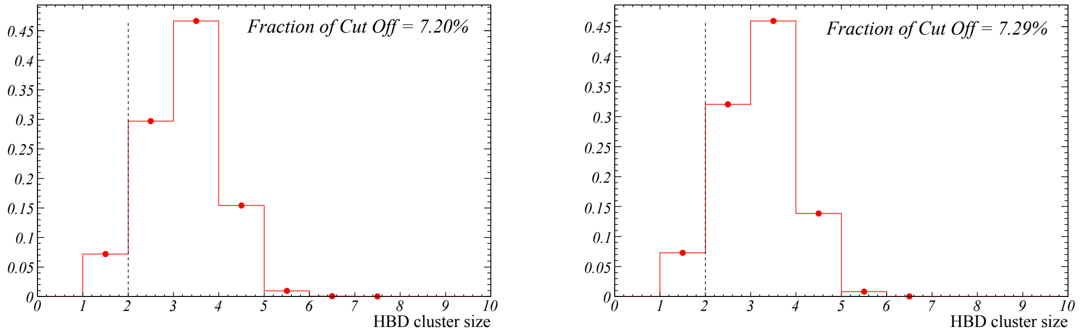

(a) Sect9 South (b) Sect9 North

Figure 4.9: HBD cluster size distributions in GEANT3 simulation without HBD cluster size cuts at a typical HBD sector. The numbers shown at corners of the plots are the fractions of cut-off electrons by the cluster size cut of size ≥ 2.

4.2.3 Trigger performance

The efficiency of the MB trigger for the hard scattering processes, including heavy flavor electron production, is $\epsilon_{\rm trig}^{\rm MB} = 79.5\% \times (1 \pm 2.5 \times 10^{-2})$. The efficiency of the ERT-E trigger for electrons under requiring the MB trigger, $\epsilon_{\rm trig}^{e|\rm MB}(p_T) \equiv \epsilon_{\rm trig}(p_T)/\epsilon_{\rm trig}^{\rm MB}$, can be calculated by the ratio of the number of the reconstructed electrons in the MB trigger dataset with coincidence of the ERT-E trigger to the one without the coincidence. The efficiency $\epsilon_{\rm trig}^{e|\rm MB}$ is shown in Fig. 4.10 as a function of p_T. Whereas we used the calculated efficiency values for the momentum region of $p_T < 1.25$ GeV/c, we assumed a saturated efficiency for $p_T > 1.25$ GeV/c and estimated the value with a fitting as shown in Fig. 4.10. The fitting result is $\epsilon_{\rm plateau} = 56.5\% \times (1 \pm 3.6 \times 10^{-2})$. The systematic uncertainty of $\epsilon_{\rm trig}^{e|\rm MB}$ for $p_T < 1.25$ GeV/c was assigned to be $\Delta\epsilon/\epsilon \sim 4\%$, which was estimated from the statistical uncertainty in the efficiency calculation, and 3.6% for $p_T > 1.25$ GeV/c from the fitting uncertainty. The total trigger efficiency $\epsilon_{\rm trig}(p_T)$ can be calculated with the above two efficiencies as $\epsilon_{\rm trig}(p_T) = \epsilon_{\rm trig}^{\rm MB} \times \epsilon_{\rm trig}^{e|\rm MB}(p_T)$.

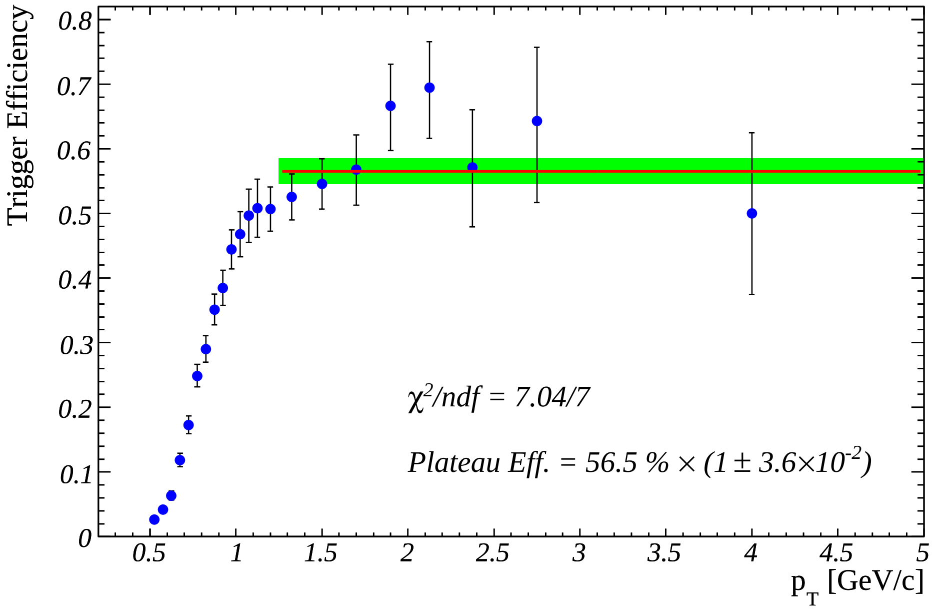

Figure 4.10: Efficiency of the electron trigger for reconstructed electrons under the condition that the MB trigger was issued. The red line represents the fitting result with the constant function and the green band represents the fitting uncertainty.

4.2.4 Cross section of heavy flavor electron

Table 4.3 summarizes the systematic uncertainties on the cross section of the heavy flavor production other than the uncertainties from the heavy flavor electron yield already shown in Table 4.1. All systematic uncertainties listed in Table 4.3 are globally correlated over whole p_T region ($p_T > 1.25$ GeV/c for the uncertainties on $\epsilon_{\rm trig}^{e|\rm MB}$).

Table 4.2: Data table for the cross section result corresponding to Fig. 4.11.

p_T[GeV/c]	$E\frac{d^3\sigma}{dp^3}$[mb×GeV^{-2}c^3]	stat. error[mb×GeV^{-2}c^3]	syst. error[mb×GeV^{-2}c^3]
0.612	2.12×10^{-3}	0.04×10^{-3}	0.47×10^{-3}
0.864	7.93×10^{-4}	0.09×10^{-4}	1.11×10^{-4}
1.115	2.78×10^{-4}	0.03×10^{-4}	0.37×10^{-4}
1.366	1.09×10^{-4}	0.02×10^{-4}	0.13×10^{-4}
1.617	4.77×10^{-5}	0.08×10^{-5}	0.58×10^{-5}
1.867	2.34×10^{-5}	0.05×10^{-5}	0.27×10^{-5}
2.118	1.15×10^{-5}	0.04×10^{-5}	0.13×10^{-5}
2.369	6.05×10^{-6}	0.20×10^{-6}	0.68×10^{-6}
2.619	3.28×10^{-6}	0.19×10^{-6}	0.37×10^{-6}
2.869	1.82×10^{-6}	0.11×10^{-6}	0.20×10^{-6}
3.120	1.08×10^{-6}	0.07×10^{-6}	0.12×10^{-6}
3.370	6.20×10^{-7}	0.41×10^{-7}	0.69×10^{-7}
3.620	4.07×10^{-7}	0.26×10^{-7}	0.45×10^{-7}
3.870	2.42×10^{-7}	0.19×10^{-7}	0.27×10^{-7}
4.121	1.59×10^{-7}	0.15×10^{-7}	0.18×10^{-7}
4.371	1.07×10^{-7}	0.11×10^{-7}	0.12×10^{-7}
4.621	8.02×10^{-8}	1.11×10^{-8}	0.89×10^{-8}
4.871	5.38×10^{-8}	0.71×10^{-8}	0.60×10^{-8}

The measured cross section of heavy flavor electrons is shown in Fig. 4.11 and tabulated in Table 4.2. A correction for bin width [110] is applied to the p_T value of each point. The figure also shows the previously published result [28]. The new result excellently agrees with the previous result within the uncertainties.

Note that in this paper we employed a new analysis method with the HBD whereas the previous measurement employed different methods, the cocktail method and the converter method. The consistency of the measured cross sections between these measurements means that we succeeded to confirm the reliability of the new analysis method. In addition, we also confirmed that the additional photonic backgrounds generated in the HBD material are enough removed to measure the heavy flavor electrons.

The electron cross section from $J/\psi \rightarrow e^+ + e^-$ decays estimated by the cocktail method [29] and a fixed order next-to-leading log (FONLL) pQCD calculation of the heavy flavor contributions to the electron spectrum [111] are also shown in Fig. 4.11. The J/ψ contribution to the heavy flavor electrons is less than 2% in $p_T < 1.25$ GeV/c and increase to ~20% until $p_T = 5.0$ GeV/c. The FONLL pQCD calculation shows that the heavy flavor electrons in the low momentum region are dominated by charm quark decays, and the contribution from bottom quarks in $p_T < 1.25$ GeV/c is less than 5%.

Table 4.3: Relative systematic uncertainties on the cross section due to uncertainties in the total sampled luminosity, trigger efficiencies, and detector acceptance. These systematic uncertainties are globally correlated in all p_T regions except $p_T < 1.25$ GeV/c for the uncertainties on $\epsilon_{\rm trig}^{e|{\rm MB}}$.

source	uncertainty	p_T range (GeV/c)
MB trig. cross sect.	9.6%	
acceptance A	8%	
reco. efficiency $\epsilon_{\rm rec}$	6%	
MB trig. efficiency $\epsilon_{\rm trig}^{\rm MB}$	2.5%	
e trig. efficiency $\epsilon_{\rm trig}^{e\|{\rm MB}}$	$\sim$ 4%	$0.50 < p_T < 1.25$
	3.6%	$1.25 < p_T$

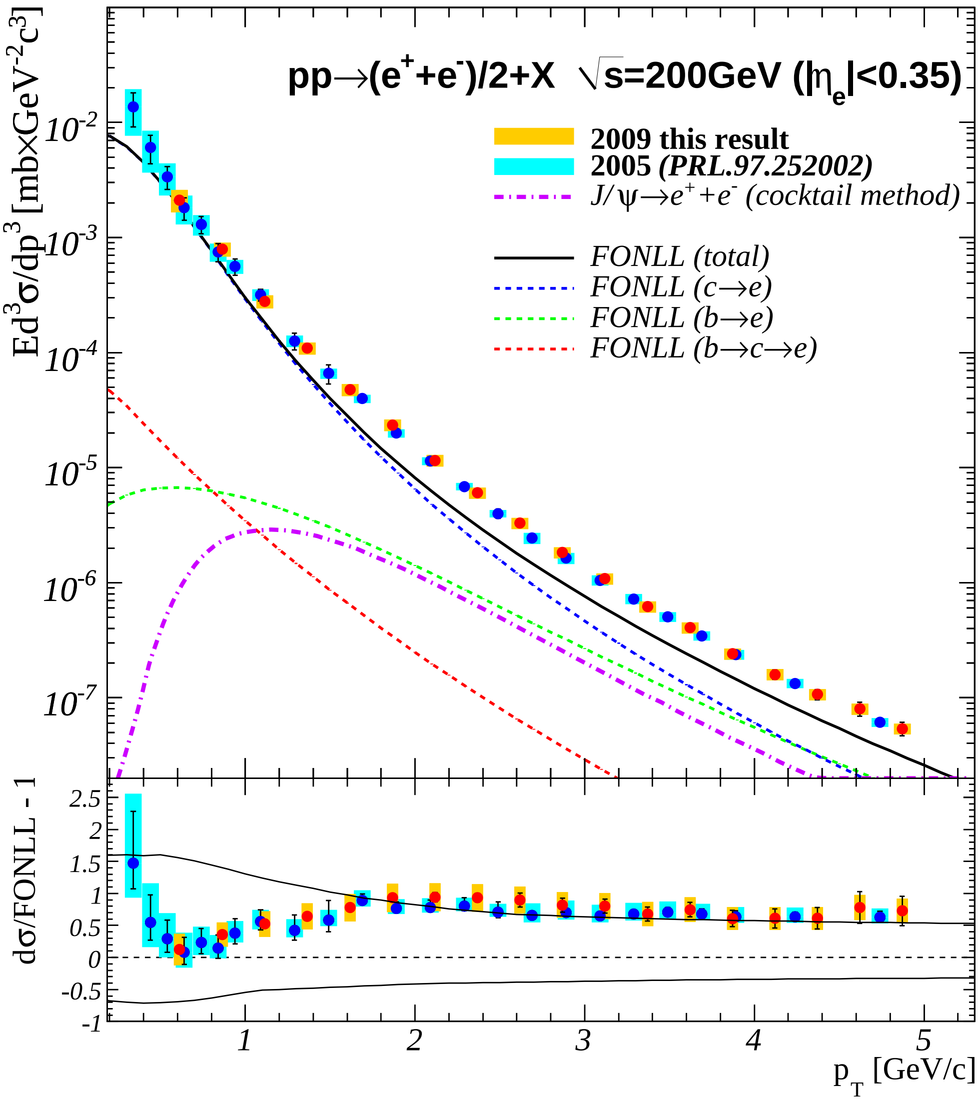

Figure 4.11: (top) Invariant differential cross sections of electrons from heavy-flavor decays. The red and the blue circles represent this analysis result and the previous result, respectively. The error bars and bands represent the statistical and systematic errors. The scaling uncertainty from the van-der-Merr scan is not included in the systematic error bands because the same uncertainty must be considered for both the results of 2009 and 2005. The purple dashed dotted line is electron cross section from $J/\psi \rightarrow e^+ + e^-$ decays estimated from the cocktail method [29]. The solid and dashed curves are the FONLL calculations. (bottom) Difference of the ratio of the data and the FONLL calculation from 1. The upper and lower curve shows the theoretical upper and lower limit of the FONLL calculation.

4.3 Spin Asymmetry of Heavy Flavor Electron

4.3.1 Beam polarization

For determination of spin asymmetry, beam polarization during the run is to be known. Fill-by-fill beam polarization is provided by the H-jet polarimeter and pC polarimeter located at IP12 as described in Appendix B. The measured beam polarization at $\sqrt{s} =$ 200 GeV collisions is shown in Fig. 4.12 [112]. During this experiment, the average beam polarizations for the Blue and Yellow beams are $P_B \sim 56\%$ and $P_Y \sim 57\%$, respectively.

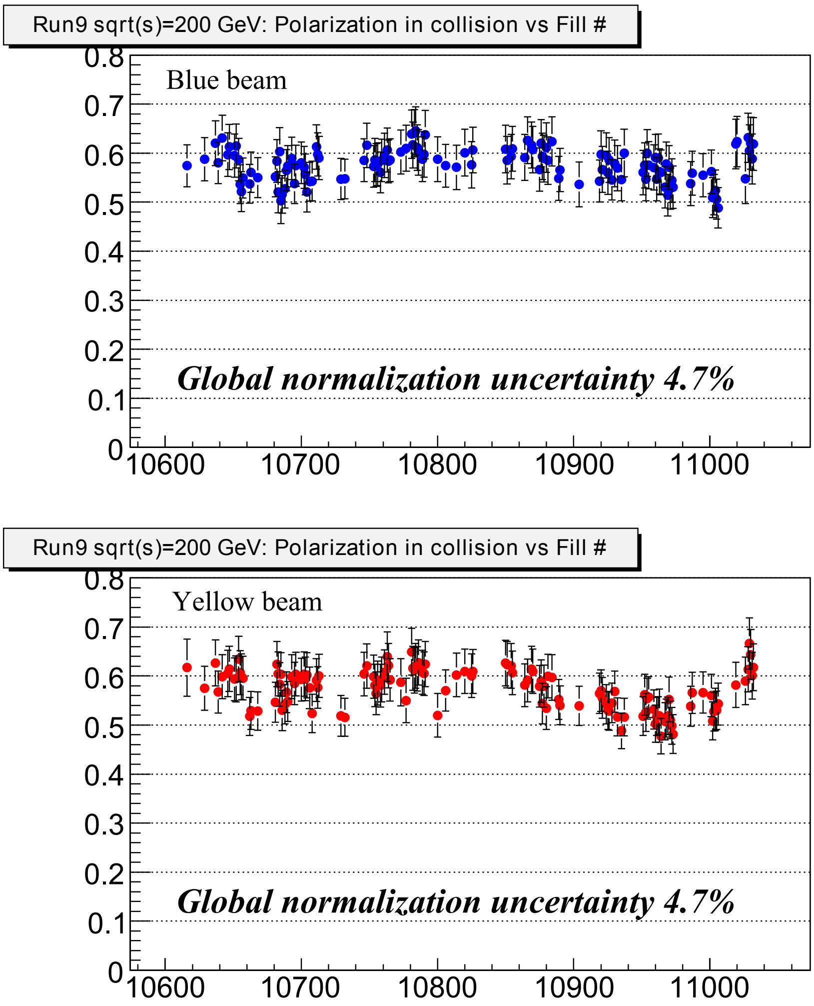

Figure 4.12: Fill-by-fill beam polarization for the Blue and Yellow beams during the 2009 $\sqrt{s} = 200$ GeV run. The top (bottom) plot corresponds to the Blue (Yellow) beam. The horizontal axis represents the fill number.

The uncertainty from the beam polarization measurement propagates into the uncertainty of resulting spin asymmetry. In this double-spin asymmetry measurement, the uncertainty on the product of the two polarization, $P_B P_Y$, propagates. This uncertainty comes from uncertainty on the normalization between the H-jet and pC measurement, time dependent inconsistency between the polarization results of the two pC polarimeters, and uncertainty on spatial profile of beam polarization. The estimated uncertainty is

$$\frac{\Delta(P_B P_Y)}{P_B P_Y} = 8.8\%. \tag{4.4}$$

4.3.2 Spin asymmetry calculation

Since parity is conserved in QCD processes, thereby finite single spin asymmetries of the QCD processes are disallowed. Therefore, using Eq. 1.39 we express the expected electron yields for each beam-helicity combination as

$$\begin{aligned} N^{\mathrm{exp}}_{++}(N_0, A_{LL}) &= N_0(1 + |P_{\mathrm{B}}P_{\mathrm{Y}}|A_{LL}) \\ N^{\mathrm{exp}}_{--}(N_0, A_{LL}) &= N_0(1 + |P_{\mathrm{B}}P_{\mathrm{Y}}|A_{LL})/r_{--} \\ N^{\mathrm{exp}}_{+-}(N_0, A_{LL}) &= N_0(1 - |P_{\mathrm{B}}P_{\mathrm{Y}}|A_{LL})/r_{+-} \\ N^{\mathrm{exp}}_{-+}(N_0, A_{LL}) &= N_0(1 - |P_{\mathrm{B}}P_{\mathrm{Y}}|A_{LL})/r_{-+}, \end{aligned} \tag{4.5}$$

where $N^{\mathrm{exp}}_{\pm\pm}(N_0, A_{LL})$ denote the expected yields for collisions between the blue beam-helicity ($\pm$) and the yellow beam-helicity ($\pm$) and N_0 is the expected yield in collisions of unpolarized beams under the same integrated luminosity as the ++ beam-helicity combination. $N^{\mathrm{exp}}_{\pm\pm}(N_0, A_{LL})$ are used for fitting functions to estimate A_{LL} as described below. P_{B} and P_{Y} represent the polarization of the beams. The relative luminosity is defined as the ratio of the luminosity in the beam-helicity combinations,

$$(\ r_{++} \equiv 1\ ) \tag{4.6}$$

$$r_{--} \equiv \frac{L_{++}}{L_{--}} \tag{4.7}$$

$$r_{+-} \equiv \frac{L_{++}}{L_{+-}} \tag{4.8}$$

$$r_{-+} \equiv \frac{L_{++}}{L_{-+}}, \tag{4.9}$$

where $L_{\pm\pm}$ represent the integrated luminosity in the beam-helicity combinations shown by the subscript. The relative luminosity is determined by the ratios of MB trigger counts in the four beam-helicity combinations. The number of the MB trigger counts is enough larger than the number of the detected electrons such that the statistical uncertainties of the $r_{\pm\pm}$ are negligibly small compared with the statistical uncertainties of the electron yield.

As discussed in Sec. 1.3.3, the following effect can create a bunch-dependent efficiency which produces an effective spin asymmetry:

bunch-by-bunch difference of length of beam bunch

The length of beam bunch along the beam axis varies bunch-by-bunch, and the Gaussian width of the track vertex distribution varies from ~ 56 cm to ~ 57 cm in the present analysis. In addition, reconstruction efficiencies of tracks from different z_{vtx} are also different. Therefore, these effects create a bunch-dependence of the reconstruction efficiency.

readout electronics specific

> Due to a readout feature of the EMCal front-end electronics, the thresholds for EMCal signals in even-number and odd-number beam crossings are not exactly same. This feature can create bias on the yield of electrons in a specific beam-helicity combination, which is critical for the spin asymmetry measurement.

The first effect is estimated by using a toy Monte Carlo calculation. The z_{vtx} dependence of the reconstruction efficiency obtained with a GEANT3 simulation was used for the calculation. As the result, the effect was found to be $A_{LL}^{\text{effective}} \sim 5\times10^{-5}$ and negligibly small in this analysis. To take account of the second effect, the even crossing data and the odd crossing data were analyzed separately. The two separated results were merged with weighted mean as explained in the following description.

The double-spin asymmetry for inclusive electrons after applying eID-Cut and npe-Cut, which include not only the heavy flavor electrons (S) but also the background electrons (BG), is determined by simultaneously fitting the yields of electrons in each of the four beam-helicity combinations with the expected values $N_{\pm\pm}^{\text{exp}}(N_0, A_{LL})$ from Eq. 4.5, where A_{LL} and N_0 are free parameters. To perform the fit, a log likelihood method assuming Poisson distributions with expected values of $N_{\pm\pm}^{\text{exp}}(N_0, A_{LL})$ (Eq. 4.5) was employed.

The fit was performed for electron yields in each fill to obtain the fill-by-fill double-spin asymmetry. Due to the EMCal readout feature, the fitting was performed for the even crossing data and odd crossing data separately, and the results were merged to obtain the final A_{LL} value. Examples of the raw yields and the fitting result at a specific fill are shown in Fig. 4.13(a). The horizontal axis of the plots corresponds to four beam-helicity combinations, $++$, $--$, $+-$, and $-+$ from left to right, and the vertical axis corresponds to measured $N_{\pm\pm}r_{\pm\pm}$ at each beam-helicity combination. The plot corresponds to electrons with transverse momentum ranging $0.75 < p_T < 1.00$ GeV/c. The red dashed lines represent the fitting results of $N_{\pm\pm}^{\text{exp}}(N_0, A_{LL})r_{\pm\pm}$ according to Eq. 4.5, and therefore the results for $++$ and $--$, and for $+-$ and $-+$ are same. To confirm the fitting quality for all fills, reduced-χ^2 (χ^2/NDF) was calculated by setting statistical uncertainty to be $\sqrt{N_{\pm\pm}}r_{\pm\pm}$. The fill-by-fill reduced-χ^2 for electrons with $0.75 < p_T < 1.00$ GeV/c is plotted in Fig. 4.13(b). The vertical axis is the reduced-χ^2 and the horizontal axis is fill number. In this figure, the red line represents $\chi^2/NDF = 1$. It is confirmed there is no significant fill dependence in reduced-χ^2. To check the reduced-χ^2 distribution, the points were projected the vertical axis. Figure 4.13(c) shows the reduced-χ^2 distributions, which are obtained by the projections of Fig. 4.13(b). The distributions should be consistent with the χ^2 distribution of $NDF = 2$ ($\propto \exp(-x/2)$), because the number of the input parameters is four ($N_{\pm\pm}$) and the number of the fitting parameters is two (N_0 and A_{LL}). The $\exp(-x/2)$ distributions fitted to the obtained reduced-χ^2 distributions is also plotted. The resulting A_{LL} of electrons with $0.75 < p_T < 1.00$ GeV/c is plotted in Fig. 4.13(d). It is confirmed that all asymmetries in different fills are consistent with each other within their statistical uncertainties. The double-spin asymmetries from the whole even or odd crossing data with fitting to the fill-by-fill asymmetry result were obtained as shown in Fig. 4.13(d) as a red line. The resulting double-spin asymmetries of even and odd crossing data are listed in Table 4.4. The asymmetries of even and odd crossing data are consistent

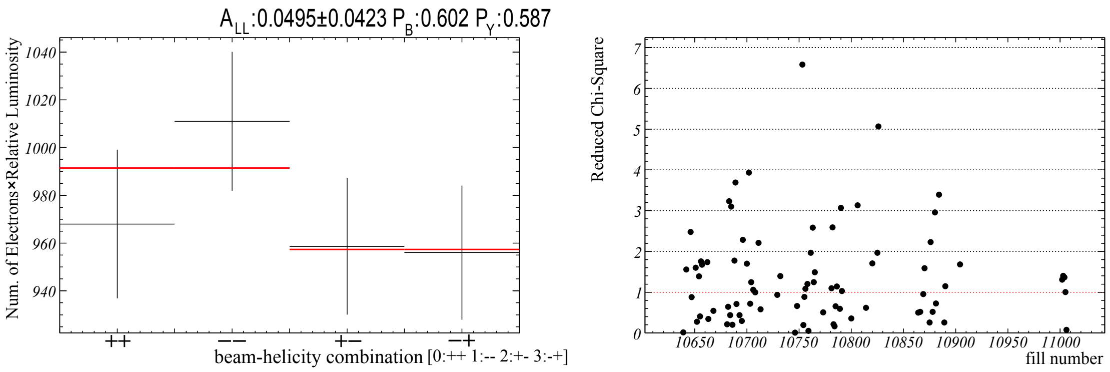

(a) Electron yield at a specific fill

(b) Reduced-χ^2 vs. fill number

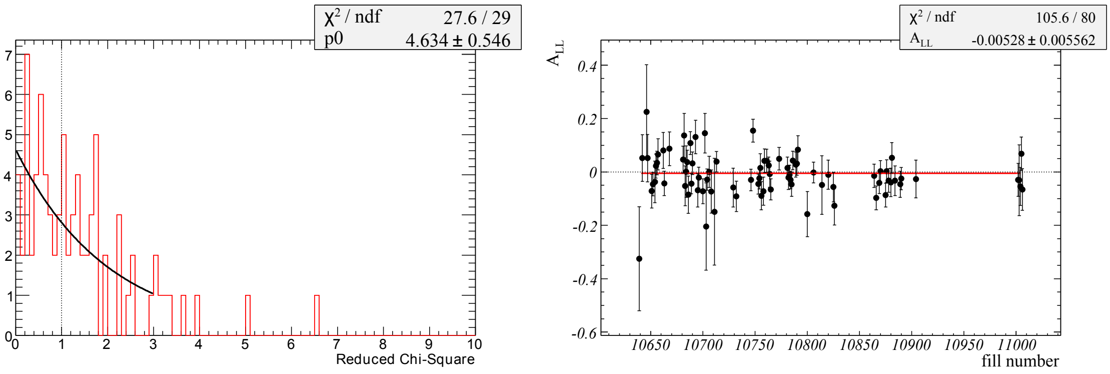

(c) Reduced-χ^2

(d) Fill-by-fill A_{LL} result

Figure 4.13: (a) An example of the electron yields for even crossing data at a specific fill. The four horizontal bins correspond to four beam-helicity combinations of $++$, $--$, $+-$, and $-+$ from left to right, respectively. The vertical axis is the electron yield normalized by the relative luminosity in each beam-helicity combination, $N_{\pm\pm}r_{\pm\pm}$. The red lines represent the A_{LL} fitting results according to Eq. 4.5. (b) Reduced-χ^2 for the A_{LL} fitting as a function of fill number (even crossing). The red line represents $\chi^2/NDF = 1$. (c) Projection of the reduced-χ^2 values for the A_{LL} fitting. (even crossing) The red curve in the plot shows the χ^2/NDF distribution where $NDF = 2$ ($\propto \exp(-x/2)$). The dashed vertical line represents the position of $\chi^2/NDF = 1$. (d) Fill-by-fill asymmetry results for even crossing data (points) and pol0 fitting (red line) for the fill-by-fill asymmetry results. The horizontal dashed line represents $A_{LL}^{S+BG} = 0$. All these four plots are results of electrons with transverse momentum ranging $0.75 < p_T < 1.00$ GeV/c.

each other. The final double-spin asymmetry for inclusive electrons, $A_{LL}^{\mathrm{S+BG}}(p_T)$, was calculated as the weighted mean of these even-crossing and odd-crossing asymmetries.

4.3.3 Background spin asymmetry

The double-spin asymmetry in the heavy flavor electron production, A_{LL}^{HFe}, was determined from

$$A_{LL}^{\mathrm{HFe}}(p_T) = \frac{1}{D(p_T)} A_{LL}^{\mathrm{S+BG}}(p_T) - \frac{1 - D(p_T)}{D(p_T)} A_{LL}^{\mathrm{BG}}(p_T) \tag{4.10}$$

Table 4.4: Table of the obtained double-spin asymmetries of inclusive electrons from even and odd crossing data.

p_T region (GeV/c)	even A_{LL}^{S+BG} ($\times 10^{-2}$)	odd A_{LL}^{S+BG} ($\times 10^{-2}$)
$0.50 < p_T < 0.75$	1.0 ± 0.6	-0.1 ± 0.7
$0.75 < p_T < 1.00$	-0.5 ± 0.6	-0.3 ± 0.6
$1.00 < p_T < 1.25$	1.0 ± 0.8	-0.5 ± 0.8
$1.25 < p_T < 1.50$	0.5 ± 1.1	1.5 ± 1.1
$1.50 < p_T < 1.75$	2.1 ± 1.6	-3.0 ± 1.7
$1.75 < p_T < 2.00$	-1.6 ± 2.3	-0.0 ± 2.3
$2.00 < p_T < 2.25$	2.1 ± 3.1	4.1 ± 3.2
$2.25 < p_T < 2.50$	-1.9 ± 4.3	-6.2 ± 4.3
$2.50 < p_T < 2.75$	-6.6 ± 5.5	-3.3 ± 5.7
$2.75 < p_T < 3.00$	-1.6 ± 7.1	11.4 ± 7.3

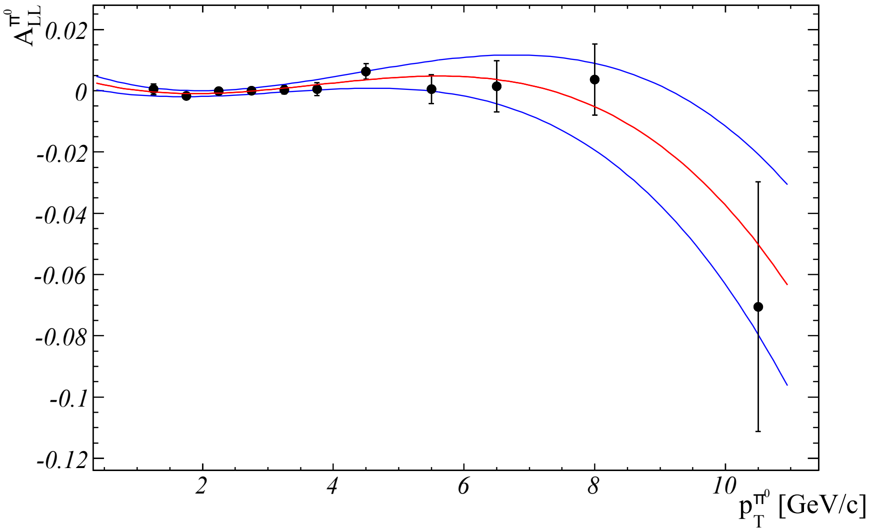

Figure 4.14: Measured π^0 double-spin asymmetry with same 2009 experiment of $\sqrt{s} =$ 200 GeV pp collision. The red curve is a cubic function fitted to $A_{LL}^{\pi^0}$. The two blue curves are also cubic functions fitted to shifted $A_{LL}^{\pi^0}$ by the uncertainties to plus and minus directions.

where A_{LL}^{BG} represents the spin asymmetries for the background electron production, and D represents the signal purity defined in Eq. 4.2 and shown in Fig. 4.3. As previously discussed, most of the background electrons come from Dalitz decays of the π^0 and η, or from conversions of photons from decays of those hadrons. The production mechanism for the π^0 and η is expected to be very similar up to $\sim$ 10 GeV/c [11, 14]. Therefore, we assume identical spectra for double-spin asymmetries of π^0 production and η production, and estimated A_{LL}^{BG} from only the π^0 double-spin asymmetry measured in this PHENIX

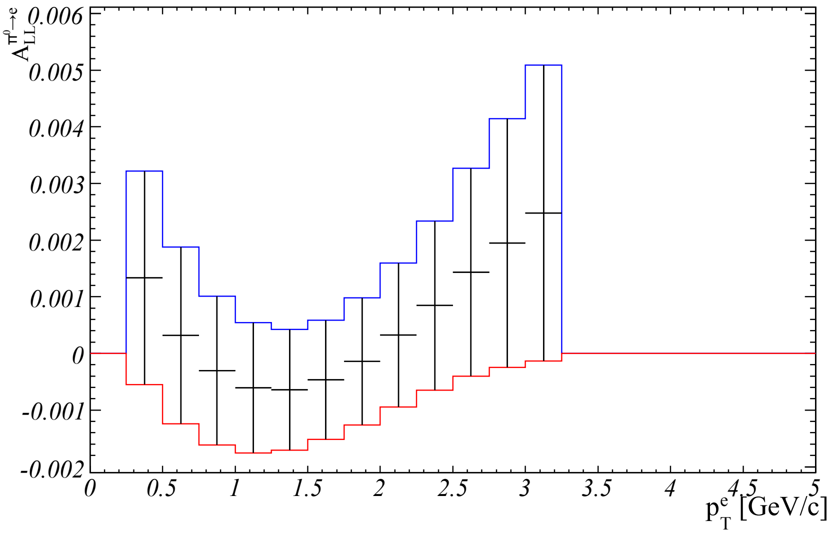

Figure 4.15: Convolution performed with the π^0 spectrum and the $A_{LL}^{\pi}(p_T^{\pi})$ for each p_T^e region. The points are the result of the convolution with the red curve in Fig. 4.14 and the blue and the red lines in this plot are the results of the convolutions with the upper and the lower blue curves in Fig. 4.14. The uncertainties of the background asymmetry are defined with the differences between the blue points and the black points, $\Delta_h(p_T^e)$, and the differences between the red points and the black points, $\Delta_l(p_T^e)$, as $\sqrt{|\Delta_h(p_T^e)\Delta_l(p_T^e)|}$.

run [73].

For $A_{LL}^{\pi^0}(p_T^{\pi^0})$ input, a result in 2009 experiment of $\sqrt{s} = 200$ GeV pp collision was used, which is shown in Fig. 4.14 [73]. To obtain the spectrum, the data are fitted with a cubic function. The fitting result is shown with the red curve in Fig. 4.14. Two curves are upper and lower uncertainty of the spectrum shape estimated by the fitting with shifted $A_{LL}^{\pi^0}$ by the uncertainties to upper and lower directions. Expected A_{LL}^{BG} from the $A_{LL}^{\pi^0}$ spectrum is simulated using a toy Monte Carlo reproducing π^0 Dalitz decay. The obtained asymmetry A_{LL}^{BG} is shown in Fig. 4.15. The points in Fig. 4.15 are the result of the convolution with the red curve in Fig. 4.14 and the blue and the red points in Fig. 4.15 are the results of the convolutions with the upper and the lower blue curves in Fig. 4.14. The resulting A_{LL}^{BG} is $-0.1 \times 10^{-2} < A_{LL}^{\mathrm{BG}} < 0.1 \times 10^{-2}$ in $0.5 < p_T < 2.5$ GeV/c and $0.1 \times 10^{-2} < A_{LL}^{\mathrm{BG}} < 0.2 \times 10^{-2}$ in $2.5 < p_T < 3.0$ GeV/c, with uncertainties less than 0.2×10^{-2}. The background asymmetry is subtracted from the inclusive electron A_{LL}^{S+BG} according to Eq. 4.10.

Transverse polarization effect

A transverse double-spin asymmetry A_{TT}, which is defined by the same formula as Eq. 1.2 for the transverse polarization, can contribute to A_{LL} through the residual transverse components of the beam polarization. The product of the transverse components of the beam polarization was measured to be $\sim 10^{-2}$ in this run. For π^0

production, the A_{TT} is expected to be $\sim 10^{-4}$ based on an NLO QCD calculation [113]. If we assume the transverse asymmetries of π^0 and heavy flavor electrons are comparable, we arrive at the value of $A_{LL} \sim 10^{-6}$. This value is quite negligible compared with the precision of the A_{LL}^{S+BG} measurement of $\sim 10^{-3}$.

4.3.4 Helicity pattern dependence

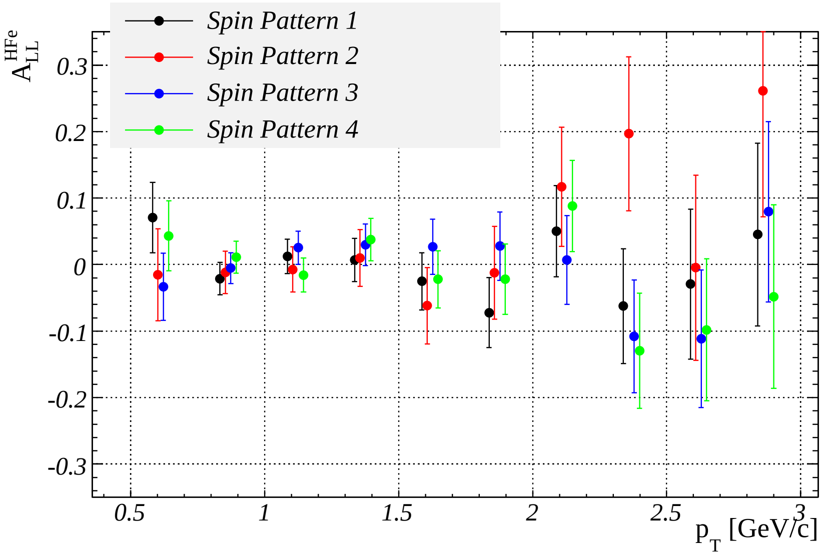

Figure 4.16: Comparison of the resulting A_{LL}^{HFe} from fills with each spin patterns. The black, red, blue, and green points represent spin patterns of $P1$, $P2$, $P3$, and $P4$, respectively.

As described in Sec. 2.1, there are four beam-helicity patterns in order to confirm no beam-helicity-pattern dependence is present. The beam-helicity-pattern dependence is produced by any correlations between raw yields in different bunches. For the confirmation that there is no such correlations, we need to check consistency between A_{LL}^{HFe}'s obtained from different beam-helicity pattern fills to confirm that there is not any effects from previous bunch, which make the measured asymmetry values incorrect. The A_{LL}^{HFe} for the four patterns are shown in Fig. 4.16. The deviations between these asymmetries are within their statistical uncertainties and we concluded there is no such effect.

4.3.5 Spin asymmetry of heavy flavor electron

Systematic uncertainties on A_{LL}^{HFe} are separated into scaling uncertainties and offset uncertainties. The scaling uncertainties come from uncertainty in the beam polarization, P_B and P_Y, and the signal purity, D. The uncertainty from the beam polarization is estimated as $\Delta(P_B P_Y)/P_B P_Y = 8.8\%$ which is globally correlated over the whole p_T range. The offset uncertainties come from uncertainties in the relative luminosity, r, and the background asymmetry, A_{LL}^{BG}. The uncertainty in the relative luminosity is

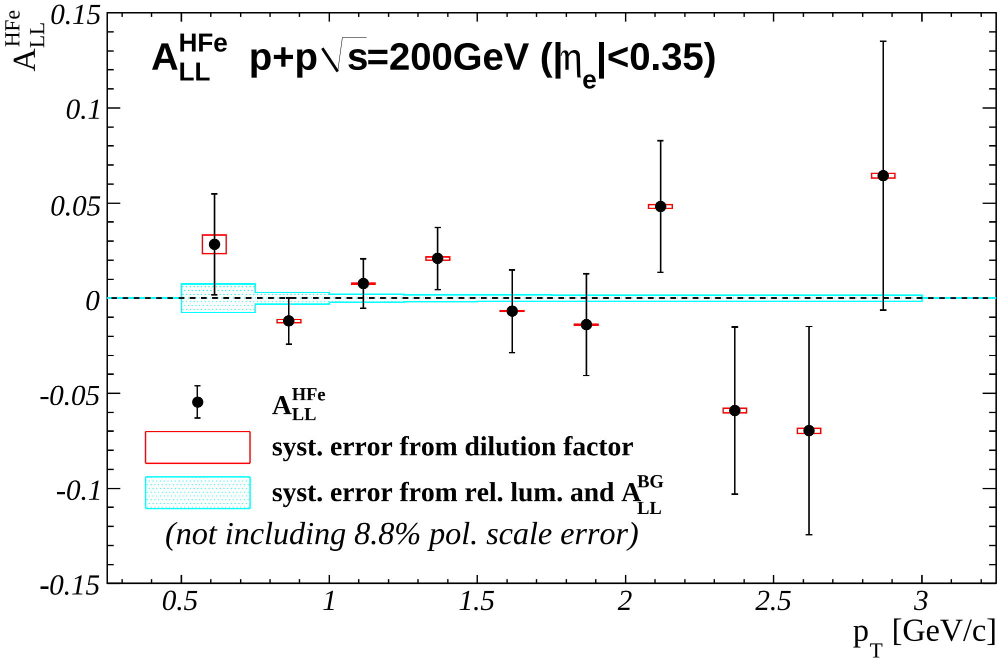

Figure 4.17: Double-spin asymmetry of the heavy flavor electron production. The red error bars represent scaling systematic uncertainties from the dilution factor and the blue error bands represent offset systematic uncertainties from relative luminosity and the background spin asymmetry.

globally correlated, and is estimated by comparing the relative luminosity measured by the MB and ZDC triggers. This uncertainty is determined to be $\Delta r = 1.4 \times 10^{-3}$. The systematic uncertainties are summarized in Table 4.5.

The result of the double-spin asymmetry of heavy flavor electrons is shown in Fig. 4.17 and tabulated in Table 4.6. We show systematic uncertainties for scaling and offset separately in the figure. The measured asymmetry is consistent with zero.

Table 4.5: Systematic uncertainties and the types of the uncertainties. The scaling uncertainty denotes an uncertainty on scaling of the raw asymmetry $A_{LL}^{\rm S+BG}$ and the offset uncertainty denotes an uncertainty on the absolute value of the asymmetry. The "global" in this table means the uncertainties are globally correlated in all p_T regions. The scaling uncertainty is represented as the ratio of the uncertainty to the signal ($\Delta S/S$) given in percent and the offset uncertainty is represented as the absolute value of the uncertainty.

source	uncertainty	type
signal purity D	$\sim 6\%$	scaling
polarization ($\frac{\Delta(P_B P_Y)}{P_B P_Y}$)	8.8%	global scaling
relative luminosity R	0.14×10^{-2}	global offset
background asymm. A_{LL}^{BG}	$0.2 \times 10^{-2} \times \frac{1-D}{D}$	offset

Table 4.6: Data table for the $A_{LL}^{\rm HF\ e}$ result corresponding to Fig. 4.17.

p_T[GeV/c]	$A_{LL}^{\rm HF\ e}$	stat. error	syst. error (offset)	syst. error (scale)
0.612	2.83×10^{-2}	2.66×10^{-2}	0.75×10^{-2}	0.50×10^{-2}
0.864	-1.20×10^{-2}	1.21×10^{-2}	0.30×10^{-2}	0.08×10^{-2}
1.115	0.76×10^{-2}	1.30×10^{-2}	0.21×10^{-2}	0.04×10^{-2}
1.366	2.08×10^{-2}	1.63×10^{-2}	0.18×10^{-2}	0.10×10^{-2}
1.617	-0.69×10^{-2}	2.18×10^{-2}	0.17×10^{-2}	0.03×10^{-2}
1.867	-1.39×10^{-2}	2.68×10^{-2}	0.16×10^{-2}	0.03×10^{-2}
2.118	4.82×10^{-2}	3.46×10^{-2}	0.16×10^{-2}	0.09×10^{-2}
2.369	-5.91×10^{-2}	4.40×10^{-2}	0.16×10^{-2}	0.11×10^{-2}
2.619	-6.97×10^{-2}	5.47×10^{-2}	0.16×10^{-2}	0.13×10^{-2}
2.869	6.43×10^{-2}	7.07×10^{-2}	0.16×10^{-2}	0.12×10^{-2}

Chapter 5

Discussion

5.1 Constraint on $\Delta g(x)$

In this section, we discuss constraint of Δg from the measured double-spin asymmetry. In p+p collisions at $\sqrt{s} = 200$ GeV, heavy flavor electrons with momentum ranging $0.50 < p_T < 1.25$ GeV/c are mainly produced by open charm events. Open charm production is well described by pQCD calculations, which can be factorized into charm quark production at the partonic level and fragmentation of the charm quarks into charmed hadrons. Using polarized and unpolarized parton distribution functions (PDFs), the respective cross sections for charm quark production are estimated. PYTHIA8 [76, 77] simulations are then used to model the fragmentation and semi-leptonic decay processes. The spin asymmetry A_{LL}^{HFe} is the ratio of the polarized and unpolarized cross sections, and a comparison between the measured and calculated values of A_{LL}^{HFe} can thereby provide constraints on the gluon polarization Δg.

For this discussion, we calculated the charm quark cross section in the partonic level using an LO pQCD calculation [25]. In LO pQCD calculations, only $gg \to c\bar{c}$ and $q\bar{q} \to c\bar{c}$ are allowed for the open charm production. The charm quarks are primarily created by the gg interaction in the unpolarized hard scattering, and the $q\bar{q}$ contribution is known to be just a few percent in this momentum region [24]. In addition, the anti-quark polarizations are known to be small from semi-inclusive DIS measurements precisely enough that both DSSV [23] and GRSV [74] expect contribution of polarized $q\bar{q}$ cross section to the double-spin asymmetry of the heavy flavor electrons in $|\eta| < 0.35$ and $p_T < 3.0$ GeV/c to be $\sim 10^{-4}$ [24], which is much smaller than the accuracy of this measurement. Therefore, in this analysis of Δg, we ignore the $q\bar{q}$ interaction and assume the asymmetries are due only to the gg interaction. Under the assumption, the spin asymmetry of the heavy flavor electrons is expected to be approximately proportional to the square of polarized gluon distribution normalized by unpolarized distribution, $|\Delta g/g(x, \mu)|^2$.

To calculate the cross section of the $gg \to c\bar{c}$ process, CTEQ6M [48] was employed for the unpolarized PDF. For the polarized PDF, we assumed $|\Delta g(x, \mu)| = Cg(x, \mu)$ where C is a constant. The charm quark mass was assumed as $m_c = 1.4$ GeV/c^2 and the factorization scale in CTEQ6 and the renormalization scale were assumed to be identical to $\mu = m_T^c \equiv \sqrt{{p_T^c}^2 + {m_c}^2}$. The resulting cross sections for a case of $C = 0.5$

are shown in Fig. 5.1. Figure 5.1(a) shows the unpolarized cross section, $\sigma^{pp\to c\bar{c}}(p_T^c, \eta^c)$, and Figure 5.1(b) shows the polarized cross section, $\Delta\sigma^{pp\to c\bar{c}}(p_T^c, \eta^c)$, and Figure 5.1(c) shows the asymmetry of the cross section, $a_{LL}^{pp\to c\bar{c}}(p_T^c, \eta^c) \equiv \Delta\sigma^{pp\to c\bar{c}}/\sigma^{pp\to c\bar{c}}(p_T^c, \eta^c)$.

The fragmentation and decay processes were simulated with PYTHIA simulation. We generated $pp \to c\bar{c} + X$ events and selected electrons from the charmed hadrons, D^+, D^0, D_s, Λ_c and their antiparticles. We scaled the charm quark yield in PYTHIA with respect to the pQCD calculated unpolarized and polarized cross sections to obtain unpolarized and polarized electron yields from charmed hadron decays under these cross sections. We also applied a pseudorapidity cut of $|\eta| < 0.35$ for the electrons to match the acceptance of the PHENIX central arms. The shape of the expected spin asymmetry $A_{LL}^{\mathrm{HFe}}(p_T)$ is then determined from the simulated electron yields.

Figure 5.2 shows the distribution of the gluon Bjorken x contributing to heavy flavor electron production in the momentum range $0.50 < p_T < 1.25$ GeV/c, from PYTHIA. Using the mean and the RMS of the distribution for $0.50 < p_T < 1.25$ GeV/c, we determine the mean x for heavy flavor electron production to be $\langle\log_{10} x\rangle = -1.6^{+0.5}_{-0.4}$.

We calculated expected $A_{LL}^{\mathrm{HFe}}(p_T)$ by varying $C = |\Delta g/g|$. Figure 5.3(a) shows several of these curves, along with the measured points. χ^2 values are calculated for each value of C, along with related uncertainties. By assuming that the systematic uncertainties on the points are correlated and represent global shifts, we defined the quantity $\hat{\chi}^2$ as

$$\begin{aligned}
\hat{\chi}^2(C) &\equiv -2\log\left((2\pi)^{\frac{n}{2}}\,\hat{P}(C)\right)\\
\hat{P}(C) &\equiv \textstyle\int dpdqN(p)N(q)\times\\
&\textstyle\prod_{i=1}^{n} N\left(\frac{\left(y_i + p\epsilon_{\mathrm{syst}}^{i\ \mathrm{offset}} - \left(1+q\gamma_{\mathrm{syst}}^{i\ \mathrm{scale}}\right)f(x_i;C)\right)}{\epsilon_{\mathrm{stat}}^{i}}\right)\\
\gamma_{\mathrm{syst}}^{i\ \mathrm{scale}} &= \sqrt{\left(\frac{\epsilon_{\mathrm{syst}}^{i\ \mathrm{scale}}}{y_i}\right)^2 + \left(\frac{\Delta(P_BP_Y)}{P_BP_Y}\right)^2},
\end{aligned}$$

where $N(X)$ denotes normal probability distribution, i.e. $N(X) = 1/\sqrt{2\pi}\exp(-X^2/2)$, n is the number of the data points and equal to three, and for the i-th data point, x_i is the p_T value, y_i is the A_{LL} value, and $\epsilon_{\mathrm{stat}}^{i}$, $\epsilon_{\mathrm{syst}}^{i\ \mathrm{offset}}$ and $\epsilon_{\mathrm{syst}}^{i\ \mathrm{scale}}$ represent the statistical, offset systematic and scaling systematic uncertainties, respectively. $f(p_T; C)$ denotes the expected $A_{LL}(p_T)$ for the parameter of $C = |\Delta g/g|$. $\Delta(P_BP_Y)$ is an uncertainty for polarization. If we set the systematic uncertainties, $\epsilon_{\mathrm{syst}}^{\mathrm{offset}}$ and $\gamma_{\mathrm{syst}}^{i\ \mathrm{scale}}$, to zero, the newly defined $\hat{\chi}^2$ is consistent with the conventional χ^2.

The resulting $\hat{\chi}^2$ curve is shown in Fig. 5.3(b), plotted as a function of $C^2 = |\Delta g/g|^2$ because the curvature becomes almost parabolic. The minimum of $\hat{\chi}^2$, $\hat{\chi}^2_{\mathrm{min}}$, is located at $|\Delta g/g|^2 = 0.0$ which is the boundary of $|\Delta g/g|^2$. $\Delta\hat{\chi}^2 \equiv \hat{\chi}^2 - \hat{\chi}^2_{\mathrm{min}} = 1$ and 9 were utilized to determine 1σ and 3σ uncertainties. With these criteria, we found the constraints on the gluon polarization are $|\Delta g/g(\langle\log_{10} x\rangle, \mu)|^2 < 3.0 \times 10^{-2}(1\sigma)$ and $10.0 \times 10^{-2}(3\sigma)$. The constraints are consistent with theoretical expectations for $\Delta g/g(x, \mu)$ at $\langle\log_{10} x\rangle = -1.6^{+0.5}_{-0.4}$ and $\mu = 1.4$ GeV which are ~ -0.006 from DSSV, ~ 0.016 from GRSV(std) and ~ 0.019 from GRSV(val) using CTEQ6 for the unpolarized PDF.

The effects of the charm quark mass and scale factor in the cross section calculation were also checked by varying the charm mass from $m_c = 1.3$ GeV/c^2 to 1.5 GeV/c^2 and the scale to $\mu^2 = 0.75{m_T^c}^2$ and $1.5{m_T^c}^2$. Figure 5.3(b) also shows the resulting $\hat{\chi}^2$ curves. Considering the variation of the crossing position at $\Delta\hat{\chi}^2 = 1$, the constraint including the uncertainties from the charm mass and the scale can be represented as $|\Delta g/g|^2 < (3.0^{+0.4}_{-0.2}(\text{mass})^{+0.5}_{-0.3}(\text{scale})) \times 10^{-2}(1\sigma)$. The square root of the constraint $|\Delta g/g|^2 < 3.0 \times 10^{-2}$ is plotted in Fig. 5.4 with other constraint of $\Delta g/g$ from SIDIS experiments. As Fig. 5.4 shows, this measurement covers the unexplored Bjorken x region and gives comparable constraint on $\Delta g/g$. It is worth to note that the present constraint on $\Delta g/g(x)$ is not exact 1σ deviation since it is square root of 1σ deviation of $|\Delta g/g(x)|^2$.

The integral of the CTEQ6 unpolarized PDF in the sensitive x region of $\langle \log_{10} x\rangle = -1.6^{+0.5}_{-0.4}$ and $\mu = 1.4$ GeV is $\int_{0.01}^{0.08} dx g(x,\mu) = 4.9$. Hence the constraint on the integral of the polarized PDF at 1σ corresponds to $|\int_{0.01}^{0.08} dx \Delta g(x,\mu)| < 0.85$. We can exclude large gluon polarization at the low Bjorken x region, $\Delta G[0.01, 0.08] \gtrsim 1$.

5.2 Future Prospect for $\Delta g(x)$ Measurement

The constraint on $\Delta g(x,\mu)$ obtained through this measurement is not enough to constrain $\Delta G(\mu)$ compared with the total proton spin 1/2. However, this study highlights the possibility for constraining $\Delta g(x,\mu)$ more precisely in the future with higher statistics and higher beam polarizations.

In addition, there are other future planned channels to investigate $\Delta g(x,\mu)$ in such small Bjorken x region. They are A_{LL} measurements of π^0 production at the PHENIX mid-rapidity region ($|\eta| < 0.35$) and the forward-rapidity region ($3.1 < |\eta| < 3.9$) in $\sqrt{s} = 510$ GeV $p + p$ collisions. The A_{LL} measurements at $\sqrt{s} = 510$ GeV are sensitive to $\Delta g(x,\mu)$ at smaller Bjorken x by a factor of about 2/5 compared with $\sqrt{s} = 200$ GeV. Especially the measurement at the forward-rapidity region can approach to rather small Bjorken x region. The sensitive Bjorken x regions for the measurements are shown in Fig. 1.18(c). These measurements will complement the heavy flavor electron measurement each other to constrain $\Delta g(x,\mu)$ at the small Bjorken x region.

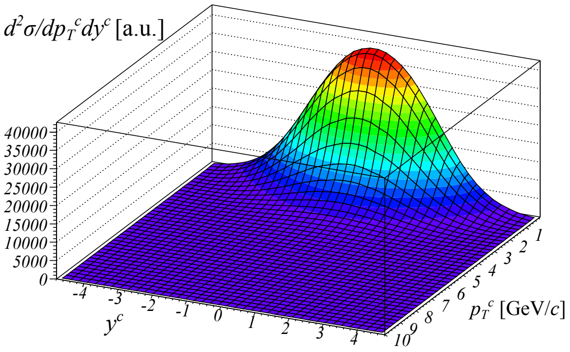

(a) Unpolarized cross section

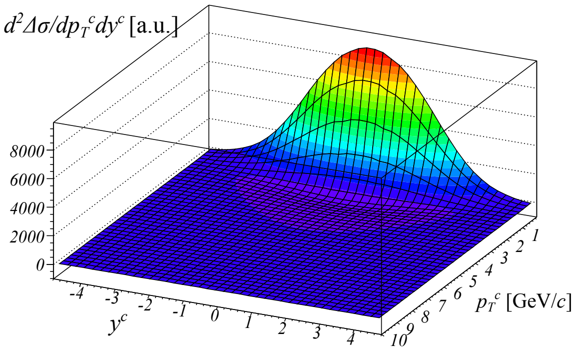

(b) Polarized cross section

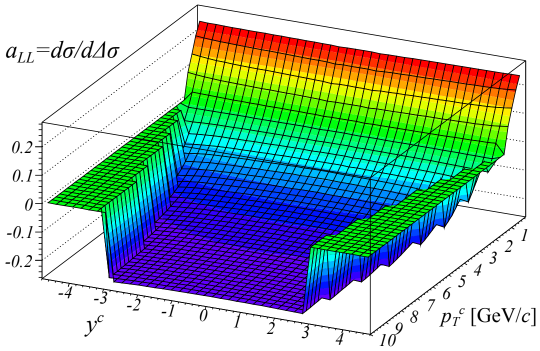

(c) Asymmetry ($a_{LL}{\equiv}d\sigma/d\Delta\sigma$)

Figure 5.1: (a) Unpolarized and (b) polarized cross section of the charm production as functions of charm transverse momentum p_T^c and charm rapidity y^c estimated by using a LO pQCD calculation [25]. In the calculation, CTEQ6M [48] was employed for the unpolarized parton distribution functions (PDF). For the polarized PDF, we assumed $|\Delta g(x,\mu)| = 0.5|g(x,\mu)|$. The charm mass was assumed as $m_c = 1.4$ GeV/c^2 and the scale factors for the factorization in CTEQ6 and the renormalization are assumed identical to $\mu = m_T^c \equiv \sqrt{{p_T^c}^2 + {m_c}^2}$. (c) Asymmetry of the cross section, $a_{LL}^{pp\to c\bar{c}}(p_T^c, y^c) \equiv \Delta\sigma^{pp\to c\bar{c}}/\sigma^{pp\to c\bar{c}}(p_T^c, y^c)$.

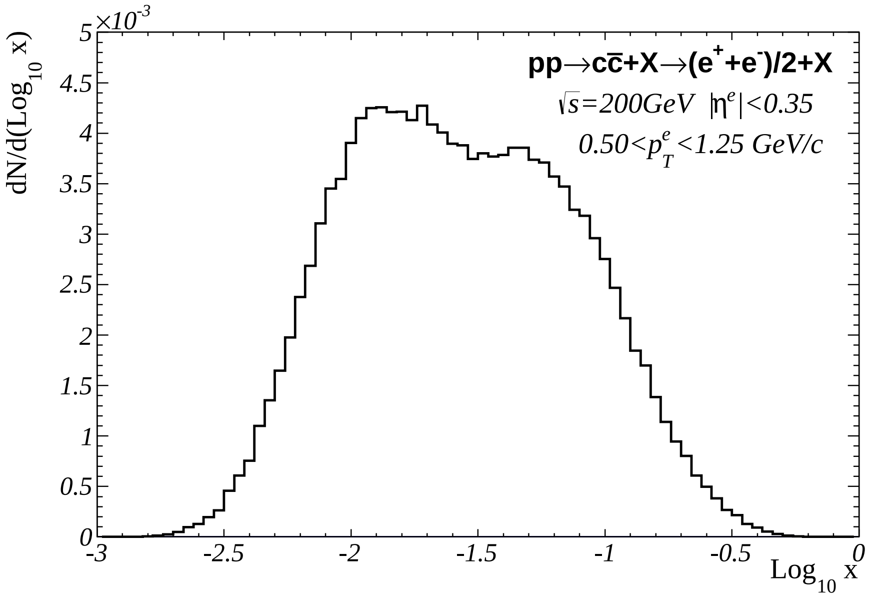

Figure 5.2: Bjorken x distribution of gluons contributing the heavy flavor electron production with momentum ranging $0.50 < p_T < 1.25$ GeV/c obtained from PYTHIA simulation. The distribution is normalized with respect to the number of total generated charmed hadrons.

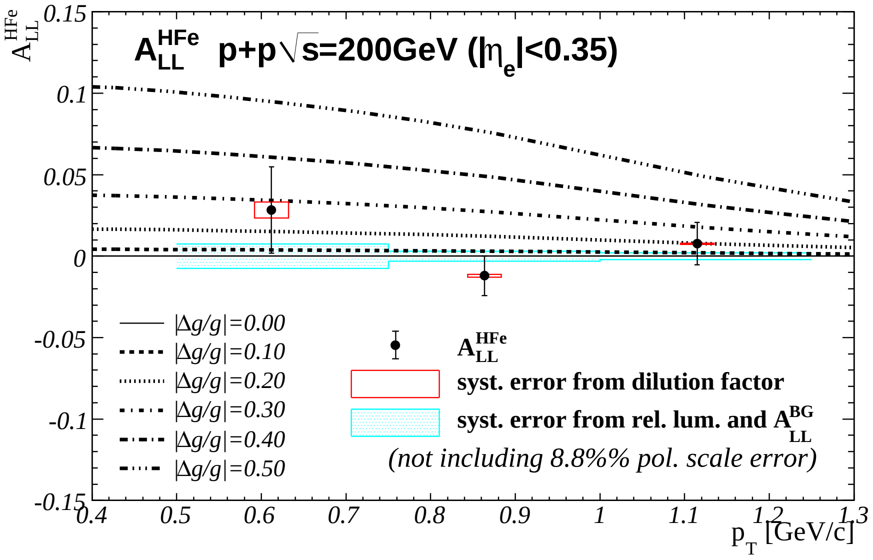

(a) Expected $A_{LL}^{\rm HFe}$ for several $|\Delta g/g|$.

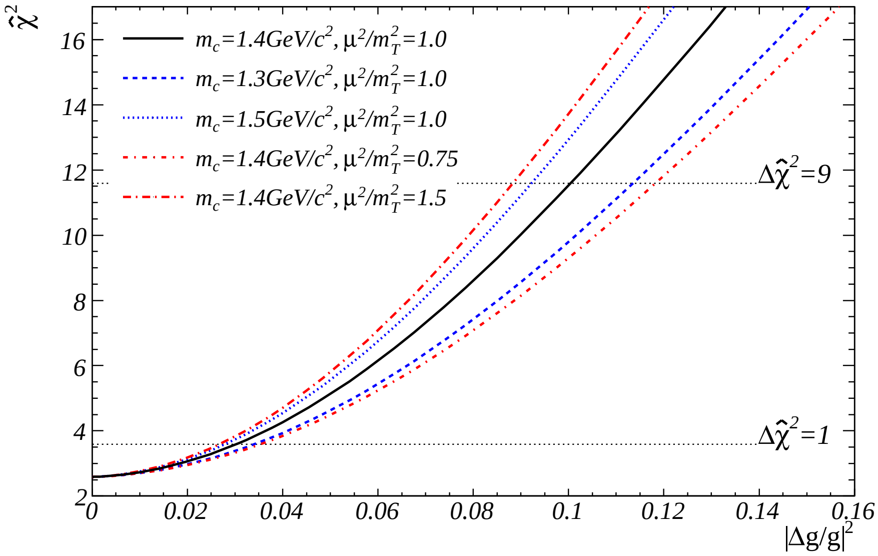

(b) $\hat{\chi}^2$ curves.

Figure 5.3: (a) $A_{LL}^{\rm HFe}$ for $|\Delta g/g| = 0.00, 0.10, 0.20, 0.30, 0.40, 0.50$ are shown as the solid line, the dashed line, the dotted line, the dashed dotted line, the long-dashed dotted line, the dashed triplicate-dotted line respectively. They are plotted with the measured data points and the notation for the error bars are same as Fig. 4.17. (b) $\hat{\chi}^2$ curves calculated from (a) as a function of $|\Delta g/g|^2$. The black solid line is the default configuration. The blue curves are after changing the charm mass to 1.3 GeV/c^2 (dashed line) and to 1.5 GeV/c^2 (dotted line) and the red curves are after changing the scale μ^2 to $0.75 {m_T^c}^2$ (dashed dotted line) and $1.5 {m_T^c}^2$ (long-dashed dotted line).

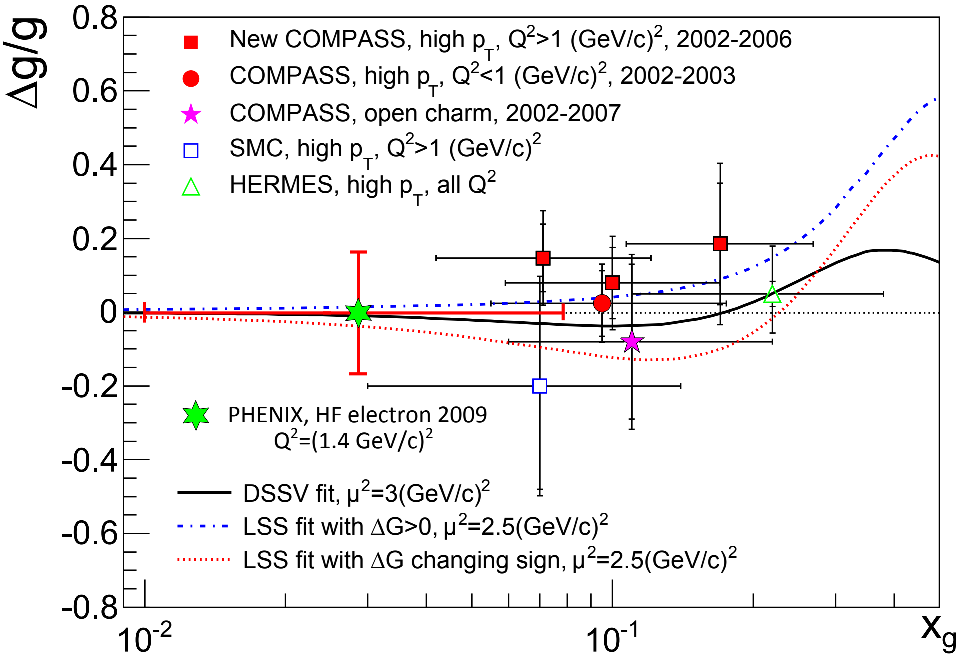

Figure 5.4: Constraint on $\Delta g/g(x)$ from this analysis, which is shown with green hexagonal star, on other constraints from SIDIS experiments shown in Fig. 1.13. The vertical error bar in our result corresponds to $|\Delta g/g(x)|^2 < 3.0 \times 10^{-2}$ (1σ), and therefore not 1σ deviation in $\Delta g/g(x)$.

Chapter 6

Conclusion

The measurement of the gluon polarization in small Bjorken x is essential to determine the total gluon polarization $G(\mu)$. Previously, achievable Bjorken x was limited up to the minimum of $2\times10^{-2} \lesssim x$ due to a minimum p_T required from pQCD calculations. To extend the Bjorken x region, the double spin asymmetry of the heavy flavor electron production is an ideal probe because enough energy scale in this production is guaranteed due to the large mass of the heavy quarks. In this work, we firstly measured the double spin asymmetry in the PHENIX experiment at RHIC (BNL) using $\sqrt{s} = 200$ GeV $p+p$ collisions, and obtained the constrain of the gluon polarization in the small Bjorken x region from the measured asymmetry.

The measurement of the heavy flavor electron production suffered large background of photonic electrons and K_{e3} electrons. In this work, we succeeded to significantly suppress the background with the new detector, HBD, and improved the signal purity by a factor of ~ 1.5 around $0.75 \lesssim p_T \lesssim 2.00$ GeV/c. Especially, the HBD also efficiently reduces the K_{e3} electrons by a factor of ~ 0.4, because the HBD requires the position of the K_{e3} decay to be close to the beam vertex, $R \sim 10$ cm. The double spin asymmetry of the K production is not well known, and therefore the reduction of the K_{e3} electrons is important to reduce uncertainty on the measurement of the spin asymmetry of heavy flavor electrons. We also succeeded to confirm the reliability of the new analysis method using the HBD by comparing the obtained cross section of the heavy flavor electron with the previous result.

We have reported on the first measurement of the longitudinal double-spin asymmetry of heavy flavor electrons, which are consistent with zero. Using this result, we obtained a constraint of $|\Delta g/g(\log_{10} x = -1.6^{+0.5}_{-0.4}, \mu = m_T^c)|^2 < 3.0 \times 10^{-2}(1\sigma)$. The result covers unexplored Bjorken x region in other $\Delta g(x, \mu)$ measurements and gives comparable constraint compared with results from SIDIS experiments. This constraint is consistent with the existing theoretical expectations with GRSV and DSSV.

With improved statistics and polarization, the helicity asymmetry of heavy flavor electron production can provide more significant constraints on the gluon polarization, and complement other measurements of $\Delta G(\mu)$. In addition, A_{LL} measurements at higher energy collisions at the PHENIX mid-rapidity and forward-rapidity regions will also help to constraint $\Delta g(x)$ at small x region.

Acknowledgments

During I performed the analysis and wrote this PhD thesis, there were many persons who provided generous support to me. I would like to express my thanks to all of them here in this article. First of all, I would like to acknowledge Professor Dr. T. Nagae, who is the leader of our laboratory, and Lecturer Dr. T. Murakami for their careful supports and suggestions to complete this thesis. I also greatly thanks to Professor Dr. N. Saito, who has supervised and educated me since I enrolled in my graduate school. He taught me the importance of the diligent attitude to research and the broad vision to physics. I would deeply thanks to Vice-Chief Scientist Dr. Y. Akiba, who provided dedicated supports and a lot of suggestions in this analysis. He also advised me the importance to take pride in my works. And I would also like to express my gratitude to Professor Dr. K. Imai, who is the former leader of our laboratory. His strong passion toward physics always encouraged me into research.

I would like to express my great thanks to also the persons who have worked on the Muon Trigger Upgrade project together with me. Though the project is not directly related to the present analysis, the time spent in the project was essential for me to become a researcher. Scientist Dr. I. Nakagawa and Associate Professor Dr. T. Mibe, who always worked hard on the project, while they sometimes made our holidays fun by holding parties and events. They taught me how we can make our research lives interesting and worthwhile. Assistant Professor Dr. Y. Fukao also worked hard and discussed with me about physics. It was precious time for me to expand my knowledge and think what we need for the future physics. I would also deeply thank to Mr. K. Shoji and Dr. K. Karatsu for telling me abundant knowledge about electronics and data analysis. I was struck by their research attitudes to investigate any details. I express my great thanks to Dr. Y. Imazu, Mr. H. Oide, Ms. S. Park, Ms. M. Karatsu, Mr. Y. Ikeda and Mr. K. Watanabe for making my research life in RIKEN and BNL glorious. They worked on the Muon Trigger Upgrade project diligently and served as the biggest driving force of the project. I thank Professor Dr. J. Lajoie and Dr. T. Kempel for their earnest efforts to complete the trigger electronics. And I would also like to express my deep acknowledgment to Professor Dr. O. Sasaki and Professional Engineer Dr. M. Ikeno for dedicated supports to product and develop our trigger electronics.

I also express great thanks to all the persons, who worked on the present analysis of the double spin asymmetry of the heavy flavor electron production. Scientist Dr. K. Okada provided sound suggestions and comments on this work and knowledge about the nucleon spin physics to me. I would acknowledge to Dr. K. Boyle, Associate Professor Dr. K. Tanida, Scientist Dr. Y. Goto, and Dr. M. Durham for advising me a lot in my analysis and the paper preparation. Professor Dr. T. Hemmick and Dr. I. J. Choi have kindly checked my publishing article. I thank Scientist Dr. M Stratmann for detailed discussions about the constraint of the gluon polarization and preparation of the calculation codes of the cross sections. I would also like to express deep thanks to Professor Dr. B. Jacak and Scientist Dr. B. Johnson for devotedly managing the publication of my article.

I would greatly acknowledge to Chief Scientist Dr. H. En'yo for supporting us by creating comfortable environment for our research. I also deeply thanks to RIKEN and RBRC office administrators, Ms. N. Kiyama, Ms. K. Suzuki, Ms. E. Adachi, Mr. K. Mabuchi, and Ms. T. Ito, for managing my business trips and assisting my research life in RIKEN and BNL. Thanks to their helps, I could concentrate on the work. And I would like to thank to all the people who enjoyed the BNL life with me and made it fun, Mr. S. Dairaku, Dr. T. Kojo, Scientist Dr. Y. Hidaka, Associated Professor Dr. K. Kondo, Associated Professor Dr. J. Tamura, Dr. T. Kanesue, Dr. Y. Yamaguchi, Dr. Y. Aramaki, Dr. K. Nakano, Dr. K. Aoki, Dr. Y. Ikeda, Mr. H. Asano, Dr. T. Misumi, Mr. R. Akimoto, Mr. T. Kawanai, Mr. M. Nihashi, and many other students from CNS, Hiroshima University, Tsukuba University, Rikkyo University, and Tokyo Institute of Technology University. I would like to give a special thanks to Scientist Dr. Y. Watanabe, Scientist Dr. S. Yokkaichi, for kindly helping me especially on computing troubles in the present analysis and cheering me up in RIKEN.

I am deeply grateful to all the members of my laboratory. I would express deeply thanks to Associate Professor Dr. T. Kawabata for telling us the fun of nuclear physics and making our laboratory more interesting. Assistant Professor Dr. M. Niiyama and Assistant Professor Dr. H. Fujioka have abundant knowledge about hadron physics, and I learned a lot of things from them. I would also thank to Mr. A. Tokiyasu and Mr. M. Moritsu for talking and counselling each other. The time spent in my laboratory with them was precious days for me.

Last, I express grateful acknowledge to my both parents for their kind supports until my graduation, for twenty-eight years. I owe them for all of my works, and dedicate this thesis to them.

Appendix A

Deep Inelastic Scattering (DIS) Experiment

The lepton-quark scattering in the DIS has same kinematics as electron-muon scattering, which is a scattering between different Dirac particles. The diagram of the electron-muon scattering is shown in Fig. A.1(a). Using the variables in the figure, the scattering amplitude in the process can be written as

$$\begin{aligned}
|\mathcal{M}_{e\text{-mu}}|^2 &= \frac{e^4}{q^4}(L^e)_{\mu\nu}(L^{\mathrm{mu}})^{\mu\nu}, && \text{(A.1)}\\
(L^e)_{\mu\nu} &\equiv \sum_{s'_e}\left[\bar{u}(k',s'_e)\gamma_\mu u(k,s_e)\right]^*\left[\bar{u}(k',s'_e)\gamma_\nu u(k,s_e)\right] \\
&= 2L^{e(S)}_{\mu\nu} + 2iL^{e(A)}_{\mu\nu}, && \text{(A.2)}\\
(L^{\mathrm{mu}})_{\mu\nu} &\equiv \sum_{s'_{\mathrm{mu}}}\left[\bar{u}(p',s'_{\mathrm{mu}})\gamma_\mu u(p,s_{\mathrm{mu}})\right]^*\left[\bar{u}(p',s'_{\mathrm{mu}})\gamma_\nu u(p,s_{\mathrm{mu}})\right] \\
&= 2L^{\mathrm{mu}(S)}_{\mu\nu} + 2iL^{\mathrm{mu}(A)}_{\mu\nu}, && \text{(A.3)}
\end{aligned}$$

where s and s' represent initial and final spin states of the leptons, respectively. To study the initial helicity dependence, the summation is taken only for the final spin states. $L^{(S)}_{\mu\nu}$ and $L^{(A)}_{\mu\nu}$ represent symmetric and asymmetric components for the commutation of μ and ν, and can be written as

$$\begin{aligned}
L^{(S)}_{\mu\nu}(k,k') &= k_\mu k'_\nu + k'_\mu k_\nu - g_{\mu\nu}(k\cdot k' - m^2), && \text{(A.4)}\\
L^{(A)}_{\mu\nu}(k,k',s) &= \epsilon_{\mu\nu\alpha\beta} m s^\alpha (k-k')^\beta && \text{(A.5)}
\end{aligned}$$

for the electron (interchange k to p, and k' to p' for the muon), where m is mass of the electron (the muon). In the muon rest frame as shown in Fig. A.1(b), ignoring the electron mass, the helicity-dependent and helicity-independent cross sections can be represented as

$$\begin{aligned}
\frac{d\sigma_{e\text{-mu}}}{d\Omega}(E,\theta) &= \frac{4\alpha^2 E'^2}{Q^4}\frac{E'}{E}\left(\cos^2\frac{\theta}{2} + \frac{Q^2}{2m_\mu^2}\sin^2\frac{\theta}{2}\right), && \text{(A.6)}\\
\frac{d\Delta\sigma_{e\text{-mu}}}{d\Omega}(E,\theta) &= \frac{\alpha^2}{Q^2}\frac{E'^2}{E^2}\frac{E+E'\cos\theta}{m_\mu}\lambda_e\lambda_{\mathrm{mu}}, && \text{(A.7)}
\end{aligned}$$

where λ_e and λ_{mu} represent incident helicities (± 1) of electron and muon in the center-of-mass system, and m_μ represent the muon mass.

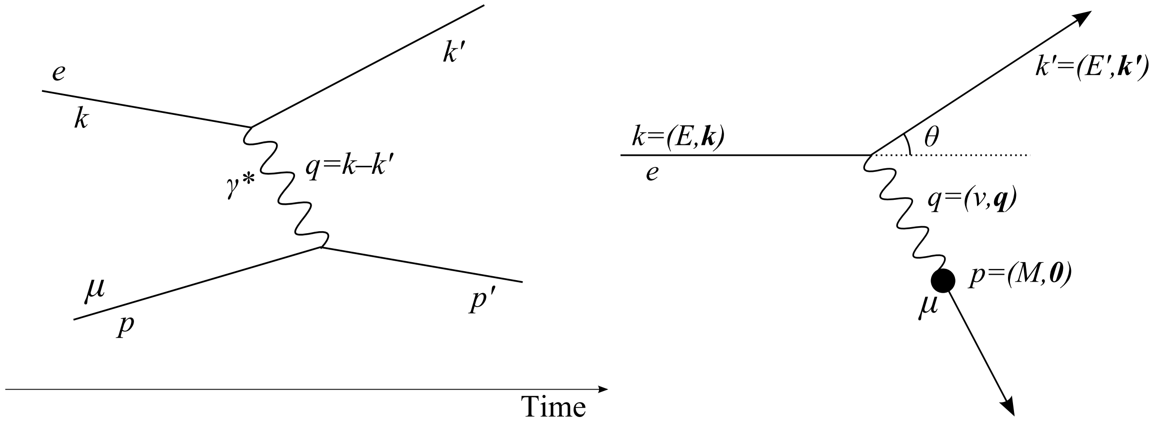

(a) Diagram of e-μ scattering. (b) Kinematics in the muon rest frame.

Figure A.1: (a) Diagram of electron-muon scattering. (b) Kinematics in the muon rest frame.

In the e-μ elastic scattering, the muon energy in the final state E' is determined from E and θ as $E' = E/(1 + (2E/m_\mu)\sin^2\theta)$. However, when we consider lepton-parton scattering, E' can not be determined only from the two variables due to the variation of the parton mass, xM. Therefore, differential form with respect to E' is better to interpret the lepton-parton cross sections. The differential of E' requires to add a delta function,

$$\delta\left(E' - \frac{E}{1 + (2E/m_\mu)\sin^2\theta}\right) = \frac{E}{E'}\,\delta\left(\nu - \frac{Q^2}{2m_\mu}\right) \tag{A.8}$$

$$= \frac{E}{E'}\frac{1}{\nu}\,\delta\left(1 - \frac{Q^2}{2m_\mu\nu}\right). \tag{A.9}$$

Then, the differential form of the cross sections (Eq. A.6 and A.7) are given as

$$\frac{d^2\sigma_{e\text{-mu}}}{d\Omega dE'}(E,\theta,E') = \frac{4\alpha^2 E'^2}{Q^4}\left(\cos^2\frac{\theta}{2} + \frac{Q^2}{2m_\mu^2}\sin^2\frac{\theta}{2}\right)\frac{1}{\nu}\,\delta\left(1 - \frac{Q^2}{2m_\mu\nu}\right), \tag{A.10}$$

$$\frac{d^2\Delta\sigma_{e\text{-mu}}}{d\Omega dE'}(E,\theta,E') = \frac{\alpha^2}{Q^2}\frac{E'}{E}\frac{E + E'\cos\theta}{m_\mu}\frac{1}{\nu}\,\delta\left(1 - \frac{Q^2}{2m_\mu\nu}\right)\lambda_e\lambda_{\mathrm{mu}}, \tag{A.11}$$

Using above results, we investigate relations between DIS cross section and quark PDF. The cross section of DIS as shown in Fig. 1.3(a) can be represented as

$$\frac{d^2\sigma_{\mathrm{DIS}}}{d\Omega dE'}(E,\theta,E') = \frac{\alpha^2}{Q^2}\frac{E'}{E}L_{\mu\nu}W^{\mu\nu}, \tag{A.12}$$

$$W_{\mu\nu}(p,q,s) \equiv \frac{1}{4\pi M}\sum_X \int \prod_{n=1}^{N_X}\left(\frac{d^3p'_n}{(2\pi)^3 2E'_n}\right) \tag{A.13}$$

$$(2\pi)^4\,\delta^4\left(p + q - \sum_{n=1}^{N_X} p'_n\right)\sum_{s_n}\langle p,s|J_\mu^\dagger|X\rangle\,\langle X|J_\nu|p,s\rangle \tag{A.14}$$

where s is initial nucleon spin and $W_{\mu\nu}$ is a hadronic tensor as a function of p, q and s, which describes hadronic interaction with virtual photon, corresponding to $L_{\mu\nu}$ of lepton. Current conservation $\partial_\mu J^\mu = 0$ requires following conditions,

$$q_\mu W^{\mu\nu} = 0, \quad q_\nu W^{\mu\nu} = 0. \tag{A.15}$$

As the result, $W_{\mu\nu}$ can be written as

$$\begin{aligned} W_{\mu\nu}(p,q,s) &= W^{(S)}_{\mu\nu}(p,q) + iW^{(A)}_{\mu\nu}(p,q,s), && \text{(A.16)} \\ W^{(S)}_{\mu\nu}(p,q) &\equiv \left(-g_{\mu\nu} + \frac{q_\mu q_\nu}{q^2}\right) W_1(\nu,q^2) \\ &\quad + \frac{1}{M^2}\left(p_\mu - \frac{p\cdot q}{q^2} q_\mu\right)\left(p_\nu - \frac{p\cdot q}{q^2} q_\nu\right) W_2(\nu,q^2), && \text{(A.17)} \\ W^{(A)}_{\mu\nu}(p,q,s) &\equiv \epsilon_{\mu\nu\alpha\beta} q^\alpha \left\{ M s^\beta G_1(\nu,q^2) + \frac{1}{M}\left((p\cdot q)\, s^\beta - (s\cdot q)\, p^\beta\right) G_2(\nu,q^2)\right\}, \\ & && \text{(A.18)} \end{aligned}$$

where M denotes the nucleon mass. W_1, W_2, G_1, and G_2 are called structure functions which describe structure of the nucleon. Especially at large Q^2 region, the structure functions represent the parton distribution, and therefore become functions of Bjorken x and almost Q^2 independent[1]. This phenomenon is called "Bjorken scaling". For convenience, following dimensionless structure functions are conventionally used,

$$\begin{aligned} F_1(x,Q^2) = MW_1, &\quad F_2(x,Q^2) = \nu W_2, \\ g_1(x,Q^2) = M^2\nu G_1, &\quad g_2(x,Q^2) = M\nu^2 G_2. \end{aligned} \tag{A.19}$$

Using above structure functions, the helicity-dependent and helicity-independent cross sections of the DIS in the nucleon rest frame can be represented as

$$\begin{aligned} \frac{d^2\sigma_{\rm DIS}}{d\Omega dE'}(E,\theta,E') &= \frac{4\alpha^2 E'^2}{Q^4}\left(\frac{2\nu}{M}\sin^2\frac{\theta}{2}F_1(x,Q^2) + \cos^2\frac{\theta}{2}F_2(x,Q^2)\right)\frac{1}{\nu}, \\ & && \text{(A.20)} \\ \frac{d^2\Delta\sigma_{\rm DIS}}{d\Omega dE'}(E,\theta,E') &= \frac{2\alpha^2}{Q^2}\frac{E'}{E}\left(\frac{E+E'\cos\theta}{M}g_1(x,Q^2) - \frac{Q^2}{M\nu}g_2(x,Q^2)\right)\frac{1}{\nu}\lambda_N\lambda_l, \\ & && \text{(A.21)} \end{aligned}$$

where λ_N and λ_l represent the initial helicities (± 1) of the nucleon and lepton in the center-of-mass system.

The DIS cross sections can be deduced also from the e-μ scattering cross sections. To translate the e-μ scattering result into the DIS cross section, we replace the muon mass m_μ to the parton mass xM, add the quark charge factor e_q^2 ($(2/3)^2$ for u, c, t and $(1/3)^2$ for d, s, b), and sum up for all quarks and anti-quarks with a weight of the unpolarized parton density $f_q(x)dx$ for helicity-independent cross section or the polarized parton

---

[1] Strictly speaking, small $\log Q^2$ dependence still appears due to higher order pQCD effect in PDF evolution as described in Sec. 1.4

density $\Delta f_q(x)dx$ for the helicity-dependent cross section. Equations A.10 and A.11 are translated to be

$$\begin{aligned}
\frac{d^2\sigma_{\rm DIS}}{d\Omega dE'} &= \sum_q e_q^2 \int_0^1 dx f_q(x) \frac{d^2\sigma_{e\text{-mu}}}{d\Omega dE'}(m_\mu \to xM) \\
&= \sum_q e_q^2 \int_0^1 dx f_q(x) \frac{4\alpha^2 E'^2}{Q^4}\left(x\cos^2\frac{\theta}{2} + \frac{\nu}{M}\sin^2\frac{\theta}{2}\right)\frac{1}{\nu}\,\delta\left(x - \frac{Q^2}{2M\nu}\right) \\
&= \frac{4\alpha^2 E'^2}{Q^4}\left(\cos^2\frac{\theta}{2}\left(\sum_q e_q^2 x f_q(x)\right) + \frac{\nu}{M}\sin^2\frac{\theta}{2}\left(\sum_q e_q^2 f_q(x)\right)\right)\frac{1}{\nu},
\end{aligned} \tag{A.22}$$

$$\begin{aligned}
\frac{d^2\Delta\sigma_{\rm DIS}}{d\Omega dE'} &= \sum_q e_q^2 \int_0^1 dx \Delta f_q(x) \frac{d^2\Delta\sigma_{e\text{-mu}}}{d\Omega dE'}(m_\mu \to xM) \\
&= \sum_q e_q^2 \int_0^1 dx \Delta f_q(x) \frac{\alpha^2}{Q^2}\frac{E'}{E}\frac{E + E'\cos\theta}{M}\frac{1}{\nu}\,\delta\left(x - \frac{Q^2}{2M\nu}\right)\lambda_N\lambda_l, \\
&= \frac{\alpha^2}{Q^2}\frac{E'}{E}\frac{E + E'\cos\theta}{M}\left(\sum_q e_q^2 \Delta f_q(x)\right)\frac{1}{\nu}\lambda_N\lambda_l.
\end{aligned} \tag{A.23}$$

Comparing between Eq. A.20 and A.22, and between Eq. A.21 and A.23, the relations between the structure functions and quark PDF are deduced as

$$F_1(x, Q^2) = \frac{1}{2}\sum_q e_q^2 f_q(x), \tag{A.24}$$

$$F_2(x, Q^2) = x\sum_q e_q^2 f_q(x), \tag{A.25}$$

$$g_1(x, Q^2) = \frac{1}{2}\sum_q e_q^2 \Delta f_q(x), \tag{A.26}$$

$$g_2(x, Q^2) = 0. \tag{A.27}$$

Therefore, the unpolarized and polarized quark PDF can be studied performing the unpolarized and polarized DIS experiments. Though this naive approximation results in $g_2 = 0$, the longitudinally polarized DIS experiment is insensitive to g_2 because the coefficient of g_2 compared with g_1 is $2Mx/(E + E'\cos\theta)$ from Eq. A.21 which is suppressed by an order of M/E. In contrast, the spin-dependent cross section with the nucleon target polarized perpendicular to the lepton spin is sensitive to g_2.

Appendix B

Polarization Measurement at RHIC

Three polarimeters are used to measure and monitor the beam polarization. Two of them are fast carbon ribbon polarimeter (pC polarimeter) [81] and polarized hydrogen gas jet target polarimeter (H-jet polarimeter) [82, 83], installed in the RHIC ring, and another is PHENIX local polarimeter [84], installed at the PHENIX experimental area. These three types of polarimeters measure a sizable transverse single spin asymmetries for elastic scattering or specific particles production. The transverse single spin asymmetry is defined as

$$A_N \equiv \frac{\sigma_L - \sigma_R}{\sigma_L + \sigma_R}, \tag{B.1}$$

where σ_L (σ_R) represents cross section of the target process with an outgoing particle in left (right) side with respect to the transverse spin direction in $p + p\uparrow$ collisions. The measurement is done by calculating a raw spin asymmetry of measured yields of the target particle, ϵ_N. The raw asymmetry can be represented as

$$\epsilon_N = PA_N, \tag{B.2}$$

where P denotes the beam polarization. Therefore, once the physics asymmetry A_N is known, the beam polarization P can be calculated as $P = \epsilon_N / A_N$. And also, by tracing ϵ_N, we can detect the fluctuation in the beam polarization during the experiment. The three types of polarimeters are introduced in this section.

The absolute value of the polarization is measured by the pC polarimeter and H-jet polarimeter. An accuracy of the polarization measurement should be achieved to $\Delta P_{\text{beam}}/P_{\text{beam}} < 5\%$ at any beam energy up to 250 GeV. Then ideal interactions for polarimetry should satisfy the following conditions:

1. well-known or measurable and non-zero analyzing power,

2. high event rate interaction (large cross-section and/or thicker target) to save data taking time,

3. similar kinematics for different beam momenta for common detector set up.

The elastic scattering of the polarized proton beam off a nuclear target A ($p\uparrow + \mathrm{A} \rightarrow p + \mathrm{A}$) in the Coulomb nuclear interference (CNI) region is an good process for this measurement. We choose proton and carbon for A. However only one measurement cannot satisfy the all requirements. Therefore, these two polarimeter complement them each other. The pC polarimeter, which satisfies item 2 and 3, serves as a semi-on-line beam polarization monitor during the beam acceleration and provides fill-by-fill offline P_{beam} results tracing the polarization changing. The H-jet polarimeter, which satisfies item 1 and 3, serves as an accurate absolute calibration for the pC polarimeter.

Fast carbon ribbon polarimeter (pC polarimeter)

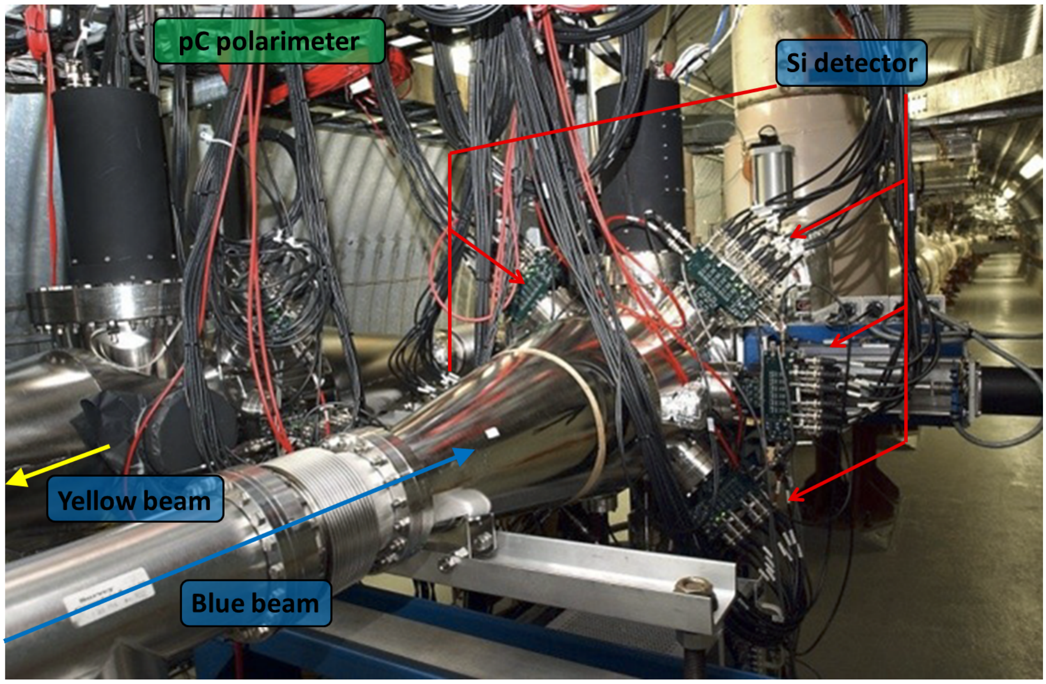

Figure B.1: Picture of pC polarimeter set up at IP12.

The pC polarimeter (Fig. B.1) is set up at the downstream position of IP12 for Blue beam and at the upstream position of IP12 for Yellow beam as shown in Fig. 2.2. This polarimeter measures the transverse single spin asymmetry in the elastic scattering between polarized proton and carbon target, A_N^{pC}, at very forward region by detecting the recoil carbons. The four-momentum transfer in the region is $-t = 0.01 - 0.02\ (\mathrm{GeV}/c)^2$. A_N^{pC} is known to be about 1.4% [81]. The target should be thin to achieve enough transparency for the recoil carbon with small energy of $0.1 - 1.0$ MeV and also for the proton beam. On the other hand, it is also required to achieve high statistics. The requirements are satisfied by using ultra-thin carbon ribbon target of $3 - 5\ \mu\mathrm{g/cm}^2$ with a width of 10 μm is used.

Figure B.2 displays the experimental setup of the pC polarimeter. The target ribbon is inserted into the beam and taken out after the measurement. Slow recoil carbons are detected by the silicon detectors placed on both sides of the target. The pC polarime-

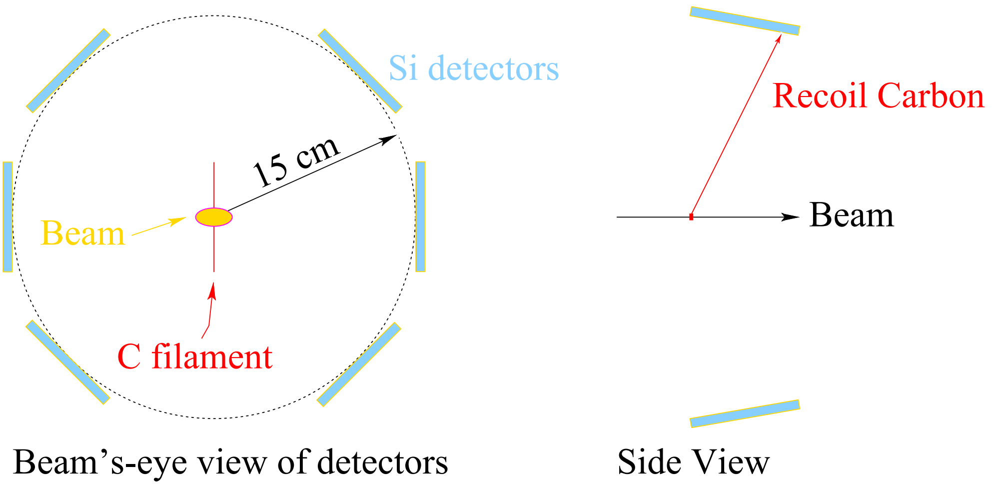

Figure B.2: The experimental setup of the pC polarimeter. Left: beam view of the detectors. The beam runs into the paper and hit the carbon ribbon target in the center of the beam pipe. Right: side view of the detectors. The beam runs from left to right. Recoil carbon is detected with the silicon detectors.

ter collects $\sim 4\times10^6$ events per one measurements which is typically one minute. It corresponds to a statistical uncertainty of 4% which is smaller compared to the systematic uncertainty of 7.2% for Blue and 9.3% for Yellow beams. The pC polarimeter confirms that the bunch by bunch polarization variation is within the uncertainty of the measurements. A_N^{pC} was not known in this energy and cannot be measured with the pC polarimeter system . In this respect, pC provides only relative variation of polarization for each fill. H-jet target polarimeter results were used to normalize the pC polarimeter results. the major source of the systematic uncertainty assigned for the beam polarizations, is the uncertainty of the absolute scale obtained with H-jet polarimeter measurement.

Polarized hydrogen gas jet polarimeter (H-jet polarimeter)

The H-jet polarimeter (Fig. B.3) is set up at IP12. This polarimeter measures the transverse single spin asymmetry in $p+p\uparrow$ elastic scattering, A_N^{pp}. Since both beam and target are polarized, A_N^{pp} can be measured by two method, namely the spin asymmetry for the target polarization and the spin asymmetry for the beam polarization. The relation between the two raw asymmetries of the yield ($\epsilon_{\rm target}$, $\epsilon_{\rm beam}$) and physics asymmetry (A_N^{pp}) is

$$A_N^{pp} = \frac{\epsilon_{\rm target}}{P_{\rm target}} = \frac{\epsilon_{\rm beam}}{P_{\rm beam}}, \tag{B.3}$$

where $P_{\rm target}$ ($P_{\rm beam}$) represents the polarization of target (beam). From this relation, the beam polarization can be determined as

$$P_{\rm beam} = P_{\rm target}\frac{\epsilon_{\rm beam}}{\epsilon_{\rm target}}. \tag{B.4}$$

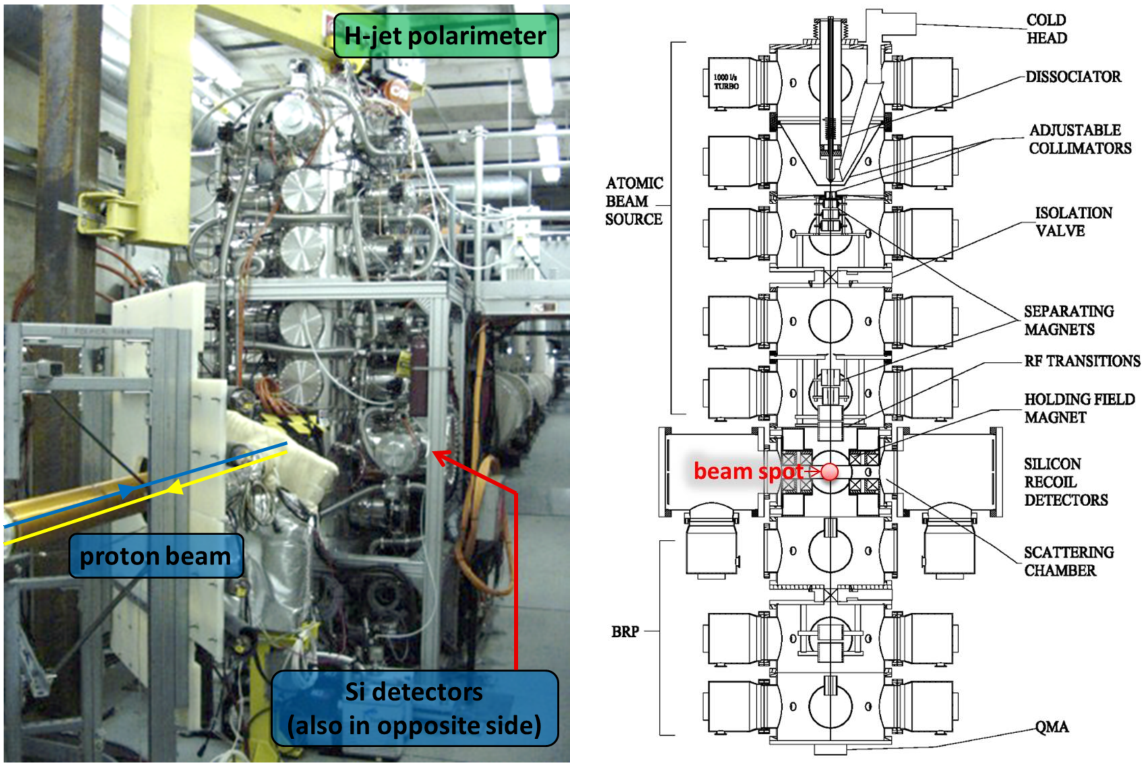

(a) (b)

Figure B.3: (a) H-jet polarimeter in IP12. (b) Schematic drawing of the H-jet polarimeter.

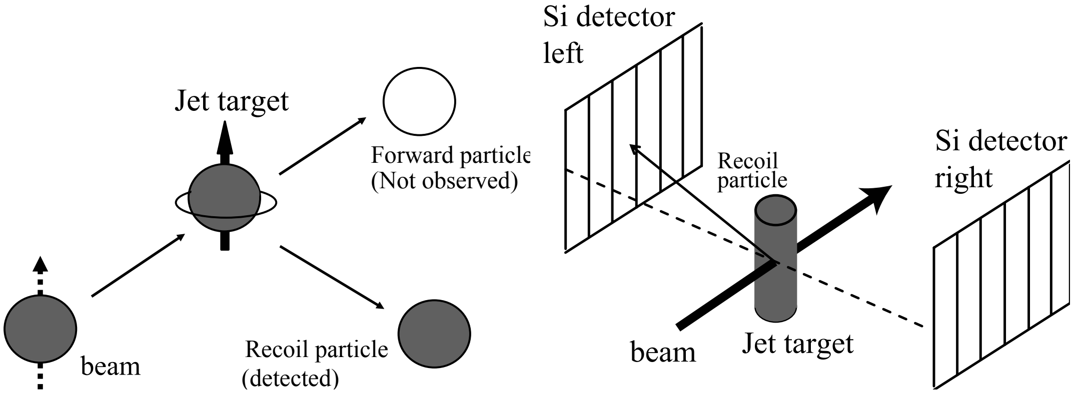

(a) (b)

Figure B.4: (a) The schematic of the $p+p$ elastic scattering process. The recoil proton is observed while the forward proton is not. (b) The experimental setup of the H-jet polarimeter. The beam penetrate the polarized jet target. The recoil proton is detected with the silicon detectors.

The advantage of the H-jet polarimeter is that we can cancel out the common factors of systematic uncertainties in $\epsilon_{\mathrm{target}}$ and ϵ_{beam}. P_{target} is measured by a Breit-Rabi polarimeter [83]. The target polarization measured in the 2004 commissioning run was

$P_{\text{target}} = 0.924 \pm 0.018$.

Figure B.4(a) illustrates the $p + p\uparrow$ elastic scattering process. the measured kinematic range is $-t = 0.001$ - 0.02 (GeV/c)^2 where the analyzing power becomes large. Figure B.4(b) shows the experimental setup of the H-jet polarimeter. The hydrogen gas jet target crosses the RHIC beam from top to bottom at a speed of 1.6×10^3 m/sec. The flow of the gas jet target is $\sim 10^2$ H atoms/sec. The target spin direction is vertical, and is reversed every 10 minutes. the recoil particle is detected with the silicon detectors which are placed on both sides of the targets.

PHENIX local polarimeter

For the study of the gluon polarization, longitudinally polarized proton collisions are necessary while the stable polarization direction of the beam in RHIC ring is vertical direction. To obtain longitudinally polarized proton collisions, the polarization orientation is rotated from vertical to longitudinal by spin rotators. The orientation in the PHENIX collision point is monitored by the PHENIX local polarimeter. This polarimeter measure single spin asymmetry of forward neutron production in $p + p$ collisions at PHENIX, A_N^n. A_N^n vanishes when the beam polarization is rotated into exactly longitudinal. Therefore the transverse component in the beam polarization can be measured with the non-zero A_N^n result. This feature is used to setup the spin rotators before the experiment and to monitor the polarization orientation and the remaining transverse component during the experiment.

Neutrons are detected with Zero-Degree Calorimeters (ZDCs) and Shower Max Detectors (SMDs). Detailed description about these detectors and the neutron detection is in Sec. 2.2.

Bibliography

[1] J. Ashman et al. *Phys. Lett. B*, 206:364, 1988.

[2] J. Ashman et al. *Nucl. Phys. B*, 328:1, 1989.

[3] J. Ellis and R.L. Jaffe. *Phys. Rev. D*, 9:1444, 1974.

[4] J. Kodaira. *Nucl. Phys. B*, 165:129, 1980.

[5] A. Airapetian et al. *Phys. Rev. D*, 75:012007, 2007.

[6] V. Y. Alexakhin et al. *Phys. Lett. B*, 647:330, 2007.

[7] V. Y. Alexakhin et al. *Phys. Lett. B*, 647:8, 2007.

[8] M.G. Alekseev et al. *Phys. Lett. B*, 690:466, 2010.

[9] M.G. Alekseev et al. *Phys. Lett. B*, 693:227, 2010.

[10] A. Adare et al. *Phys. Rev. Let.*, 103:012003, 2009.

[11] A. Adare et al. *Phys. Rev. D*, 76:051106, 2007.

[12] S. S. Adler et al. *Phys. Rev. D*, 73:091102, 2006.

[13] A. Adare et al. *Phys. Rev. D*, 79:012003, 2009.

[14] A. Adare et al. *Phys. Rev. D*, 83:032001, 2011.

[15] P. Djawotho et al. *arXiv*, 1106.5769, 2011.

[16] B.I. Abelev et al. *Phys. Rev. Let.*, 100:232003, 2008.

[17] A. Adare et al. *Phys. Rev. D*, 84:012006, 2011.

[18] Adeva B. et al. *Phys. Lett. B*, 420:180, 1998.

[19] A. Airpetian et al. *Phys. Rev. D*, 71:012003, 2005.

[20] A. Airpetian et al. *Phys. Lett. B*, 666:446, 2008.

[21] M. Alekseev et al. *Phys. Lett. B*, 680:217, 2009.

[22] M. Alekseev et al. *Phys. Lett. B*, 693:227, 2010.

[23] D. de Florian et al. *Phys. Rev. D*, 80:034030, 2009.

[24] J. Riedl, A. Schafer, and M. Stratmann. *Phys. Rev. D*, 80:114020, 2009.

[25] M. Karliner and R. W. Robinett. *Phys. Lett. B*, 324:209, 1994.

[26] I. Bojak and M. Stratmann. *Phys. Rev. D*, 67:034010, 2003.

[27] I. Bojak. *ArXiv:hep-ph*, 0005120, 2000.

[28] S.S. Adler et al. Single electrons from heavy-flavor decays in p+p collisions at sqrt(s)=200gev. *Phys. Rev. Let.*, 96:032001, 2006.

[29] A. Adare et al. *Phys. Rev. C*, 84:044905, 2011.

[30] S.D. Bass. *The Spin Structure of the Proton.* World Scientific, 1989.

[31] S.D. Bass. *Rev. Mod. Phys.*, 77:1257, 2005.

[32] G. Sterman et al. *Rev. Mod. Phys.*, 67:157, 1995.

[33] M. Anselmino et al. *Phys. Rep.*, 261:1, 1995.

[34] E.W. Hughes et al. *Ann. Rev. Nucl. Part. Sci.*, 49:303, 1999.

[35] B.W. Fillipone et al. *Adv. Nucl. Phys.*, 26:1, 2001.

[36] R.L. Jaffe et al. *ArXiv/hep-ph*, 9602236, 1996.

[37] B. Lampe et al. *Phys. Rept.*, 332:1, 2000.

[38] V. Barone et al. *Phys. Rep.*, 359:1, 2002.

[39] R.L. Jaffe and N. Saito. *Phys. Lett. B*, 382:165, 1996.

[40] F.E. Close. *An Introduction to Quarks and Partons.* Academic, New York, 1979.

[41] F.E. Close and R.G. Milner. *Phys. Rev. D*, 44, 1991.

[42] S.B. Libby and G. Sterman. *Phys. Rev. D*, 18:3252, 1978.

[43] J.C. Collins et al. *Nucle. Phys. B*, 261:104, 1985.

[44] J.C. Collins et al. *Nucle. Phys. B*, 394:169, 1993.

[45] J. Babcock et al. *Nucle. Phys. B*, 19:1483, 1979.

[46] G. Bunce et al. *Annu. Rev. Nucl. Part. Sci.*, 50:525, 2000.

[47] G. Altarelli. *Phys. Rept.*, 81:1, 1982.

[48] J. Pumplin et al. *JHEP*, 07:012, 2002.

[49] H.L. Lai et al. *Phys. Rev.*, D82:074024, 2010.

[50] A.D. Martin et al. *Eur. Phys. J.*, C63:189, 2009.

[51] R.D. Ball et al. *Nucl. Phys.*, B849:296, 2011.

[52] R.D. Ball et al. *arXiv*, page 1107.2652, 2011.

[53] F.D. Aaron et al. *JHEP*, 1001:109, 2010.

[54] S. Alekhin et al. *Phys. Rev.*, D81:014032, 2010.

[55] M. Gluck et al. *Eur. Phys. J.*, C53:355, 2008.

[56] P. Jimenez-Delgado and E. Reya. *Phys. Rev.*, D79:074023, 2009.

[57] R.L. Jaffe and A. Manohar. *Nucl. Phys. B*, 337:509, 1990.

[58] A. Chodos et al. *Phys. Rev. D*, 9:3471, 1974.

[59] P.N. Bogoliubov. *Ann. Inst. H. Poincare*, 8:163, 1967.

[60] R.L.. Jaffe. *Proc. Topical Conf. Baryon Resonances*, 1976.

[61] J. Beringer et al. *Phys. Rev. D*, 86:010001, 2012.

[62] E. Leader et al. *Phys. Rev. D*, 73:034023, 2006.

[63] G. Altarelli et al. *Phys. Lett. B*, 212:391, 1988.

[64] R.D. Carlitz et al. *Phys. Lett. B*, 214:229, 1988.

[65] D.L. Adams et al. *Phys. Lett. B*, 336:269, 1994.

[66] Airapetian A. et al. *JHEP*, 1008:130, 2010.

[67] Adeva B. et al. *Phys. Rev. D*, 70:012002, 2004.

[68] C. Adolph et al. *arXiv*, 1202.4064, 2012.

[69] M.G. Alekseev et al. *Phys. Lett. B*, 676:31, 2009.

[70] D. de Florian et al. *Phys. Rev. Lett.*, 101:072001, 2008.

[71] E. Leader et al. *Phys. Rev. D*, 82:114018, 2010.

[72] L. Adamczyk et al. *arXiv*, 1205.2735, 2012.

[73] A. Manion et al. *J. Phys. Conf. Ser.*, 295:012070, 2011.

[74] M. Glück et al. *Phys. Rev. D*, 63:094005, 2001.

[75] M. Hirai et al. *Nucl. Phys. B*, 813:106, 2009.

[76] T. Sjostrand et al. *arXiv*, 0710.3820, 2007.

[77] T. Sjostrand et al. *JHEP*, 0605:026, 2006.

[78] A. Adare et al. *Phys. Rev. D*, 83:052004, 2011.

[79] GEANT 3.2.1 Manual. `http://wwwasdoc.web.cern.ch/wwwasdoc/pdfdir/geant.pdf`, 1994.

[80] A. N. Zelenski et al. *Hyperfine Interaction*, 127:475, 2000.

[81] O. Jinnouchi et al. *arXiv:nucl-ex*, 0412053, 2004.

[82] H. Okada et al. *Phys. Lett. B*, 638:450, 2006.

[83] H. Okada et al. *arXiv*, 0712.1389, 2007.

[84] Y. Fukao et al. *Phys. Lett. B*, 650:325, 2007.

[85] K. Adcox et al. *Nucl. Instrum. Methods Phys. Res., Sect. A*, 499:469, 2003.

[86] K. Adcox et al. *Nucl. Instrum. Methods Phys. Res., Sect. A*, 499:480, 2003.

[87] K. Adcox et al. *Nucl. Instrum. Methods Phys. Res., Sect. A*, 499:489, 2003.

[88] M. Aizawa et al. *Nucl. Instrum. Methods Phys. Res., Sect. A*, 499:508, 2003.

[89] L. Aphecetche et al. *Nucl. Instrum. Methods Phys. Res., Sect. A*, 499:521, 2003.

[90] H. Akikawa et al. *Nucl. Instrum. Methods Phys. Res., Sect. A*, 499:537, 2003.

[91] M. Allen et al. *Nucl. Instrum. Methods Phys. Res., Sect. A*, 499:549, 2003.

[92] W. Anderson et al. Design, construction, operation and performance of a hadron blind detector for the phenix experiment. *Nucl. Instr. and Meth. A*, 646:35, 2011.

[93] Z. Fraenkel et al. *Nucl. Instr. and Meth. A*, 546:466, 2005.

[94] A. Kazlov et al. *Nucl. Instrum. Methods Phys. Res., Sect. A*, 523:345, 2004.

[95] BNL Instrumentation Division. `http://www.inst.bnl.gov/`.

[96] C. Y. Chi et al. *Proceedings of the 2007 IEEE NSS/MIC Conference*, 2007.

[97] K. Barish. Studying the Spin Structure of Nucleons with High-Energy Polarized Protons. `http://www.phenix.bnl.gov/WWW/trigger/pp/c-arm/doc/Ken001010/doe-proposal.ps`. restricted to PHENIX collaborators.

[98] S.S. Adler et al. *Nucl. Instrum. Methods Phys. Res., Sect. A*, 499:560, 2003.

[99] J. T. Mitchell et al. *Nucl. Instrum. Meth.*, A482:491, 2002.

[100] K. Chikanian et al. *Nucl. Instrum. Meth.*, A371:480, 1996.

[101] D. Ben-Tzvi et al. *Pattern Recognition Lett.*, 11:167, 1990.

[102] M. Ohlsson et al. *Comp. Phys. Commun.*, 71:77, 1992.

[103] J. Myrheim and L. Bugge. *Nucl. Instrum. Meth.*, 160:43, 1979.

[104] H. Torii. *Ph. D. thesis*, 2004.

[105] K. Karatsu. *Ph. D. thesis*, 2011.

[106] T. C. Awes et al. *arXiv*, nucl-ex/0202009, 2002.

[107] Y. Fukao. *Ph. D. thesis*, 2007.

[108] K. Aoki. *Ph. D. thesis*, 2009.

[109] S.S. Adler et al. *Phys. Rev. Let.*, 91:241803, 2003.

[110] G.D. Lafferty and T.R. Wyatt. *Nucl. Instrum. Methods Phys. Res., Sect. A*, 355:541, 1995.

[111] M. Cacciari, P. Nason, and R. Vogt. *Phys. Rev. Let.*, 95:122001, 2005.

[112] RHIC Polarization Measurement at 2009 pp collisions. `http://www4.rcf.bnl.gov/~cnipol/pubdocs/Run09Offline/`.

[113] A. Mukherjee et al. *Phys. Rev. D*, 72:034011, 2005.